

UNIVERSITY OF STRATHCLYDE

ELECTRONIC & ELECTRICAL ENGINEERING DEPARTMENT

CENTRE FOR ULTRASONIC ENGINEERING

3D-Printing Technology Applied to the Development of Bio-Inspired Functional Acoustic Systems

Author:

Roger DOMINGO-ROCA

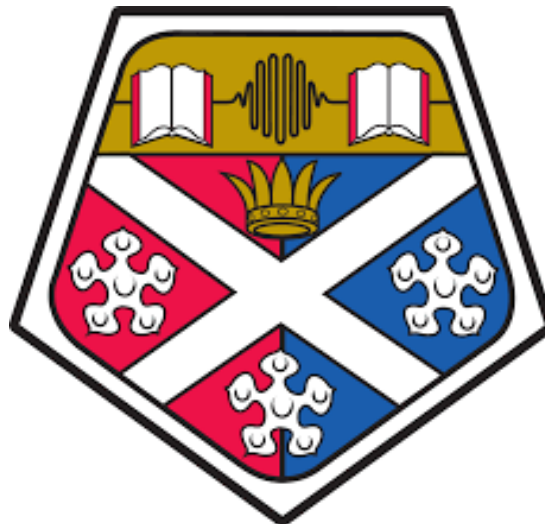
Supervisors:

Prof. James WINDMILL

Dr. Joseph JACKSON

Submitted for the degree of Doctor of Philosophy,

November 12, 2018



This thesis is the result of the author's original research. It has been composed by the author and has not been previously submitted for examination which has led to the award of a degree.

The copyright if this thesis belongs to the author under the terms of the United Kingdom Copyright Acts as qualified by University of Strathclyde Regulation 3.50. Due acknowledgement must always be made of the use of any material contained in, or derived from, this thesis.

Signed:

Date:

The thesis work has been published in part. The candidate carried out all the experimental work and contributed to all data analysis and writing of the manuscripts.

Signed:

Date:

List of Acronyms

1D - One-dimensional

2D - Two-dimensional **3D** - Three-dimensional

BEMA - Bisphenol-A ethoxylate dimethacrylate

BS - Beam splitter

CAD - Computer-aided design

CT - Computer tomography

DCD - Direct current demagnetization

DNA - Deoxyribonucleic acid

DPOAE - Distortion product otoacoustic emissions

EAP - Electroactive polymers

EBM - Electron beam melting

EDS - Electron dispersive spectroscopy

EMM - Effective modal mass

EMMF - Effective modal mass fraction

FB - Folded body

FDM - Fused deposited modelling

FEA - Finite element analysis

FEM - Finite element model

FFT - Fast Fourier transform

FRP - Free radical photopolymerization

FVF - Filler volume fraction

FWF - Filler weight fraction

HIL - Linear isotropic homogeneous

IPA - Isopropyl alcohol

IRM - Isothermal remanent magnetization

ISS - International Space Station

LENS - Laser engineered net shaping

LDV - Laser Doppler vibrometry

LOM - Laminated object manufacturing

MEMS - Microelectromechanical systems

MJM - Multi-Jet modelling

MPF - Modal participation factor

MWCNT - Multi-wall carbon nanotubes

N/S - North-South

PEGDA - Poly(ethylene glycol) diacrylate

PI - Photoinitiator

PLT - Paper lamination technology

PMN-PT - Lead magnesium-lead titanate

PS - Photoinitiating system

PSL - Plastic sheet lamination

PV - Pyriform vesicle

RFP - Rapid freeze prototyping

RP - Rapid prototyping

SEM - Scanning electron microscopy

SLS - Selective laser sintering

SPL dB - Sound pressure level expressed in decibels

STL - Stereolithography

TM - Traveling wave

TW - Traveling wave

UV - Ultraviolet

VSM - Vibrating sample magnetometer

Abstract

Examples of bio-inspired technology can be found almost everywhere in society: robots with specific capabilities, materials with unique physical and chemical properties, aerodynamic systems, and architectonic structures are a few examples of taking profit of evolution-driven processes to solve common engineering problems. One field of research taking advantage of bio-inspiration is that of acoustical engineering, aiming to find solutions to problems arising from the miniaturisation of microphones and loudspeakers. Studying the auditory organs of insects to seek inspiration for new design structures is one of the best ways to solve such an important problem. Another discipline of science that has experienced a research boom is that of materials science, as development of new materials has attracted the attention of researchers. In addition, three-dimensional (3D) printers have contributed to further development in materials science making the production process more efficient.

The aim of this research is to bring these fields of science together to develop novel bioinspired, polymer-based sensors presenting functional specific acoustic properties after 3D-printing. While the study of complex biological hearing systems provides inspiration to develop sensors featuring specific properties, the use of polymer-based materials allows the customization of the manufacturing process, as the produced parts adapt to the desired needs.

In this thesis one such insect auditory system that has been thoroughly studied is that of the desert locust *Schistocerca gregaria* as it presents a simple structure that allows for acoustic frequency selectivity and displays nonlinear acoustic phenomena. Prior to the development of a bio-inspired system, a mathematical description of the mechanical response of such a structure is presented. Furthermore, the physical behaviours measured on the locust tympanal membrane have been studied using finite element analysis. The 3D-printed functional sensors have been used to determine the degree of accuracy between experimental and theoretical results.

Acknowledgements

First and foremost I would like to express my thanks to my supervisors Prof. James Windmill and Dr. Joseph Jackson for all their advice, close support, encouragement, and patience throughout my PhD research. I am very thankful for all the opportunities and resources provided which contributed to a unique research experience. Without their knowledge and expertise in different fields of scientific research this thesis would have not been possible.

I would also like to thank Elizabeeth Klenschi for her deep knowledge and expertise in the field of biology, as well as for all the endless locust-related conversations we have had in the last three and a half years. I am also thankful to all the other members of the CUE Bioacoustics team, past and present, in particular Dr. David Mackie for his technical support and advice involving the equipment in the CUE Bioacoustics Main Lab. Special thanks to Grant Smile for his guidance, advice, and help with screen-printing techniques and mechanical mixing machinery, as well as for his endless help when poling the piezoelectric composites. Thanks also to Jose Guerreiro, Dr. Jeremy Gibson, Dr. Benjamin Tiller, Dr. Andrew Reid, Dr. Francesco Guarato, Dr. Yansheng Zhang, and Walter Galbraith for many helpful discussions about electronics, biology, 3D-printing, and finite element simulation techniques, which all have been of extreme importance and relevance for this PhD project. I would also like to thank the rest of the CUE members, as even if they have been involved in the group for a small amount of time, they all have been very encouraging and helpful. I do not want to forget about Tommy, Rhona, and Lynn, as without their support, help, kind words, and endless off-topic conversations the research time would have not been as enjoyable as it has been.

Thank you also to Prof. Thomas Thomson and Dr. Alex Lincoln from the University of Manchester for providing me with the opportunity to visit and use their facilities and technical equipment as well as providing their support and deep knowledge about magnetic properties of materials. Thanks also to Dr.

Milovan Cardona for his guidance and help using the mechanical testing techniques and SEM machinery at the University of Strathclyde Biomedical Engineering group. I would also like to thank Prof. Jordi Sort from the Universitat Autònoma de Barcelona for his unconditional support during these three and a half years and the uncountable emails, chats, phone, and face-to-face conversations we have had about several fields of science, specially about nanoindentation and mechanical and magnetic properties of materials, which have been of maximal relevance for the writing of this thesis.

Thanks to European Research Council for providing funding for this research under the European Union's Seventh Framework Programme (FP/2007-2013)/ERC Grant Agreement n.[615030].

Contents

List of Figures	xi
List of Tables	xxiii
1 Introduction	1
1.1 Basic principles of sound	4
1.2 Interaction of sound waves with solid structures	7
1.2.1 Reflection	8
1.2.2 Refraction	9
1.2.3 Diffraction	10
1.2.4 The Doppler effect	11
1.3 Attenuation of sound	12
1.4 Hearing systems in biology	13
1.4.1 Distortion product otoacoustic emissions	14
1.4.2 The Duffing oscillator	17
1.4.3 Hearing systems: the locust tympanum membrane	19
2 3D Printing	27
2.1 Polymers: types and main characteristics	29
2.1.1 Natural polymers	29
2.1.2 Synthetic polymers	30
2.2 Classification of polymers	31
2.2.1 Classification based on their chain structure	31
2.2.2 Mode of polymerization	31
2.2.3 Physical properties	32

2.3	Development of 3D-printable materials	33
2.3.1	The polymerization process	36
2.3.2	Cross-linking	39
2.3.3	Photopolymerization	40
2.3.4	The stereolithography process	45
2.3.5	Importance of nanoparticle size	51
3	Mechanical Properties	53
3.1	Mechanical characterization of materials	54
3.1.1	Concepts of strain and stress	54
3.1.2	Elastic properties of materials	56
3.2	Nanoindentation	61
3.3	The Oliver-Pharr method	65
3.4	Composite materials	67
3.4.1	Stiffness	68
3.4.2	Strength	69
3.5	Theoretical modelling of mechanical properties	70
3.5.1	Kerener equation	71
3.5.2	Einstein equation	71
3.5.3	Sato and Furukawa model	71
4	Basic Concepts of Piezoelectricity and Magnetism	73
4.1	Piezoelectricity	73
4.1.1	Introduction	73
4.1.2	Mathematical description	75
4.1.3	Piezoelectricity in polymers	76
4.2	Magnetism	82
4.2.1	Introduction	82
4.2.2	Susceptibility and permeability	86
4.2.3	Diamagnetism	88
4.2.4	Paramagnetism	88
4.2.5	Ferromagnetism	89

4.2.6	Antiferromagnetism	89
4.2.7	Ferrimagnetism	90
4.2.8	Superparamagnetism	90
5	Experimental Techniques	92
5.1	3D Laser Doppler vibrometer	92
5.1.1	Resolution limits and sources of error of the LDV	95
5.2	Finite element simulation	96
5.2.1	FEM process	98
5.2.2	Eigenproblem simulations	102
5.2.3	Acoustic-structure interaction	103
5.3	Vibrating sample magnetometer	104
5.4	Scanning electron microscopy	109
6	Experimental results	111
6.1	Describing the locust's tympanum membrane: mathematical models	111
6.1.1	Mathematical models	113
6.1.2	Variations of the model	120
6.1.3	Understanding the generation of DPOAEs	122
6.1.4	Application of the mathematical models	126
6.2	Development of 3D-printable materials	132
6.2.1	Synthesis of 3D-printable materials	134
6.2.2	Morphological study	136
6.2.3	Mechanical properties	139
6.2.4	Piezoelectric composite materials	151
6.2.5	Magnetic composite materials	153
6.3	3D-printed parts and sensors	165
6.3.1	Cochlea-based passive sound amplifiers: mechanical resonators	165
6.3.2	Locust TM-based resonators	168
6.3.3	Functional bioinspired systems	181
7	Conclusions and Future Work	187

A Solution to the single Duffing oscillator	i
B Application of the perturbation method to solve the double-frequency driven single Duffing oscillator	v
C Solution to a system of coupled Duffing oscillators	x

References

List of Figures

- 1.1 Sketch of the propagation of an acoustic longitudinal wave. When the particles of the medium compress, an increase of pressure takes place, whereas when the particles of the medium are rarefacted, a decrease of pressure occurs. Pressure attenuates as a function of $1/r$, where r is the distance from the sound source. Image obtained from [23] 5
- 1.2 Sketch of the phenomenon of reflection on a flat surface when an incident wave hits a hard or a soft boundary. The angle φ represents the incidence angle of the incoming wave, which is the same as the reflection angle. It must be noted that the acoustic wave will not be totally reflected as transmission will also take place. 8
- 1.3 (a) Sketch of refraction when a wave is transmitted from one medium with associated refraction index n_1 to a different medium with different refraction index n_2 . φ_1 is the incidence angle of the wave with the vertical, and φ_2 is the refraction angle of the wave when transmitted to the second medium, and (b) shows an example of light refraction where it can be clearly seen how the diagonal lines change their direction after being refracted by a water-filled glass. 9
- 1.4 Schematic representation of the motion (left to right) of an object (solid black circle) with a velocity v , and emitting at a frequency f_s . An observer located at the right-hand side of the emitter will receive a higher frequency than f_s and a lower wavelength, as it can be checked using Eq.(1.1). On the other hand, a receiver located at the left-hand side of the emitter, will receive a lower frequency than f_s . This increment and decrease of frequency is represented by the circular lines getting closer and further away, respectively. 11
- 1.5 Sketch of the spherical coordinates system, where θ is defined as the *azimuth* angle in the xy -plane ($0 \leq \theta \leq 2\pi$), φ is defined as the *polar* (or *zenith*) angle in the positive z -axis ($0 \leq \varphi \leq \pi$), and r is the radius of the sphere. The boldface quantities represent the vectors of the spherical-coordinate system. 12

1.6	Graphical representation of ideal intermodulation. The abscissa shows the frequency in kHz and the ordinate represents the amplitude of the motion in arbitrary units. In this example the input frequencies are $f_1 = 10$ kHz and $f_2 = 12$ kHz, to which corresponds the major value of amplitude (in theory they should have the same amplitude, but when working with biological systems one needs to be slightly larger than the other for reasons discussed later in this Chapter). The peaks corresponding to $f_{m,n}$ frequencies have a decreasing value in amplitude as their order increase. Image obtained from [50].	15
1.7	Comparison of a linear and a Duffing system. Whereas the linear system presents one unique value of amplitude at each frequency, a Duffing oscillator can present up to three values of amplitude at given frequencies. The dotted part of the graph represents the continuity of the function, but it does not plot real values. When the curve bends to the right, the system behaves like a hardening spring, whereas when it bends to the left, it behaves like a softening spring. Image obtained from [52].	17
1.8	Scanning electron microscopy (SEM) image of the locust TM (right ear). The different regions of the TM can be observed in different shades of grey and outlined by dashed lines. Low and high frequencies are detected more efficiently in the thick and thin regions, respectively. The folded body (FB) is attached to the thick membrane and it is outlined with a continuous ellipse in the most anterior region of the TM. The area surrounding the pyriform vesicle (PV), is also highlighted with a continuous line on the thin membrane. Image kindly provided by Prof. James Windmill from his study on the presence of traveling waves in migratory locusts [11] and edited by Roger Domingo-Roca.	20
1.9	SEM image of the cavities present within the locust TM. The black arrow indicates an artefact formed by the redeposition of liquid during focused ion beam milling. This image suggests that these cavities are present around the pyriform vesicle (PV) of the locust tympanum membrane (TM), helping the propagation of mechanical waves generated by acoustic stimulation toward relevant scholopidial attachment points. Image obtained from [77].	25

2.1	The left hand side image shows the basic structure of a hydrocarbon (ethane, C_2H_6), whereas the right hand side image shows the basic structure of an amino acid, where three main parts can be distinguished: the amino group (in blue), the carboxyl group (in red), and the radical (side chain, in light grey).	36
2.2	Average molecular weight of chain-growth and step-growth processes as a function of monomer concentration. This graph shows how the average molecular weight of chain-growth and step-growth polymers changes with monomer concentration. This image also shows that whereas step-growth polymers will slowly increase their average molecular weight, the opposite will be observed in chain-growth polymers. Graph obtained from the <i>Polymer database</i> , [125].	39
2.3	Schematic representation of cross-linking in a polymer. The dashed lines between solid black circles (reactive ends) represent the short-length cross-linking chains whereas solid lines represent polymeric chains. This representation gives an idea of why a higher density of cross-links provides a higher degree of three-dimensional stability.	40
2.4	Sketch of the different steps of the free radical polymerization process. In the initiation step, a source of energy breaks a carbon-carbon bond and two reactive units with a free electron are created. During the propagation step, this free electron reacts with the electrons of carbon-carbon double bonds, generating a new bond between the initial fragment and the monomer. Termination process happens when two free electrons are paired together. Image redrawn from [130].	44
2.5	Full cycle to build one layer when using the STL approach of ASIGA. Firstly, the building block approaches to the building tray where liquid polymer is placed. Once the building block makes contact with the building tray membrane, the first layer of the part is projected onto it (yellow triangle), and the slider removes the excess of polymer. When the slider has completed its trajectory, ultraviolet light (purple triangle) is applied onto the first layer such that the liquid polymer solidifies. Finally, the building block is removed from the building tray and the full process is repeated projecting all the layers composing the sample.	47
2.6	Sketch of the stairstepping effect appearing when 3D-printing a part using the STL method. In this representation it can be seen how the layer thickness influences the stairstepping effect; the thinner the layer is, less pronounced this effect will be.	48

2.7	Sketch of placement of the supports when 3D-printing solid and hollow parts. The solid part only needs to be supported by external supports, whereas the hollow part, apart from the external supports, also needs internal supports to avoid the part to collapse.	49
3.1	Sketch of shearing deformation of a material when a load is applied transversely to the specimen, as indicated by the big arrow on top. Here it can be seen how the different layers of the material are displaced when shearing is applied.	58
3.2	Sketch of shear strain generated on a sample of initial length L . The total shear displacement at a shear angle γ is denoted by δ	58
3.3	Sketch of a stress-strain curve illustrating the phenomenon of elastic recovery during plastic deformation, where the two loading processes and the unloading process are shown. This figure also shows the two yield points, denoted by σ_{y0} and σ_{yi} , and highlighting the elastic strain recovery using a dashed vertical line.	60
3.4	Load-displacement ($P - h$) curve obtained in a nanoindentation assay. Three parts can be differentiated: the loading stage (where the load is applied and the corresponding penetration depth is recorded in small increments of P), the holding segment (where P is kept constant for a certain time, leading to a uniform penetration depth), and the unloading stage (where P is removed and the corresponding penetration depth is recorded).	62
3.5	Typical pop-in events in a nanoindentation load-displacement curve. Pop-in events are indicated with arrows during the loading stage, which appear due to dislocations nucleation, rupture of thin films, strain transfer across grain boundaries, crack formation, or phase transformations.	63
3.6	Sketch of the different tip geometries that can be used to perform nanoindentation tests.	63
3.7	Schematic representation of the indenter at specimen surface at full load and unload and the parameters characterising the contact geometry.	66
4.1	(a) Shows a sketch of the crystallographic structure of BaTiO_3 , where the Ba^{2+} , O^{2-} , and Ti^{4+} ions are highlighted. Image obtained from [167]. (b) Shows a sketch of three different ways of polarization. The top-left, top-right, and bottom sketches correspond to electronic, ionic, and orientational, respectively.	74

4.2	Classification of two-phase (ceramic-polymer) composites with respect to connectivity. Two configurations are shown for connectivities 3-2 and 3-3. This representation shows how piezoelectric structures embedded within polymeric matrices can be distributed. . . .	78
4.3	Sketch of the relationship between coercive field and magnetic NP size, discerning between single- and multi-domain regimes, as well as the superparamagnetic and the ferromagnetic behaviours. For small very small nanoparticle (NP) sizes, the coercive field is zero as they are single domain NPs and thermal agitation is non-negligible and generates fluctuations, providing eventual zero coercive field (superparamagnetic regime). As NP size increases, they are still single domain but in a regime where thermal agitation is not relevant, and the coercive field starts increasing within a regime where inversion of magnetization happens via coherent rotation. As NP size keeps increasing, they become multidomain and the rotation of the magnetic domains takes place through the movement of the domain walls within the NP, leading to lower coercive fields.	87
5.1	Sketch of the schematic set up of the used LDV. BS_i are beam splitters and $\lambda/4$ is a quarter wave plate. The Bragg cell (BC) is an acousto-optical modulator that creates an additional frequency-shifted beam for the reference beam, allowing the interferometer to be directional. Scanning mirrors, which are controlled by the Polytec software, allow for accurate positioning and scanning of the surface to be measured.	93
5.2	Screen shot of the COMSOL interface when the second step (building the geometry) is finished. It can be seen in the top part of the left-hand-side tree under Model Builder that Global Definitions can be introduced before building the geometry of the system. COMSOL presents a geometry builder that allows the creation of different shapes (in this case introducing a cylinder, as it can be seen in the building tree under Model Builder). . .	99
5.3	Screen shot of the COMSOL interface after applying the mesh, which can be finely tuned by the user by selecting different mesh geometries and sizes. A full customization of the mesh is also possible as mesh gradients can be applied, as well as it is possible to define different mesh sizes for different domains.	101
5.4	Schematic representation of the vibrating sample magnetometer. The sample is placed between the two pick-up coils that detect the change of magnetic field when the sample is vibrated.	105

5.5	Hysteresis loops for a ferromagnetic material. (a) Shows the $M - H$ plot, with remanent magnetisation at $H = 0$ and intrinsic coercive field denoted by H_{ci} (field at which magnetisation is reversed). M_r is the saturation magnetisation. (b) Shows the $B - H$ plot, with remanent induction B_r at $H = 0$ and coercive field H_c . Figure obtained from [216].	106
5.6	Schematic $\Delta I(H)$ curves illustrating different coupling regimes. A sharp positive delta-I peak is associated with exchange coupled systems, whereas a broad, negative delta-I peak is attributed to dipolar coupled systems. Image obtained from [214].	109
5.7	Types of electrons and radiation generated inside the sample in a SEM when irradiated with an electron beam. The type of electrons and radiation determine the penetration depth of the electrons within the sample.	110
6.1	SEM image of the locust TM (as presented in Fig. 1.8) in which the studied transect, composed by 13 points, is shown in yellow. The points were named correspondingly to their proximity to the FB, number 1 being the closest one and 13 the one located further away of it. SEM image obtained by Prof. James Windmill, published in his work <i>Tympanal travelling waves in migratory locusts</i> [11] and edited by Roger Domingo-Roca. Transect line representation in accordance to measurements performed by our colleagues.	112
6.2	Simplified mechanical representation of the locust's tympanum membrane. The three masses represent different experimental points and the fixed point (represented by a vertical line with diagonal smaller lines) represents the FB.	113
6.3	Sketch of a 2D array of coupled oscillators that describe the membrane. The oscillators and the springs could present, respectively, different values of m and k . As a further consideration, one could also assume that the oscillators are not only connected to their first neighbours (as denoted by continuous springs), but also to their second-second order neighbours by springs of the same/different k (as denoted by dashed springs).	122
6.4	Sketch of two Duffing coupled oscillators. This model needs to include both a dashpot and a spring between each oscillator to account for viscous effects.	125
6.5	The top-left graph shows the mechanical deflection of the locust TM in the time domain of point 1 (P1) of the studied transects (as shown in Fig. 6.1) when driven at 5 kHz.	126

6.6	(a)-(d) Show the fitting of the experimental data using the unforced coupled mathematical model described previously in this Chapter for P1, P5, P6, and P13 respectively. The fitting was done over 4.5 ms, but here only 4 cycles are shown over 0.875 ms.	127
6.7	(a)-(d) Show the fitting of the experimental data using the forced coupled mathematical model described previously in this Chapter for P1, P5, P6, and P13 respectively. The measurements were obtained at 5 kHz. The fitting was done over 4.5 ms, but here only 4 cycles are shown over 0.875 ms.	129
6.8	(a)-(d) Show the fitting of the experimental data using the forced coupled complex mathematical model described previously in this Chapter for P1, P5, P6, and P13 respectively. The fitting was done over 4.5 ms, but here only 4 cycles are shown over 0.875 ms.	130
6.9	The left-hand-side image shows the response of the locust membrane near the PV in both y - and z - axes when excited at 1 and 1.1 kHz at the same time. It can be observed that maximum velocity happens at the driving frequencies. Furthermore, generation of harmonics and distortion product otoacoustic emissions can also be observed. The right-hand-side graph shows the simulation obtained from the proposed mathematical model described in this section.	133
6.10	(a) Shows the molecular structure of Irgacure 819 and (b) shows its light absorption spectrum with the peak highlighted with a black dashed line. Image obtained from [226].	133
6.11	SEM images of screen-printed BaTiO ₃ NPs (33 wt%) embedded within BEMA. (a) Cross-section of one of the screen-printed magnetic samples in which the layers can be seen, (b) Cross-section of one of the screen-printed piezoelectric samples at higher magnification, (c) On-top image that shows NP agglomeration on the surface of the composite, and (d) One of the screen-printed samples when one of the layers has been removed.	137
6.12	SEM images of the 3D- and screen-printed magnetite NPs (50 wt%) embedded within PEGDA. (a) Cross-section of one of the 3D-printed magnetic samples in which the 3D-printed layers can be seen, (b) The edge of one of the 3D-printed samples, (c) Cross section of one of the screen printed samples, and (d) One of the screen-printed samples when one of the layers has been removed.	138

6.13 (a), (b), and (c) show, respectively, the simulation results of the mechanical properties (elastic modulus, E_c , longitudinal velocity, $v_c^{(L)}$, and acoustic impedance, Z_c) as a function of the filler volume fraction when working with particulate composite materials. Plots obtained when using Eq.(6.71)-(6.74).	141
6.14 (a) and (b) show the load-displacement curves of BEMA and PEGDA, respectively, with Iracure 819 (1 wt%) and SUDAN I (0.2 wt%), without any NP loading. BEMA presents an elastic behaviour (as the initial penetration depth is fully recovered) whereas PEGDA shows a plastic mechanical behaviour (as permanent deformation is induced and the initial penetration depth is not recovered) in which crack formation is promoted (pop-in event), as shown in the top-left corner graph.	143
6.15 P-h loop of PlasWhite in which a maximum applied load of 10 mN has been applied. PlasWhite presents plastic mechanical behaviour as the initial penetration depth is not recovered during nanoindentation.	144
6.16 (a) and (b) Show the $P - h$ curves of different regions of piezo-BEMA composites, revealing a local changes of the mechanical behaviour of the sample attributed to NPs agglomeration. This same mechanical behaviour was measured for most BEMA-based composites, being more apparent at higher weight loadings. (c) Shows the $P - h$ curve of BaTiO ₃ NPs embedded within PEGDA. The same mechanical behaviour was observed in all the PEGDA-based composites.	146
6.17 (a)-(d) Show the plots of both the theoretical and experimental elastic moduli of the different particulate composites for (a) BTO:BEMA composites UV-cured for 4 seconds, (b) BTO:BEMA composites fully cured, (c) Fe ₃ O ₄ :BEMA fully cured, and (d) BTO:PEGDA, respectively. Constant values of BEMA and PEGDA are shown in red lines in the four graphs. In (a), the experimental results perfectly match the Sato and Furukawa model, being the two plots superimposed.	150
6.18 (a) and (b) Show the d_{33} values the 200 nm and 500 nm PEGDA- and BEMA-based piezoelectric composite materials, respectively. The solid points connected by solid lines represent experimental points, and the blue dashed lines show the exponential growth trend, which is not the fitting function of the experimental data.	153

6.19	3D-printed and screen-printed samples. The big samples lie on a 3D-printed support made of commercially-available 3D-printable materials. (a) and (b) show the top and front view of the samples, respectively.	154
6.20	$M - H$ hysteresis loop of (a) Fe_3O_4 composites at 25 wt% and 50 wt% concentrations, and (b) Fe composites at 50 wt% and 75 wt%. It can be seen from (a) and (b) that the magnetite-based composites present a ferromagnetic behaviour, whereas the iron-based composites present superparamagnetic behaviour, respectively.	154
6.21	Hysteresis loop of the hybrid magnetic composite material, composed by several layers of Fe(50):Irg.BEMA, and $\text{Fe}_3\text{O}_4(50)$:Irg.BEMA. The top-left corner graph shows a close-up look at the low-field regime in which the ferromagnetic behaviour of the sample can be observed.	156
6.22	$dB/dH - H$ plot derived from the $M - H$ curves measured using the VSM. The H_c values are highlighted. This is the example for $\text{Fe}_3\text{O}_4(25)$:Irg.BEMA, but all the $dB/dH - H$ gave the same shape, providing maximum dB/dH values at H_c	156
6.23	Change of magnetic moment of the synthesized magnetic composites, ΔM curves for the Fe_3O_4 composite at 50 wt % within PEGDA (solid black squares), and for the Fe_3O_4 composite at 50 wt% within BEMA (empty squares).	157
6.24	Fitting of the $M - H$ curve of one of the Fe composites using the Langevin function. The empty squares show the experimental data and the continuous red line shows the fitting function.	158
6.25	(a) Shows a surface plot of the orientation and intensity of the measured magnetic field of the magnetic domains of the small non-poled 3D-printed sample and (b) shows its 3D representation. The light yellow surface represents the geometry of the surface.	160
6.26	(a) Shows a surface plot of the orientation and intensity of the measured magnetic field of the magnetic domains of the NdFeB and (b) shows its 3D representation. The light yellow surface represents the geometry of the surface.	161
6.27	(a)-(c) Show the experimental plot of the magnetic field orientation and intensity after magnetic polling of the 3D-printed big square thick, the 3D-printed square thin, and the 3D-printed small square samples, respectively. (d)-(f) Show the 3D representation of the intensity and orientation of the magnetic field created by the samples, where the light yellow surfaces indicate the geometry of the samples.	163

6.28	3D-printed magnetic hollow half-sphere. The 1mm holes are separated 0.5 mm from each other. The diameter of the base is 10 mm. The magnetic structure was 3D-printed on a 0.2 mm BEMA base. The corresponding computer-aided design (CAD) file is shown in the top-left corner.	164
6.29	Dimensions in mm of (a) a reference disk, and (b) golden-ratio tube with an interface, highlighted in red.	165
6.30	Schematic set up to test the acoustic response of the 3D-printed sensor. The loudspeaker sits behind the sensor at a distance that ensures the far-field regime, and the 3D-LDV head stays on top of the sensor. The sensor was fixed on the table, and a Bruer & Kjaer 4138 microphone was used as a reference.	166
6.31	The black, red, and blue lines show the displacement in the z -axis of the reference disk (plotted as an average of three different samples), the resonator with interface, and the resonator without interface, respectively. The top-right corner graph shows a closer look to lower frequencies (below 4 kHz).	167
6.32	Sketch of the first 3D-printed locust-inspired resonator. The top and bottom images show, respectively, the top and side view of the resonator with its corresponding dimensions.	169
6.33	Sketch of the resonator with the support structure. The top and bottom images show, respectively, the top and side view of the resonator when the supports are added.	169
6.34	(a-c) Simulation (left) and experimental (right) mechanical deflection of the 3D-printed resonator at 1 kHz, 2.2 kHz, and 5 kHz respectively.	172
6.35	(a-c) Show the representation of the TWs observed in COMSOL, the locust TM, and the 3D-printed resonator, respectively. The middle image was kindly provided by Prof. Windmill, from his work <i>Tympanal travelling waves in migratory locusts</i> [11]. In this image, Windmill <i>et al.</i> plotted the measured gain as a function of the distance across the locust TM.	172
6.36	Dimensions of the 3D-printed samples including several cavities in different distributions (a) resonator with one cavity in the thick region, (b) resonator with two square cavities in the thick region, and (c) resonator with two rectangular cavities in the thick region. The space between the cavities and the wall is 1 mm, and the space separating the cavities is 0.5 mm. (a) is 9.5 mm in length and 5 mm in wide, (b) are 5 mm side squares, and (c) are 10.5 mm length and 2.75 mm wide.	174

6.37	Plots of the average surface displacement and average surface velocity of the 3D-printed resonators when stimulated under single tone stimuli. (a) and (b) show the plots for all the samples in which the ones without cavities are highlighted. (c) and (d) show the plots of the resonators presenting one cavity, (e) and (f) show the plots of the resonators presenting two square cavities, and (g) and (h) show the plots of the resonators presenting two rectangular cavities.	176
6.38	3D LDV top images of the thick membrane of the different 3D-printed resonators when stimulated by single tone stimuli. Traveling waves and their direction of propagation can be seen for (a) the solid resonator at 7 kHz, (b) 1 air-filled cavity resonator at 1.2 kHz, (c) 1 IPA-filled cavity resonator at 2.38 kHz, (d) 2 air-filled square cavities resonator at 4.5 kHz, (e) 2 IPA-filled square cavities resonator at 5.627 kHz, (f) 2 air-filled cavities resonator at 6 kHz, (g) 2 air-filled rectangular cavities resonator at 3.86 kHz, and (h) 2 IPA-filled rectangular cavities resonator at 5 kHz.	180
6.39	Wave velocity of the traveling waves measured in the different BEMA (Irgacure 819 1 wt%, and SUDAN I 0.2 wt%) resonators at several frequencies	181
6.40	Locust tympanal membrane (TM) bio-inspired 3D-printed sensor and its corresponding computer-aided design (CAD) file. The sensor is divided into two regions: a thick region and a thin region responding to lower and higher frequencies, respectively. The sensor was 3D-printed in BEMA (1 wt% Irgacure 819, 0.2 wt% SUDAN I), and the piezoelectric layers were 3D-printed using BTO(33)@BEMA(1 wt% Irgacure819, 0.2 wt% SUDAN I).	182
6.41	Average displacement values of the different regions of the 3D-printed bio-inspired piezoelectric sensor when electrically stimulated within the frequency range of 1 kHz to 17 kHz.	182
6.42	(a) Shows the acoustic input signal at 15 kHz consisting of a burst of 2 cycles every 100 ms. (b) Shows the response of the 3D-printed device with its two well-differentiated regions at 1.8 kHz after averaging 128 times. The response is divided between the electromagnetic and the acoustic responses. The same experiment was performed within the range of 1 kHz to 17 kHz in steps of 1 kHz. (c) Shows the normalized values of the output voltage of the different regions under acoustic stimulation within the same frequency range, revealing larger output voltages in the thick region at all the studied frequencies.	183

6.43	Normalized values of the output voltage of the different regions of the sensor with PVDF films under acoustic stimulation within the frequency range of 1 kHz to 17 kHz in steps of 1 kHz revealing larger voltage outputs at lower frequencies in the thick region and <i>vice versa</i> .	185
6.44	Plot of the response of the device when two PVDF films are attached onto it, which is divided into the electromagnetic (dash-line box) and the acoustic response (solid-line box). The same experiment was repeated for all the sensors in the range of frequencies from 1 kHz to 17 kHz. All the measurements were averaged 128 times.	186
7.1	Representation of the positive feedback full process. Starting with mathematical models of biological phenomena combined with functional 3D-printable materials it is possible to develop simple bio-inspired sensors and compare its response with the predicted by simulation techniques. Once such behaviour has been confirmed, it is possible to add an extra degree of complexity into the system and 3D-print more realistic samples and measure them again to compare its behaviour with that of the simplified sample. The observed differences can provide explanation of why specific biophysical phenomena take place in concrete organs of some animals.	193
A.1	(a) Shows the power spectrum of a single Duffing oscillator excited by a single frequency ω_1 . The plot was obtained by using the parameters $\epsilon = 5$, $A = 1$, and $\omega_1 = 10$, all of them expressed in arbitrary units (a. u.). (b) Shows the power spectrum of a single Duffing oscillator excited by two external frequencies at the same time. The plot was obtained by using the parameters $\epsilon = 5$, $A = 1$, $\omega_1 = 10$, and $\omega_2 = 11$.	iv
B.1	(a) and (b) Show the amplitude vs frequency representation of $\omega^{(2)2}$ and $\omega^{(3,4)2}$, respectively. The parameters used to plot these graphics are $\epsilon = 1$, $F = 10$, $m = 1$, $\gamma_{1,1}$, and $k = 1$, all in arbitrary units.	viii
B.2	Amplitude vs ω^2	ix

List of Tables

2.1	Summary of the different 3D-printing approaches, their resolution and size limitations, and the materials they use. Data obtained from [93–96]	28
2.2	Companies using different 3D-printable materials in very contrasting projects, both in the micro- and macroscale.	34
2.3	Some typical polymers, classification, and characteristics. Table obtained from <i>Stereolithography. Materials, Processes, and Applications</i> [109]	35
2.4	Factors influencing the behaviour of photopolymer systems. Table obtained from <i>Stereolithography. Materials, Processes and Applications</i> [109].	42
3.1	Elastic moduli (E) of ceramics (left-hand-side column), and polymers (right-hand-side column) showing a difference of several orders of magnitude between them due to the strength of the ionic bonds. Values obtained from <i>KYOCERA, Fine Ceramics (Advanced Ceramics)</i> [147] and <i>The Engineering Toolbox, Polymers - Physical Properties</i> [148].	56
3.2	Mechanical properties of some composite reinforcing fibres. Table obtained from <i>Encyclopaedia of Polymer Science and Engineering</i> [157].	68
4.1	Material properties of piezocomposites. Table obtained from [175]	80
4.2	Main characteristics of the different magnetic materials and representation of the alignment of their magnetic moments.	85
6.1	Fitting details when using the unforced coupled mathematical model.	128
6.2	Fitting details when using the unforced coupled mathematical model.	130
6.3	Fitting details when using the forced complex coupled mathematical model.	131

6.4	Values of elastic modulus (E) and hardness (H) of both 3D-printable BEMA and 3D-printable PEGDA obtained from the $P-h$ curves using Eq.(3.21)-(3.26). The reported values of both H and E are an average of 36 tests performed on each sample.	145
6.5	Mechanical properties of the BEMA- and PEGDA-based functional composite materials. Exposure time refers to how long each layer was cured under UV light (in seconds). The sizes of the NPs were 500 nm, 50-100 nm, and 25 nm for BaTiO ₃ , Fe ₃ O ₄ , and Fe, respectively.	147
6.6	Prediction of the mechanical properties of the BEMA- and PEGDA-based functional composite materials using the two models described earlier in this section: E_{SF} using Eq.(3.36) and E_{M2} using Eq.(6.71) $j = 0$ unless otherwise stated. The sizes of the NPs were 500 nm, 50-100 nm, and 25 nm for BaTiO ₃ , Fe ₃ O ₄ , and Fe, respectively.	149
6.7	d_{33} values of BaTiO ₃ samples embedded within PEGDA at different loading rates and poled for 30 minutes, 1 hour, and 2 hours, respectively. Used BaTiO ₃ size was 500 nm. . .	152
6.8	Values of the magnetisation of saturation and the intensity of the coercive field of all the synthesized samples. The number in parenthesis corresponds to the wt % of magnetic NPs. Irg and Tri stand for Irgacure 819 and triarylsulfonium hexafluorophosphate salts mixed 50% in propylene carbonate, which are two different photoinitiators. The layered hybrid consisted of alternate 500 μ m layers of Fe(50):Irg.BEMA and Fe ₃ O ₄ (50):Irg.BEMA. . . .	155
6.9	NPs sizes determined from the $M-H$ plots using Eq.(4.20). Two sizes were determined for each sample in which the experimental and the fitting M_r values were used.	159
6.10	Values of the average amplitude of motion of the thick and thin regions of the 3D-printed resonator in the vertical direction (z -axis) under single frequency acoustic stimulation. . .	171
6.11	Values of the velocities and wavelengths of the TWs measured onto the 3D-printed sensor.	172
6.12	First characteristic frequencies (expressed in kHz) of the thick region of the 3D-printed resonators.	175
6.13	Values of v_{TW} and λ_{TW} of the measured TWs onto the 3D-printed samples.	178

Chapter 1

Introduction

The process of evolution through natural selection permits biological systems to display simple yet efficient adaptations to perform elaborate functions and address complex challenges. Observation and understanding of such adaptations provide huge inspiration that can be applied to solve modern human problems. This approach, known as bio-inspiration, is a rapidly growing field of research and has become a very common tool during recent years within a wide range of applications such as medicine, chemistry, robotics [1–4], and more. Taking inspiration from natural systems has already allowed scientists to develop aerodynamic systems, robots with specific capabilities, and materials that display unique properties [3, 5, 6]. One such approach of the application of biomimicry can be found in the study of acoustic systems inspiring the design of novel artificial acoustic sensors. The ability to hear is a fundamental tool for biological organisms to sense and interact with their environment as it displays great sensitivity, compatibility with environmental conditions, sophistication and complexity of the response, some features that cannot be currently matched by engineered sensors or transducers. All these characteristics assist biological organisms to detect prey, predators and conspecifics. Similarly sound production can be used for communication and vision purposes (*i.e.* use of ultrasound by nocturnal bats). As sound carries a very low level of energy, biological sound sensors must inherently be very sensitive, reaching the point to be able to detect sub-nanometre sound particle displacement. Insects are thought to be the first animals to have evolved the ability to detect sounds [7], and it is currently believed that hearing has evolved at least nineteen times independently within this class [8]. Several hundred million years of evolution, combined with the phenomenal diversification resulting from all these independent but convergent evolutionary adaptations mean that, today, the diversity of functions and modalities involved in sound detection in insects is unparalleled in the animal world. Contingent

on the species, insects present different ways of detecting and processing sound, and of all this variety to detect acoustic energy, tympanal ears are the most akin in structure and organization to traditional microphones; in a typical insect tympanal organ, the tympanum stretches over a fluid-filled cavity onto which specialised mechanoreceptors (sensory cells, *scolopidia*) attach. The tympanum is set in motion by incoming sounds, in an analogous way as a traditional microphone does, and its mechanical behaviour is then transduced into an electrical signal that is interpreted by the central nervous system [9]. One of the many insects displaying some form of tympanal hearing are locusts, which have long been the subject of studies related to biomechanics, physiology, and ecology of insect hearing [10]. Even though presenting a simple structure, the locust tympanum membrane has been reported to present acoustic frequency selectivity, to exhibit traveling waves (TW) across the membrane, and display nonlinear mechanical behaviours in the form of distortion product otoacoustic emissions (DPOAEs) [11], which are natural manifestations of intermodulation occurring within the system.

The presence of complex phenomena in a simple miniaturised system like the locust tympanum membrane (TM) provides a unique opportunity to develop bio-inspired resonators, sensors, and actuators taking advantage of them, which can be exploited in the acoustic field to develop, for instance, acoustic aid devices. The best way to develop these sensors is through three-dimensional (3D) printing technology, as it permits rapid manufacturing and presents a high degree of personalization of the desired part.

Even though it was developed 30 years ago, 3D-printing technology has arisen as one of the main fields of research and development in the scope of science during the last decade due to its implementation in several research fields such as space engineering, development of micro- and nano-devices and sensors, biomedicine and many more [12–15]. What started as a tool to simply develop specific prototypes in a quicker way has now become a worldwide industry, impacting the world from several perspectives, as it encompasses from the development of the smallest biorobots one could think of, up to the manufacturing of large modules to build houses [16]. The development of micro-devices requires small and complex structures that can be built rapidly and at low cost yet, typically, the most common polymer-based microelectromechanical systems (MEMS) approaches are slow and time consuming. 3D-printing techniques, whether they use solid-, liquid-, or powder-based approaches, permit the rapid production of complex and accurate geometries from computer-aided design (CAD) files, with polymers

being the materials that play the most prominent roles amongst commercial 3D-printable materials. One of the main disadvantages of these materials when using them for rapid prototyping purposes is that the functionality of the resulting parts solely relies on their mechanical and geometric properties. However, providing new functionalities to these materials becomes relatively easy when embedding specific ceramics and/or metals within the polymeric matrix. Liquid-based approaches using light-responsive polymers facilitate the development of functional 3D-printable composites as they enable a quick and simple suspension of nanostructures within the photo-curable polymeric matrix, which solidifies after exposure to ultraviolet (UV) light.

One of the main reasons why 3D printing technology has become such an important tool in science is due to the boom in materials' science research: development of specific materials with very interesting physical properties such as graphene, super hydrophobic materials, or conductive inks [17–19] has produced a direct effect in the development of additive manufacturing technology in order to customize and optimize the production processes in terms of time- and cost- efficiency. Notwithstanding, as one could think that additive manufacturing techniques can only be applied in very specific fields within science, this technology has also been applied in diverse disciplines such as architecture [20], art [21], or food industry [22], making the impact of 3D printers more and more present in our daily lives.

The objective of this thesis is to 3D-print bio-inspired polymer-based functional sensors, resonators, and actuators. To do so, it is necessary to deeply understand the underlying biophysical acoustic phenomena, develop mathematical models explaining them, understand the principles and limitations of stereolithography (STL) 3D-printing, and understand the physics behind polymer-based composite materials. When all these fields have been properly understood, it is possible to combine them to develop the final product.

Chapter 1 presents a description of the basic characteristics of sound, as well as it presents the hearing systems that have been relevant for this work. Chapter 2 gives an insight and thorough discussion about 3D-printing, including their different types and materials. This chapter focuses on polymers and also discusses the most common methods to develop polymers that can be 3D-printed using the stereolithography technique, as this is the 3D-printing method used in this thesis. Chapter 3 discusses the importance and relevance of the mechanical properties of materials, as well as it

presents nanoindentation, the technique used to evaluate the mechanical properties of the developed materials. This chapter also focuses some attention on how to determine the mechanical properties of composite materials. This chapter is important for the thesis the mechanical properties of materials have a direct influence on the design of the final sensors. Chapter 4 presents the basic principles of magnetism and piezoelectricity, as these will become fundamental to understand when 3D-printing functional polymer-based materials to be implemented in the developed sensors. Chapter 5 introduces the experimental techniques used in the thesis, including 3D laser Doppler vibrometry, finite element simulation, vibrating sample magnetometer, and scanning electron microscopy. Chapter 6 presents all the experimental results obtained during the course of the thesis as well as its discussion, relating it to the theory introduced in the previous chapters. Finally, Chapter 7 presents the conclusions of the work as well as it presents the future work to be done and how to move forward with the development of functional 3D-printable polymer-based bioinspired sensors.

1.1 Basic principles of sound

Sound arises from the coupling of small vibrations of the particles of a medium, which are displaced from their equilibrium position and collide with each other. As an example, the beat of the wings of a hummingbird produces sound due to the oscillation of the air particles generated by the flapping of the wings.

Sound is an *acoustic* wave, but there are other types of waves in nature, such as electromagnetic, seismic, or phononic waves. Irrespective of their origin, all of them can be classified as *longitudinal* or *transverse*. The former are those in which both the displacement of the propagation of the medium and the wave are in the same direction, producing *compressions* and *rarefactions* of the particles of the medium, and consequently generating a local increase and decrease of pressure (see Fig.1.1). On the other hand, *transverse* waves are those in which the displacement of the propagation medium is in the perpendicular direction to the displacement direction of the wave.

Waves present several characteristic parameters such as *wavelength*, and *frequency*. Wavelength, λ , is the length of one cycle and it is measured in length units, and frequency, f , is the number of cycles that the particles of the medium complete in one second (*e.g.* if the antenna of a mosquito moves back and forth 100 times in one second, it's frequency is of 100 Hz). The inverse of frequency is called *period*, T ,

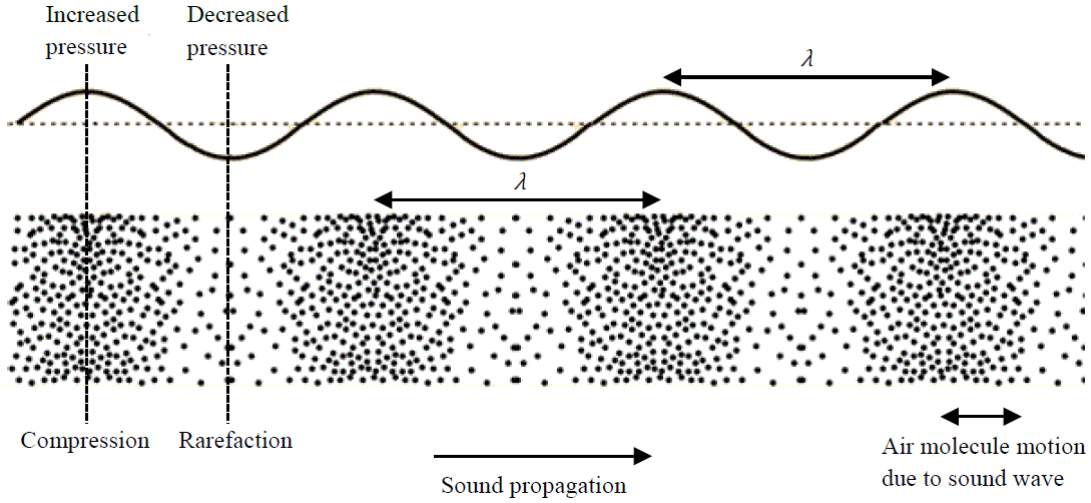


Fig. 1.1. Sketch of the propagation of an acoustic longitudinal wave. When the particles of the medium compress, an increase of pressure takes place, whereas when the particles of the medium are rarefacted, a decrease of pressure occurs. Pressure attenuates as a function of $1/r$, where r is the distance from the sound source. Image obtained from [23]

and it indicates the amount of time needed to complete a full cycle. These two quantities are related to each other through the speed of sound, c , as shown in Eq.(1.1).

$$c = f\lambda = \lambda/T \quad (1.1)$$

The speed of sound is an intrinsic property of the medium in which the waves travel and takes the value of 343 m/s in air. Speed of sound shows a slight dependence with pressure, making valid the assumption that it remains roughly constant at different heights. In an ideal gas, the speed of sound depends on its temperature, humidity, and composition [24–26], and it can be predicted using the Newton-Laplace equation, Eq.(1.2).

$$c = \sqrt{B/\rho} \quad (1.2)$$

where B is the bulk modulus, and ρ is the density of the propagation medium. As it might have been noted by the reader, bulk modulus is not an intrinsic property of fluids, but it can be estimated by multiplying the pressure by a dimensionless adiabatic¹ index. Hence, Eq.(1.2) becomes:

$$c = \sqrt{(\partial p/\partial \rho)_s} \quad (1.3)$$

where the sub-index s denotes the derivative of the pressure (p) with respect to the density of the medium in isentropic conditions (*i.e.* at constant entropy).

¹An adiabatic process is that in which there is no interchange of heat nor matter between the system and its surroundings, and energy is uniquely transmitted as work.

Nevertheless, waves do not always travel and sometimes can be enclosed within structures such as tubes, strings, or pipes. Thus, it is possible to discern between *standing* and *traveling* waves. The first ones are those that occur within an enclosed fluid-filled space, like those generated in organ pipes and in wind music instruments, whereas the second type of waves are those are unbounded by the propagation medium. The displacement of a traveling wave with amplitude of motion A is described by a simple function of space and time, as shown in Eq.(1.4).

$$y(x, t) = A \sin \left[\frac{2\pi(x - ct)}{\lambda} \right] \quad (1.4)$$

It is possible to study Eq.(1.4) in further detail in order to obtain some characteristic parameters of the wave. If Eq.(1.4) is expanded using Eq.(1.1):

$$y(x, t) = A \sin \left[\frac{2\pi x}{\lambda} - \frac{2\pi ct}{\lambda} \right] = A \sin \left[\frac{2\pi x}{\lambda} - \frac{2\pi t}{T} \right] \quad (1.5)$$

where $2\pi/T = 2\pi f$ is the *angular frequency*, and its denoted by ω . Its analogous expression in space is the *wave number*, $k = 2\pi/\lambda$, which becomes the *wave vector*, \vec{k} , in multidimensional systems. Thus, Eq.(1.5) can be re-written, in one dimension, as:

$$y(x, t) = A \sin[kx - \omega t + \phi] \quad (1.6)$$

where a phase ϕ has been introduced and it is determined by the initial conditions of the system. Eq.(1.6) is a solution of the *wave equation*, which describes the propagation of waves in space, and is given by Eq.(1.7).

$$\frac{\partial^2 u}{\partial t^2} = v^2 \nabla^2 u \quad (1.7)$$

where v is the *phase velocity* ($v = \omega/k$), which determines the rate of propagation of the phase of the wave in space, and u is a scalar function containing the displacement information of the system ($u = u(x_1, x_2, \dots, x_n; t)$). Thus, from all these definitions, it can be understood that traveling waves are those which transmit energy from one position of space to another irrespectively of the media in which they propagate. Following this definition, therefore, it is possible to understand standing waves as two traveling waves moving in opposite directions in which, when superimposed, there is no energy flow in any direction [27].

As sound is a mechanical wave consisting of several compressions and rarefactions of the medium in which it travels, it transmits both kinetic energy (due to the movement of the particles of the media),

and potential energy (because of the change of pressure in the media). As the wave propagates, its energy is transmitted at the *wave velocity* at the same time that a part of it is dissipated due to thermal energy. The energy carried by a sound wave is inherently low and it can be calculated using Eq.(1.8).

$$E_s = \int_S \left[\int^{\Delta t} I_s(\vec{r}, t) dt \right] dS \quad (1.8)$$

where S is the surface through which the wave travels, Δt is the time interval, and $I_s(\vec{r}, t)$ is the acoustic intensity, which is a function of space (\vec{r}) and time (t).

Apart from the classical understanding of a wave, the quantum theory has its *own* sound waves, called *phonons*, which are generated in solid lattices of atoms as a consequence of their vibrations. Whereas sound waves in fluids only have a longitudinal component, in solids they have both longitudinal and transverse components due to the arrangement of the atoms of the solid medium, giving rise to very interesting physical phenomena that are further out of the scope of this thesis.

1.2 Interaction of sound waves with solid structures

Sound waves have the ability to interact with each other when coexisting in a same medium, producing the phenomenon of *interference*. This interference can be either *constructive*, when the amplitudes of the waves add, or *destructive*, when the two interfering waves are out of phase and their corresponding amplitudes subtract. These interference patterns are mathematically described, respectively, by the conditions shown in Eq.(1.9) and only apply to *coherent*² and *monochromatic*³ waves.

$$\Delta l = m\lambda \quad , \quad \Delta l = \left(m + \frac{1}{2} \right) \lambda \quad (1.9)$$

where Δl is the path difference between the two waves, and m is an integer.

Apart from interacting with each other, sound waves can also interact with solid structures, producing several physical phenomena such as *reflection*, *refraction*, and *diffraction* among others, with these three the most relevant ones. The material properties of the solid material as well as the incidence angle of the sound wave will determine the type of interaction occurring between the wave and the solid structure.

²The emitted waves are identical, keeping a constant phase different.

³The waves have the same wavelength.

1.2.1 Reflection

Reflection of waves (schematically shown in Fig. 1.2) happens when a wave traveling through a medium encounters a surface of a different medium and it is bounced back to the first medium. The main characteristic of reflection is that the angle of the incident wave is the same as the angle of the reflected wave in flat surfaces. It must be noted that as audible sound has a frequency range from around 20 Hz to 17 kHz, there is a broad band of associated wavelengths to these sound waves, and all of them will be reflected in a different way when interacting with the same surface.

This process is not the only one that takes place when a wave hits a surface, as the reflected wave can interfere with the incoming wave creating constructive or destructive interference patterns, which can lead to the creation of *standing waves*, that create a local increase of pressure near the surface where the waves have been reflected off. It is important to mention that when sound waves in air encounter a hard surface, there is no change of their phase because the hard surface has a much larger acoustic impedance⁴ than that of air. When a sound wave transmitting through a solid encounters an air boundary, the reflected wave will present a phase shift with respect to the incoming wave due to the transmission of the wave from a high acoustic-impedance medium to a low-acoustic impedance one.

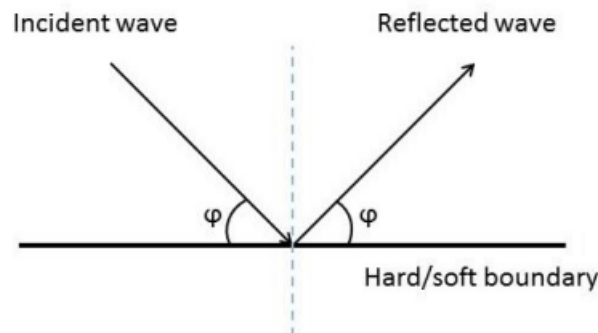


Fig. 1.2. Sketch of the phenomenon of reflection on a flat surface when an incident wave hits a hard or a soft boundary. The angle φ represents the incidence angle of the incoming wave, which is the same as the reflection angle. It must be noted that the acoustic wave will not be totally reflected as transmission will also take place.

When sound waves are reflected by concave surfaces instead of flat surfaces the local sound level increases. This is because when the reflected sound wave is concentrated in a narrow area, the sound reflection can be strong enough to be audible as sound amplification. Furthermore, concave surfaces can also generate multiple reflections. Depending on the position of the source reception of sound will be

⁴Acoustic impedance represents the opposition of a system to acoustic flow.

different; at the centre all reflections will be heard, whereas away from the centre the reflections will move away and then back again [28, 29]. The enhancement of reflected sound by concave surfaces can present some advantages for specific applications in small spaces, whereas in larger spaces they will lead to late reflections that will be heard as echo or reverberation. All these sound phenomena arising from the interaction of sound with curved surfaces are the centre of study in architecture and music fields to optimize the acoustics of auditoriums, theatres and other rooms.

1.2.2 Refraction

Refraction is the change of direction of a wave when it is transmitted from one medium with *refractive index* n_1 to another medium with a different refractive index n_2 (see Fig. 1.3a). An illustrative example of refraction of light waves can be seen in Fig. 1.3b and extrapolated to other types of wave. Refraction can be easily understood from conservation of energy and momentum, as the phase velocity of the waves changes when the transmission medium changes. The change of direction of a refracted wave is

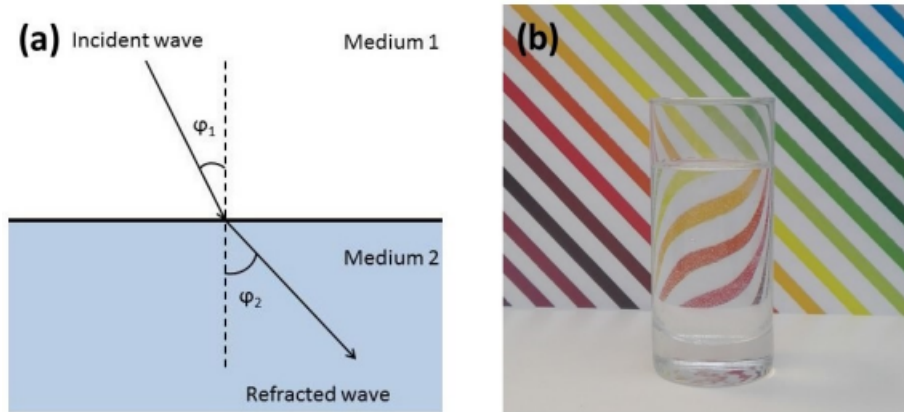


Fig. 1.3. (a) Sketch of refraction when a wave is transmitted from one medium with associated refraction index n_1 to a different medium with different refraction index n_2 . φ_1 is the incidence angle of the wave with the vertical, and φ_2 is the refraction angle of the wave when transmitted to the second medium, and (b) shows an example of light refraction where it can be clearly seen how the diagonal lines change their direction after being refracted by a water-filled glass.

mathematically described using Snell's law, as shown in Eq.(1.10).

$$\frac{\sin(\varphi_1)}{\sin(\varphi_2)} = \frac{v_1}{v_2} = \frac{\lambda_1}{\lambda_2} = \frac{n_2}{n_1} \quad (1.10)$$

where φ_1 , and φ_2 are the incident and transmitted angles of the wave, v_1 and v_2 are their corresponding phase velocities, λ_1 and λ_2 are the wavelengths of the incident and transmitted waves, respectively, and n_1 and n_2 are the refractive indices of the propagation and transmission media. Some observations must

be done from Eq.(1.10); when a wave travels from media in which $n_1 > n_2$, it is possible to find a situation in which Eq.(1.10) becomes:

$$\sin(\varphi_2) = \sin(\varphi_1) \frac{n_1}{n_2} > 1 \quad (1.11)$$

which is not a real solution. Thus, in these situations the wave is completely reflected to the first medium, a phenomenon known as *total internal reflection*. It is possible, thus, to determine which is the maximum angle of incidence of the wave that will produce refraction, called *critical angle*, φ_c , and given by Eq.(1.12).

$$\varphi_c = \arcsin\left(\frac{n_2}{n_1}\right) \quad (1.12)$$

However, sound waves do not usually encounter abrupt changes in medium properties but their wave speed shows a smooth dependence on temperature [30, 31]. Thus, in sound waves refraction is not only created by the change of medium itself but it can also be generated by changes of temperature in the medium of propagation. As an example, the local increase of temperature of air (which therefore leads to a decrease of its density) near the ground will make sound waves bend due to an increase of their velocity of propagation in such regions.

1.2.3 Diffraction

Diffraction is the phenomenon that makes a wave spread when it encounters an obstacle of small size compared with its wavelength. One of the main characteristics of diffraction is that it is more pronounced for larger wavelengths, leading to weaker diffraction of waves of lower wavelength. In loudspeakers, for instance, as the bass frequencies have longer wavelength compared to the size of the loudspeaker, the emitted sound will spread out more than traveling straight ahead. Thus, diffraction is responsible for hearing low frequencies around obstacles better than high frequencies in the same location. Nevertheless, this becomes a notable problem for communication of some mammals. For instance, for mating and migrating purposes, elephants must emit waves of very low frequency that can travel long distances without interacting with the surrounding vegetation and other obstacles in order to enable synchronized movements between them even when they cannot see each other. If the emitted frequency was higher, it would interact with all the obstacles between the animals leading to a decrease of the intensity of the emitted signal and, therefore, being a real problem for their communication [32]. A similar effect happens with ultrasound waves in flying locusts, producing the distortion of the acoustic field [33].

Scientists have started developing several metamaterials in order to beat the acoustic diffraction

limit⁵ [34, 35] and reduce the effect of this undesired phenomenon when it comes to acoustic engineering applications in a smart way.

1.2.4 The Doppler effect

The Doppler effect is a phenomenon observed in both sound and light waves, as well as it takes place in both classical and relativistic physical phenomena. It consists in the perceived change (or shift) of the frequency of a wave emitted by a source that moves with respect to a receiver. Considering the one dimensional case in the classical limit, the frequency shift generated by the Doppler effect can be determined using Eq.(1.13).

$$f_r = \left(\frac{c + v_r}{c + v_s} \right) f_s = \left(1 + \frac{\Delta v}{c} \right) f_s \quad (1.13)$$

where f_r is the received frequency, f_s is the source (emitted) frequency, c is the wave speed in the transmission medium, and v_r and v_s are the receptor and emitter velocities, respectively.

Thus, it is easy to see that the received frequency increases when the emitter and the receptor approach ($\Delta v > 0$), and it decreases when the emitter and the receptor move away from each other, as shown in Fig. 1.4. A clarifying example of this phenomenon is the sound emitted by the siren of an ambulance.

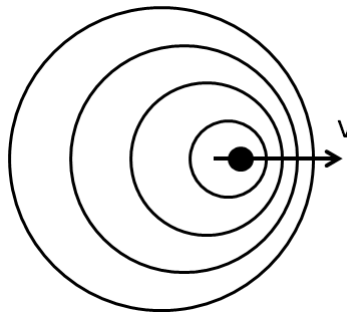


Fig. 1.4. Schematic representation of the motion (left to right) of an object (solid black circle) with a velocity v , and emitting at a frequency f_s . An observer located at the right-hand side of the emitter will receive a higher frequency than f_s and a lower wavelength, as it can be checked using Eq.(1.1). On the other hand, a receiver located at the left-hand side of the emitter, will receive a lower frequency than f_s . This increment and decrease of frequency is represented by the circular lines getting closer and further away, respectively.

⁵The acoustic diffraction limit is the uncontrollable bending of waves (either sound, light, or any other type) when trying to focus them in spaces smaller than one wavelength.

1.3 Attenuation of sound

As described earlier in Section 1.1, sound has two components associated with the propagation of the wave: particle velocity, which leads to a compression and rarefaction of the particles of the medium, and pressure. Both of these components attenuate with distance when traveling in a medium, which can be easily explained using spherical coordinates (see Fig. 1.5). In spherical coordinates, the Cartesian components x , y , and z can be expressed as shown in Eq.(1.14).

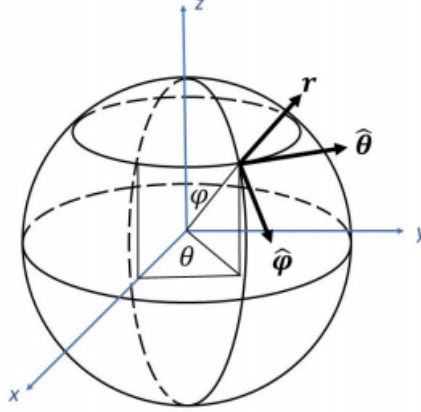


Fig. 1.5. Sketch of the spherical coordinates system, where θ is defined as the *azimuth* angle in the xy -plane ($0 \leq \theta \leq 2\pi$), φ is defined as the *polar* (or *zenith*) angle in the positive z -axis ($0 \leq \varphi \leq \pi$), and r is the radius of the sphere. The boldface quantities represent the vectors of the spherical-coordinate system.

$$\begin{cases} x = r \sin \varphi \cos \theta \\ y = r \sin \varphi \sin \theta \\ z = r \cos \varphi \end{cases} \quad (1.14)$$

Thus, the wave equation in spherical coordinates can be rewritten as:

$$\frac{\partial^2 u}{\partial t^2} = v^2 \frac{\partial^2 u}{\partial r^2} + \frac{2}{r} \frac{\partial u}{\partial r} + \frac{1}{r^2 \sin \varphi} \frac{\partial}{\partial \varphi} (\sin(\varphi)) \frac{\partial u}{\partial \varphi} + \frac{1}{r^2 \sin^2(\varphi)} \frac{\partial^2 u}{\partial \theta^2} \quad (1.15)$$

Where it must be noted that $v = c$. The solution to Eq.(1.15) is given by:

$$u(r, t) = - \left(\frac{1}{r} + ik \right) \frac{A}{r} e^{ik(ct-r)} \quad (1.16)$$

where A is the amplitude given by the initial conditions of the system. The pressure of a spherical wave is given by Eq.(1.17) [36].

$$p(r, t) = - \frac{ikcA\rho}{r} e^{ik(ct-r)} \quad (1.17)$$

where ρ is the density of the medium where the wave propagates. As $\lambda = 2\pi/k$, it is possible to express both Eq.(1.16) and Eq.(1.17) as a function of wavelength, which permits studying both the *near field*

(when $r \ll \lambda$) and the *far field* (when $r \gtrsim \lambda$) regimes. Thus, in the near field regime the velocity of the wave has a dependence of $u \propto 1/r^2$, and the pressure goes as $p \propto 1/r$. On the other hand, in the far field regime, both the particle velocity and the pressure of the wave attenuate as $1/r$. Hence, as both components attenuate at the same rate in the far field approximation, they are a good tool for long distance acoustic communication.

From pressure, p , it is possible to define the sound pressure level, which is expressed in decibels (SPL dB), and is the ratio between sound pressure and a reference pressure, p_0 , which usually refers to the threshold level for human hearing and it takes a value of $20 \mu\text{Pa}$. SPL dB is defined using a logarithmic scale, shown in Eq.(1.18) [37].

$$SPL = 10 \log_{10} \left(\frac{p}{p_0} \right)^2 = 20 \log_{10} \left(\frac{p}{p_0} \right) \quad (1.18)$$

It must be noted from Eq.(1.18) that at p_0 the SPL dB is, by definition, 0 dB, which corresponds to the human hearing threshold. This same threshold becomes 60 dB underwater due to the use of a different sound pressure reference value ($10 \mu\text{Pa}$). These different reference pressures must be considered when trying to compare SPLs in different propagation media, as a same applied pressure will result in a different SPL value.

Being able to detect such SPL values, their changes, and discern between different frequencies, altogether with its corresponding processing through the central nervous system is what allows communication all over the animal world.

1.4 Hearing systems in biology

Detecting, processing, and locating sound is a fundamental tool for biological organisms to sense and interact with the environment. Such a complex process is not uniquely achieved by hearing systems of specific species but for a large diversity of them. Insects are not an exception and they have been found to use several mechanisms to detect, process, and interpret sound in different manners depending on the species [11, 38–41]. Insects are thought to be the first animals to develop sound perceiving organs, evolving in three major behavioural contexts in 400 million years [7]. The insects' auditory organs are known to be of ciliary origin [42], are found in different anatomical locations depending on the species [43], and their nature depend on which component of sound they can detect; if they detect sound

pressure, they are of *tympanal* nature, whereas if they detect particle velocity are of *flagellar* nature [43]. Auditory organs with tympana have evolved, at least, 18 times independently [7]. Irrespective of their location and shape, all tympanal ears are composed by eardrums of thinned cuticle which vibrate in response of airborne sounds. The tympanum is typically backed by a tracheal space, even though there are several species in which the tympanum is backed by a fluid instead [44]. Furthermore, a sensory organ able to transduce the mechanical motion of the tympanum generated by the incoming sound into an electrical signal that can be interpreted by the central nervous system is also needed. The sensory cells that perform this transduction are called *scolopidia*, are of different types, and in some insects only a few of them are needed to execute this function, whereas in other species more than 2000 of these sensory cells are needed. Scolopidia are generally located at specific positions of the tympanum, as certain sound-transmitting structures help frequency analysis.

Recent studies have shown that some insects like *katydids* process sound in a similar manner as mammals do, showing a convergent evolution of the hearing systems between insects and mammals [39, 40]. This convergent evolution shows that a complex way of detecting and processing sound energy is possible in the micro-scale and, therefore, it could open the doors to the improvement in the design and performance of novel acoustic micro-sensors, actuators, systems, and devices.

1.4.1 Distortion product otoacoustic emissions

It is well known that all acoustic phenomena necessarily become nonlinear at high intensities. When the human ear is stimulated by two different input sounds of different frequency (f_1 and f_2 , being $f_1 < f_2$) at the same time at high intensity, the difference frequency $f_2 - f_1$ is additionally heard [45, 46]. This third frequency is generated in the ear, but it is also known that a difference frequency can be produced in a nonlinear medium (such as air) during the propagation of a sound wave [47]. Even more, if the circumstances permit it, it is possible to generate a series of frequencies as a linear combination of both f_1 and f_2 , such as $f_{mn} = mf_1 \pm nf_2$, where m and n are integers. These frequencies are distortion product otoacoustic emissions (DPOAE), or intermodulation (see Fig. 1.6), and are present in a large variety of biological and engineered systems. The presence of DPOAEs can be used to determine the sensitivity and functioning of human hearing, as it has been observed that people with damaged hearing organs show a lower production of DPOAEs [48]. Even though it has been thought for a long time that DPOAEs are one of the characteristics of active hearing, it is believed that systems with a high degree

of nonlinearity can also generate them in a passive way [49].

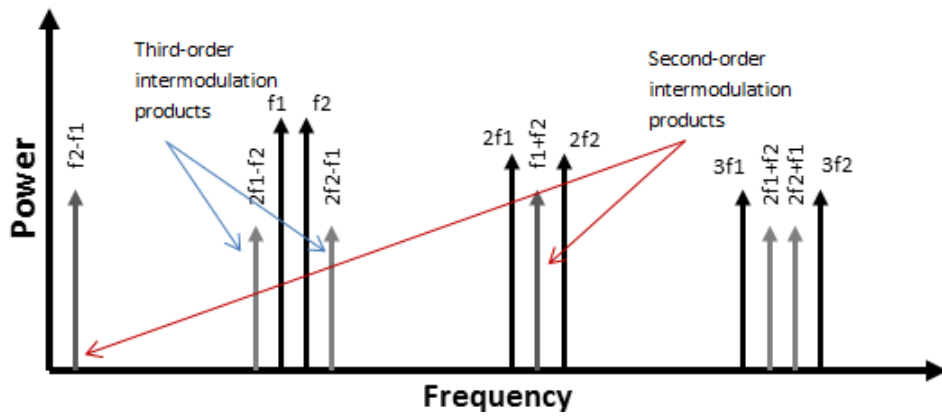


Fig. 1.6. Graphical representation of ideal intermodulation. The abscissa shows the frequency in kHz and the ordinate represents the amplitude of the motion in arbitrary units. In this example the input frequencies are $f_1 = 10$ kHz and $f_2 = 12$ kHz, to which corresponds the major value of amplitude (in theory they should have the same amplitude, but when working with biological systems one needs to be slightly larger than the other for reasons discussed later in this Chapter). The peaks corresponding to $f_{m,n}$ frequencies have a decreasing value in amplitude as their order increase. Image obtained from [50].

Nonlinear effects in oscillators (either mechanical, chemical, electrical, or biological) can be determined by studying the relationship between two of the oscillator's properties, for instance, determining the amplitude of motion of the oscillator as a function of frequency. Depending on the parameters of the system, such as its degree of nonlinearity and its damping mechanisms, the differential equation(s) that describes its motion will be different.

When studying these kinds of systems, it is possible to discern between two cases: (i) damped and (ii) undamped oscillations. If there is no damping, there exists an oscillation that is either in phase with the exciting force or 90 degrees out of phase with it. If, on the other hand, damping is present in the studied system, an out of phase response oscillation (with respect to the exciting force) is expected [51]. As mentioned earlier in this section, it is possible to obtain the frequency of the oscillation as a function of the amplitude of motion, as shown in Eq.(1.19).

$$\omega = \omega(F, A) \tag{1.19}$$

where F is the exciting force acting on the system and A is the amplitude of motion. Eq.(1.19) shows that the frequency of the system depends on both the exciting force and the amplitude of oscillation, such as (see Appendix A for further detail):

$$\omega^2 = 1 + \frac{3\epsilon A^2}{4} \pm \frac{F}{A} \tag{1.20}$$

where ϵ is a mathematical parameter that controls the degree of damping of the system. The response from Eq.(1.20) is plotted in Fig. 1.7.

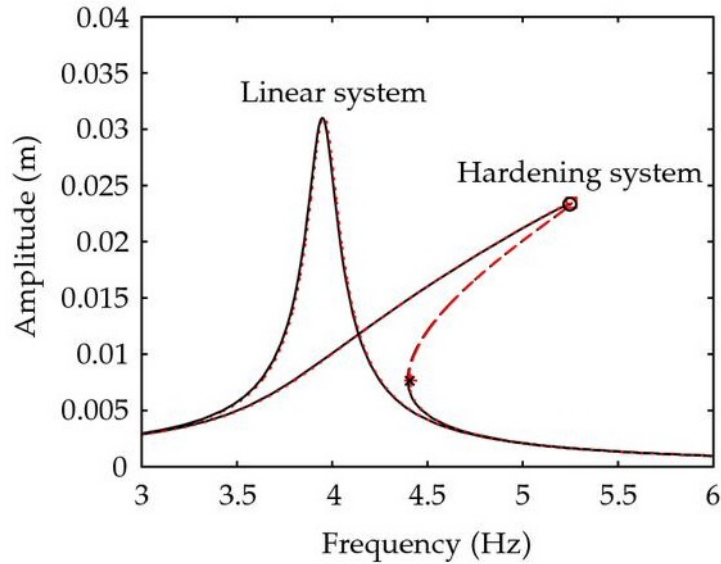


Fig. 1.7. Comparison of a linear and a Duffing system. Whereas the linear system presents one unique value of amplitude at each frequency, a Duffing oscillator can present up to three values of amplitude at given frequencies. The dotted part of the graph represents the continuity of the function, but it does not plot real values. When the curve bends to the right, the system behaves like a hardening spring, whereas when it bends to the left, it behaves like a softening spring. Image obtained from [52].

This dependence of frequency with both A and F is the result of the Duffing equation, which is a second order differential equation that describes certain damped oscillators driven by a cubic potential. This makes Duffing oscillators behave linearly near to the equilibrium position but present a nonlinear behaviour away from it. Fig. 1.7 shows what is called the *skeleton curve*. The portion of the response curve in the left-hand side of the skeleton curve corresponds to forced oscillations in phase with the exciting force, whereas the portion in the right-hand side of the skeleton curve corresponds to forced oscillation out of phase with the exciting force [51]. When the curve bends to the right as shown in Fig. 1.7, the system behaves as a hardening spring, whereas when it bends to the left, the system behaves like a softening spring [51].

1.4.2 The Duffing oscillator

Nonlinear systems, even when not influenced by any random forces or conditions of the environment and with very few degrees of freedom present random behaviour and lead to deterministic chaos. Such processes have been long subject of discussion among scientists [53], who have succeeded to develop several models to accurately describe them [54, 55]. Non-linear systems arise from many different sources such as frictional forces, acceleration in non-inertial systems, or anharmonic potentials amongst many

other. Small variations of the physical laws influencing the system yield to extremely complicated sets of equations to solve, making the use of computers necessary to solve them numerically. For instance, Lorenz was able to develop a set of differential equations to model thermal convection, a phenomenon that describes the dynamics of gases and fluids in the transition from laminar flow to turbulence [56].

One of the most used methods is to linearise physical laws in order to simplify their analysis and facilitate the solving process of systems ruled by non-linear equations [57]. Usually, the first term of a Taylor series is discussed, neglecting terms of higher order, and the simplified system is discussed rather than the original one. If higher order terms are considered, it will be more complex to solve. As an example, consider the electric polarization of a material, which is proportional to the applied electric field. Nevertheless, for strong fields the electric susceptibility is itself a function of the external field, leading to a non-linear dependency of polarization that must be taken into consideration.

The Duffing oscillator is one of the prototype systems of nonlinear dynamics, first introduced to study anharmonic oscillations by Georg Duffing and, later on, chaotic nonlinear dynamic systems. The Duffing equation has been used to describe and model a large variety of physical systems such as nonlinear electronic circuits [58], ionization waves in plasma [59], or superconductive parametric amplifiers [60].

The Duffing equation is a second-order non-linear differential equation (see Eq.(1.21)) with a restoring force given by $F = -x - \epsilon x^3$. When $\epsilon > 0$ the system is driven by a hardening spring, whereas when $\epsilon < 0$ the system is then driven by a softening spring. One of the main characteristics of a Duffing oscillator is that it is a perturbation of a single harmonic oscillator by introducing a nonlinear spring, leading to a non-periodic motion (*i.e.* the position versus time plot does not follow an exact repetition).

$$\frac{d^2x}{dt^2} + 2\epsilon k \frac{dx}{dt} + x + \epsilon x^3 = \epsilon F_0 \cos(\omega t + \delta) \quad (1.21)$$

It must be noted that the Duffing equation uniquely differs from the forced/damped harmonic oscillator equations by a nonlinear term proportional to x^3 , which dramatically changes the dynamics of the system.

1.4.3 Hearing systems: the locust tympanum membrane

An acoustic organ highly relevant for this thesis is that of the locust, as its simple shape and morphology are able to generate relevant physical phenomena at a small-size scale such as acoustic frequency discrimination and nonlinear effects like DPOAEs, as well as sound localization [11, 61]. These features are a source of inspiration to develop engineered systems, devices, sensors, and actuators able to solve specific problems.

As previously mentioned in this Section, the tympanal membrane, TM, is a thin cuticle membrane stretched over a fluid-filled chamber that allows certain animals to detect the pressure component of sound [9]. Changes in sound pressure generate a proportional force onto the TM, which consequently deflects. If such a pressure remained constant, the deflection of the TM would also be constant, but as these variations of pressure are oscillatory, they therefore produce an oscillatory motion of the TM. The mechanical motion of the TM is converted into an electrical signal through the scolopidia (or mechanoreceptors) attached to strategic points of the membrane, which are stretched and compressed. These mechanoreceptors can be classified in four different categories [62, 63]:

- Pacinian corpuscles: pressure sensors connected to a sensory neuron that can be isolated due to their large size.
- Meissner corpuscles: adapt quickly to a stimulus and are activated when the stimulus is removed.
- Merkel cells: unlike Pacinian and Meissner corpuscles they do not adapt quickly to a given stimulus, but they generate nerve impulses as long as the stimulus is present.
- Muscle spindles: stretch receptors within the muscle constituted by a sensory nerve and spindle fibres.

The morphology of the locust's TM shows variations depending on the species [64, 65]; it has been described to present a pear-shape [66] of around 2.5×2.5 mm in size at its widest in desert locusts (*Schistocerca gregaria*), whereas it consists of a thin oval disk of around 1.5×1 mm in migratory locusts (*Locusta migratoria*) [67]. Regarding its thickness Pumphrey *et al.* reported a thickness of $0.5 \mu\text{m}$ in the most posterior part and $11 \mu\text{m}$ at the most anterior one [67], whereas Gray measured a thickness between $2 \mu\text{m}$ and $3 \mu\text{m}$ [66]. Stephen and Bennet-Clark were able to measure a minimum thickness of $0.6 \mu\text{m}$ at the higher area of the thin membrane region (see Fig. 1.8), and a maximum value of $20 \mu\text{m}$

at the bottom of the thick membrane region [41]. Hence a main conclusion can be made from all these studies; the locust's TM can be divided into two main regions: (i) the *thin membrane*, and (ii) the *thick membrane*, which are two connected different areas of cuticle, and being the thick membrane located ventro-anteriorly from the thin membrane (as shown in Fig. 1.8).

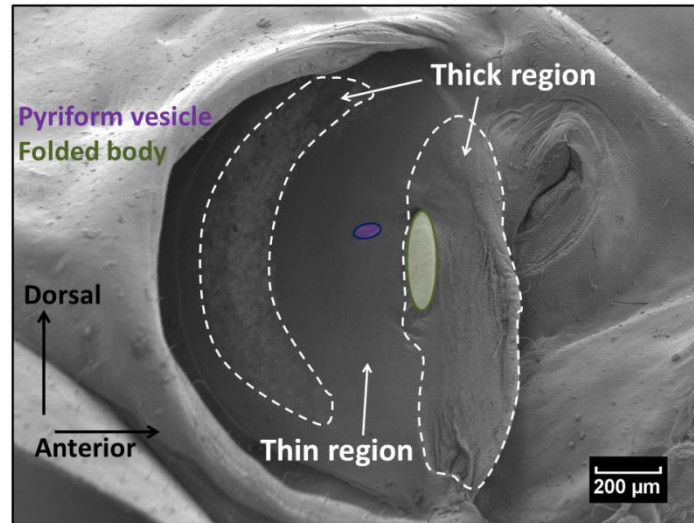


Fig. 1.8. Scanning electron microscopy (SEM) image of the locust TM (right ear). The different regions of the TM can be observed in different shades of grey and outlined by dashed lines. Low and high frequencies are detected more efficiently in the thick and thin regions, respectively. The folded body (FB) is attached to the thick membrane and it is outlined with a continuous ellipse in the most anterior region of the TM. The area surrounding the pyriiform vesicle (PV), is also highlighted with a continuous line on the thin membrane. Image kindly provided by Prof. James Windmill from his study on the presence of traveling waves in migratory locusts [11] and edited by Roger Domingo-Roca.

It must be noted that the locust TM does not consist of a single layer of cuticle but it is something more complex as it is composed by three different layers named *endocuticle*, *mesocuticle*, and *exocuticle*, going from the innermost layer to the outermost one. Stephen and Bennet-Clark studied the locusts' TM in depth and reported that the mesocuticle is impregnated with lipids or proteins, making this part of cuticle stiffer due to smaller interstitial spaces, as well as they described the exocuticle as brittle and stiff [41].

Different regions of cuticle are visible on the membrane where the mechanosensory cells are attached. Michelsen studied these different regions and their attachment points [68], reporting a region of thicker

sclerotized⁶ cuticle called the *folded body* (FB), which attaches to the thicker membrane, where a fold is present (as it can be seen in Fig. 1.8, followed by a thinning of the membrane. Another sclerotized cuticle region on the locust TM is the *elevated process*, which is a hollow, tubular-shaped invagination that ventrally merges with the FB. The third sclerotized cuticle region described by Michelsen is the *styliform body*, which Gray reported to have a concave and flat shape [66] that widens in one of its ends to stay connected to the elevated process. Its dimensions were estimated by Stephen and Bennet-Clark, who reported an egg-shape of around $300 \times 200 \mu\text{m}$ [41]. The *pyriform vesicle*, PV, is the last of the sclerotized cuticle attachment points described by Michelsen on the locust TM, being the smallest one of all the described structures and basically consisting of a thickening of the eardrum cuticle connected to the elevated process. All these four attachment structures merge together into the Müller's organ, described by Michelsen as an irregular spheroid with dimensions of approximately $400 \times 200 \mu\text{m}$ [68] that contains between 60 and 120 scolopidia that allow the locust TM to detect tiny mechanical deflections of the sub-nanometre order [11]. These four bodies have attached to them different scolopidial groups, each of them able to detect different frequencies and named by Gray as groups *a*, *b*, *c*, and *d* [66]. In Michelsen's work *The physiology of the locust's ear (I-III)*, the *a*, *c*, and *d* groups are described to be oriented in three perpendicular planes, whereas the *b* group is described to be placed in the same plane as the *a* group, comprising approximately half of the total receptor cells [68].

Early neurophysiological studies of the locust TM showed no evidence of frequency discrimination: Pumphrey and Rawdon-Smith showed that at 3 kHz the whole system seems to display maximum sensitivity, recording a threshold of 20 dB SPL above that of the human hearing, but with a lack of synchronization between the neural response and frequency of the stimulus, leading to the conclusion that frequency discrimination was not possible in the locust hearing system [67]. Later studies from Horridge, Popov, and Michelsen revealed that the different sensory cells responded to different frequencies: the *a* group was observed to show an average characteristic frequency of around 3.7 kHz, and some of them revealed a second peak at 8 kHz, whereas others were observed to appear between 6 kHz and 7 kHz. The cells of the *b* group revealed characteristic frequency peaks at both 3.4 kHz and 8 kHz, and a smaller peak at 5 kHz, whereas the cells from the *c* group were observed to show high sensitivity at

⁶Sclerotised is a biological term to indicate stiffened or hardened state by cross-linking to other molecules. Sclerotised and unsclerotised cuticles are present in nature, such as the fangs in spiders (sclerotized state) or the honeybee larvae unsclerotised cuticle.

lower frequencies, *i.e.* at 1.5 kHz, and in the range of 2 kHz to 3 kHz. Finally, the *d* group showed a better sensitivity at high frequencies, in the range between 10 kHz and 14 kHz, as well as revealing a second maximum at 19 kHz [69–71] when playing pure tone stimuli at sound pressure levels between 96 and 112 dB SPL. Some years later, Jacobs *et al.* studied again the sensitivity of the different sensory cells on the locust TM [64] testing the animals with frequencies ranging from 100 Hz up to 40 kHz at intensities between 25 and 90 dB SPL, and using different tone pulses (either 100 ms or 20 ms with a repetition rate of 3.3 Hz). Under these conditions, Jacob *et al.* found that the highest sensitivity of the hearing threshold of several animals was at 2 kHz and 5 kHz, with a threshold between 37 and 40 dB SPL.

Studies from Michelsen and Stephen and Bennet-Clark also kept the focus on determining the mass of the different organs and regions of the locust TM. Michelsen performed a fine surgery technique to remove the TM of the abdomen of the locust, and after measuring 13 different samples he worked out a measured average mass of $3.0 \pm 1.0 \mu\text{g}$. Furthermore, Michelsen was able to reveal that when the Müller’s organ is swollen the total mass of the TM increases up to $50 \mu\text{g}$. Finally, Michelsen determined that the mass of the thin part of the membrane has a weight of $7.7 \pm 1.7 \mu\text{g}$ [68]. On the other hand, Stephen and Bennet-Clark studied the mass of the different regions of the membrane more in depth, reporting a total measured mass of $10.1 \mu\text{g}$ for the thin region, $10.7 \mu\text{g}$ for the thick region (resulting in $20.9 \mu\text{g}$ for the totality of the membrane), and a measured mass of between $8.5 \mu\text{g}$ and $12.5 \mu\text{g}$ for the Müller’s organ [41].

Once the authors had measured the mass of the TM they used it in order to determine the theoretical fundamental resonant frequencies of the acoustic organ using Eq.(1.22). To do so, both Michelsen and Stephen and Bennet-Clark assumed that the thin membrane could vibrate in an independent way than the rest of the membrane [41, 68]:

$$f = \frac{0.383}{a} \sqrt{\frac{T}{\sigma}} \quad (1.22)$$

where a is the radius (assuming a uniform circular body in vacuum), T is the tension per unit length, and σ is the mass per unit area. The tension per unit length can be expressed as shown in Eq.(1.23) [68].

$$T \approx \frac{1}{8\pi c_m} \quad (1.23)$$

where c_m is the compliance of the membrane. These studies yielded to a fundamental mode of 3.4 kHz for the thin membrane, and symmetric circular modes at frequencies of 8.1 kHz, 12.9 kHz, and 17.9 kHz. These frequencies were studied by Michelsen at different SPL values (between 96 dB SPL and 112

dB SPL) under laser holography to see the vibration of the locust TM under pure tone stimuli [68], measuring amplitudes of up the micrometre scale due to the high applied SPL values.

More accurate and realistic studies of the locust TM response were performed by Windmill *et al.* years later applying a stimulus of 60 dB SPL and measuring the mechanical deflection of the membrane using laser Doppler vibrometry [11], a much more reliable technique than the ones used by Michelsen and Stephen and Bennet-Clark in their studies, capable to detect sub-micron (down to picometers) motion. In the study ran by Windmill *et al.*, the full locust TM was scanned when playing a wideband signal with the animal placed in a position to ensure the far-field regime of the sound source for the relevant frequency range (3-30 kHz) [11]. These measurements revealed coherence between amplitude and phase data of the mechanical response of the membrane for every scanned point, ensuring data reliability. The authors found increasing amplitude of vibration in the PV as a function of frequency, as well as frequencies of interest at 3.3 kHz, 6.1 kHz, 12.21 kHz, and 22.76 kHz, where traveling waves were observed rather than standing wave patterns, traveling towards the thick part of the membrane. These phenomena were studied at different incidence angles, establishing a relationship between the angle of incidence of the sound field with the propagation path of the traveling wave. The authors also measured the tympanal mechanical deflection of dead desert locusts and compared the frequency response to that observed in living animals, and no difference was observed when comparing the two groups across multiple different frequencies. This lead to the conclusion that the traveling waves, TW, present on the locust TM are not generated by any complicated physiological process. Such results lead Windmill *et al.* to study TWs on the locust TM in deeper detail [72]. They found that TWs generated by different sound stimuli on the locust TM exhibit specific vibrational patterns on the membrane, leading to energy transduction to specific sites of the membrane, and concluding that the locust TM does not behave like a conventional drum skin as it starts oscillating at one unique location to then generate a wave that travels to another position of the TM, an analogous behaviour to that of the basilar membrane of the human's cochlea [72].

Another relevant feature of the locust hearing organ is its ability to detect where sound comes from. An important parameter to understand directional hearing in the locust is how its body interferes with the sound field as the relationship between its size and the sound wavelength determines the amount of scattering leading to pressure variation at the ear, becoming significant at 5 and 15 kHz. At

these frequencies, the maximum difference in sound pressure range from 6 to 8 dB. Sound over-pressure at the right and left ears of the locust finds its maximum at rotations of 30 degrees and 330 degrees of the azimuthal angle, respectively, whereas the maximum under-pressure occurs at 180 degrees for both ears [73]. Attenuation of sound in the locust hearing system revealed a dependence on the amount of tissue between the ears, being inversely proportional to it for frequencies from 3.5 kHz to about 12 kHz.

Even though it is well known that nonlinear effects are present in almost all biological and physical systems, Möckel *et al.* investigated the presence of DPOAEs on the locusts TM as they are thought to act as an indicator of the presence of nonlinear effects. The aim of their work was to set the constraints of DPOAEs generation on the migratory locusts TM [74]. To do so, the researchers removed the d cells group, which are the most sensitive to sound frequencies above 12 kHz, and stimulated the tympanal organ with two pure tones ($f_1 < f_2$), being f_1 10 dB SPL above f_2 . This set up was chosen as it had been shown in previous studies to lead to the highest DPOAE levels, creating a dominant peak at $2f_1 - f_2$ [75]. This $2f_1 - f_2$ frequency was found to be maximal at the so-called optimum ratio f_2/f_1 , which appears to be between 1.1 and 1.4 [75]. Thus, to measure DPOAEs on the locust TM, Möckel *et al.* measured the response of the membrane over a wide frequency range (5-30 kHz), with f_2/f_1 ratios between 1.04 and 1.08, with stimuli levels of 60/50 dB SPL, and they found, like Kössl *et al.* did, that the most prominent emission in the locust ear corresponds to the $2f_1 - f_2$ frequency, finding other emissions at $2f_2 - f_1$ and $3f_1 - f_2$. In mammalian hearing systems these emissions have already been demonstrated to be driven by active processes involving the outer hair cells of the basilar membrane of the cochlea [76]. These active processes seem to improve signal detection by increasing the gain of the system when stimulated at quiet yet ecologically-relevant signals. In locusts, however, it appears that hypoxic animals still display nonlinear acoustic responses and still emit those distortions, albeit at a lower amplitude than control groups. This observation suggests that DPOAEs are produced by a combination of both passive and active mechanisms within the locust ear. More specifically, the heterogeneous structure of the TM could be coupled to an active stimulation by the scolopidia in a fashion analogous to the action of cochlear outer hair cells on the basilar membrane in mammals. Scolopidia are suspected to be the source of those emissions in insects, as they are known to be the site of mechano-electrical transduction, and hypoxia is likely to transiently disable those receptors, resulting in the observed decrease in DPOAEs amplitude under those conditions. However, there is yet no clear understanding of the specific interactions between the scolopidia and the TM that could lead to the latter being driven by the former. Indeed, the

mechanisms underlying the transduction of the mechanical motion of the membrane into an electrical signal by those receptors are not fully understood, and it can be reasonably expected that the opposite interaction involves the same components within the receptor. Further research regarding the relationship between the locust's TM morphology and structure with sound energy localization and frequency analysis revealed the presence of lipid-filled cavities within specific regions of the membrane, as shown in Fig. 1.9.

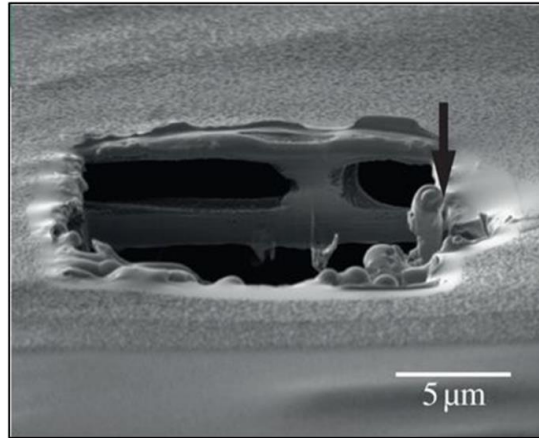


Fig. 1.9. SEM image of the cavities present within the locust TM. The black arrow indicates an artefact formed by the redeposition of liquid during focused ion beam milling. This image suggests that these cavities are present around the pyriform vesicle (PV) of the locust tympanum membrane (TM), helping the propagation of mechanical waves generated by acoustic stimulation toward relevant scholopodial attachment points. Image obtained from [77].

These are thought to be involved in frequency discrimination processes as well as playing an important role in the damping mechanisms that take place across the locust TM [77]. Indeed, damping of flexural waves in liquid-solid interface systems increases with frequency [78, 79] in frequency-dependent damping systems.

Complementarily, these lipid-filled chambers may also affect the surface velocity of the flexural waves generated by the incoming sound waves, as Gubaidullin *et al.* showed that surface velocity of flexural waves slightly decreases with frequency [79].

Understanding the acoustic dynamics of any hearing system provides relevant information about how such a system collects and processes acoustic energy, and can unveil the evolutionary function of such adaptations. Chapter 1 presents the basic concepts of sound as well as it thoroughly discusses

the sound mechanics, morphology and structure of the locust TM. This is important for this work as the locust TM presents a very simple structure with, mainly, two well-differentiated regions that detect different frequencies, allowing for acoustic frequency selectivity in a very simple yet efficient manner. This structure can be exploited to develop 3D-printed structures, resonators, actuators, and sensors that allow for acoustic frequency selection in the microscale and that could be used, for instance, as hearing aids devices. On top of this, if the 3D-printed sensors present the nonlinear effects observed on the locust TM, this work could also give some insight of how these nonlinear effects, mainly DPOAEs, are generated.

Chapter 2

3D Printing

Additive manufacturing technology, developed at the Massachusetts Institute of Technology (MIT), has been recently used in a wide range of fields: in science it has been applied to areas such as medicine, biology, and materials science, among many others. But further to its scientific applicability, additive manufacturing techniques have relevance in other diverse disciplines such as art, fashion, and food industry [1, 2, 80–90].

This increase in the use of additive manufacturing, also known as 3D printing, during recent years has allowed improving some key characteristics of the resulting 3D-printed part such as building efficiency, 3D-printing resolution, and functionality of the 3D-printed parts [91]. Furthermore, the need for 3D-printing different parts of different sizes to use in a wide range of applications has permitted the development of different 3D-printing techniques that use different physical methods to build the 3D-printed part [92]. Even though each of these techniques present a long list of pros and cons, all of them have a common denominator: the *personalization* of the desired 3D-printed part, which allows the full customization not only in terms of geometry and structure of the desired 3D-printed part, but also in terms of optimization of the 3D-printing parameters in order to keep a good balance between 3D-printing time and resolution. On the other hand, 3D-printing techniques share some disadvantages that need to be improved to enhance the applicability of this technology, such as copyright issues, size and materials limitations, and production of non-environmentally-friendly waste.

The different 3D-printing approaches can be liquid-based, solid-based, and powder-based [93]. The first category includes stereolithography (STL) [93]. The second category encompasses techniques

like fused deposition modelling (FDM), laminated object manufacturing (LOM), Multi-Jet modelling system (MJM), plastic sheet lamination (PSL), and paper lamination technology (PLT) among many others [93]. Lastly, the most commonly used powder-based rapid prototyping (RP) systems include selective laser sintering (SLS), laser engineered net shaping (LENS), and electron beam melting (EBM) [93]. One of the major problems of 3D-printing techniques is that not all of them can be used at a same spatial resolution nor can use the same materials, with the liquid-based approaches being more efficient to 3D-print different types of polymers, and the solid-based approaches more reliable when 3D-printing electronic circuits, for example [94, 95]. Furthermore, liquid-based approaches yield better surface resolution than solid-, and powder-based RP approaches [93]. However, the residual stress arising from the phase transformation of the material (from liquid to solid) tends to cause curling during the building process [96]. Table 2.1 presents a brief summary of the different 3D-printing types, their resolution, and the materials they use.

3D-printing approach	Resolution (layer thickness)	Materials
STL	10 μm	Photocurable resins
FDM	100 μm	Plastics
LOM	112 μm	Paper
MJM	16 μm	Photocurable resins
PSL	100 μm	Plastic sheets
PLT	100 μm	Paper
SLS	60 μm	Plastics
LENS	400 μm	Metal components
EBM	50 μm	Metal components

Table 2.1. Summary of the different 3D-printing approaches, their resolution and size limitations, and the materials they use. Data obtained from [93–96]

In this thesis 3D-printing has been used as a tool to develop parts and sensors in the microscale in a time-efficient manner. Furthermore, 3D-printing allows the user to a degree of personalization in terms of built geometries and materials that other manufacturing techniques do not permit. In the course of this research an ASIGA PicoPlus Pro27 3D-printer (ASIGA, Anaheim Hills, California, USA)

has been used to build and develop all the parts and devices. This uses a liquid-based approach to build the desired parts by means of STL. In this Chapter some of the key characteristics and parameters for STL 3D-printing are discussed as well as the basics of the polymerization process.

2.1 Polymers: types and main characteristics

Polymers, commonly known as plastics, are organic compounds consisting of long chains assembled by smaller repeated molecule units (*monomers*), which are formed by the process of *polymerization* [97]. Polymers are present in our daily lives and are used for wrapping and packing, for textile purposes, to develop parts of automobiles, and for electronic applications among many others [97].

Polymers can be split in two different types: *synthetic* (which are derived from petroleum oil) and *natural* polymers, and can be classified in different ways depending on the arrangement of their chains (*homopolymers* and *copolymers*), depending on their mode of polymerization (*addition polymers* and *condensation polymers*), or as a function of their physical response to heating (*thermoplastics* and *thermosets*) [97].

2.1.1 Natural polymers

Natural polymers are those which are present in, or created by, living organisms, including polymers from renewable sources that can be polymerized to create bio-plastics. Natural polymers compose most of the structures of living things, with the most famous one being deoxyribonucleic acid (DNA), and can be of three different types: (i) *polynucleotides*, which are chains of nucleotides, (ii) *polyamides*, which are chains of proteins, and (iii) *polysaccharides*, which are chains of sugars [98].

Among the different types of natural polymers, *cellulose* is the most abundant carbohydrate in the world (a 40% of all the organic matter is cellulose [98]), it is the main constituent of plants, and it is also present in algae, bacteria, fungi, and animals. *Chitin* is a polysaccharide similar to cellulose (it replaces the OH group on the C-2 carbon of each glucose units with an $-\text{NHCOCH}_3$ group), and it is the second most abundant polysaccharide in the world, playing a key role in the cell walls of fungi and in the exoskeletons of spiders, insects, and crustaceans [98]. Another relevant natural polymer is *collagen*, which has found several applications in tissue engineering and repair [99] as well as for medical

implants [100] due to its ability to polymerize in three-dimensional fibrous matrices. Other relevant natural polymers are *starch*, *casein*, *fibrogen*, *lipids*, *silks* or *natural rubber* amongst many others [98].

Natural polymers can form natural reinforced fibres, which can be subdivided depending on their origins (if they come from plants, animals or minerals) [98]. All plant fibres are composed of cellulose (leaves, seed, fruit, wood and cereal among others) whereas all animal fibres consist of proteins (hair, silk and wool) [98].

2.1.2 Synthetic polymers

Synthetic polymers are man-made macromolecules that consist of repeating monomers, and have become increasingly popular due to the fact that there are several ways of producing and modify chemical structures in an economic and unlimited way to produce materials with specific properties [101, 102]. Nevertheless, this unlimited use of petroleum resources opens the debate, one more time, of the impact of plastics in the environment, empowering the use and development of eco-friendly technologies to develop the same (or very similar) materials with the same characteristics [103].

Synthetic polymers are usually hard to break and cheap to make and shape [104]. One of the most common synthetic polymers is *polyethylene* (made of *ethane* monomers), which can be used to make very large objects like tubes, and it can also be used to build smaller objects such as bottles to pack liquids (which are actually not made of polyethylene but from a very similar synthetic polymer called *polyethylene terephthalate*, PTE, or PETE) or toys [104].

Other synthetic polymers developed so far are *nylon*, which has the tendency to become hydrophilic, *polyvinyl chloride*, which is one of the most produced synthetic polymers in the world and it is used for construction purposes and cable insulation, low-density *polyethylene*, which are the most common synthetic polymers and are widely used in households, and *polypropylene*, which is used in a wide range of applications such as packing, labelling, textiles, reusable containers, laboratory equipment, and many more [?].

2.2 Classification of polymers

As previously mentioned in this Chapter, synthetic polymers can be comprised in several classifications, depending on several parameters such as the structure of their chains, their mode of polymerization, and their physical response to temperature.

2.2.1 Classification based on their chain structure

Polymers can be grouped based upon the chemical structure of their backbones. *Homopolymers* are those polymers in which a single monomer unit is polymerized into a macromolecule [105]. On the other hand, *copolymers* are those in which the macromolecule is formed from two or more monomers [105]. It is possible to develop *copolymers* in a way in which the monomers are randomly distributed, providing a degree of personalization to the developer in terms of mechanical properties.

Polymers can be *linear* (composed of chainlike molecules which can be viscous liquids or solids with varying degrees of crystallinity, and can dissolve in certain liquids and melt upon heating), or *cross-linked* (networks of molecular structure that do not dissolve in solvents and do not melt upon heating, and can be formed by *addition* or *condensation*, as discussed later in this section) [106].

2.2.2 Mode of polymerization

Polymers can also be classified depending on their mechanism of polymerization, being *addition* and *condensation* the most common ones.

- Addition polymers are created through free electrons present in double bonds, which are used to bond two monomer molecules together [105]. Thus, double bonds become single bonds such that no atoms are lost. The most important addition process is called *chain-growth*, which is discussed in further detail later in this Chapter. Polymers that form through this process are low- and high-density polyethylene, PVC, polypropylene, and polystyrene.
- Condensation polymers usually occur with the generation of a byproduct such as water [105]. Polymers created through this process are commonly known as *step-growth* polymers (as discussed in further detail later in this Chapter). In contrast to addition polymers, which are created by carbon-carbon bond creation, condensation polymers grow by carbon-heteroatom bond formation (C-O, C-N, for instance). These polymers could be thought to be alternating *copolymers*, but the

repeating monomer unit is usually defined as a combined moiety.

Condensation polymers usually require a source of energy to form, growing slower and resulting in lower molecular weights than addition polymers [107]. Another big difference between these two processes is that in condensation polymers the terminal functional ends of the chain remain active, allowing groups of shorter chains combine into longer chains in the late stage of the polymerization process. If these functional groups are polar, the chain-chain interaction is enhanced, especially if they involve hydrogen bonding, furthermore, contributing to crystallinity of the polymer.

The materials used in this thesis are condensation polymers.

2.2.3 Physical properties

Depending on the thermal response of the polymers, they can be classified as:

- **Thermoplastics:** are linked by intermolecular interactions or van der Waals forces and can form linear or branched structures [105]. These polymers soften when they are heated and become rigid when cooled down [105]. Furthermore, depending on the degree of the intermolecular interaction between the chains, thermoplastics can present *amorphous* (which are disordered chains) or *crystalline* (the chains acquire an ordered structure) structures, with co-existing phases in specific materials [108]. Whereas the amorphous structure of the polymer is directly related to its elastic properties, the crystalline structure is responsible for the resistance of the polymer to stress [108]. Thus, the concentration of polymers with amorphous or crystalline structure will determine the mechanical properties of the thermoplastic.
- **Thermosetting:** are made by polymers joined together by chemical bonds and acquire a highly cross-linked structure [108]. These plastics soften when heated, harden permanently, and decompose when reheated [105]. The high degree of cross-linking of thermoset materials provides a low degree of elasticity [108]. The main characteristic of these materials is the *gel point*, which is an abrupt change in viscosity where *gelation* is reflected as a loss of fluidity (*i.e.* when they move from viscous liquid state to solid state). When the *gel point* has been overcome, the material stops flowing and it cannot be moulded anymore (a key aspect for stereolithography 3D-printing purposes).

Elastomers can also be added in this section, which are polymers that are joined by chemical bonds reaching a low degree of cross-linking in their structure [105]. The main characteristic property of these

materials is that when stress is applied to them, the length and size of the chains increase, and as soon as stress is removed they come back to their initial length. Elastomers present a high degree of flexibility and elasticity before they break[108]. Depending on the strength and density of the chemical bonds that keep the chains of the polymer together, elastomers can present very similar mechanical properties to those observed in thermosets and thermoplastics. Thus, they can be sub-classified as (i) *thermoset elastomers* which are elastomers that do not melt when heated, and (ii) *thermoplastic elastomers* which are elastomers that melt when heated.

2.3 Development of 3D-printable materials

An important part of the research conducted during this thesis consisted of the development of new 3D-printable composite functional materials to be used in liquid-based approaches for STL, as the number of commercially available resins for STL purposes is very low. Furthermore, the few commercially available materials for 3D-printing using the STL technique are polymeric materials (plastics) that when 3D-printed do not present any kind of functionality apart from the one provided by its own structure, and geometry of the 3D-printed part. Some of their characteristics are shown in Table 2.3 [109].

Company	Materials	Applications/Projects
ASIGA [114]	Plastics	Jewellery, dental, and microscale applications.
Stratasys [115]	Thermoplastics	Biocompatibility, and dental.
ProtoLabs [116]	Plastics and metals	Large scale 3D-printing.
Handsmith [117]	N/A	3D-printing bionic hands.
Saphium [118]	Compostable plastics	Environmentally-friendly 3D-printing.
Markforged [119]	Metals	Carbon fibre printing.
Cartesian Co [120]	Metals	3D-print electronic systems.
Biobots [121]	Tissue and cartilage	3D-printing organs.
Made in Space [122]	N/A	3D-printing in International Space Station (ISS).
ApisCor [123]	N/A	3D-printing houses.
Natural Machines [124]	N/A	3D-print food.

Table 2.2. Companies using different 3D-printable materials in very contrasting projects, both in the micro- and macroscale.

The majority of the polymers developed to use in STL machines are based on low-molecular weight multi-functional monomers that form networks through polymerisation (see Section 2.2) and cross-linking when adding a photo-initiator. Molecular weight, as well as its distribution, play a key role in the mechanical and thermo-physical properties of a polymer; those with a small number of repeated oligomers will be soft (or even liquid) and present low strength values, whereas those with higher numbers of repeated oligomers and a higher molecular weight will be solid and present larger hardness values. This increase in the mechanical and visco-elastic properties with molecular weight reaches a maximum value at a specific molecular weight, independently of the length of the polymeric chain, and following an asymptotic approach. The first resins developed for STL 3D-printing were rigid, glassy, and brittle [110], but in the last decades several polymers that cover a wide range of mechanical properties have been developed [111–113], and are constantly improving to make this range wider, as well as making them useful not only for prototypes or mechanical applications, but also for functional parts. Table 2.2 shows different companies using several 3D-printable materials that can be used in very contrasting fields, both in the micro- and macroscale.

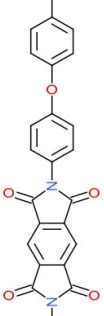
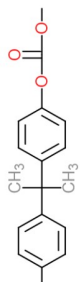
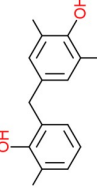
Polymer	Repeat unit	Commodity Polymer	Engineering Polymer	Step growth	Chain growth
Polyethylene (low density)	$-\text{CH}_2\text{CH}_2-$	YES	-	-	YES
Polyethylene (high density)	$-\text{CH}_2\text{CH}_2-$	YES	-	-	YES
Polypropylene	$-\text{CH}_2\text{CH}(\text{CH}_3)-$	YES	-	-	YES
Poly(vinyl chloride)	$-\text{CH}_2\text{CHCl}-$	YES	-	-	YES
Polystyrene	$-\text{CH}_2\text{CHPh}-$	YES	-	-	YES
Polyethylene Terephthalate	$-\text{OCH}_2\text{CH}_2\text{O}-(\text{C}_6\text{H}_4)-$	YES	YES	YES	-
Polyamide	e.g. $-\text{CONH}(\text{CH}_2)_5-$	-	YES	YES	-
Polyimide		-	YES	YES	-
Polycarbonate		-	YES	YES	-
Phenol formaldehyde resin		-	-	-	-
Rubber	$-\text{CH}_2\text{C}(\text{CH}_3)=\text{CHCH}_2-$	-	-	YES	-

Table 2.3. Some typical polymers, classification, and characteristics. Table obtained from *Stereolithography. Materials, Processes, and Applications* [109]

In order to move this project forward, it was necessary to develop new functional composite 3D-printable materials that would work when using the STL RP approach. The first step was to develop several non-functional materials as a proof of concept that the possibility of 3D-printing new polymer-based non-commercial materials using an ASIGA PicoPlus27 is real when properly adjusting the 3D-printing parameters and settings of the 3D printer.

2.3.1 The polymerization process

Polymerization is the chemical process through which several monomers can be combined to form a polymer or a polymeric compound, consisting of the repetitive bonding of small molecules [106]. Monomers are single small molecules, such as hydrocarbons or amino acids (see Fig. 2.1) [106]. These monomer molecules, which can be alike or different compounds, combine in high numbers to form longer chains with strong physical properties, such as elasticity, high tensile strength or the ability to form fibres, for example.

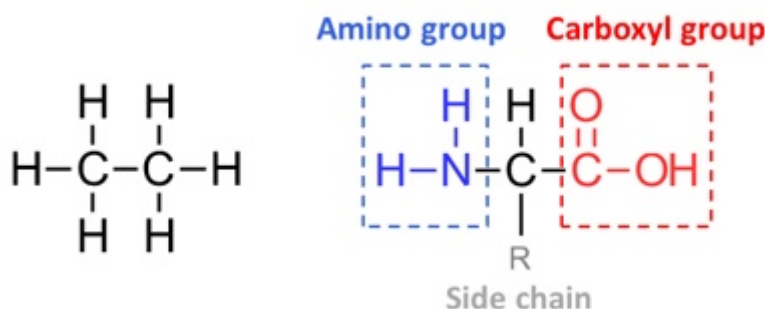


Fig. 2.1. The left hand side image shows the basic structure of a hydrocarbon (ethane, C_2H_6), whereas the right hand side image shows the basic structure of an amino acid, where three main parts can be distinguished: the amino group (in blue), the carboxyl group (in red), and the radical (side chain, in light grey).

In nature, polymerization is a very common process in several fields; for instance, enzymes carry out polymerization to form proteins, carbohydrates, and nucleic acid [106]. On the other hand, when developing specific polymer-based materials, polymerization of monomers is a chemical reaction that needs to be performed under highly controlled conditions, as some polymerization processes are exothermic and if performed under the wrong or inadequate conditions could lead to explosions or fires. The polymerization process does not follow a unique path, but it can be performed in several ways, leading to a polymer classification according to the way in which the propagation of their chains occur.

1. **Step growth polymerization:** step growth polymers are formed by stepwise reaction between

bi-functional (or multi-functional) groups of monomers. As a result, and after a repeated number of steps, a high-molecular-weight polymer is formed. Due to the nature of the polymerization mechanism, the reaction has to proceed for a long time in order to achieve high-molecular-weight polymers. In the step growth polymerization process, branched polymers can be produced if monomers have more than two reactive sites (as shown in Fig. 2.1). The most relevant step growth process is *condensation*.

- (a) **Condensation polymerization:** this type of polymerization often occurs with loss of a small byproduct, such as water, and generally combines two different components in an alternating structure. Condensation polymers tend to form in a slow way, often requiring heat, and being lower in molecular weight [125]. In this type of polymerization, the terminal functional groups remain active such that shorter chains can combine in late stages of the polymerization process. Another important feature is the presence of polar functional groups on the chains, which enhance the chain-chain attractions, providing a higher degree of crystallinity and tensile strength to the resulting polymer, especially when involving hydrogen atoms. Examples of condensation polymerization are polyesters, polyamides, proteins, and polysaccharides [125].

2. **Chain growth polymerization:** chain growth polymers are formed by addition of monomers to a growing chain. This polymerisation process consists of three main steps: *initiation*, *propagation*, and *termination*. The initiation process can be split into two steps: the formation of a chain carrier (R^*) from a suitable initiator, which can be either an ion or a free radical (leading to cationic/anionic polymerization and free-radical polymerization processes), and the reaction of a radical with the first monomer molecule, which is called the *activated polymer*. The activated monomer can rapidly react with other monomer units, so while the reaction progresses the active centre propagates down the polymer chain. During this process, several thousands of additions may occur in a very small timeframe [125]. The termination stage is reached when two free radicals combine to form a single polymer molecule which cannot react with more monomer units [125]. Termination can happen in two ways: by combination of two radicals or by disproportionation, which usually involves the transfer of a hydrogen atom.

- (a) **Addition polymerization:** in this case, monomers need an initiator to start a chain reaction to form polymers without forming byproducts. It consists of three main parts: *initiation*, *propagation*, and *termination*. The initiation step starts when a peroxide molecule (H_2O_2)

breaks up into two reactive free radicals, where the required energy to start the process can be provided by light or heat [125]. The initiation stage has another step, consisting of the attachment of the free radical of the initiator to a monomer molecule, creating a new free radical called the *activated monomer*. When the monomer has been activated, the propagation step starts taking place, and is the most time consuming step of the whole process. This step consists of the attachment of the activated monomer to the double bond of another monomer molecule. This action is repeated over and over again leading to long polymer chains (notice that the polymer only grows at the reactive end, the one with unpaired electrons). When two free radicals combine to form a stable bond, the polymer cannot grow anymore, leading to the termination of the polymerization process [125].

Because of the nature of the polymerization process, chain-growth polymers are less readily formed photochemically, where the use of an initiator is unnecessary [125]. However, high molecular-weight polymers are difficult to obtain and are often produced from functionality¹, leading to higher intermolecular forces in engineered polymers than in commodity polymers, making them useful for applications that require high mechanical strength. While the synthetic origin of a polymer is important from the point of view in which the polymer is processed, it is also a major factor in determining the properties of the materials, as processing techniques such as extrusion or spinning provide additional mechanical strength to the polymer through promoting backbone crystallization and alignment [125].

Fig. 2.2 illustrates the difference between step growth and chain growth processes: whereas in chain-growth polymerization processes the average molecular weight is achieved at low concentration values, for step-growth polymerization processes a higher concentration is required to achieve the same average molecular weight.

¹The functionality of a monomer is the number of bonds that a monomer's repeating unit forms in a polymer with other monomers. Different functionality, denoted as f , leads to the formation of different types of polymer such as linear or cross-linked

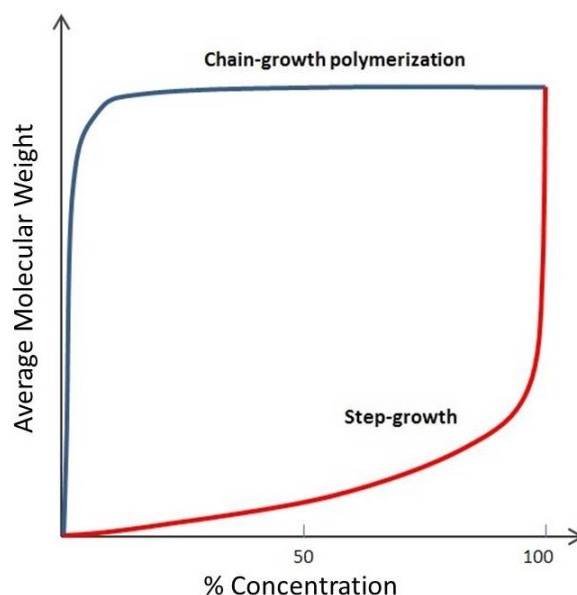


Fig. 2.2. Average molecular weight of chain-growth and step-growth processes as a function of monomer concentration. This graph shows how the average molecular weight of chain-growth and step-growth polymers changes with monomer concentration. This image also shows that whereas step-growth polymers will slowly increase their average molecular weight, the opposite will be observed in chain-growth polymers. Graph obtained from the *Polymer database*, [125].

2.3.2 Cross-linking

An important property of polymers is their ability to form *cross-links* between neighbouring chains (see Fig. 2.3). Cross-linking has as a main consequence the restriction of translational mobility of the chains of the polymer, which provides stability in all three dimensions [126]. These polymers, furthermore, cannot melt or dissolve, which becomes a key property in the development of 3D parts since it ensures that the final material can be separated from the monomer or prepolymer. The presence of reactive units in the chain of a polymer allows the formation of post-polymerization² cross-links, as it is the case in many stereolithographic techniques.

The density of cross-links will have a high impact on the properties of the cross-linked polymer; whereas low density of cross-links will provide rubber elasticity to the polymer (allowing reversible deformation), on the other hand, a high density of cross-links will yield to hard resinous materials [126].

Even though there are several ways to produce 3D polymeric materials, cross-linking (also known as *photochemical polymerization*) is one of the most common processes as the use of optical techniques,

²Ideally forming systems that have side groups that present different reactivity to the polymerisable units in the monomers prior to polymerization.

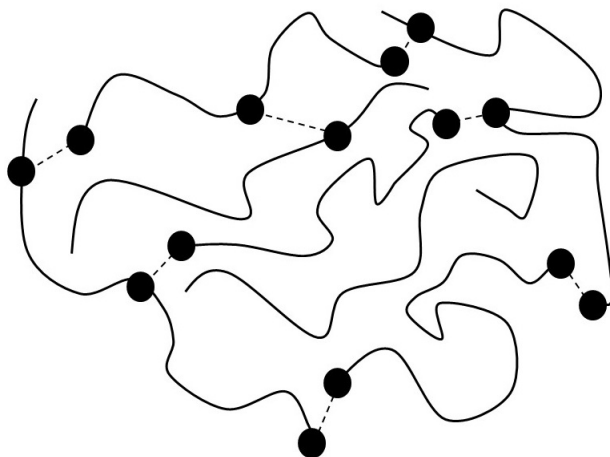


Fig. 2.3. Schematic representation of cross-linking in a polymer. The dashed lines between solid black circles (reactive ends) represent the short-length cross-linking chains whereas solid lines represent polymeric chains. This representation gives an idea of why a higher density of cross-links provides a higher degree of three-dimensional stability.

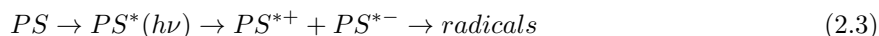
such as lasers, allow a high level of both spatial control and resolution.

2.3.3 Photopolymerization

Generally the polymerization process needs an energy input to start the chain reaction, the most common energy sources being heat or light. When the required energy to start the initiation step is obtained from light, the process is called *photopolymerization*. The photopolymerization process demands low electrical power input as well as a low operation temperature, and it is a process during which no volatile organic compounds are released [127].

Photopolymerization processes involve a polymerizable radical or cationic matrix and a photoinitiating system. Free radical photopolymerization (FRP) and cationic photopolymerization are the most relevant photopolymerization processes, with the first being the most common one. A photoinitiating system (PS) contains at least a photoinitiator (PI) and/or photosensitizer, which absorbs light and needs to be selected to absorb the irradiation wavelength [128]. Upon excitation the PI becomes excited (PI^*) and generates a radical, R^* . When a PS is used and excited, the excitation has to move from PS^* to PI by energy (Eq.2.2), or electron transfer (Eq.2.3): the same R^* is formed or new ion radicals are created, respectively [127].





In cationic photopolymerization, onium salts (Ph_2I) are used as PI [128]. Their photosensitized decomposition occurs according to energy (Eq.2.6) or electron transfer (Eq.2.7), similarly than in FRP processes.

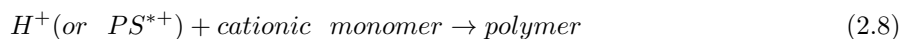
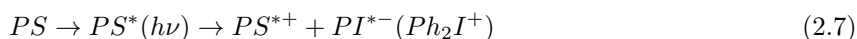


Table 2.4 shows the consequences of the factors induced by photopolymerization processes.

Free-Radical Systems

Although photopolymerization can be induced in a number of ways, the most commonly used systems involve the mediation of free radicals, which can be generated *via* homolysis of weak bonds under incidence of light.

Free-radical systems (FRS) are used to make polymers from small molecules containing carbon-carbon double bonds (*vinyl* monomers) [129]. The process starts when the initiator splits, separating the pair of electrons of the bond and leaving the initial molecule divided into two parts, each one containing an unpaired electron. These molecules are called *free radicals*. These unpaired electrons have the ability to swap themselves with pairs of electrons arising from carbon-carbon double bonds, forming a new chemical bond between the initiator fragment and one of the double bond carbons of the monomer molecule. Because this electron associates itself with a non-bonded carbon atom, the starting point is reached again generating a new radical that will repeat the full process, forming new radicals over and over again (propagation step). When a reaction can self-perpetuate, it is called a *chain reaction*. The termination step can happen, mainly, in two ways due to the instability of the radicals.

Factor	Consequence
Switch from mono to diacrylate	Rate of polymerization increases and material becomes cross-linked; flexibility decreases; hardness increases, improved solvent resistance.
Switch from di- to tri-acrylate	Rate of polymerization increases and material becomes cross-linked; flexibility decreases; hardness increases improved solvent resistance more unreacted alkene groups.
Use of styrene rather than acrylate	Lower cure speed
Changing the linking groups in a diacrylate	Aliphatic polyurethane give soft flexible materials; aromatic polyesters and polyethers produce hard scratch resistant coatings.
Use of mono-acrylate containing 2 oxygen atoms in a heterocyclic structure	Greatly enhanced activity of speed of cure.
Pigmented system	Polymerization is less efficient as less light available to interior of sample. Specialist initiator required.
Change of excitation wavelength to shorter UV	Resolution improves, problems into penetration depth into the sample.
Use of siloxane system	Lower glass transition temperature, and more flexible final product.
Cationic system	Oxygen less important; reaction may continue in dark. In general cationic polymerization is slower than radical process (particularly for epoxy systems). Moisture interferes with cationic systems – not with radicals. Shrinkage less of a problem for cationic systems.

Table 2.4. Factors influencing the behaviour of photopolymer systems. Table obtained from *Stereolithography. Materials, Processes and Applications* [109].

1. Coupling: when two different growing chain ends find each other, as the two unpaired electrons join to form a pair and, therefore, a new chemical bond joining the two chains.
2. Disproportionation: when two growing chain ends come close together, one of the unpaired electrons (corresponding to one of the chain ends) tries to find a free electron elsewhere from the other chain end, finding it in the carbon-hydrogen bond of the carbon atom *next* to the other carbon radical. At this point, the free electron takes both the hydrogen atom and one of the electrons, leaving the first chain with no unpaired electrons, and the end carbon sharing eight electrons with other carbon and hydrogen atoms. Therefore, the two carbon radicals can join their unpaired electrons to form a chemical bond between the two carbon atoms. Because the two atoms already shared a pair of electrons, the second shared pair creates a double bond at the end of the polymer chain. Sometimes, the unpaired electron at the end of a growing chain will pair itself with an electron from a carbon-hydrogen bond along the backbone of another polymer chain, leaving an unpaired electron that cannot form another double bond as previously described, but it can start a reaction with another monomer molecule as the initiator did at the start of the reaction. This process starts a new chain growing in the middle of the first chain, giving as a result a *branched polymer* [129].

The FRS polymerization process is shown in Fig. 2.4.

Cationic systems

In chain-growth processes, photoinitiation is also very common and cationic systems are somehow complimentary of free-radical systems. Furthermore, they offer the potential of post-polymerization cross-linking. There are two ways in which the chemical reaction can start [131].

1. The cation species may themselves initiate polymerization.
2. The cation species may generate Brönsted acids which then react with the monomer.

A main difference between free-radical and cationic systems is that the latter can proceed in the presence of oxygen and polymerization can take place in the absence of light once ionic species have been produced, which is in high contrast with free-radical systems as the reaction would stop in a fraction of a second after the removal of the light source.

Cationic polymerization allows the development of polymers by adding monomer chains together, as described in the previous section for free-radical systems. The main difference with free-radical

monomer molecule and so on.

When all the electrons have rearranged themselves (due to the presence of hydrogen atoms in the monomer groups, which will break away very easily attracted by the pair of electrons of the carbon-carbon double bond in the polymer molecule), the polymer chain becomes neutral and can no longer react and grow. Notwithstanding, the new cation can start a new chain growth process in the same way as the initiator did. At times, the unshared pairs of electrons from the chlorine atom of the initiator will react with the cationic carbon atom and will join the polymer forming a double bond. Therefore, the polymer will not be able to chemically react again and the termination step is reached [131].

In FRP, the selection of near UV/visible photosensitive systems for industrial applications is quite easy, whereas in cationic photopolymerization, as the PIs mainly absorb in the UV regime, the search and design of suitable PS compounds as energy or electron donors for visible light-induced polymerizations are necessary, but this appears as a rather complex task for the photocuring of coatings in industrial lines.

Free radical promoted cationic polymerization (a reaction produced from a radical source which is oxidized to form a cation) is one of the most interesting and promising ways for cationic polymerization under exposure at wavelengths $\lambda > 350$ nm (and up to 700 nm) due to its versatility, but the occurrence of efficient reactions is not so trivial, and the oxygen quenching of the radicals is detrimental [127].

2.3.4 The stereolithography process

STL is one of the most adaptable 3D-printing approaches as it gives the user a high degree of versatility when designing structures, as well as the scale at which those can be built. STL is an additive manufacturing process that permits the fabrication of a part from CAD files [109] or user-developed masks. There are several ways to develop these CAD files: (i) using computer drawing tools and software like SolidWorks, PTC Creo, or AutoCAD among many others, (ii) importing an object obtained from scanning techniques such as magnetic resonance imaging or tomography techniques, and (iii) using mathematical equations that describe specific surfaces and geometries.

The CAD file determines the size, morphology, structure, and topography of the desired 3D-printable part to be built. The first step when it comes to STL 3D-printing is to import the designed CAD file

into a software provided by the 3D-printer's company, which allows to virtually place and orient the part in the accurate way in which it will be 3D-printed. To do so, the CAD file needs to be saved using the *.stl* format in which the part has been divided into small tetrahedrons (at a resolution chosen by the designer) that when summed up form the surface of the designed 3D structure. Before 3D-printing, it is necessary to add supports that will make the sample attach to the holder or building platform. The structure, geometry, and density of supports can be controlled in the software, as well as other parameters like the self-support angle, the side-feature size, the material strength, the support spacing, the torsion tolerance, the contact width, over-shooting, maximum width, and their aspect ratio.

After the part has been virtually placed, the software slices the part into different layers, whose thickness is determined by the software (in the case of an ASIGA PicoPlus27 3D printer, it is possible to choose thicknesses of 10, 25, 50, 75, 100, 125, and 150 microns). This slice thickness remains constant during the full 3D-printing process.

The process of manufacturing 3D objects using the STL approach is based on the solidification of a liquid resin by spatially controlling the photo-polymerization process. Once the building block has lowered down and is in contact with the liquid, the pattern of the part is projected onto it and is cured under UV light, which allows the photo-polymerization process to happen and it hardens the first layer of polymer. When the first layer has been solidified, the building block moves away and the second layer is projected onto it, repeating the previous process until the entire part is built. The full cycle is shown in Fig. 2.5.

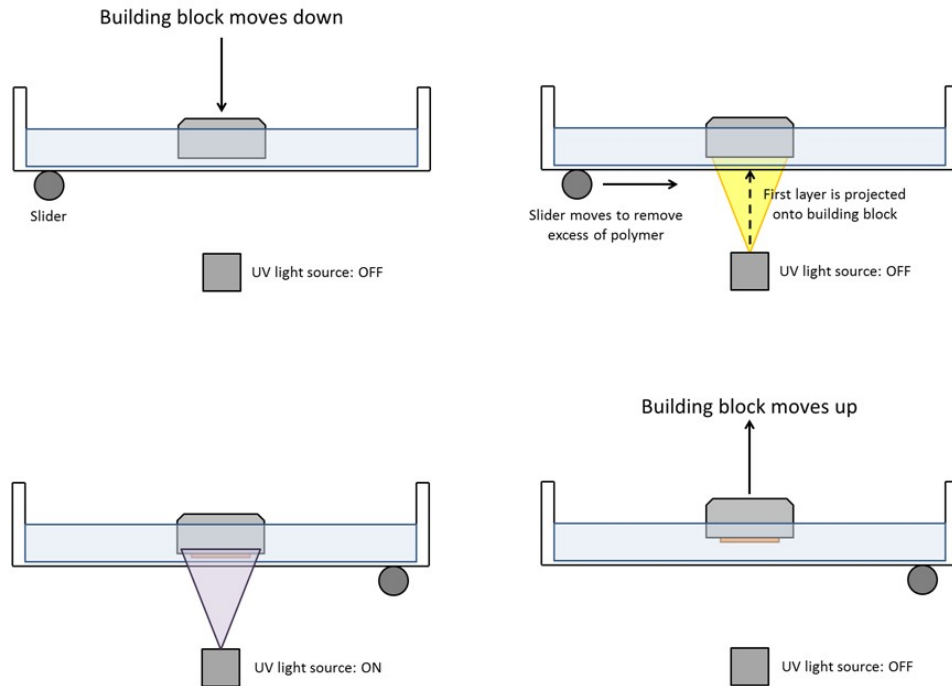


Fig. 2.5. Full cycle to build one layer when using the STL approach of ASIGA. Firstly, the building block approaches to the building tray where liquid polymer is placed. Once the building block makes contact with the building tray membrane, the first layer of the part is projected onto it (yellow triangle), and the slider removes the excess of polymer. When the slider has completed its trajectory, ultraviolet light (purple triangle) is applied onto the first layer such that the liquid polymer solidifies. Finally, the building block is removed from the building tray and the full process is repeated projecting all the layers composing the sample.

Parameters to adjust in liquid-based RP approaches

When 3D-printing an object several parameters must be adjusted, such as the building orientation (which can affect the mechanical properties of the object [132]), the layer thickness, and the working temperature (which becomes extremely relevant when 3D-printing waxes that are solid below a certain temperature), among others. All of these properties can affect the resolution of the 3D-printed part.

Another important factor to consider when 3D-printing a part is the *stairstepping* effect, which can be easily understood when looking at Fig. 2.6 [133].

The stairstepping effect becomes more apparent when 3D-printing parts with curved surfaces using liquid-based techniques, and in some cases it may be impossible to eliminate, but it is possible to reduce it by orienting the part in a certain way. Even though a proper orientation of the part will reduce

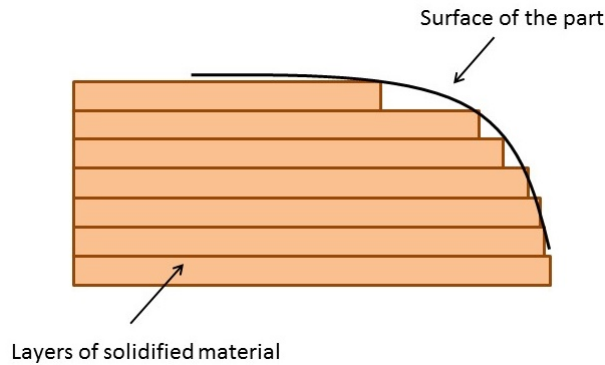


Fig. 2.6. Sketch of the stairstepping effect appearing when 3D-printing a part using the STL method. In this representation it can be seen how the layer thickness influences the stairstepping effect; the thinner the layer is, less pronounced this effect will be.

the stairstepping effect and 3D-print it with a better resolution, it will increase the 3D-printing time, which sometimes is counterproductive. Therefore, it is important to keep a good balance between surface resolution and 3D-printing time to make the whole process more effective, as the best surface resolution will lead to 3D-printing times longer 24 hours, and quick 3D-printed parts will lead to bad surface resolution. Ultimately, though, surface quality of the 3D-printed part is more important than 3D-printing time.

Supports

When building a part using a liquid-based approach, support structures are necessary in order to make sure that the 3D-printed part attaches to the building block. These supports provide the means to detach the part from the platform on which it has been built. Additionally, overhanging features need support structures to prevent them from sagging during the building process. Therefore, the addition of supports is one of the most important features when deciding how to orient a part, as its size directly affects the build time. The amount of support structures is also important; if the supports are too large, the part will need a time-consuming post-processing step in order to remove all the supports by hand without damaging the surface of the part. Currently the post-processing step is not automated, meaning that the number of used supports should be minimised when possible. Furthermore, the fact that the supports need to be removed by hand, affects the quality of the 3D-printed part. For processes employing external support structures, (such as STL processes), the material consumed includes two parts: (i) the amount of material used to build the supports themselves, and (ii) the amount of material used to build the structure. The software can calculate an estimation of the amount of supports needed in a

specific part depending on the area that needs supports in order to properly attach it to the building block.

Supports can be added when 3D-printing any type of object, and irrespective of whether the part of interest is solid or it has a hollow region (see Fig. 2.7).

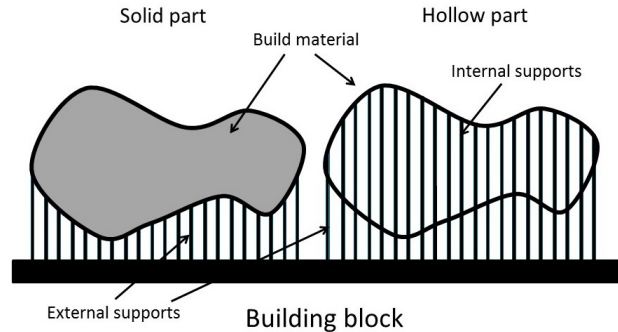


Fig. 2.7. Sketch of placement of the supports when 3D-printing solid and hollow parts. The solid part only needs to be supported by external supports, whereas the hollow part, apart from the external supports, also needs internal supports to avoid the part to collapse.

There are two key points to be noted here. First of all, ASIGA's Composer software allows the user to define the strength of the support structures, a parameter that is very useful when 3D-printing large parts. If the part is too big, using standard supports might not be useful, as the part may fail on the building block due to its own weight. Increasing the strength of the supports might help to overcome this issue since stronger supports are built using slightly longer burn-in exposure times. Secondly, it is also important to take care of the use and placement of internal supports. If the user is only interested in the surface of the 3D-printed part and the inside region is not relevant for the final purpose, then internal supports will be placed and kept within the part, as they will keep the structure stable. Nevertheless, if the user is interested in 3D-printing hollow relevant parts, it is important to find a way to remove the internal supports without damaging the structure. In some cases, though, simply by orienting the part in a specific way internal supports will not be needed as the structure of the part itself will act as a support. In other cases, generally when 3D-printing complex structures, the use of internal supports is unavoidable.

General orientation characteristics

Ideally a 3D-printed part should not only accomplish the resolution and quality requirements, but it also should be built at the lowest cost and time. Hence, the selection of optimal orientation is actually a multi-criterion optimisation problem. The selection of the building direction affects the volume of

building inaccuracy, as well as leading to variation in the quality of the built part. The manufacturing time of an RP part consists, mainly, of three components; *(i)* pre-processing time, which encompasses the CAD file development and the virtual placement of the part onto the building block in the correct orientation, as well as adding the supports, *(ii)* fabrication time, which is the time that it takes for the 3D printer to build the part irrespective of the approach used, and *(iii)* post-processing time, which depends on the geometry of the 3D-printed part as well as the approach used. When using a solid-based RP approach, the post-processing step mainly consists on the removal of the supports (if used), whereas this step is more time-consuming if the liquid-based RP approach has been used, as it implies the removal of the excess of polymer, the removal of the supports, and its posterior exposure to UV light in order to finalise the polymerization process. Furthermore, when 3D-printing specific functional materials such as piezoelectric materials and irrespective of the used approach, the post-processing step includes the poling process of the 3D-printed sample. Generally, the pre-processing step is the quickest one when compared to the other two steps. The major concern of building cost when considering part orientation in RP processes is the material cost. Generally, the building cost is chosen as the main optimisation objective [134].

There are several general orientation characteristics that are considered to affect the part [133].

1. The height of the object is directly related to the build time, so its orientation in the build direction becomes fundamental.
2. When external supports are needed, it is necessary to consider:
 - (a) The volume of material used to build the supports, which wastes both material and build time.
 - (b) The contact area of the supports with the object, as reducing it implies a decrease of the build time.
3. Reduce the stairstepping effect by orienting the object properly.

One of the most important sources of inaccuracy when 3D-printing a part is the stairstepping effect which affects the vertical surfaces less than the horizontal faces. To maximize the surface accuracy, the surface may be oriented as near to vertical as possible.

2.3.5 Importance of nanoparticle size

Nanocomposites show various profits apart of low-cost, high accessibility, and easy fabrication, such as high levels of electromechanical, magnetic, and optical properties as well as the tuning of their mechanical properties [135–137]. To develop polymer-ceramic composite materials, ceramic (nano-, and/or micro-) particles are suspended in the resin to be, afterwards, photo-polymerised during the STL process. Nevertheless, this process is more difficult than 3D-printing photo-polymers as the viscosity of the resin drastically increases, meaning that high weight fractions of the ceramic (nano-) powder are difficult to embed into the polymer chain, as it leads to poor 3D-printing resolution. Moreover, when using ceramic nanoparticles within a polymer, it is important to take into account the size of the nanoparticles, as using large sizes will result in poor 3D-printing resolution due to light scattering, as discussed later in this Chapter. At the same time, the nanoparticle’s size must be as uniform as possible and smaller than the thickness of the 3D-printed layers; whereas the former will provide better output signals that will improve the sensors’ response and facilitate the post-processing process, the latter will provide better 3D-printing resolution. Nanoparticle size (d_{NP}) is an important characteristic to consider when developing polymer-ceramic functional composites because of the scattering processes arising from solid-light interactions.

- $d_{NP} > \lambda$: The light coming from the source will scatter and reflection can occur.
- $d_{NP} \ll \lambda$: Rayleigh scattering can appear, which is proportional to the sixth power of the nanoparticle’s diameter. It also depends on the wavelength of the light ($\propto \lambda^{-4}$), leading to stronger scattering at lower wavelengths.
- Mie scattering: is a common type of scattering when using spherical particles of any size. This type of scattering is not highly dependent on the light wavelength, but it is sensitive to particle size ($\propto d_{NP}^2$), coinciding with the Rayleigh scattering regime when the size of the particles is much smaller than the wavelength of the light.
- Tyndall scattering: it is similar to Mie scattering but it is not restricted to the spherical shape of the particles. It commonly appears in colloidal mixtures and suspensions.

Apart from the scattering processes, the nanoparticle’s size is also important when considering the output signal of the functional material, as they influence the resulting mechanical properties of the resulting composite [138]. Thus, if the nanoparticle’s size is too small, the nanoparticle’s volume

fraction that the user will be able to embed within the polymer will be higher, but the final functional output could be too low or, eventually, zero, making the resulting part not very useful for practical applications. Hence, the addition of UV blockers within the polymer-ceramic mixture is important in order to avoid the scattered UV-light rays initiating an undesired photo-polymerisation process. In order to avoid all this complex optimization process, some authors have simply fabricated their samples by making a big composite structure by STL and burning the excess of polymer out by pyrolysis [136, 139].

When added within a polymer, NPs can be easily aggregated and agglomerated during the production process. This agglomeration, which is created by the attracting van der Waals forces between NPs and can be easily broken by mechanical forces, prevents the improvement of specific properties of the nanocomposites. Even though it might appear to be a tricky parameter to control, several studies have shown different ways to solve this problem, such as the use of surfactants, particle coating, application of a compatibilizer, or charging the filler surface to separate them via electrostatic repulsion [140, 141]. Optimization of building parameters has also been shown to lead to a more uniform distribution of the NPs within the polymer, reducing the aggregates [142].

Chapter 2 provides wide and thorough insight of 3D-printing technology. This is provided because 3D-printing has become one of the key areas for the development of this work, as all the developed sensors and resonators have been built using this approach. Understanding the polymerization process and the types of polymers (with contrasting properties) that can be developed in a simple manner is important for this thesis as it provides the basic information to develop user-custom materials that allow the fabrication of bioinspired parts. STL 3D-printing has been chosen given its advantages over other types of additive manufacturing techniques, being the most important feature its ability to build user-costume parts in the microscale in a time-efficient manner. Using the knowledge provided in Chapter 1 it has been possible to 3D-print bioinspired sensors with specific capabilities such as acoustic frequency selectivity (see Chapter 6).

Chapter 3

Mechanical Properties

The mechanical behaviour of a material describes how this will respond to specific forces. This behaviour is a highly relevant parameter to take into consideration when developing new materials, as they will determine the mechanical response of the sample when interacting with several fields and forces. Key mechanical properties to consider when designing and developing new materials are *stiffness*, *strength*, *hardness*, *ductility*, *toughness*, and *elastic modulus*, even though other mechanical properties can also be studied. The mechanical properties of materials are not constant and often depend on some environmental parameters such as temperature [143], loading rate [144], and other conditions that often lead to local variability in the values obtained when measuring them, as described later in this chapter. Seemingly identical tests over identical samples of an identical material can produce slightly different results. Therefore, multiple tests are commonly conducted to determine mechanical properties and the reported values can be an averaged value or a range of values that show variability.

The tests used in this thesis to determine the mechanical properties of the developed materials are *nanindentation* and *tensile testing*. These two tests are equally valid but they are used to measure different mechanical properties of the material: whereas, on one hand, nanindentation provides a good estimation of both the elastic modulus and hardness of the material, it cannot determine in an accurate way its tensile strength or the Poisson's ratio. On the other hand, tensile testing provides a good approximation of the yield strength value as well as its ultimate yield strength, which both depend on the deformation suffered by the material.

In this thesis, nanindentation tests have been performed on several polymer-based 3D-printable

materials in order to determine both the hardness and elastic moduli of the as-synthesized materials by applying the method of Oliver and Pharr [145], as this technique provides more accurate values than tensile testing and it allows the user to find a unique value of the aforementioned mechanical properties (by averaging) and to determine local variability of such mechanical properties depending on non-homogeneous phenomena taking place on the material, such as non-uniform distribution of nanoparticles within a matrix (when testing composite materials), or the presence of dislocations and grain size effects (when working with non-composite materials) [145].

3.1 Mechanical characterization of materials

3.1.1 Concepts of strain and stress

When applying load forces to samples of different dimensions, the deformation suffered by them is not comparable unless a normalization process is followed. The strength of *uniaxially*¹ loaded samples is related to its cross-sectional area. Therefore, depending on the performed mechanical test the relevant area will be that perpendicular to the force (in tension and compression tests), or that perpendicular to the axis of rotation (in shear or torsion tests). Thus, the stress experienced by a sample of area A when a force F is applied onto it is described by Eq.(3.1).

$$\sigma = F/A \quad (3.1)$$

Furthermore, when applying a force onto a specific sample, it suffers a change of its dimensions called deformation elongation, ΔL , as a result of tensile or compressive stress. Thus, to enable comparison between samples of different length, elongation also needs to be normalized with respect to the original length of the sample, L . This is called *strain* and it is expressed by Eq.(3.2).

$$\varepsilon = L/\Delta L \quad (3.2)$$

When applying torsional or shear stresses to the sample, the deformation is given by the angle of torsion, ϑ , and the *shear strain*, γ , is given by:

$$\gamma = \tan(\vartheta) \quad (3.3)$$

These two quantities, strain and stress, play a key role in the mechanical response of materials as their relationship will determine how the materials behave mechanically. Depending on this relationship, materials can experience *elastic*, and *plastic* deformations:

¹Loading occurs in one unique direction. Metals are usually tested under uniaxial stress.

- Elastic deformation: when the material returns to its initial dimensions after the applied stress is removed. In elastic deformation, the mechanical deflection is reversible and is not permanent. It works for small stress values except in the case of rubbers, for which it also applies at high stress values.
- Anelasticity: these materials behave like elastic materials in which the stress-strain curve is not directly reversible. In these materials, it takes some time before the strain returns to zero, an effect that can be significant in polymers.
- Plastic deformation: when the material does not return to its initial dimensions after the applied stress is removed. In plastic deformation, the mechanical deflection is irreversible and permanent.

Therefore, if the deformation of a material is elastic, the stress and strain are related through a linear relationship called Hooke's law, shown in Eq.(3.4).

$$\sigma = E\varepsilon \tag{3.4}$$

where E is the Young's modulus (or modulus of elasticity) and it is determined by the initial slope of the stress-strain curve. Otherwise, when the stress-strain relationship is not linear, E is given by the local slope of the curve:

$$E = \frac{d\sigma}{d\varepsilon} \tag{3.5}$$

Elastic modulus is a measure of the *stiffness* of the material, which decreases with temperature in oxide compounds [146]. It is important to distinguish stiffness, which is a measure of the load needed to induce permanent deformation in the material, from *strength*, which refers to the material's resistance to failure (either if it is by fracture or excessive deformation). As elastic moduli are related with the first derivative of the force with respect to the intermolecular distance (or the second derivative with respect to the interatomic potential), ceramics present larger values of E due to the strength of the ionic bonds, whereas in polymers the values of E are lower due to the weakness of their covalent bonds. An example of these values can be observed in Table 3.1. As the interatomic distances depend on the orientation of the crystals, it must be noted that E is *anisotropic* for single crystals, whereas it is *isotropic* for randomly oriented polycrystals.

Ceramics	E [GPa]	Polymers	E [GPa]
Sapphire (Al_2O_3)	470	Epoxy, resin, glass filled	20
Cermet (TiC-TiN); Silicon carbide (SiC)	440	Phenol formaldehyde, mica filled	17-35
Alumina (Al_2O_3)	360	Urea formaldehyde, cellulose filled	7-10
Aluminum nitride (AlN)	320	Melamine formaldehyde, fabric filled	7
Silicon nitride (Si_3N_4)	300	PVC; Polystyrene	3.4
Mullite ($3\text{Al}_2\text{O}_3\text{-}2\text{SiO}_2$)	210	Acrylic (metacrylate)	3
Zirconia (ZrO_2)	200	Nylon	2.4
Yttria (Y_2O_3)	160	Cellulose nitrate; Cellulose acetate	1.4
Forsterite (2MgO-SiO_2)	150	Polypropylene	1.3
Cordierite ($2\text{MgO-}2\text{Al}_2\text{O}_3\text{-}5\text{SiO}_2$)	140	Polyethylene	0.7
Steatite (MgO-SiO_2)	120	PTFE	0.3

Table 3.1. Elastic moduli (E) of ceramics (left-hand-side column), and polymers (right-hand-side column) showing a difference of several orders of magnitude between them due to the strength of the ionic bonds. Values obtained from *KYOCERA, Fine Ceramics (Advanced Ceramics)* [147] and *The Engineering Toolbox, Polymers - Physical Properties* [148].

3.1.2 Elastic properties of materials

When materials experience tension they shrink laterally, whereas when they are subject to compression, they bulge. The ratio between the lateral and axial strains, ν , is commonly known as the Poisson's ratio.

$$\nu = -\varepsilon_{lateral}/\varepsilon_{axial} \quad (3.6)$$

where the minus sign in Eq.(3.6) accounts for the change between the lateral and longitudinal strains.

When a material is uniquely subjected to a stress in the x direction, σ_x , it will experience strain in that same direction given by Eq.(3.4), $\varepsilon_x = \sigma_x/E$. Otherwise, when stress is applied in the y direction, σ_y , it will induce an x -direction strain given by the definition of Poisson's ratio $\varepsilon_x = -\nu\varepsilon_y = \nu(\sigma_y/E)$. When the material is subjected to both σ_x and σ_y at the same time, the effects can be superimposed as the governing equations follow a linear relationship:

$$\varepsilon_x = \frac{\sigma_x}{E} - \frac{\nu\sigma_y}{E} = \frac{1}{E}(\sigma_x - \nu\sigma_y) \quad (3.7)$$

$$\varepsilon_y = \frac{\sigma_y}{E} - \frac{\nu\sigma_x}{E} = \frac{1}{E}(\sigma_y - \nu\sigma_x) \quad (3.8)$$

When no stress components act in the z direction, the material is called to be in a state of *plane stress*, a phenomenon that commonly occurs in thin sheets loaded within their own plane. The z components of the stress vanish at the surface because there are no forces acting externally in that direction to balance them. However, a state of plane stress is not a plane strain as the sheet will experience a strain in the z direction equal to the Poisson's strain contributed by the x and y stresses.

$$\varepsilon = -\frac{\nu}{E}(\sigma_x + \sigma_y) \quad (3.9)$$

Therefore, Poisson's ratio can be related to the *compressibility* of the material, K , also called bulk modulus, which is by definition the ratio of pressure, p , divided by a unit relative decrease in volume ΔV [149].

$$K = \frac{-p}{\Delta V/V} \quad (3.10)$$

In Eq.(3.10), the minus sign indicates that a compressive pressure produces a negative volume change. It can be shown that for isotropic materials (*i.e.* $\sigma_z = 0$) the bulk modulus is related to the elastic modulus and the Poisson's ratio through Eq.(3.11).

$$K = \frac{-p}{\Delta V/V} = \frac{\sigma_\nu}{\varepsilon_\nu} = \frac{\sigma_x + \sigma_y + \sigma_z}{3(\varepsilon_x + \varepsilon_y + \varepsilon_z)} = \frac{E}{3(1 - 2\nu)} \quad (3.11)$$

As ν approaches 0.5, Eq.(3.11) becomes unbounded. Thus, ν cannot be larger than 0.5 since that would mean an increase of volume when applying a positive pressure onto the sample.

Not all deformations are elongational or compressive; the concept of strain also needs to account for *shearing* effects, schematically shown in Fig. 3.1. Shearing effects take into consideration the deformation that the material experiences when a transversal load is applied onto it, leading to a variation of the right angles of the sample.

When shearing stresses are applied, the horizontal 'lines' tend to slide relative to each other changing the right angles shown as solid lines in Fig. 3.1. This term is called *direct shear*. *Shear stress* is denoted by τ to differentiate it from elongation/compressive stress, σ , and it is expressed analogously to Eq.(3.1).

$$\tau = F/A \quad (3.12)$$

The practical difference between extensional and transverse stresses is that whereas the first one pulls the parallel planes within the material apart promoting crack formation and growth, the second one results in planes sliding along each other, leading to yield and plastic slip. Furthermore, any shearing that causes tangential sliding of these horizontal planes is accompanied by an equal tendency to slide vertical planes

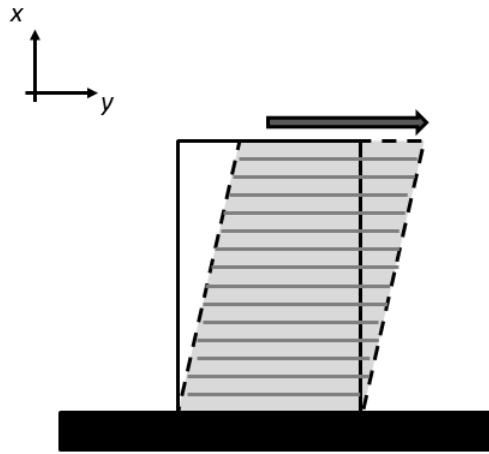


Fig. 3.1. Sketch of shearing deformation of a material when a load is applied transversely to the specimen, as indicated by the big arrow on top. Here it can be seen how the different layers of the material are displaced when shearing is applied.

(i.e., $\tau_{xy} = \tau_{yx}$). As it happens when applying extensional stresses, shear strain occurs when shearing stresses (τ_{xy}) are applied, which is denoted by γ_{xy} (see Fig. 3.2).

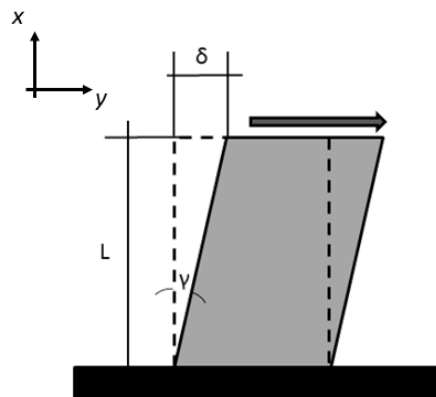


Fig. 3.2. Sketch of shear strain generated on a sample of initial length L . The total shear displacement at a shear angle γ is denoted by δ .

where the change in the vertical angle, γ , is given by:

$$\frac{\delta}{L} = \tan(\gamma) \quad (3.13)$$

At sufficiently small loads, it has been experimentally shown that shear stress follows a linear relationship with shear strain, as it happens in extensional stress. This analogous Hooke's law for shear stress is shown in Eq.(3.14) and relates τ_{xy} and γ_{xy} through the *shear modulus*, G .

$$\tau_{xy} = G\gamma_{xy} \quad (3.14)$$

When studying isotropic materials, the Poisson effect does not appear in shear and, therefore, shear strain is not influenced by the presence of normal stresses. Similarly, the application of shearing stresses has no influence on normal strains.

For plane stress situations (without shearing stress components in the z direction), the constitutive equations can be written as:

$$\begin{cases} \varepsilon_x = (\sigma_x - \nu\sigma_y)/E \\ \varepsilon_y = (\sigma_y - \nu\sigma_x)/E \\ \varepsilon_z = \tau_{xy}/G \end{cases} \quad (3.15)$$

Similarly as in Eq.(3.10), a relationship between the shear and elastic moduli can be obtained:

$$G = \frac{E}{2(1 + \nu)} \quad (3.16)$$

When the applied stress onto the sample is too large, the corresponding strain does not behave proportionally to the stress. The point at which this change of behaviour happens is called the *yield point* (which is characterized by the *yield stress* and its corresponding *yield strain*), further of which the material starts a permanent deformation entering the so-called *plastic regime*. Beyond this point, therefore, Hooke's law is not valid anymore. When the material enters the plastic regime and stress is removed, the material presents a permanent strain. If a stress is then reapplied to the material, it will first respond elastically until it reaches a new yield point higher than the original one, a phenomenon known as *elastic recovery during plastic deformation* (see Fig. 3.3).

The physical explanation to plastic deformation is the motion and propagation of dislocations, causing the breaking and the reforming of the bonds within the material. As stress continues in the plastic regime, the stress-strain curve passes through a maximum value, the tensile strength σ_{TS} , and it breaks at the so-called *fracture point*. When designing materials for structural applications, the yield stress is usually a more important parameter to consider than tensile strength.

The stress-strain curves are also useful to determine the *resilience* of the material, which is the amount of elastic energy stored per unit volume and can be found under the elastic region of the stress-strain curve. Analogously, it is possible to define the *toughness* of a material, which is its ability to absorb energy up to fracture. In this case, this amount of energy per unit volume is represented by the total area under the strain-stress curve, including its resilience.

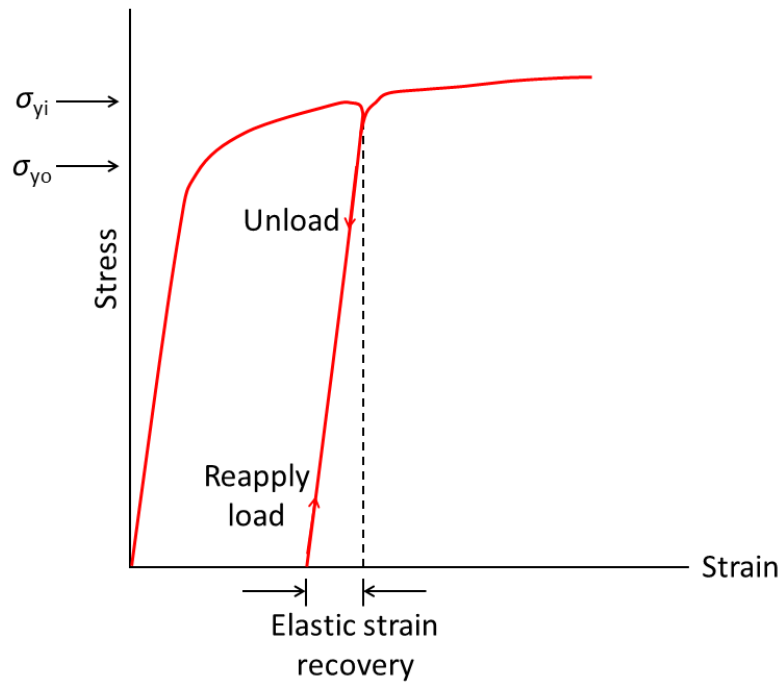


Fig. 3.3. Sketch of a stress-strain curve illustrating the phenomenon of elastic recovery during plastic deformation, where the two loading processes and the unloading process are shown. This figure also shows the two yield points, denoted by σ_{y_0} and σ_{y_i} , and highlighting the elastic strain recovery using a dashed vertical line.

Another interesting mechanical property of a material is its *ductility*, which corresponds to its ability to deform before fracture and it can be expressed either as a percentage of maximum elongation (ε_{max}), or as a percentage of maximum area reduction, which are measured after fracture and are expressed by Eq.(3.17) and Eq.(3.18).

$$\%EL = \varepsilon_{max} * 100 \quad (3.17)$$

$$\%AR = (A_0 - A_t)/A_0 \quad (3.18)$$

Finally, the *hardness* of a material can be defined as its resistance to plastic deformation. Hardness has been historically measured using empirical scales depending on the ability of the material to scratch, being diamond the hardest material and talc the softest one. Standard tests are used to determine hardness values (see Section 3.3: The method of Oliver and Pharr) in order to allow a numerical normalised comparison between them.

As previously mentioned in this Chapter, the mechanical properties of a same material do not reproduce exactly due to variations in test equipment, procedure, and specimen fabrication among many other parameters that will be thoroughly discussed in later sections of this Chapter. Even when

all these parameters are perfectly controlled, variations in the mechanical properties occur due to non-homogeneous composition and structure of the material [150].

3.2 Nanoindentation

Indentation testing is a simple method that essentially consists of probing the material of interest with an indenter tip which mechanical properties (mainly Young's modulus and Poisson's ratio) are known. Nanoindentation is an indentation test in which the length scale of the penetration is measured in nanometres due to the small forces involved, of the order of the mN. Apart from the displacement scale involved, the distinguishing feature of most nanoindentation tests is the indirect measurement of the contact area (area of contact between the indenter and the specimen), unlike in tensile testing. The contact area, A , is determined from the depth of penetration of the indenter into the specimen instead of the direct measure of the indenter residual impression left in the specimen surface upon the removal of load [151].

Nanoindentation technique allows the determination of some mechanical properties such as hardness, elastic modulus, strain-hardening exponent, fracture toughness, and viscoelastic properties. The test procedure involves a loading sequence followed by an unloading stage where both the applied load, P , and the penetration depth, h , are recorded during the entire test (see Fig. 3.4).

The loading part usually consists of an initial elastic contact followed by plastic flow, or yield, within the specimen at higher loads. During unloading, if yield has occurred, the load-displacement ($P - h$) curve data follows a different path than the loading stage. At zero applied loads, a residual impression is left on the specimen's surface. For viscoelastic materials, the indentation test is accompanied by a *creep curve*, which is obtained by holding the load constant (usually at maximum load), and monitoring the change in depth with time [151]. The global shape of the $P - h$ curves differs from one material to another and these variations reflect, usually, different mechanical properties [152].

Furthermore, $P - h$ curves are not only useful to determine the mechanical properties of materials as their shape can provide important information of events happening in the material during the test. An example is shown in Fig. 3.5, which shows local perturbations and discontinuities (called *pop in* events) measured in load-controlled experiments. These *pop-in* events are often observed on metals or

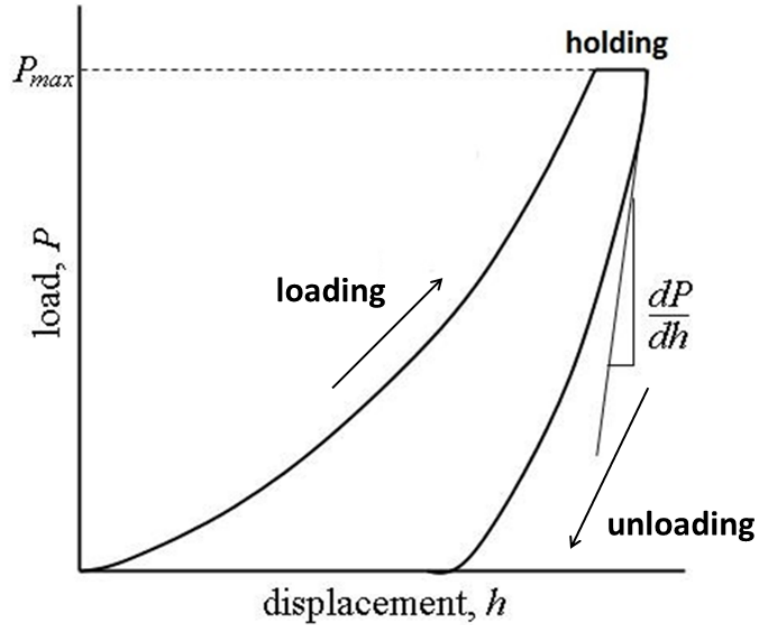


Fig. 3.4. Load-displacement ($P-h$) curve obtained in a nanoindentation assay. Three parts can be differentiated: the loading stage (where the load is applied and the corresponding penetration depth is recorded in small increments of P), the holding segment (where P is kept constant for a certain time, leading to a uniform penetration depth), and the unloading stage (where P is removed and the corresponding penetration depth is recorded).

metallic thin films, ceramics, metallic glasses, semiconductors, and hard brittle thin films deposited on soft elastoplastic substrates [151, 152], and they can be explained depending on the indented specimen and the experimental conditions (time, temperature, indenter's geometry, strain rate, ...), indicating: dislocations nucleation, rupture of hard brittle films onto elastoplastic substrates, strain transfer across grain boundaries (in metals), crack formation, and phase transformations [151–153].

These measured perturbations are characteristic of energy-absorbing or energy-releasing events occurring beneath the indenter tip [151]. The example shown in Fig. 3.5 denotes strong dislocation activity during a shallow indentation. Additional effects like shear localization into the so-called shear bands (in bulk metallic glasses) or phase transformations can also be detected as sudden events by load-displacement curves.

Nanoindentation hardness tests are generally performed with either spherical or pyramidal indenters. Nevertheless, such tests can be performed using different tip geometries, as shown in Fig. 3.6.

Different tip geometries can give slightly different values of the measured mechanical properties as they depend on their projected area onto the surface of the material, as it will be seen in next section.

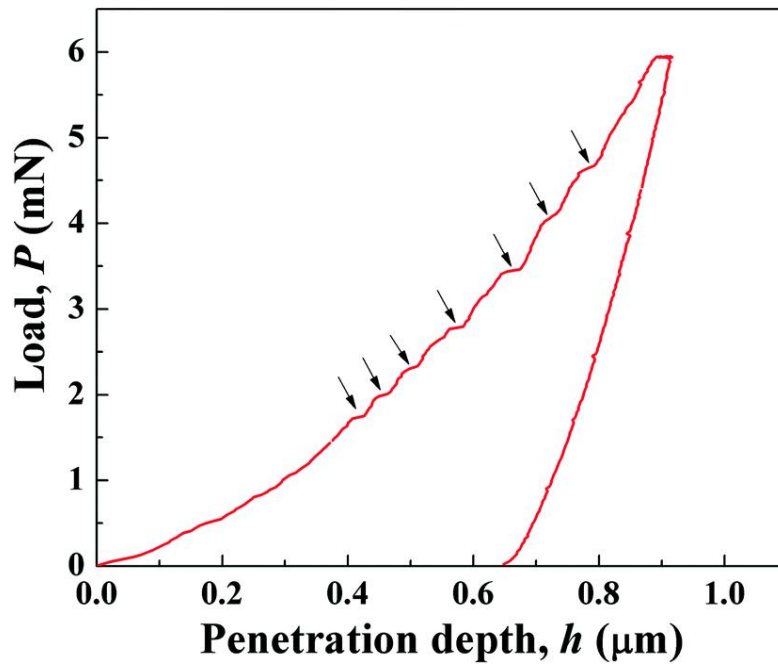


Fig. 3.5. Typical pop-in events in a nanoindentation load-displacement curve. Pop-in events are indicated with arrows during the loading stage, which appear due to dislocations nucleation, rupture of thin films, strain transfer across grain boundaries, crack formation, or phase transformations.

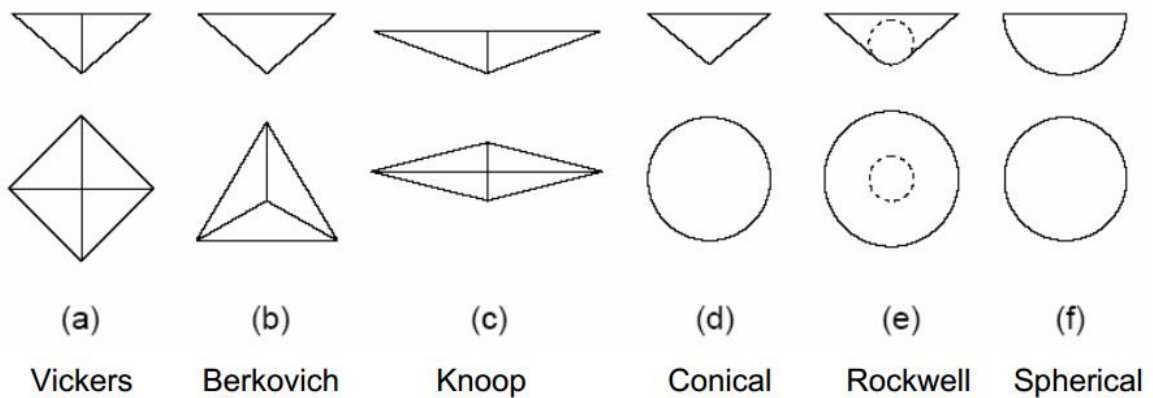


Fig. 3.6. Sketch of the different tip geometries that can be used to perform nanoindentation tests.

Therefore, it is not possible to directly compare the results obtained in nanoindentation tests when using different tips. In this project all the measurements have been performed using a Berkovich tip, which is a three-sided pyramidal-shaped tip that presents some advantages over other tips, such as a well-defined sharp geometry, promoting plastic deformation into the surface, and allowing a good measure of both E and H .

In the classical indentation load-control mode, some parameters must be adjusted before starting the nanoindentation measurements:

- Loading rate: the loading rate, dP/dt , determines the depth rate, dh/dt , and consequently the strain rate, $dh/(hdt)$. This parameter influences the response of rate-sensitive materials, such as plastics or polymers.
- Loading time: this parameter is important because the behaviour of the tested material can be time-dependent (*e.g.* in plastics, concrete or wood) due to the effect of *thermal drift*. Thermal drift is a common observation in temperature sensitive electronics and is typically in the range of 0.1-1 nm/s. It can be estimated and subtracted from the measurement to gain the true penetration. The correction of the thermal drift is given by Eq.(3.19), where T_d is the thermal drift in nm/s , and t stands for the loading time.

$$h_{corrected} = h_{measured} - T_d t \quad (3.19)$$

- Initial penetration is an unavoidable part of the depth that is lost before contact is detected. It can be neglected if the contact force is set small or estimated using extrapolation to the zero force level.

Other parameters to adjust before starting nanoindentation tests are the surface roughness (if surface roughness is too large compared with the penetration depth, the contact equations become invalid), the layer thickness (must be ten times larger than the penetration depth exerted by the indenter, otherwise the substrate influences the measurement and evaluation of the materials constants [154]), and the material creep (which can influence the evaluation of elastic properties). All these effects can be minimized using long dwell periods.

Once the tests have been carried out, some corrections must be applied due to artefacts associated with the load-unload procedure. Others arise from environmental changes during the test and the non-ideal

shape of the indenter. In addition, there are a number of material-related issues that also affect the validity of the results. The most important ones are the indentation size effect, piling-up, and sinking-in [151].

- Thermal drift: there are two types of drift behaviour that can be detected in nanoindentation experiments; the first one is creep within the material as a result of plastic flow, and the second one (which is indistinguishable from specimen creep) is a change of the instrument due to thermal expansion or contraction of the machine [151].
- Instrument compliance: the instrument's frame deflects as a reaction of the force applied to the sample. Therefore, correction due to the compliance of the frame is needed as shown in Eq.(3.20).

$$h_{corrected} = h_{measured} - h_f = h_{measured} - C_f P \quad (3.20)$$

where h_f is the frame deflection, P stands for the applied force, and C_f is the frame compliance. The compliance of the loading instrument is defined as the deflection of the instrument divided by the load [151].

- Indenter shape functions: the indenter tip cannot be prepared in a perfect geometrical shape. Therefore, corrections due to the real shape, especially at shallow contact depths are necessary. These corrections become of prime importance at small penetration depths.

The data obtained using the nanoindentation technique can be treated with the method of Oliver and Pharr in order to determine the mechanical properties of the studied material.

3.3 The Oliver-Pharr method

W. C. Oliver and G. M. Pharr developed a method to determine the mechanical properties (hardness and elastic modulus) of a material from indentation load-displacement data obtained during one cycle of loading and unloading [145]. For modelling purposes, Oliver and Pharr supposed that the deformation during the loading process contained both elastic and plastic contributions as the permanent hardness impression forms. During unloading, the authors assumed that only the elastic displacements were recovered. For this reason, the method does not apply to materials in which plasticity reverses during unloading [155].

There are three important quantities that must be determined from $P - h$ curves in order to

calculate the mechanical properties of the specimen: the maximum load (P_{max}), the maximum penetration depth (h_{max}), and the elastic unloading stiffness ($S = dP/dh$), defined as the slope of the upper portion of the unloading curve during the initial steps of the unloading (as shown in Fig. 3.4). The accuracy of H and E measurements inherently depends on how well these parameters can be measured experimentally. Another important quantity is the final penetration depth (h_f), which is defined as the permanent depth of penetration after the indenter is fully unloaded.

The exact procedure to measure H and E is based on the unloading process, which is assumed to be purely elastic, and the behaviour of the Berkovich indenter, which is modelled by a conical indenter. Fig. 3.7 shows a schematic illustration of the indenter and specimen surface at full load and unload.

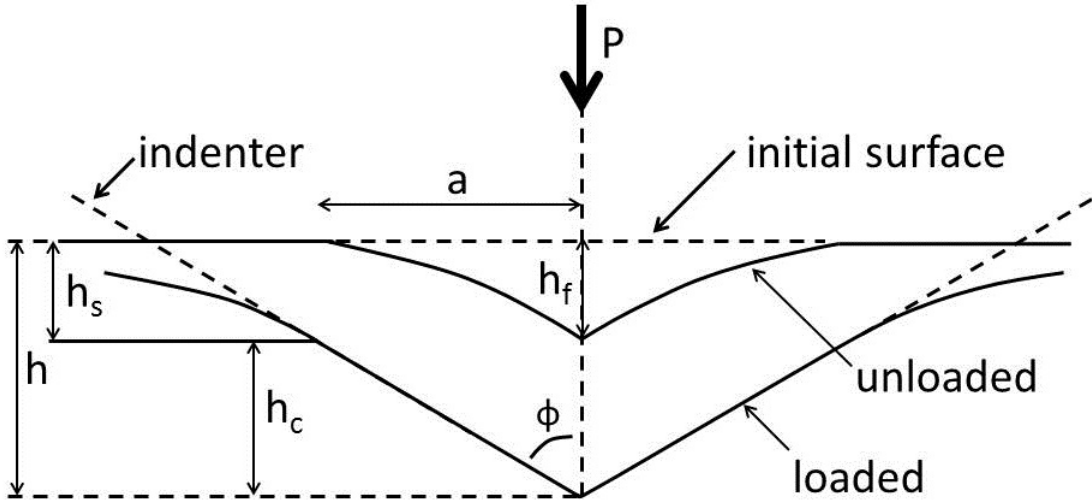


Fig. 3.7. Schematic representation of the indenter at specimen surface at full load and unload and the parameters characterising the contact geometry.

Assuming that pile-up is negligible, the elastic models show that the amount of sink-in (h_s) is given by:

$$h_s = \epsilon \frac{P_{max}}{S} \quad (3.21)$$

where ϵ is a constant that depends on the geometry of the indenter, and takes a value of 0.75 for a Berkovich tip. The depth along which contact is made between the indenter and the specimen is:

$$h_c = h - h_s = h - \epsilon \frac{P_{max}}{S} \quad (3.22)$$

In a first approximation, the projected contact area, A , can be taken to be equal to the one for a perfect indenter. For instance, for a Berkovich indenter, the relationship between A and the contact depth h_c is

given by [156]:

$$A = F(h_c) = 24.56h_c^2 \quad (3.23)$$

Once the projected contact area has been determined, H can be calculated from:

$$H = P_{max}/A \quad (3.24)$$

Whereas H can be easily determined by knowing P_{max} and A , obtaining E requires some previous calculations, including the reduced elastic modulus, E_r , which can be easily evaluated from its relationship with A and S :

$$S = \beta \frac{2}{\sqrt{\pi}} E_r \sqrt{A} \quad (3.25)$$

β is the so-called King's factor, a dimensionless correction factor that depends on the geometry of the indenter and takes the value of 1.034 for a Berkovich tip. In the original method for measuring H and E_r , β was taken as unity. Traditionally β has been used to account for deviations in stiffness caused by the lack of axial symmetry for pyramidal indenters. However, it has been shown that in some cases β can significantly deviate from unity [155].

E_r which is also known as *effective elastic modulus*, is defined as:

$$\frac{1}{E_r} = \frac{1 - \nu_m^2}{E_m} + \frac{1 - \nu_i^2}{E_i} \quad (3.26)$$

where E is the elastic modulus, and ν is the Poisson's ratio, and the sub-index i refers to the indenter (which is made of diamond, $E_i = 1140$ GPa, and $\nu_i = 0.07$), and the sub-index m refers to the material. The reduced elastic modulus takes into consideration the fact that elastic displacements occur both in the indenter and the sample.

As it can be observed from Eq.(3.24), and Eq.(3.25), determining the contact area of the indenter over the sample is of prime importance in order to achieve a good approximation of both H and E .

3.4 Composite materials

The term *composite* usually refers to a matrix of material reinforced with fibres, nanoparticles, nanorods or any other type of filler. As it can be seen from Table 3.2, the fibres used in modern composites have strengths and stiffnesses far above those traditional bulk materials.

The materials shown in Table 3.2 are usually used as fibres, and are typically embedded within a matrix

Material	E [GPa]	σ_h [GPa]	ϵ_h [GPa]	ρ [Mg/m ³]	E/ρ [MJ/kg]	σ_h/ρ [MJ/kg]
E-glass	72.4	2.4	2.6	2.54	28.5	0.95
S-glass	85.5	4.5	2.0	2.49	34.3	1.8
Aramid	124	3.6	2.3	1.45	86	2.5
Boron	400	3.5	1.0	2.45	163	1.43
HS graphite	253	4.5	1.1	1.80	140	2.5
HM graphite	520	2.4	0.6	1.85	281	1.3

Table 3.2. Mechanical properties of some composite reinforcing fibres. Table obtained from *Encyclopaedia of Polymer Science and Engineering* [157].

material which has the function to transfer loads to the fibres, as well as to protect them from abrasion and environmental attack. Even though several metals and glasses can be used as matrices (which are expensive and largely restricted to R&D laboratories), polymers are much more commonly used, being thermoplastic polymers increasingly popular materials [157].

3.4.1 Stiffness

When embedding nanoparticles and/or nanorods within a matrix, they tend to be randomly oriented, whereas fibres are easier to orient in specific directions; for instance, arranging them to be oriented in the direction expected to have the highest stress. Such a material is said to be *anisotropic*, and controlling it is important for specific applications. Therefore, at a microscopic level the properties of these composites are determined by the distribution and orientation of the filler, as well as by the mechanical properties of both the matrix and the filler. Considering a material of unit dimensions containing a volume fraction V_f of fibres oriented in a single direction, the matrix volume fraction is $V_m = 1 - V_f$. Thus, if a stress σ_1 is applied in the fibre direction, both the matrix and fibre phases act in parallel to support such load and, therefore, the strains in each phase must be the same, a phenomenon known as *isostrain*, being:

$$\epsilon_f = \epsilon_m = \epsilon_1 \quad (3.27)$$

In order to balance the total load on the material, the forces in each phase must add:

$$\sigma_1 = \sigma_f V_f + \sigma_m V_m = E_f \epsilon_1 V_f + E_m \epsilon_m V_m \quad (3.28)$$

The stiffness in the fibre direction is found when dividing by the strain:

$$E_c = \frac{\sigma_1}{\epsilon_1} = V_f E_f + V_m E_m \quad (3.29)$$

Eq.(3.29) is known as the *rule of mixtures* and it predicts the composite elastic modulus in terms of the moduli of the constituent phases and their corresponding volume fractions [158].

If the stress is applied in the direction transverse to the fibres, the stresses in both the fibres and the matrix are equal (in the ideal case, which is known as *isostress*), and the deflections add to give the overall transverse deflection. In this case it can be shown that:

$$\frac{1}{E_c} = \frac{V_f}{E_f} + \frac{V_m}{E_m} \quad (3.30)$$

It must be noted that in this case, the stiffness of the composite increases much slower than the previous case as volume fraction of the filler is increased [158].

The properties of composite materials must represent an average value of the properties of their individual components, which is a sensitive function of the microstructural geometry [159]. In more complex composites, nevertheless, Eq.(3.29) represents an upper limit of the composite modulus, while Eq.(3.30) is the lower bound. Most practical cases will be somewhere in between these two values, which has attracted the attention of researchers to develop mathematical models to explain such behaviours. Perhaps the most popular model is an empirical one known as the Halpin-Tsai equation [160].

$$E = \frac{E_m [E_f + \xi (V_f E_f + V_m E_m)]}{V_f E_m + V_m E_f + \xi E_m} \quad (3.31)$$

Here, ξ is an adjustable parameter that results in series coupling for $\xi = 0$, and parallel averaging for very large values of ξ , recovering Eq.(3.29) and Eq.(3.30) respectively in such extreme cases.

3.4.2 Strength

The rule of mixtures also applies to determine the strength of composite materials in a similar way as the one used for stiffness. Considering a unidirectionally reinforced composite strained up to the point at which the fibres begin to break, ϵ_{fb} , the transmitted stress is given by the product of stiffnesses.

$$\sigma_b = \epsilon_{fb} E_1 = V_f \sigma_{fb} + (1 - V_f) \sigma_m \quad (3.32)$$

The stress suffered by the matrix is $\sigma_m = \epsilon_{fb} E_m$. However, Eq.(3.32) is not a realistic expression for low filler concentrations since the breaking strain of the matrix is usually greater than that of the fibres.

A couple of considerations must be taken into account at this point: (i) if the matrix had no filler within it, it would fail at stresses given by $\sigma_{mb} = E_m \epsilon_{mb}$, and (ii) if the filler was considered to carry no load, the strength of the composite would fall off with filler concentration according to $\sigma_c = (1 - V_f) \sigma_{mb}$.

Since the breaking strength measured in composite materials is greater than the two previous expressions, there exists a range of filler fraction that weakens the composite by the addition of filler.

3.5 Theoretical modelling of mechanical properties

The nature of the tensile response of a polymer depends on its chemical structure, its molecular weight and distribution, the conditions of its preparation, and the extension of cross-linking or branching [161]. The mechanical behaviour of filled-polymer systems has attracted the attention of many investigators due to their importance for engineering applications [162]. Researchers have tried to model such mechanical properties from a mathematical point of view and, as a result, a variety of mathematical models have been developed to predict not only the modulus of composite materials but also other mechanical properties like tensile strength as a function of the filler's volume fraction.

Obviously, the mechanical properties of filled composites are affected by a large number of parameters such as particle size and shape of the filler, filler orientation, adhesion between the matrix and the filler, filler fraction, or exposure time to UV light when using photo-sensitive polymers among others [108].

Tensile modulus seems to be one of the easiest mechanical properties to predict as it is a bulk parameter that strongly depends on the geometry of the sample, filler concentration, and particle size distribution. Therefore, several theories have been developed to estimate the tensile modulus of composite materials in terms of different parameters, and those developed by Einstein [108], Kerener [163], and Sato and Furukawa [164] are the most relevant ones. Whereas Kerener's equation presents an upper bound of the modulus, both Einstein's and Sato and Furukawa's equations introduce an adhesion parameter between the filler and the polymer.

3.5.1 Kerener equation

Kerener's equation can be used to determine the elastic modulus of composite materials.

$$E_c = E_m = \left(1 + \frac{V_f 15(1 - \nu)}{V_m(8 - 10\nu)} \right) \quad (3.33)$$

where V_m is the matrix volume fraction and ν is its Poisson's ratio. For expansible polymers incorporating rigid spherical particles featuring adhesion, Kerener's equation can be used to estimate the elastic modulus.

3.5.2 Einstein equation

Einstein developed two different equations to determine the elastic modulus of composite materials. In the first model, the adhesion between matrix and filler was considered, whereas in the second model a fixed adhesion parameter was included.

$$E_c = E_m (1 + V_f) \quad (3.34)$$

$$E_c = E_m (1 + 2.5V_f) \quad (3.35)$$

where E_c and E_m are the Young's modulus of the composite and the matrix respectively, V_f is the filler volume percentage, and the factor 2.5 in Eq.(3.35) accounts for adhesion between filler and polymer.

3.5.3 Sato and Furukawa model

Sato and Furukawa developed an expression to determine the elastic modulus of a composite material in which a filler is embedded within a matrix. Unlike Einstein's equation, Sato and Furukawa assumed that the adhesion between the matrix and the filler, which they denoted as j , is not constant and it depends on several parameters.

$$E_c = E_m \left[\left(1 + \frac{V_f^{2/3}}{2 - 2V_f^{1/3}} \right) (1 - \psi j) - \frac{V_f^{2/3} \psi j}{(1 - V_f^{1/3}) V_f} \right] \quad (3.36)$$

$$\psi = \frac{V_f}{3} \left(\frac{1 + V_f^{1/3} - V_f^{2/3}}{1 - V_f^{1/3} + V_f^{2/3}} \right) \quad (3.37)$$

In this model, j is constrained between 1 and 0, being 1 poor adhesion between the filler and the matrix, and 0 perfect adhesion between them. Some experiments have revealed that the results given by this model are placed in between Kerener and Sato and Furukawa relations with perfect adhesion.

All these predictions assume that the matrix and the filler have, only, an appreciable degree of

interaction in which the polymer matrix is stiffened by the particulate filler. In most conventionally filled polymer systems the modulus increases linearly with the filler volume fraction. The increase of modulus is mainly governed by the particle size of the filler [165].

This Chapter discusses the different mechanical properties that must be considered when developing new 3D-printable materials. These mechanical properties are important for the resulting developed parts as they will directly influence the response of the 3D-printed sensors, altogether with their shape, geometry, and dimensions. Developing 3D-printable materials with contrasting mechanical properties provides an extra degree of flexibility in the manufacturing process. Furthermore, this Chapter provides several mathematical models that predict the resulting mechanical properties of composite materials. These models have been really helpful during this thesis as a way to confirm the experimental results.

Chapter 4

Basic Concepts of Piezoelectricity and Magnetism

4.1 Piezoelectricity

4.1.1 Introduction

Piezoelectric materials are materials with the ability to convert mechanical energy into electrical energy and vice versa. Piezoelectric materials find applications in many fields of science such as energy harvesters or power generators [166], but the amount of energy they produce is still low and must be optimized. The piezoelectric effect was discovered in 1880 by the Curie brothers when they found that when applying a mechanical stress into specific materials, those generated a voltage proportional to the applied stress. Piezoelectric materials can be either natural (quartz being the the most common natural piezoelectric material) or man-made [167]. The latter are usually ceramics and are more efficient than natural piezoelectrics. On the other hand, processes to develop man-made piezoelectric materials are usually complex due to complicated crystalline structures [167].

The nature of piezoelectric materials is closely related to the significant quantity of electric dipoles present in them [167]. These dipoles can be induced in several ways, such as ions present on a crystal lattice with asymmetric charge surroundings (such as in barium titanate, BaTiO_3 , as shown in Fig. 4.1a), or by certain molecular groups with specific electrical properties.

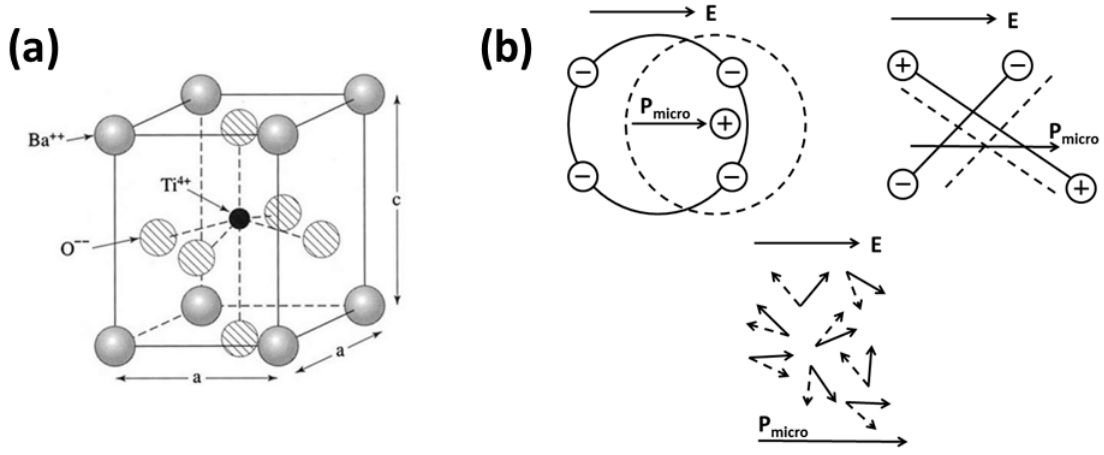


Fig. 4.1. (a) Shows a sketch of the crystallographic structure of BaTiO₃, where the Ba²⁺, O²⁻, and Ti⁴⁺ ions are highlighted. Image obtained from [167]. (b) Shows a sketch of three different ways of polarization. The top-left, top-right, and bottom sketches correspond to electronic, ionic, and orientational, respectively.

It must be noted that dipoles are vectors and thus they have a value and direction according to the distribution of surrounding charges. Generally, dipoles tend to have the same direction when next to each other, and altogether they form Weiss domains, which are usually randomly oriented but can be aligned through the poling process, in which a strong electric field is applied across the material. Hence, when a dielectric is placed in an electric field, the electric charges in its molecules redistribute themselves microscopically, resulting in a macroscopic polarization. This microscopic redistribution of the electric charges can take place in several ways such as electronic, ionic, and orientational, as illustrated in Fig. 4.1b. Nevertheless, it must be noted that not all piezoelectric materials can be poled depending on the nature of the dipole (if it is induced by ion or molecular groups). Consequently, the larger the applied mechanical stress, the larger the change in polarization and higher values of output voltage are obtained. Independently of the polarization method, the material is induced a macroscopic polarization vector per unit volume given by:

$$\vec{P} = \lim_{\Delta v \rightarrow 0} \frac{\sum \vec{P}_{micro}}{\Delta v} \quad (4.1)$$

The change in \vec{P} appears as a variation of surface charge density upon the crystal faces. It has been shown that in certain materials polarization can be induced through mechanical loads, a phenomenon known as *direct* piezoelectric effect and that can be induced at specific angles depending on the degree of anisotropy of the material. Thus, when the applied load is reversed so is the induced polarization. Furthermore, when a voltage is applied to the material presenting this characteristic, it suffers a mechanical deflection, a phenomenon known as *converse* piezoelectric effect. Both the direct and

converse piezoelectric effects generate work on the piezoelectric material.

Piezoelectric behaviour in materials can be observed below a certain temperature known as Curie temperature, T_C . Above T_C , the crystalline structure will present a simple cubic symmetry and, therefore, no dipoles will be generated. On the other hand, below T_C the crystal will present either a tetragonal or a rhombohedral symmetry, generating as a consequence the presence of dipole moments. As previously mentioned, when the dipoles are aligned in (roughly) the same direction the material presents a value of polarization, whereas if they are randomly oriented the material results with negligible polarization. When this happens the material needs to be exposed to strong \vec{E} in order to re-orient the domains in the same direction as the applied electric field and result, therefore, with a permanent polarization. This permanent polarization is the remanent polarization after the electric field has been removed, which appears as a consequence of the hysteric behaviour of the material and it is stronger in the direction of the field. Such a transformation must be done below the Curie temperature so that dipoles can be created.

The output voltage produced by piezoelectric materials can be used to develop sensors and actuators by connecting the material to a circuit. For most applications involving piezoelectric materials, the goal is to convert the maximum amount of mechanical energy into electrical energy, providing as much current as possible. In fact, resonant circuits are an ideal tool to optimize the measured signal.

4.1.2 Mathematical description

The equations governing piezoelectric materials involve entities that cannot be experimentally measured. As previously mentioned in this Chapter, a piezoelectric device creates an internal electric field when a mechanical stress is applied in it (and vice versa). Thus, depending on the material, an electrical field in a specific direction will lead to a mechanical deflection in any direction, which is mathematically explained using tensors. It is possible, though, to simplify the equations and calculations by considering materials in which the electric field is created in one unique direction (generally considered to be either parallel or perpendicular to the applied stress). Equations of piezoelectricity are given by (when assuming no variation with temperature and low frequencies):

$$\vec{D} = d_1 \vec{T} + \epsilon^T \vec{E} \quad (4.2)$$

$$\vec{S} = s^E \vec{T} + d_2 \vec{E} \quad (4.3)$$

where \vec{D} is the electric displacement, d_1 and d_2 are piezoelectric charge coefficients (for the direct and converse piezoelectric effect, respectively), \vec{T} stands for mechanical stress, ϵ^T is the permittivity at constant stress, \vec{E} is the applied electric field, \vec{S} is the mechanical strain, and s^E is the mechanical compliance. The tensors s^E , d , and ϵ^T are given in matrix form as:

$$\begin{bmatrix} s_{11}^E & s_{12}^E & s_{13}^E & s_{14}^E & s_{15}^E & s_{16}^E \\ s_{21}^E & s_{22}^E & s_{23}^E & s_{24}^E & s_{25}^E & s_{26}^E \\ s_{31}^E & s_{32}^E & s_{33}^E & s_{34}^E & s_{35}^E & s_{36}^E \\ s_{41}^E & s_{42}^E & s_{43}^E & s_{44}^E & s_{45}^E & s_{46}^E \\ s_{51}^E & s_{52}^E & s_{53}^E & s_{54}^E & s_{55}^E & s_{56}^E \\ s_{61}^E & s_{62}^E & s_{63}^E & s_{64}^E & s_{65}^E & s_{66}^E \end{bmatrix}, \begin{bmatrix} d_{11} & d_{12} & d_{13} \\ d_{21} & d_{22} & d_{23} \\ d_{31} & d_{32} & d_{33} \\ d_{41} & d_{42} & d_{43} \\ d_{51} & d_{52} & d_{53} \\ d_{61} & d_{62} & d_{63} \end{bmatrix}, \begin{bmatrix} \epsilon_{11}^T & \epsilon_{12}^T & \epsilon_{13}^T \\ \epsilon_{21}^T & \epsilon_{22}^T & \epsilon_{23}^T \\ \epsilon_{31}^T & \epsilon_{32}^T & \epsilon_{33}^T \end{bmatrix} \quad (4.4)$$

In many cases, the s^E , d , and ϵ tensors can be simplified and some of the terms become zero due to the symmetry of the lattice. Equations (4.2) and (4.3) establish a relationship between the mechanical and electric behaviours of the material. Whereas Eq.(4.2) shows that a part of the electrical field applied to the material is converted into mechanical stress, Eq.(4.3) shows the opposite trend, in which a part of the mechanical stress applied onto the material is converted into electrical energy. The reader must note that Eq.(4.2) becomes the equation of the electric displacement field in the absence of mechanical stress on the sample ($\vec{D} = \epsilon^T \vec{E}$), and Eq.(4.3) becomes the Hooke's law ($\vec{S} = s^E \vec{T}$) in the absence of an external electric field \vec{E} .

For most piezoelectric materials $d_1 = d_2 \equiv d$, and hence:

$$\vec{S} = s^E (1 - k^2) \vec{T} + \frac{d}{\epsilon^T} \vec{D} \quad (4.5)$$

where $k = d/\sqrt{s^E \epsilon^T}$ is the electromechanical coupling coefficient, which gives an indication of how effectively a piezoelectric material converts electrical energy into mechanical energy or vice versa. When $k = 0$, Eq.(4.5) becomes Hooke's law, meaning that all the energy in the material is mechanical energy.

4.1.3 Piezoelectricity in polymers

Since the idea of MEMS emerged in the 1980s, it has been noticed that piezoelectric materials can add extra functionality to them, leading to the development of piezoMEMS that present several applications, such as in automotive industry or smart phones [168]. These systems are mainly based in inorganic materials (such as lead zirconate titanate, PZT), which present some challenges such as high temperature

processing for thin films, polar reorientation, toxicity, and mainly the high production cost [168]. All these inconveniences led scientists to use polymeric materials. Some of the advantages polymeric materials present with respect to inorganic ceramics are their degree of mechanical flexibility, needed for some applications and a feature that inorganic materials do not present, and the low production cost in terms of both materials cost and processing technology [168]. Furthermore, these polymers used to develop new MEMS sensors can provide extra features to the resulting devices due to their semiconducting, conducting, and electroactive properties [168].

Electroactive polymers (EAP) are materials that mechanically deform when an electric current is applied through them, and can be classified as electronic and ionic EAPs according to their operation principle. Whereas in electronic EAPs the electromechanical transduction is created due to the electrostatic modification of dipoles, in ionic EAPs such process is generated by the ionic changes of the material. There are several types of piezoelectric polymers: (i) bulk polymers, consisting of solid polymer films with a piezoelectric mechanism through their molecular structure and its corresponding arrangement, (ii) piezoelectric composite polymers, which are structures with integrated piezoelectric ceramics responsible to generate the piezoelectric effect (these types of piezopolymers take advantage of both the high mechanical flexibility of the polymers and the high electromechanical coupling of the ceramics), (iii) voided charged polymers, consisting of polymer films in which gas voids are introduced and their corresponding surface is electrically charged in a way to form internal dipoles (it is interesting that the polarization of these dipoles changes with the amount of stress applied on them), and (iv) piezoparticles suspended into polymer matrices, in which nanoparticles of ceramic piezoelectric material (such as barium titanate, or PZT) are introduced within a polymeric matrix, which is the responsible to provide a high degree of mechanical flexibility to the system. Depending on the distribution of the ceramic materials within the polymeric matrix several types of connectivity can be defined, as shown in Fig. 4.2, going from 0-0 (in which the ceramic and the polymer are not inter-connected in any way) to 3-3 (in which both the ceramic material and the polymer are inter-connected in the 3 dimensions of space) connectivities. Embedding rods or particles in a polymer are the most common arrangements when using these type of materials for electromechanical devices. Furthermore, several numerical and analytical models have been developed to determine the properties of the resulting piezocomposites (which will be discussed in Chapter 6, section 6.2) [169–171], becoming extremely useful when designing new composite materials and predicting their corresponding material properties (electrical, mechanical,

and electromechanical). Due to the polymer's low acoustic impedance, piezocomposites have become the preferred materials to use in acoustic devices.

(1,3) piezocomposites usually consist of cylindrical pillars embedded in a polymer matrix and are used for applications in centimetre-scale acoustic sensors [172] and energy harvesting [173], but most of them present some disadvantages related to the fabrication process and the size of rods, limiting their degree of applicability. (0-3) piezocomposites, on the other hand, are much easier to prepare as they mix the inorganic piezoelectric particles with the polymer before the latter is cured. Furthermore, the small size of the used NPs leads to a better integration of such materials in microscale applications.

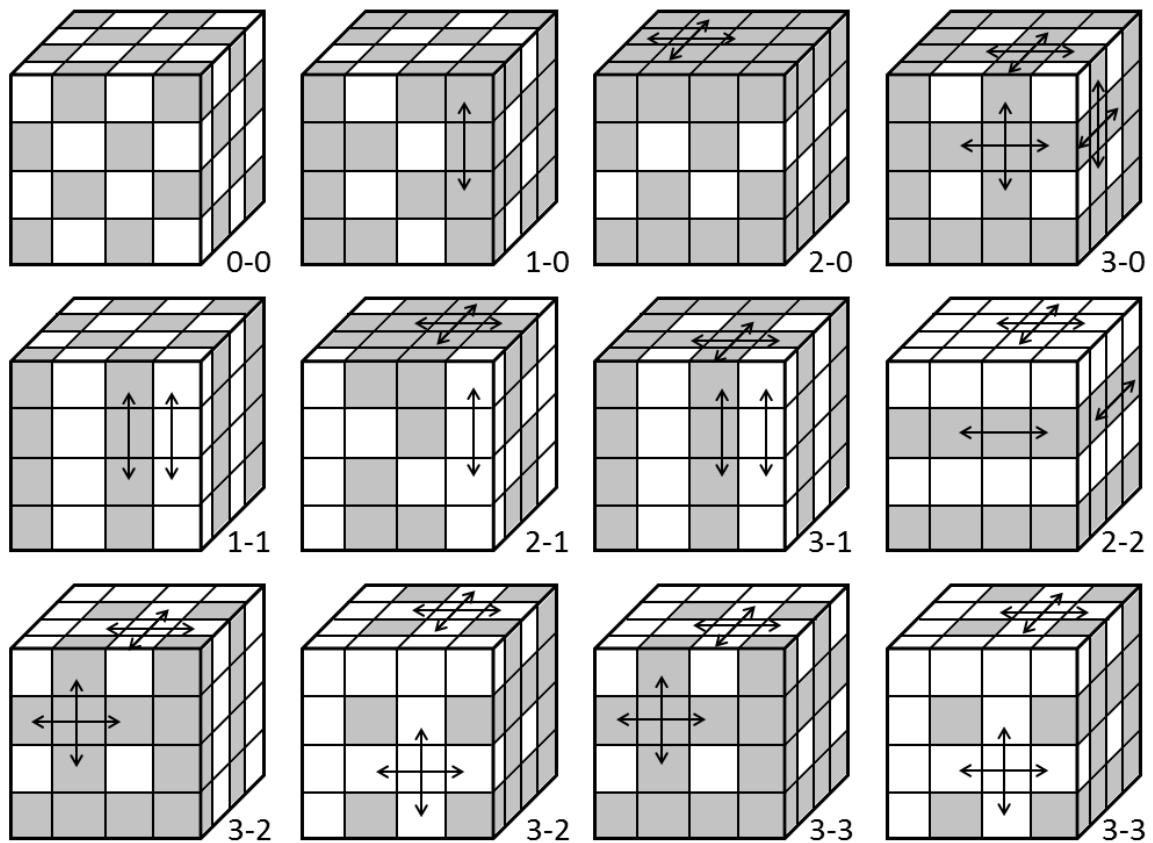


Fig. 4.2. Classification of two-phase (ceramic-polymer) composites with respect to connectivity. Two configurations are shown for connectivities 3-2 and 3-3. This representation shows how piezoelectric structures embedded within polymeric matrices can be distributed.

In order to sustain the orientation state of the molecular dipoles in piezopolymers a poling process is needed, which is typically performed by electrode poling or corona poling. The electrode poling is simpler than the corona poling, in which conductive electrodes are deposited on both sides of the sample

to apply a high voltage across the polymer [174]. It must be noted, though, that applying such high electric fields could lead to polymer break down [174]. In order to minimise these effects, the poling process should be performed either in a vacuum chamber or in an electrically insulating fluid (such as silicon oil). The degree of alignment of the dipoles with the direction of the applied \vec{E} , and therefore the piezoelectric coefficient d of the material, depends on a series of parameters: the strength of the applied field, the application time, the temperature at which the polling process has been performed (and its uniformity), and the impurities present in the sample. Unlike in electrode polling processes, corona polling only requires one of the surfaces of the material to be covered with an electrode. A needle made of conductive material is held on top of the piezoelectric material surface, with its electroded surface in contact with a hot plate, and a high voltage is applied through it, usually in dry air or in an argon atmosphere. The gas molecules near the tip are ionized and accelerated towards the electrode. This same process can be run using several tips in specific arrangements, which altogether with the voltage applied will control the amount of charge deposited onto the sample. The hot plate is used to provide a better control of the polling process. The temperature required for both methods has been found to not go beyond 300 °C in the literature [172, 173, 175, 176]. Apart from direct electroding and corona polling processes, there are other ways to reorganise the dipoles of a piezoelectric material, such as electron beam poling [177], in which an electron beam is used to deposit electrons on the surface of the piezoelectric polymer in a similar manner as the corona polling process, or soft X-ray ionization, which becomes highly useful for voided charged polymers.

Table 4.1 presents some of the material properties of three different piezocomposites to show how much variability can be obtained in their design. PMN-0.29PT/epoxy composite and ZnO/SU-8 20% show how piezoelectric nanostructures can be introduced in different epoxies (being the latter photocurable) to produce contrasting piezoelectric properties. On the other hand, MFC is the leading low-profile actuator and sensor offering high performance, flexibility, and reliability in cost-competitive devices.

Material property	PMN-0.29PT/epoxy composite	MFC	ZnO/SU-8 20%
Density (kg/m ³)	500	5440	-
Young's modulus (GPa)	-	30	12.3
Dielectric constant, ϵ_r	2000	~850	~7
d_{33} (pC/N)	1200	374	5-8
d_{31} (pC/N)	-	170	5
k_{33}	0.85	0.53	0.07-0.12
k_{31}	-	0.34	0.07

Table 4.1. Material properties of piezocomposites. Table obtained from [175]

Several works have studied the piezoelectric response of different inorganic ceramic materials dispersed in polymer matrices and their corresponding applications [172, 173, 175, 176, 178, 179]. An example is the use of ZnO NPs (with diameter size < 100 nm) dispersed in SU-8 as energy harvester [176]. Regardless of the low coupling coefficient of ZnO, this piezocomposite has been successfully used for several applications, as its importance lies in the selection of SU-8 as matrix polymer due to its photocurable properties [176]. Hence, different weight concentrations of ZnO embedded within SU-8 have been studied, revealing that values higher than a 20 wt% should not be used in order to obtain good patternability, as under such conditions the curing time increases up to 6 times with respect to pure SU-8 [176]. Park *et al.* used multi-walled carbon nanotubes (MWCNT) together with BaTiO₃ to enhance NP orientation during the poling process and, therefore, the piezoresponse [178]. Kim *et al.* focused on the synthesis of highly piezoelectric NPs to use them in piezocomposites allowing an improvement not only of the degree of applicability of such materials but also enhancing the piezoelectric coefficients allowing a more efficient energy transduction, such as the case of lead magnesium-lead titanate (PMN-PT), in which the ratio of PMN to PT affects both the coupling coefficient and the Curie temperature [179].

BaTiO₃ is a widely-studied piezoelectric ceramic material [180, 181], both in its bulk form and its different nanostructures, being paraelectric (cubic crystallographic structure) above 125 °C, and ferroelectric (tetragonal crystallographic structure) in the range 8-25 °C [181]. Using BaTiO₃ dots, rods, or nanotubes highly influences its ferroelectric properties due to the imbalance between the Coulomb interactions (long-range interactions, modified due to a lack of periodicity of the lattice) and the covalent

interactions (short-range interactions, modified near the surface boundary) caused by atomic off-centre displacements, reaching d_{33} values above 400 pC/N [182]. When embedding ceramic piezoelectric NPs within a polymeric matrix, the piezoelectric domains stay randomly oriented within the polymer chains after the photo-polymerization process, making the application of an electric field (\vec{E}) to force the electric charges to redistribute themselves microscopically necessary, resulting in a macroscopic polarization of the sample that depends on the degree of anisotropy of the material. If the applied \vec{E} is not large enough, the electric charges will not receive enough energy to be reoriented in the direction of the applied field, whereas if it is too high, it leads to electric breakdown of the sample due to an excess of provided energy. Different ceramic piezoelectric materials, which are transversely isotropic, have distinct ranges of optimum poling \vec{E} , as its internal energy density must remain positive since it must be minimal in a state of equilibrium [183]. Nevertheless, when dealing with composites that include piezoelectric NPs, factors like NP concentration, size, and distribution play an important role [184]. Temperature, T , is also a key parameter to control during poling processes: for instance, the application of \vec{E} above T_C and a controlled decrease of T would be more efficient as the process is energetically favourable. Nevertheless, in most cases the melting temperature of the polymer is below T_C . Furthermore, before 3D-printing, the optimum NP size must be selected to ensure a proper balance between 3D-printing resolution and piezoelectric output.

When using these materials for specific sensing applications, there are three main parameters that must be taken into consideration to select what type of piezocomposite must be used. Two of these criteria are directly related to the mechanical properties of the piezocomposite: (i) the minimum response required for the application, a factor directly related to the coupling coefficient of the material, which is directly related to both the mechanical and dielectric loss factors as the higher they are the less energy will be converted, and (ii) the lifetime of the application, as the devices required for specific applications require operation at high temperatures for long time periods, meaning that the required piezocomposites must present both a high Curie temperature and be less affected by aging effects [175]. The third criterion is related to the fabrication process of the material, with its degree of integration a highly relevant parameter to take into consideration. Several piezopolymers have been used to develop acoustic transducers that operate in different acoustic ranges including audio, ultrasonic, and infrasonic frequency ranges, with applications in microphones, loudspeakers, and ultrasonic transducers that can be applied in many different fields such as material fracture, device failure, medical imaging, or automated

machinery [175]. Developing different types of acoustic sensors further demonstrates that the used piezopolymers can operate through different principles. For instance, acoustic emission sensors are only based on the passive detection of the acoustic signal due to the mechanical change of the sensor, whereas ultrasonic transducers transmit a signal to remeasure it after reflection and detect any changes produced in the reflected wave [175].

This thesis focuses on the development of (0-3) 3D-printable piezocomposites embedding BaTiO₃ NPs within different polymer matrices that present different mechanical behaviours, studying the influence of different BaTiO₃ weight percentages in the piezoelectric properties of the resulting composites, but this will be thoroughly discussed in Chapter 6, section 6.2.

4.2 Magnetism

4.2.1 Introduction

Magnetism has always been a field of interest for scientific research since its discovery in 1064, attributed to Zheng Gongliang [185] who discovered that iron could reach a thermoremanent magnetisation state when heated up. After several centuries of research, it was in the seventeenth and eighteenth centuries when magnetism became a field of large interest. It was in 1743 when Daniel Bernoulli invented the horseshoe magnet in which the magnet will not destroy itself in its own demagnetising field, which has remained as one of the icons of magnetism up to the present day.

In 1820, Hans-Christian Oersted discovered the relationship between magnetism and electricity [186] following the work done by other scientists in the prior years. Oersted demonstrated that a current passing through a wire generates a circular field able to detect a compass needle, which supposed a revolution in electromagnetic science. Several researchers such as Ampère and Faraday developed theories to determine the magnetic fields created by currents flowing in different geometries, and discovered the electromagnetic induction phenomenon, leading to the connection between magnetism and light described by the magneto-optic Faraday effect. It was all this work which inspired James Clark Maxwell to develop a unification theory of magnetism, electricity, and light described by his well-known equations (not discussed in this thesis). One of the main conclusions of Maxwell's work was

the relationship between the electric and magnetic constants (ϵ_0 and μ_0), given by:

$$\sqrt{\epsilon_0\mu_0} = \frac{1}{c} \quad (4.6)$$

Probably, one of the most astonishing manifestation of magnetism in solids is the spontaneous magnetisation of ferromagnetic materials. The main characteristic of any ferromagnetic material (either if it is a pure element or a composite material) is the irreversibility of the magnetisation \vec{M} to an applied magnetic field \vec{H} . Hard magnetic materials present broad square $M(H)$ loops, whereas soft magnetic materials present narrow loops. This phenomenon does not mean that some materials are better or worse than others, but simply means that they have a different range of applicability, as hard magnetic materials are permanent magnets whereas soft magnetic materials are temporary magnets. Two characteristic parameters of the material can be obtained from hysteresis loops: the coercive field (H_C) which represents at which given field the magnetisation changes its sign, and the remanent (or saturation) magnetisation (M_r), which is the maximum value of magnetisation the material will achieve. Another important parameter of magnetic materials is their Curie temperature, T_C , below which the spontaneous magnetisation is reversible, and above which the spontaneous magnetisation is zero.

It must be noted that the magnetic field described by the Biot-Savart law and the Maxwell's equations (even though not presented in this thesis) is denoted by \vec{B} , whereas hysteresis loops use the magnetic field \vec{H} . This nomenclature is necessary when studying magnetic materials: \vec{B} is the magnetic field generated by electric currents in conductors, moving charges, and magnetic moments and it is expressed in Tesla (T). On the other hand, \vec{H} is called the magnetic field strength. The distinction between \vec{B} and \vec{H} is straight forward in free space:

$$\vec{B} = \mu_0\vec{H} \quad (4.7)$$

Hence, Maxwell's equations can be modified in order to satisfy \vec{H} , but for the Ampère's law to be satisfied, it is necessary to redefine the relationship between \vec{B} and \vec{H} such that:

$$\vec{H} = \vec{B}/\mu_0 - \vec{M} \quad (4.8)$$

The H -field will not be generated only by conduction currents, but any magnet will produce an H -field within its own volume and around it. Hence, Eq.(4.8) can be rearranged such that:

$$\vec{B} = \mu_0(\vec{H} + \vec{M}) \quad (4.9)$$

Thus, in free space $\vec{M} = 0$, Eq.(4.7) is recovered in which case \vec{B} and \vec{H} are qualitatively the same. Within a magnetic material, though, \vec{B} and \vec{H} are quite different and are oppositely directed. Whereas \vec{H} is a conservative field (*i.e.* $\nabla \times \vec{H} = 0$), \vec{B} is a solenoidal field (*i.e.* $\nabla \cdot \vec{B} = 0$). Hence, hysteresis loops are plotted using \vec{H} because it is possible to attribute an \vec{H} value at each point within the material and, thus, \vec{B} can be calculated from Eq.(4.9).

All materials can be classified in terms of their magnetic behaviour depending on their bulk magnetic susceptibility (χ). The two most common types of magnetism are *paramagnetism* and *diamagnetism*, which account for most of the elements of the periodic table at room temperature. These elements are usually referred to as non-magnetic materials, whereas those usually referred to be magnetic are classified as *ferromagnetic* materials (Fe, Co, and Ni). The only other type of magnetism observed in pure elements at room temperature is *antiferromagnetism*, observed in Cr. Nevertheless, magnetic materials can also be classified as *ferrimagnetic* materials even though such behaviour is not observed in pure elements but it can be found in composite materials such as ferrites. Table 4.2 shows the main characteristics of each type of magnetic behaviour.

Iron (II,III) oxide, more commonly known as magnetite (Fe_3O_4), is the most magnetic of all natural minerals, it crystallises with a cubic inverse spinel structure at room temperature [187], and it presents ferrimagnetic behaviour in its bulk form with a Curie temperature of 858 K. Magnetite NPs exhibit very different magnetic properties to those observed in its corresponding bulk state due to finite size effects, as mentioned in Chapter 4, section 4.2 [188–190]. When cooled down, magnetite undergoes a crystal structure phase transition to a monoclinic crystal lattice in which its magnetic, electrical, and thermal properties are modified [191]. This crystal structure phase transition, which takes place around 120 K, is known as Verwey transition and it is dependent on domain-state, grain size, and iron-oxygen stoichiometry [192]. Magnetite has been found to be present in some animals and bacteria [193, 194], in human brain tissue [195], where it is thought to play an important role in long-term memory [196], and in various igneous rocks [187]. In its bulk state it presents a ferromagnetic behaviour, whereas it shows a superparamagnetic behaviour when working with magnetite NPs below a specific size [188], making it suitable for applications in chemistry [197], medical diagnosis [198], and storage devices [199], among many others. Magnetite is used instead of other highly magnetic materials, such as cobalt or nickel, because both the latter elements are remarkably toxic and present an electronic configuration that easily








Type	Atomic behaviour	Susceptibility	Representation
Diamagnetism	Atoms present no	Small and negative	
	magnetic moment.	$(-10^{-5} \leq \chi \leq -10^{-6})$.	
Paramagnetism	Atoms present	Small and positive	
	randomly oriented magnetic moments.	$(10^{-5} \leq \chi \leq 10^{-2})$.	
Ferromagnetism	Atoms present	Large below T_C .	
	magnetic moments aligned in parallel.		
Antiferromagnet	Atoms present	Small and positive	
	magnetic moments aligned in antiparallel.		
Ferrimagnetism	Atoms present	Large below T_C .	
	magnetic moments mixed in parallel and antiparallel.		

Table 4.2. Main characteristics of the different magnetic materials and representation of the alignment of their magnetic moments.

yields to oxidation.

One important feature that must be taken into consideration when working with magnetic NPs is their size as it plays a key role in the final magnetic properties. Working with large NP sizes implies that there exist several magnetic domains within the particle, making the inversion of magnetization happen through the movement of the walls of the domains rather than spin rotation, resulting in low values of coercive field (see Fig. 4.3). When the NP size is reduced they become single domain, and thus the inversion of magnetization happens via *coherent rotation*, which has a high energetic cost and leads to an increase of the coercive field. Otherwise, if the size of the NPs is too small, thermal agitation is non-negligible and provokes fluctuations and, therefore, H_c decreases again becoming eventually zero (*i.e.*, transition from ferromagnetic to superparamagnetic, as shown in Fig. 4.3). When embedding magnetic NPs within a polymeric matrix, their concentration will not only have a direct effect on the magnetization of saturation, which will increase as a function of the content of magnetic material, but will also influence the coercive field; if NPs are very close to each other, dipolar magnetic interactions will occur.

4.2.2 Susceptibility and permeability

The simplest materials are linear, isotropic, and homogeneous (HIL), which in magnetism means that the susceptibility (or applied field) is small and, therefore, a small magnetisation is induced in the same direction as the external applied field (H').

$$\vec{M} = \chi' \vec{H}' \quad (4.10)$$

where χ' is a dimensionless scalar called external susceptibility. The magnetisation \vec{M} is related to the internal field \vec{H} by:

$$\vec{M} = \chi \vec{H} \quad (4.11)$$

where χ is the internal susceptibility that follows from:

$$1/\chi = 1/\chi' - \mathcal{N} \quad (4.12)$$

where \mathcal{N} is a demagnetizing factor. As long as χ is small (as it takes values of the order between 10^{-5} to 10^{-2} and -10^{-5} for paramagnets and diamagnets, respectively) the difference between χ and χ' can be neglected. Nevertheless, this assumption cannot be made for all materials such as superconductors, paramagnets close to T_C , or ferromagnets. It must be noted that χ diverges as $T \rightarrow T_C$, but χ' never

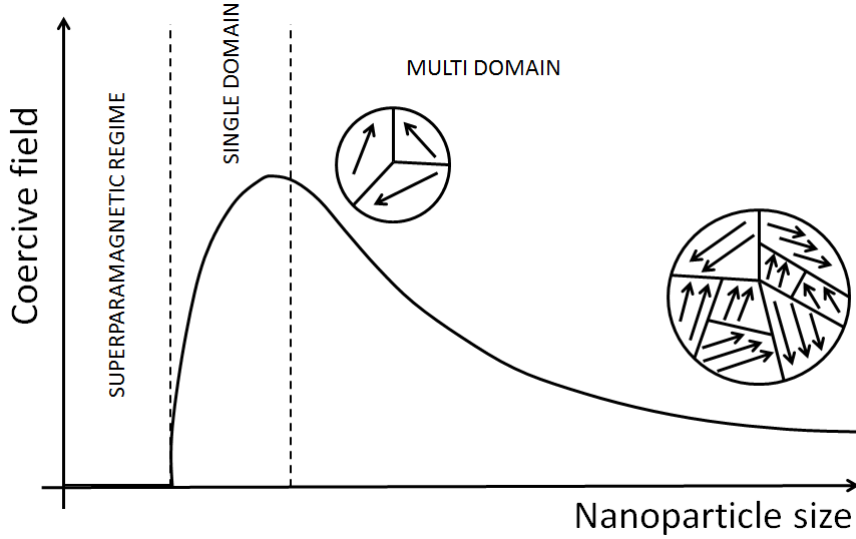


Fig. 4.3. Sketch of the relationship between coercive field and magnetic NP size, discerning between single- and multi-domain regimes, as well as the superparamagnetic and the ferromagnetic behaviours. For small very small nanoparticle (NP) sizes, the coercive field is zero as they are single domain NPs and thermal agitation is non-negligible and generates fluctuations, providing eventual zero coercive field (superparamagnetic regime). As NP size increases, they are still single domain but in a regime where thermal agitation is not relevant, and the coercive field starts increasing within a regime where inversion of magnetization happens via coherent rotation. As NP size keeps increasing, they become multidomain and the rotation of the magnetic domains takes place through the movement of the domain walls within the NP, leading to lower coercive fields.

exceeds $1/\mathcal{N}$ [185]. It must be further noted that in single crystals, χ may take different values in different crystallographic directions, meaning that when studying Eq.(4.11) it becomes a symmetric second-rank tensor χ_{ij} with three independent components in the principal-axis Cartesian coordinate system.

Permeability, μ , can be related to susceptibility as it can be derived from Eq.(4.9), becoming:

$$\vec{B} = \mu_0(\vec{H} + \vec{M}) = \mu_0(1 + \chi)\vec{H} \quad (4.13)$$

when considering HIL materials. It must be mentioned that μ_0 stands for the vacuum permeability and μ is defined as $\mu = (1 + \chi)$. A relative permeability, μ_r , is defined as $\mu_r = \mu/\mu_0$. Hence, Eq.(4.13) can be rewritten as:

$$\vec{B} = \mu_0\mu_r\vec{H} = \mu\vec{H} \quad (4.14)$$

Permeability is usually related to soft (ferro)magnetic materials, as μ_r can take very large values, up to the order of 10^4 [200].

4.2.3 Diamagnetism

When there is no applied field, the atoms of a diamagnet do not present any magnetic moment, but as soon as a field \vec{H} is applied, a magnetisation \vec{M} is induced in the opposite direction to that of the applied field. All materials have a diamagnetic effect which is usually masked by larger paramagnetic or ferromagnetic terms. The value of susceptibility is independent of temperature. Superconductors exhibit diamagnetic hysteresis loops below their superconducting transition temperature.

4.2.4 Paramagnetism

Several theories have been developed to study paramagnetic materials [185, 201]. The Langevin model, which is valid for materials with non-interacting localised electrons, states that each atom presents a randomly oriented magnetic moment as a result of thermal agitation. When an external magnetic field is applied, these magnetic moments are slightly aligned with the direction of the applied field, producing a small magnetisation. Thermal agitation increases with temperature, thus making harder to align the magnetic moments of the atoms and therefore leading to a decrease of the susceptibility of the material. This phenomenon is known as the Curie law and it can be expressed as a function of the Curie constant (C):

$$\chi = C/T \quad (4.15)$$

Materials which obey this law are those in which the magnetic moments are localised at the atomic (or ionic) sites and where there is no interaction between neighbouring magnetic moments. This is the case of some hydrated salts of transition metals, as the metallic ion is surrounded by a number of non-magnetic ions/atoms that do not permit interaction between magnetic moments.

Actually, the Curie law is a particular case of a more general law called the Weiss-Curie law, which incorporates the temperature constant θ proposed for ferromagnetic materials and accounts for the interaction between magnetic moments:

$$\chi = \frac{C}{T - \theta} \quad (4.16)$$

Thus, it can be easily seen that when θ equals zero, the Curie law is recovered. On the other hand, when θ is non-zero, this means that there exists a magnetic interaction between the magnetic moments of the material, which becomes paramagnetic exclusively above a certain transition temperature. When θ is positive the material is ferromagnetic below the transition temperature, and thus $\theta = T_C$. If θ is negative

the material is antiferromagnetic below the transition temperature, called Néel temperature (T_N), but in this case, unlike in the previous case, θ is unrelated to T_N . The reader must notice that this equation is only valid when the material is in a paramagnetic state, and it is not further valid for those materials (metals) in which the electrons contributing to the magnetic moment are not localised.

4.2.5 Ferromagnetism

Ferromagnetism can only take place when the atoms in the lattice are arranged such that their magnetic moments can interact and align parallel to each other. Weiss explained this effect using the classical theory by the presence of a molecular field within the ferromagnetic material [202]. This field is sufficient to magnetise the material to saturation. On the other hand, when using the quantum theory, it is possible to explain ferromagnetism in terms of an exchange interaction between neighbouring magnetic moments.

Weiss described the presence of magnetic domains within the material, which are regions where the atomic magnetic moments are aligned [202]. The movement of these domains determines how the material responds to magnetic fields and, as a consequence, susceptibility is a function of the applied field. Therefore, ferromagnetic materials are usually compared in terms of saturation magnetisation, which corresponds to the magnetisation of the material when all the magnetic domains are aligned, rather than susceptibility. It must be noted that when ferromagnetic materials are heated up, thermal agitation plays an important role and the degree of alignment of the atomic magnetic moments decreases leading to a decrease of the magnetisation of saturation. Eventually, thermal agitation becomes so great that the material becomes paramagnetic. The temperature of this transition is T_C above which the susceptibility varies according to the Curie-Weiss law [202].

4.2.6 Antiferromagnetism

Antiferromagnetic materials (which is only exhibited by Cr in pure elements) can be explained in an analogous way as ferromagnetic materials with the exception that the exchange interaction between neighbouring atoms leads to the antiparallel alignment of the atomic magnetic moments. Hence, the magnetic field cancels out and the material appears to behave in the same way as a paramagnetic material. As it happens with ferromagnetic materials, antiferromagnets become paramagnets above a transition temperature T_N .

4.2.7 Ferrimagnetism

This type of magnetic behaviour can be only observed in composite materials, which present much more complex crystal structures than pure elements. In these materials, the exchange interactions lead to parallel alignment of atoms in some of the crystal sites and antiparallel alignment of others. The material breaks down in magnetic domains just like a ferromagnet does, and the magnetic behaviour is also very similar, although ferrimagnetic materials usually present lower saturation magnetisation values. A clear example is barium ferrite, in which the unit cell contains 64 ions of which the barium and oxygen ones present no magnetic moment, 16 Fe^{+3} ions have moments aligned in parallel, and 8 Fe^{+3} ions are aligned antiparallel giving a net magnetisation parallel to the applied field, but with a relatively low magnitude as only 1/8 of the ions contribute to the magnetisation of the material.

An in-depth explanation of the theory of paramagnetism, ferromagnetism, and antiferromagnetism is given in *Magnetism and Magnetic Materials* [200], to which the reader can refer to in case if interested in this subject. The full detailed explanation of such theory, including quantum effects and probability calculus is out of the scope of this thesis.

4.2.8 Superparamagnetism

Apart from the types of magnetism previously described in this section, it is possible to find materials that present the phenomenon known as *superparamagnetism*. This happens when a material is composed by several non-interacting very small magnetic domains dispersed in a non-magnetic medium, usually when working with NPs, which behave like paramagnetic macrospins. As particle's size increases, it adopts magnetic configurations governed by the balance of anisotropy, exchange, and magnetic dipole interactions. Superparamagnets can be used in several technological applications such as in hard drive disks or ferrofluids.

The energy of a single-domain magnetic grain with uniaxial anisotropy under an external applied field is given by the sum of its magnetic anisotropy and Zeeman energies¹. In the absence of an external magnetic field there are two energetically equally favourable directions, which are both parallel to the easy axis of magnetisation with an energy barrier between them of KV (where K is an anisotropy

¹The Zeeman energy is the potential energy corresponding to an external magnetic field. Each magnetic moment has a given Zeeman energy. The reader can refer to *Magnetism and Magnetic Materials* [200] for further information.

parameter, and V is the volume of the magnetic domain). Nevertheless, if temperature is high enough, thermal energy ($k_B T$, where k_B is the Boltzmann constant) can overcome such energetic barrier and, therefore, the grain's magnetisation changes direction.

On the other hand, in the presence of an external magnetic field, the energy of a magnetic domain is lower when magnetisation points along the external magnetic field than when it points towards the opposite direction.

When using superparamagnetic materials for specific applications, the grain size must be as uniform as possible in order to optimize the response of the device. There are several ways to determine the size distribution of a sample: (i) using TEM or SEM equipment, and (ii) determining a macroscopic property of the sample and then deriving the parameters of size distribution based on physical models, being the Langevin model the most common one. Magnetisation curves ($M(H)$) below and above the blocking temperature² (T_B) are qualitatively different. When $T \geq T_B$ it is possible to determine the grain size distribution parameters. Under such conditions, the Zeeman energy is much larger than the anisotropy energy. Assuming then that all domains have magnetic moments of the same size, it is possible to apply the Langevin theory and replace the Langevin function for a Brillouin function given by:

$$M = M_r L(x) = M_r \left[\coth(x) - \frac{1}{x} \right] \quad (4.17)$$

In this case, the variable x is given by $\mu H / k_B T$, leading to:

$$\frac{M}{M_r} = \coth \left(\frac{\mu H}{k_B T} \right) - \frac{k_B T}{\mu H} \quad (4.18)$$

It is also possible to establish a relationship between μ and the size of the particles by using the relationship [203]:

$$\mu = \frac{\pi M_r d^3}{6} \quad (4.19)$$

Thus, Eq.(4.18) becomes:

$$\frac{M}{M_r} = \coth \left(\frac{\pi M_r d^3 H}{6 k_B T} \right) - \frac{6 k_B T}{\pi M_r d^3 H} \quad (4.20)$$

As all the other parameters can be obtained from the $M-H$ curve, it is easy to determine the distribution size of the superparamagnetic particles using Eq.(4.20).

²The blocking temperature is defined as the temperature at which the relaxation time due to thermal agitation equals the experiment timescale (t_{exp}). Thus, the blocking temperature is not uniquely defined for a given material due to its dependency with t_{exp}

Chapter 5

Experimental Techniques

5.1 3D Laser Doppler vibrometer

The motion of insect tympana when forced by sound is generally too small to be detected using conventional optical techniques. Indeed, some previous work studying such structures involved large stimuli amplitudes such that the oscillations could be optically observed [41]. These stimuli, however, were generally orders of magnitude louder than sound levels to which acoustic structures would respond to in their natural environment. Thus, a different approach must be used in order to investigate these structures at biologically relevant stimuli. Laser Doppler vibrometry (LDV) has become a powerful technique in recent years to detect sub-nanometre motion in a contactless manner not only in biological structures [204] but also in engineered systems and sensors [205]. The development of this instrumentations in three dimensions of space (3D LDV) has enabled scientists to study not only the motion of structures in the out-of-plane axis but also to examine all the relevant physical phenomena that take place in-plane, rapidly increasing the knowledge of biological sensing. Moreover, the ability to detect sub-micron motion has allowed to measure artificial non-linear effects generated as a consequence of the high intensity of the driving sound field.

All types of LDV (1D, 2D, and 3D) use the same principle to detect motion of the sample of interest based on the Mach-Zehnder interferometer, which consists of the splitting of the initial laser beam and recombining it using a second beam splitter, generating a (relative) phase difference between the two beams that therefore creates an interference pattern at the detector. The LDV exploits this effect (see Fig. 5.1) by firing a laser into a moving object, giving rise to a non-contact measuring

technique. The intensity of the laser can be adjusted by the user so the sample (either if biological or not) does not suffer any damage produced by the focusing of the laser to a small point and allowing an *in-vivo* and *in-situ* measurement of the mechanical response of the sample to an acoustic stimulus.

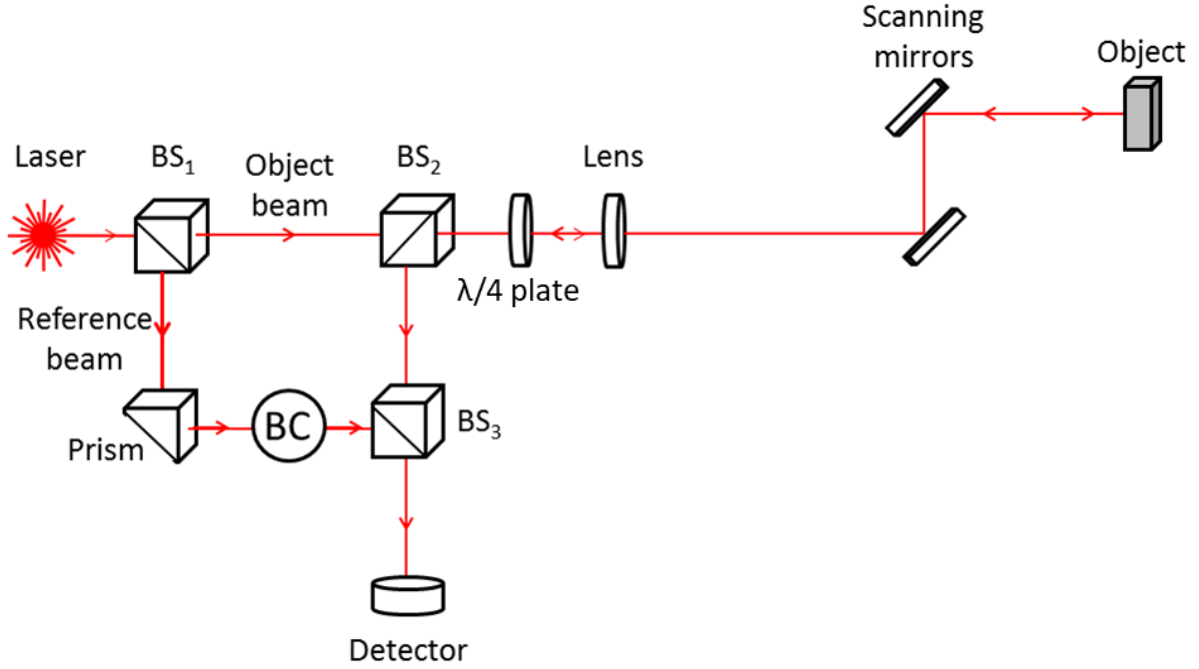


Fig. 5.1. Sketch of the schematic set up of the used LDV. BS_i are beam splitters and $\lambda/4$ is a quarter wave plate. The Bragg cell (BC) is an acousto-optical modulator that creates an additional frequency-shifted beam for the reference beam, allowing the interferometer to be directional. Scanning mirrors, which are controlled by the Polytec software, allow for accurate positioning and scanning of the surface to be measured.

To detect sub-micron motion, LDV techniques exploit the Doppler effect (detailed in Section 1.2.4) inferring a velocity from a Doppler-shifted signal. The laser beam is focused onto the vibrating surface and scattered back. This backscattered signal is Doppler-shifted (by a frequency f_d) as a consequence of the velocity, v , of motion of the studied sample:

$$f_d = 2\frac{v}{\lambda} \quad (5.1)$$

The laser beam is first split in a reference and an object beam through a first beam splitter (BS_1). The object beam passes through a quarter-wave plate ($\lambda/4$) and it is then focused by a movable lens onto the scanning mirrors that allow for accurate positioning of the laser spot onto the surface. The object beam is then backscattered with a Doppler-shift proportional to the surface velocity of the object and returns through the $\lambda/4$ plate to be split again by the second beam splitter (BS_2), where it is transmitted towards the detector. On the other hand, the reference beam is directed to the detector using a prism and after passing through a Bragg cell, which uses the acousto-optical effect (consisting

of the modification of the refractive index) to induce a frequency shift in the laser beam as it passes through the cell. Thus, the reference beam is shifted and directed towards the detector by the third beam splitter (BS₃). It must be noted that even though the interference pattern generated by the reference signal and the Doppler-shifted signal is enough to determine the surface velocity of the moving object, this is an average value of two combined signals, and it is thus not directional. This is the reason why the LDV system shifts the reference beam using a Bragg cell.

This phenomenon can be easily understood if considering two signals with frequencies f_1 and f_2 , which lead to a beat frequency of $\frac{1}{2}|f_1 - f_2|$. In the LDV $f_2 = f_1 \pm f_d$, and therefore $|f_1 - (f_1 \pm f_d)| = |\pm f_d|$, which is independent of the direction of movement of the object. Thus, splitting (adding an extra shift using the acousto-optical effect) the reference beam into a third frequency f_3 leads to a beating frequency $|f_3 \pm f_d|$, allowing to determine directionality.

The LDV technique has been long applied to detect sub-micron and sub-nanometre motion of biological samples such as tympanal membranes of locusts, moths, and cicadas as well as it has been used to detect the antennae motion of mosquitoes, *Drosophila* flies, and many other Dipterian flies [11, 206–209]. Nevertheless, the majority of these experiments have been performed using a 1D LDV, restricting the types of experiments that can be performed as ultimately all stimuli and motion should be in one unique direction. Furthermore, measuring in one unique direction implies a careful treatment of the obtained data, as tilting of the vibrating sample could lead to the measurement of artificial phenomena or a decrease of the absolute amplitude of motion in the axis of interest.

Scanning complex-shaped surfaces presents a particularly demanding scenario in which the direction of the measured vibration changes with both the scanning angle relative to the LDV and the measured surface. These limitations can be overcome by simultaneously measuring all the vibration components and knowing (or determining) the 3D geometry [210]. To do so, a 3D LDV is needed, in which three independent interferometers are included, each of them controlled by a central data management system. These interferometers are arranged on a fixed support and their scanning heads are positioned at 0, 90, and 270 degrees, respectively. In order to scan a single point, each of the independent heads needs to be positioned at that exact point (with a permitted source of error). All the experiments conducted in the course of this thesis were performed using a 3D LDV system with an MSA-100-3D scanning head

(Polytec, Waldbrom, Germany), which combines an optical microscope and uses one unique laser source and three detector heads positioned as previously discussed.

5.1.1 Resolution limits and sources of error of the LDV

Resolution is a crucial parameter when storing data using LDV techniques that can be highly affected by several components. The main three noise sources that affect the resolution of the measured data are light induced noise (shot noise), thermal noise (Johnson noise, arising from both the detector and preamplifier), signal processing noise, and signal processing noise. Furthermore, there is an ultimate limiting factor when using the LDV which is the signal-to-noise ratio of the photo detector output [211].

One of the main advantages of detecting coherent light by means of interferometry is that the optical amplification of the AC current can be expressed as a function of both the measurement beam power (P_m) and reference beam power (P_r). However, the sum power $P_m + P_r$ generates both DC current and shot noise which can be expressed as [211]:

$$i_{sh}^2 = 2KqB(P_m + P_r) \quad (5.2)$$

where B is the detector bandwidth, K is the detector sensitivity factor, and q is the electron charge. One of the most important sources of noise is thermal noise, which can be determined from [211]:

$$i_{th}^2 = \frac{4k_BTB}{R} \quad (5.3)$$

where k_B is the Boltzmann's constant, T stands for the absolute temperature, and R is the detector load resistance.

In order to obtain the best signal-to-noise ratio, the reference beam power is usually chosen such that the shot noise power significantly exceeds the thermal noise power under specific conditions, a point generally achieved when $P_r + P_m < 1$ mV [211]. It can further be demonstrated that phase noise (equivalent to displacement noise) exhibits white noise characteristics, whereas velocity noise is proportional to frequency. These relationships explain why velocity noise increases with frequency whereas displacement noise remains constant over frequency [211]. It is possible to obtain sub-nanometre resolution either under the condition of sufficiently small resolution bandwidth of the signal acquisition system or running enough averages.

When using LDV techniques it is necessary to take into consideration the possible sources of

error apart from the cause and origin of noise. The main factors contributing to uncertainties when using the LDV are basically due to perturbations in the movement of the object (which arise from external sources), and the finite accuracy of the laser beam position on the measured object [212], which are reduced by the manufacturer's software using a Fourier transform filter and an average function over the measured data.

5.2 Finite element simulation

Usually any engineering problem or biological phenomenon present in nature can be evaluated and approached from a mathematical point of view using a set of differential and/or integral equations that describe the system governed by principles such as Newton's laws, conservation of mass and energy, the laws of thermodynamics or Maxwell's electromagnetic equations amongst many others. Most of the times, though, when studying three-dimensional systems the equations governing the physical phenomena cannot be analytically solved and a computational solution is needed. Such solutions become more and more cumbersome when studying systems of complex arbitrary geometries with varying thickness, composed by several materials (which can be both isotropic and anisotropic) that encapsulate several aspects of physics, leading to meaningless solutions. The best approach to solve these complex systems governed by multiple physics is the numerical method known as finite element analysis (FEA). FEA has been successfully applied in several fields involving very different physical processes such as structural mechanics, fluid dynamics, electrostatic problems, thermodynamic systems, or acoustic interactions among many other fields.

A finite element model (FEM) is a virtual representation developed to study the complex phenomena taking place on the system of interest. FEMs can be developed either by creating CAD files that emulate the system or by importing post-processed micro computer tomography (CT) scanned files into the simulation software. Both methods present pros and cons: when working with simplified user-developed CAD files emulating the system, association of material properties and boundary conditions of all the sub-domains will be straight forward, but the simulation results will not be as accurate as they would be when working with a scan of the real system itself. On the other hand, importing a microCT scanned part could imply several difficulties when defining the material properties and boundary conditions of all the sub-domains for the several physics ruling the system, but at the same time the results will be much

more accurate and realistic after a long computation time. Irrespectively of what method is chosen by the user, the FEM will be constituted of several domains which can be associated to their corresponding material (either if it is a solid, liquid or a gas) and its corresponding boundary conditions in accordance of what physics rule the system. These domains need to be then sub-divided into smaller sub-sections using meshes of simple geometries (usually tetrahedrons) of finite size. Sometimes it is possible that a simple 3D reconstruction of the system does not provide accurate results or takes too long to process. In that case, there exists the possibility to develop a 2D file and apply symmetry conditions in order to simplify the full process. In these cases, the mesh usually subdivides the domains in small triangles of finite size.

As the domains are subdivided into a finite number of smaller finite parts, the vertices and edges of the mesh are in contact with each other, leading to a series of finite nodes to which the degrees of freedom of the system are assigned. Depending on the physics governing the system, the corresponding differential equations will encompass these degrees of freedom and will be applied to every single node of the mesh. By determining the response in each node, as each node is in contact with other nodes controlling therefore the behaviour of the consecutive element, it is possible to determine an approximation of the behaviour of the system as a whole resulting from a matrix of differential equations. These differential equations contain the basic information of each one of the nodes in which the domain has been meshed, including their corresponding material properties as well as their initial and boundary conditions, which simplify the model by reducing the number of degrees of freedom present within the system. Thus, as the number of nodes in a continuum is infinite, it must be noted that even in the most realistic of simulations, the final result is only an approximation of the real behaviour of the system, which accuracy directly depends on the mesh resolution.

During the course of this thesis FEA simulations have been used to find solutions to the eigenproblem formulation, a technique thoroughly used to determine the characteristic values (eigenvalues) of the system and its corresponding characteristic vectors (eigenvectors) which usually provide the characteristic (natural) shapes of vibration under the characteristic frequencies. An easy example to illustrate this phenomenon is to imagine a system of two oscillators coupled in one dimension and which motion is constrained in that same dimension. Imagine the eigenvalues of the system are ω_1 and ω_2 and their corresponding eigenvectors are given by $\vec{\xi}_1 = A(1,1)$ and $\vec{\xi}_2 = A(1,-1)$, where A is a normalization

constant. This means that the first eigenvector, $\vec{\xi}_1$, describes the motion of the oscillators in the same direction and with the same amplitude when driven by the first eigenfrequency ω_1 , whereas the second eigenvector, $\vec{\xi}_2$, reveals that the two oscillators move with the same amplitude but in opposite directions when driven by the eigenfrequency ω_2 .

COMSOL Multiphysics[®] (version 5.3, COMSOL, Inc. Burlington, MA, USA) has been extensively used throughout this research as it permits to model several multiphysics applications. One of the main advantages of this software is that it provides several modules that allow to combine different study types through coupled solvers, enhancing its degree of applicability. In this thesis the acoustic module has been thoroughly used, specifically that in which it is possible to study the interaction of incoming acoustic fields with solid structures that further present solid-liquid interfaces.

5.2.1 FEM process

Finite element models can be constructed by following a series of steps. Before importing or constructing the CAD file the type of physics and study to evaluate must be selected, so the corresponding adequate differential equations can be applied to solve the system. Once these have been selected, it is possible to add in the study a series of parameters and definitions that COMSOL will store, including geometrical dimensions, some material properties, or parametrisations of the system, among many others, that allow rapid and simple computation of the model (see left-hand-side tree under Model Builder in Fig. 5.2). One important feature of COMSOL is that once these parameters have been saved either as Local or Global Definitions, there exists the possibility to run several simulations at the same time in which all these parameters are combined within a user-defined range (solving through parametric sweeps). As all the initial parameters have been defined, one can start building (or importing) the desired geometry (see Fig. 5.2).

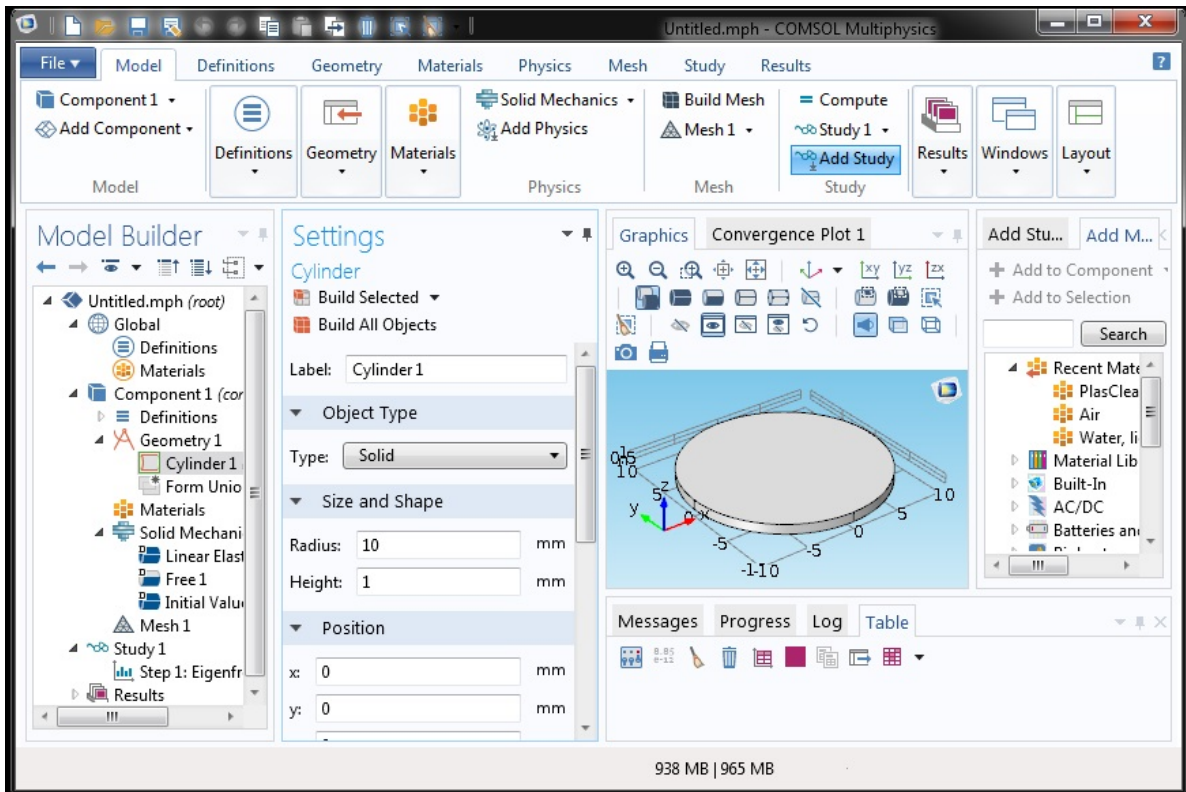


Fig. 5.2. Screen shot of the COMSOL interface when the second step (building the geometry) is finished. It can be seen in the top part of the left-hand-side tree under Model Builder that Global Definitions can be introduced before building the geometry of the system. COMSOL presents a geometry builder that allows the creation of different shapes (in this case introducing a cylinder, as it can be seen in the building tree under Model Builder).

The built-in geometry will be partitioned in several domains, each of which can be attributed its own mechanical properties and boundary conditions. In the case illustrated in Fig. 5.2 one unique domain is created. When studying fairly simple geometries and systems, the geometry builder provided by COMSOL was used, whereas when more complex geometries and structures had to be studied, the 3D-CAD software PTC Creo[®] was used, which provides several exportable formats compatible with COMSOL.

The next step is to specify the material properties of the different domains. As previously stated in this Section, COMSOL permits the user to define several types of materials (either isotropic and anisotropic) in all the three states of matter and including a plasma simulation study. These materials can be combined within a same study using COMSOL, allowing for high complexity when designing the system of interest.

Specification of the materials of the different domains can be user-defined by introducing the required mechanical properties (in this case only the density, elastic modulus, and Poisson's ratio of

the materials are needed) or either COMSOL-defined materials from the Materials Library (including solid, liquid, and gaseous materials) can be used, which present all the necessary properties to run the simulation. It must be noted that one unique material can be attributed to a domain and thus, if more than one material is needed, such domain must be sub-divided into several domains (*i.e.* when working with air-filled cavities enclosed within a membrane, such cavities must be added inside the membrane as a second, third, ..., n^{th} domain, and air must be selected for those specific domains). When using predefined materials from the COMSOL Materials Library, it is also possible to change specific parameters in order to fulfil the user's needs and reproduce the material properties in the most exact way possible, as some of the pre-defined material properties are given at specific temperatures and pressures (usually defined under normal conditions, *i.e.* $T = 293$ K and $P = 1$ atm). Nevertheless, changing these parameters can be sometimes challenging when dealing with anisotropic materials or changing asymmetric inherent properties of a material (such as specific piezoelectric constants, for instance) as they imply the modification of all the components of a large matrix of values.

The following step is to apply the boundary conditions of the system. First of all it must be noted by the reader that every physics presents different boundary conditions, *i.e.* the Solid Mechanics physics will allow to pre-load, fix, or roll specific surfaces, edges or points whereas an acoustics physics will allow to set hard and soft acoustic boundaries and add incident plane, cylindrical, or spherical pressure fields among others. It must be further noted that in order to provide a specific part of the domain specific boundary conditions, such domain must be ruled by the corresponding physics (for instance, it will not be possible to define a surface as the incoming acoustic field if its corresponding domain is defined under the Solid Mechanics physics). Defining boundary conditions is the simplification of the problem by reducing the amount of degrees of freedom present in the system. Such boundary conditions are applied by right-clicking the desired physics under Model Builder in the left-hand-side tree (Solid Mechanics in this case), select the desired boundary condition (here the edges of the disk are fixed), and finally select the desired surface, edge, or point of the domain.

Once all the boundary conditions have been applied to the desired domains, the upcoming step is to generate the mesh of the system (see Fig. 5.3). As previously stated in this section, the finer the mesh the more accurate the solution will be but, at the same time, the longer it will take to compute. Therefore, the mesh must be established in order to obtain a reasonable balance between computation time and results accuracy. To define the mesh of the system, COMSOL will provide several options in order to obtain a mesh as accurate as possible. To start with, COMSOL will show different mesh geometries depending on the dimensionality of the system (for example triangles or quadrilaterals when working in 2D systems, and tetrahedral or hexahedral shapes when working with 3D systems). These shapes can then be attributed to different sizes defined by the software, but if those do not meet the needs of the user, there exists the possibility to customize them by introducing new minimum, maximum, and step sizes of the user-defined mesh. Furthermore, it is possible to attribute different mesh sizes and geometries to different domains. Moreover, if this customization process does not fulfil the user's needs, COMSOL gives the possibility to use complex meshes based on gradients around a point, a line or an edge as well as it permits the projection of a 2D mesh in a 3D space. Fig. 5.3 shows the application of a Physics-controlled mesh with an element 'Extra fine' size (also predefined by COMSOL).

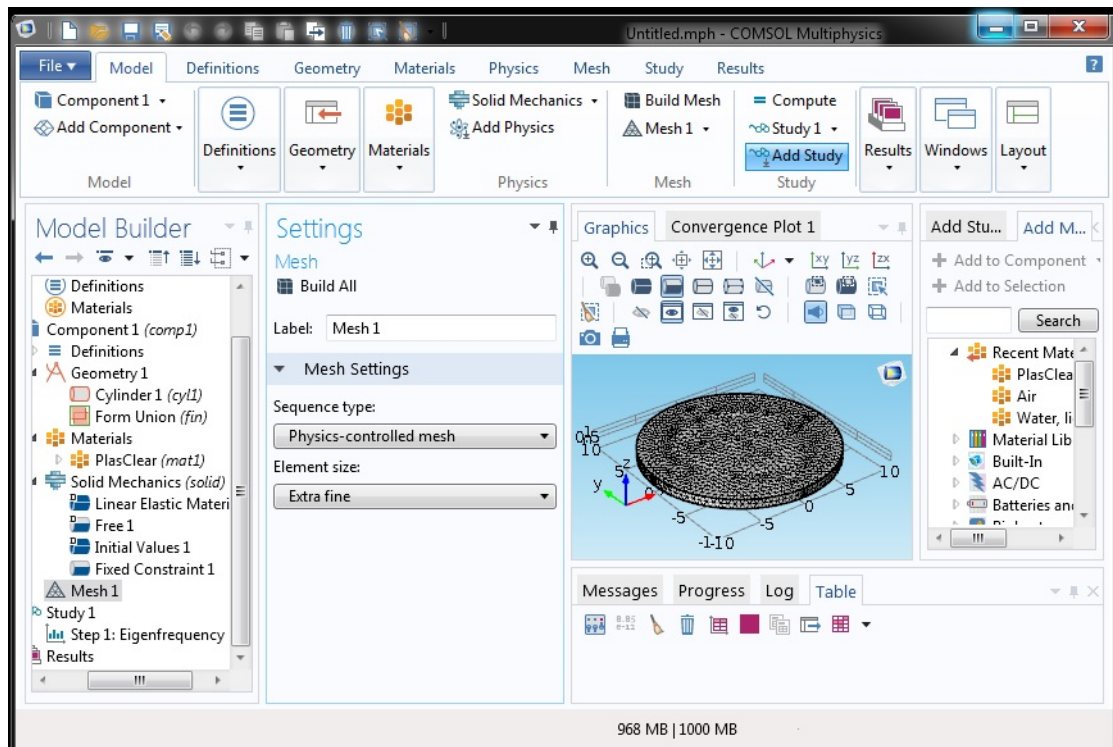


Fig. 5.3. Screen shot of the COMSOL interface after applying the mesh, which can be finely tuned by the user by selecting different mesh geometries and sizes. A full customization of the mesh is also possible as mesh gradients can be applied, as well as it is possible to define different mesh sizes for different domains.

Finally, the study settings must be defined, being the COMSOL default solver the best option as it provides accurate results after optimisation of the computational resources. As previously discussed, it is possible to run parametric sweeps in which the solutions are obtained as the combination of several user predefined parameters.

5.2.2 Eigenproblem simulations

COMSOL provides the adequate interface to determine the characteristic frequencies of solid bodies, which are responsible of their eigenmodes and corresponding eigenvectors. These characteristic frequencies depend on the geometry of the studied body and some of its mechanical properties such as the Young's modulus, the Poisson's ratio, and the density of the material.

When determining the eigenfrequencies of a solid body with COMSOL, all the previously described steps must be followed and, finally, select the number of characteristic frequencies of interest. Furthermore, there is also the option to look for a certain number of eigenfrequencies around a specific value. When the simulation is finished, COMSOL provides a visualization of the mechanical behaviour of every mode, in which it is possible to visualize different physical properties such as mechanical deflection, stress, velocity, and acceleration of the body among others. Thus, the default solver settings for the output eigenvectors is for normalisation with respect to the RMS values.

The most important feature when running a modal analysis of a solid body, is that the normalisation solver settings must be changed from RMS to mass matrix so the modal participation factors (MPF) in the three dimensions of space can be determined for each mode. Squaring the MPFs_{*i*} (where $i = x, y, z$) for each mode results in the effective modal mass (EMM) of that mode in SI units.

$$EMMI_{ij} = MPF_{ij}^2 \quad (5.4)$$

where $i = 1, 2, \dots, n$ in direction $j = x, y, z$. The mass of the body is determined by COMSOL using the following equation:

$$m_b = \frac{\rho}{V_b} \quad (5.5)$$

where m_b is the total mass of the studied body, ρ is its density, and V_b is the total volume of the studied body. If the shape of the body of interest is simple enough it is possible to work out its total volume analytically, but for complex geometries COMSOL provides a tool that allows to approximately

determine the total volume of the studied body. Determining these two quantities, EMM_{ij} and m_b , accurately determines the effective modal mass fraction (EMMF) as a percentage.

$$EMMF_{ij} = \frac{EMM_{ij}}{m_b} \quad (5.6)$$

EMMF is an indication of the strength (or significance) of a vibration mode. Thus, modes with relatively high EMM values can be readily excited by base excitation, whether those presenting low EMM values they cannot be readily excited in this same manner.

5.2.3 Acoustic-structure interaction

The reader must have noted at this point that the eigenproblem analysis using the Solid Mechanics module of COMSOL does not provide any type of solution when a solid body interacts with an external force field. To do so, COMSOL provides several modules that allow the user to determine what the physical response of a specific body will be when affected by an external field (*e.g.* electromagnetic, fluid flow & heat transfer, chemical engineering, and acoustic modules) in which it is possible to define the object ruled by the physical laws that govern the system by defining specific extra domains in which the desired force field propagates. During this research the acoustics module has been thoroughly used as it allows to study the two-way coupling between a structure's mechanical response and the pressure wave propagating through the surrounding fluid. COMSOL calculates how the pressure wave propagates through the defined fluid domain and determines the fluctuations caused by it (using the Helmholtz equation, see Eq.(5.7)), determining how the propagation of the pressure wave affects the solid body.

$$-\frac{1}{\rho_f} \nabla^2 p - \frac{\omega^2 p}{\rho_f c^2} = 0 \quad (5.7)$$

where ρ_f is the density of the fluid, p is the harmonic acoustic pressure (expressed as $p = p_0 e^{i\omega t}$), ω is the angular frequency, and c is the speed of sound. The vibration of the solid body within the fluid is controlled by the corresponding frequency response analysis provided by the structural mechanics module (hence an example of multiphysics analysis in COMSOL), and it is generated as a response to the harmonic load. The FEA solver determines the steady-state solution by using both a force and a phase that depend on the driving angular frequency ($F(\omega)$ and $\varphi(\omega)$, respectively). COMSOL's software then determines the displacement field in an oscillatory solution consisting of a displacement amplitude and its corresponding phase.

As previously mentioned in this section, when studying the interaction between a solid body with

an external force field, several domains in which the different physics have been defined are needed. In this case, building a sphere of fluid and placing the solid body in the centre ensures the far-field regime. Thus, apart from any mechanical boundary conditions defined in the solid mechanics module, defining the boundary conditions and the pressure wave is needed in the fluid domain. The coupling between the two physics is given by the system in different ways for exterior and interior boundaries. Whereas in exterior boundaries the coupling is given by the system of equations (5.8), interior boundaries are coupled by the system of equations (5.9), representing a pressure drop in the solid structure directly proportional to the acoustic load:

$$\begin{cases} -\mathbf{n} \cdot \left(-\frac{1}{\rho} (\nabla p - q_d) \right) = -\mathbf{n} \cdot u_{tt} \\ \mathbf{F}_A = p \mathbf{n} \end{cases} \quad (5.8)$$

where \mathbf{n} is the normal surface unit vector, p is the total pressure field, q_d is a dipolar source (which is an optional feature and sometimes taken to be 0), u_{tt} stands for the second derivative of displacement over time (*i.e.* acceleration), and \mathbf{F}_A is the load applied onto the solid body.

$$\begin{cases} -\mathbf{n} \cdot \left(-\frac{1}{\rho} (\nabla p - q_d) \right)_1 = \mathbf{n} \cdot u_{tt} \\ -\mathbf{n} \cdot \left(-\frac{1}{\rho} (\nabla p - q_d) \right)_2 = -\mathbf{n} \cdot u_{tt} \\ \mathbf{F}_A = (p_1 - p_2) \mathbf{n} \end{cases} \quad (5.9)$$

Irrespective of the type of wave used to drive the system (plane, cylindrical or spherical), it is important to define boundary conditions such that internal reflections are eliminated within the domain. Furthermore, the incident wave direction can be user-defined by including new parameters. In this case the angles are defined as θ and φ such that spherical coordinates presented in section 1.3 can be reproduced by building the vectors $\vec{k}_1 = \sin(\theta) \times \cos(\varphi)$, $\vec{k}_2 = \sin(\theta) \times \sin(\varphi)$, and $\vec{k}_3 = \cos(\theta)$ when using plane waves as acoustic stimulation source. The final step before running the simulation is to select the solver settings and the frequency range by selecting a minimum, maximum, and step value of frequency that will control the excitation frequency.

5.3 Vibrating sample magnetometer

A vibrating sample magnetometer (VSM) permits an in-depth study of the magnetic properties of materials, providing a recording of the $M - H$ hysteresis loops as well as an analysis of the magnetic

moment of the samples (ΔM), which characterizes the magnetic interactions in particulate media [213, 214]. The ΔM plot is defined by Eq.(5.10) [215]. The positive/negative ΔM s are usually interpreted in terms of magnetizing/demagnetizing-like interactions between ferromagnetic particles, as described later in this section.

$$\Delta M = m_{rs} - [2m_{IRM}(H) - m_{DCD}(-H)] \quad (5.10)$$

where m_{IRM} is the magnetic moment of the isothermal remanent magnetization (IRM) process at the corresponding applied H , m_{rs} is the remanent saturation magnetic moment, and m_{DCD} is the magnetic moment on the DC demagnetization (DCD) curve for the value $-H$.

To measure the magnetic properties of materials using a VSM, the sample is introduced in a constant magnetic field that induces a magnetisation to the sample. As the magnetised sample is vibrated, it introduces perturbations in the external magnetic field, which can be detected by a set of coils located around the sample. A basic scheme of the VSM is shown in Fig. 5.4.

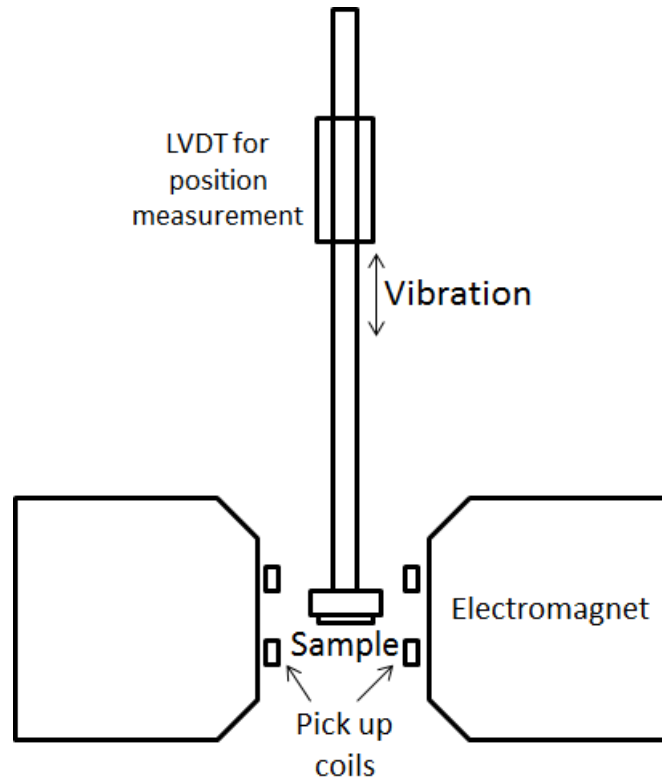


Fig. 5.4. Schematic representation of the vibrating sample magnetometer. The sample is placed between the two pick-up coils that detect the change of magnetic field when the sample is vibrated.

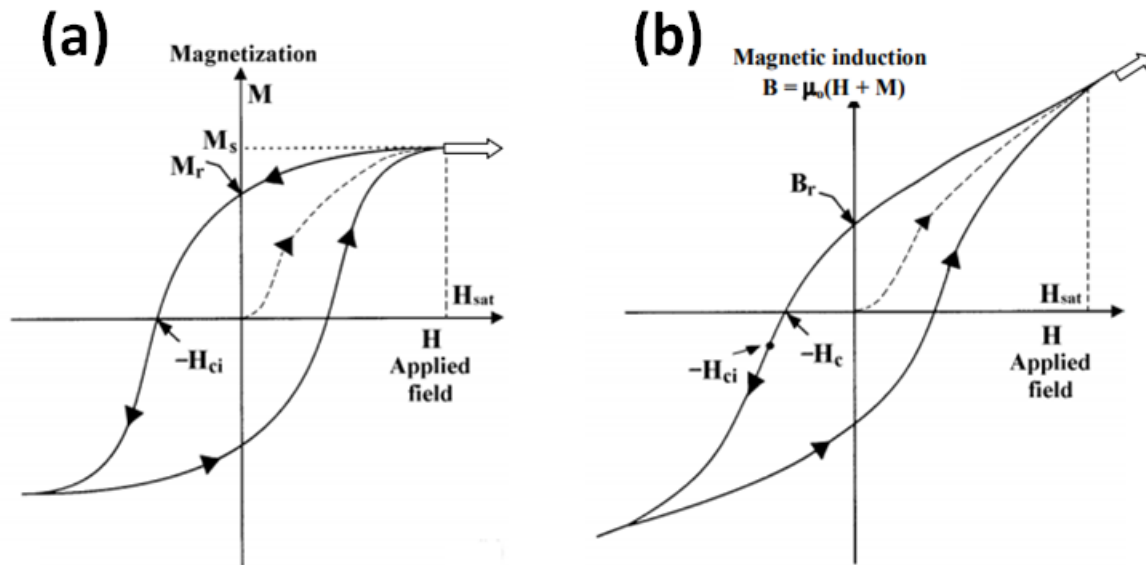


Fig. 5.5. Hysteresis loops for a ferromagnetic material. (a) Shows the $M - H$ plot, with remanent magnetisation at $H = 0$ and intrinsic coercive field denoted by H_{ci} (field at which magnetisation is reversed). M_r is the saturation magnetisation. (b) Shows the $B - H$ plot, with remanent induction B_r at $H = 0$ and coercive field H_c . Figure obtained from [216].

The magnetic hysteresis loop

VSM apparatus permit to trace magnetic hysteresis $M - H$ loops, which permit to determine the characteristic magnetic properties of the studied material such as its coercivity, remanent magnetisation, if the material is a hard or a soft magnet, and its magnetic behaviour. Notwithstanding, it is also possible to trace the $B - H$ hysteresis loops, which implicitly provide the same information as the $M - H$ loops, but generally lead to confusion of some parameters. One clear example of such confusion is the definition of the coercive field. As mentioned in Chapter 4, Section 4.2, the coercive field is defined as the field at which the magnetisation M changes its sign. This is referred in some works as the *intrinsic* coercive field, as it can be shown in Fig. 5.5, where H_c^{int} suffers a shift in the loop when recording $M - H$ loops than when recording $B - H$ loops.

Notwithstanding, the majority of soft magnetic materials present, albeit not identical, very similar values of coercive field and intrinsic coercive field. On the other hand, for hard magnetic materials these values are significantly different and non-equivalent.

One main difference can be observed between Fig. 5.5(a) and Fig. 5.5(b), which is that after saturation has been reached, the $M - H$ loop becomes a straight line with zero slope, whereas in the $B - H$ loop the slope of the line represents the magnetic susceptibility. A distinction between isotropic and anisotropic materials must be done at this point; whereas in the former the magnetisation process does not depend on the orientation of the sample, it does in the latter, firstly magnetising the easy axis at low values of H . In both cases once the magnetisation point has been reached, the magnetisation curves do not follow back the original trace (shown using dashed lines in Fig. 5.5). This phenomenon happens because of the irreversibility of the domain wall displacements and, therefore, when the external applied field is removed, the sample will retain some magnetisation due to the magnetic domains aligned with H . These values of magnetisation at $H = 0$ are defined as remanent magnetisation/induction. It is possible to discern between hard and soft magnetic materials using the area they enclose in the loop: whereas hard magnetic materials present a large hysteresis area, soft magnetic materials present a low hysteresis area.

IRM and DCD curves

VSM also permit to plot the IRM and DCD curves, as previously mentioned in this Section. Plotting these curves and following the adequate post-processing it is possible to determine the type of interaction within the magnetic material, which can be: (i) exchange coupled systems or (ii) dipolar coupled systems.

The IRM remanence curve is measured on a previously demagnetised material, which is then subjected to a positive applied field at which point the magnetisation is measured. The applied field is then removed and the remanent magnetisation is measured. The full cycle is then repeated increasing the applied H until saturation is reached. Hence, as IRM only accounts for remanent moments, the IRM curve represents the irreversible changes in magnetisation.

The DCD remanence curve is obtained by first saturating the material through a positive field and then applying a known reverse field at which the measurement is taken. The reverse field is then

reduced to zero and the remanent magnetisation is measured. The process is then repeated increasing the reverse field until negative saturation is reached. In both IRM and DCD curves the measurements taken in the applied field contain contributions from both reversible and irreversible magnetisation processes, while the remanent measurement contains only the irreversible contribution. Hence, using the IRM and DCD curves it is possible to quantitatively determine the relative importance of each stage of the reversal process.

Interaction effects in particulate magnetic materials can be studied by combining the IRM and DCD curves. One of the approximations providing such information is the Wohlfarth relation (Eq.(5.11)) [217], which was derived from an assembly of non-interacting single-domain particles with uniaxial anisotropy and with the magnetisation reversal happening by coherent rotation.

$$I_d(H) = 1 - 2I_r(H) \quad (5.11)$$

where $I_d(H)$ and $I_r(H)$ are the normalised DCD remanence curve and the normalised IRM curves, respectively. As Eq.(5.11) was determined from a non-interacting system, it can be concluded that any deviations in experimental data can be attributed to certain interactions. Researchers have modified the Wohlfarth model to explicitly account for interactions [214]:

$$\Delta I(H) = I_d(H) - [1 - 2I_r(H)] \quad (5.12)$$

Hence, the plot of $\Delta I(H)$ (usually referred to as ΔM) against H gives a characteristic curve of the interactions present in the system. Several conclusions can be obtained when the dominant reversal process is the same for both the IRM and the DCD curves. The first involves the sign of $\Delta I(H)$: when $\Delta I(H) > 0$ the interactions present on the system are such that they imply magnetising interactions, usually associated to exchange interactions. On the other hand, when $\Delta I(H) < 0$ the interactions present on the system are such that they imply demagnetising interactions, associated to materials like particle systems and particulate recording media where the coupling is dipolar in nature. Examples of positive and negative $\Delta I(H)$ curves are shown in Fig. 5.6.

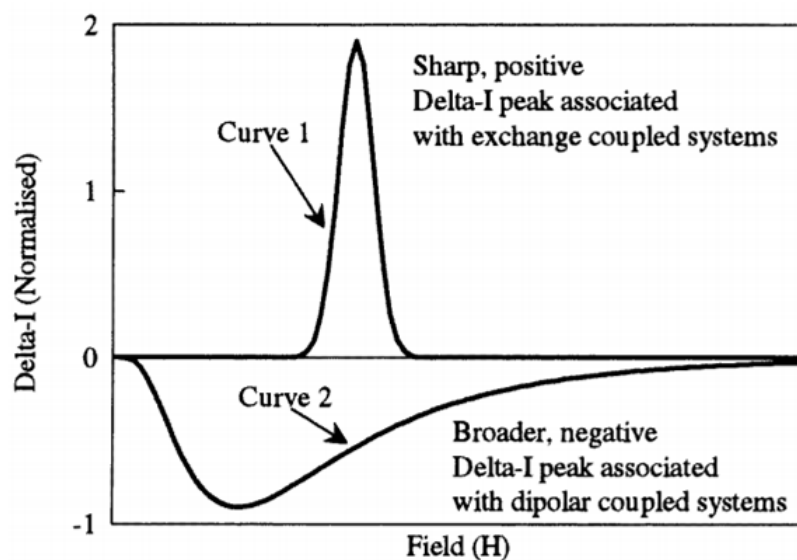


Fig. 5.6. Schematic $\Delta I(H)$ curves illustrating different coupling regimes. A sharp positive delta-I peak is associated with exchange coupled systems, whereas a broad, negative delta-I peak is attributed to dipolar coupled systems. Image obtained from [214].

5.4 Scanning electron microscopy

The morphological study of the synthesized particulate composites was carried out using SEM, which uses an electron beam instead of light in order to achieve smaller wavelengths and obtain higher resolution, providing a higher magnified image of the surface of the material. When an electron beam arrives at the surface of a sample, some electrons can penetrate into it. The depth of this penetration directly depends on the atomic number of the constituents of the specimen. The electrons lose their kinetic energy as they go deeper into the sample. In the zone of penetration, a certain number of interactions between the electrons of the beam and the atoms of the sample take place and, as a consequence, in this zone different types of signals can be detected, as shown in Fig. 5.7 [218].

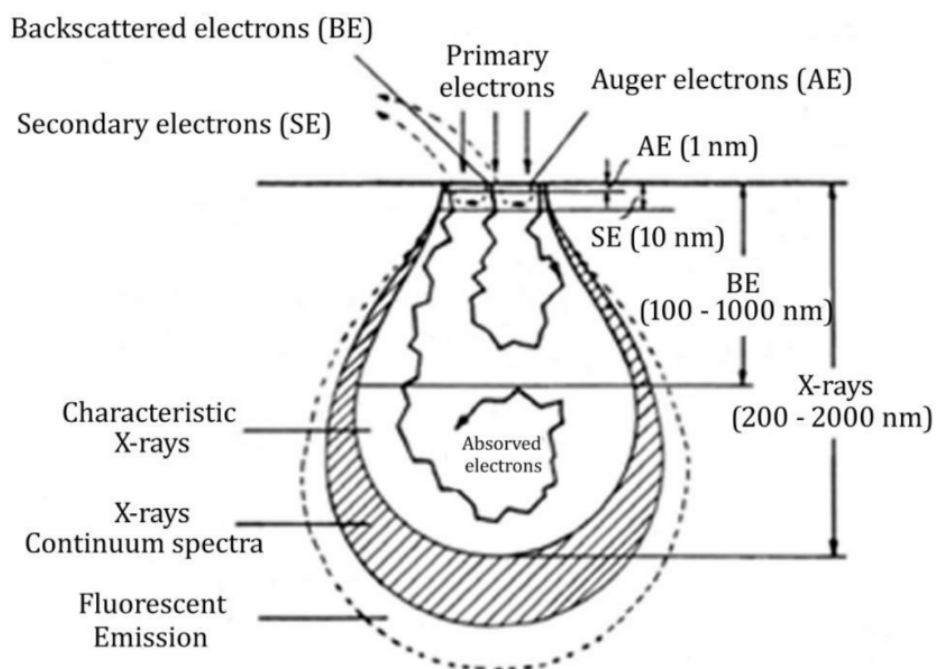


Fig. 5.7. Types of electrons and radiation generated inside the sample in a SEM when irradiated with an electron beam. The type of electrons and radiation determine the penetration depth of the electrons within the sample.

Chapter 6

Experimental results

6.1 Describing the locust's tympanum membrane: mathematical models

As described in Chapter 1, subsections 1.4.1 and 1.4.3 the locust tympanum membrane (TM) has been widely studied in recent years due to the physical phenomena taking place on it, allowing for directional sound detection and acoustic frequency selection at the micro-scale and assisting the animal in biological functions such as mating, swarming, or predator/prey localization [219].

Malkin *et al.* simulated the locust TM as a circular stiff plate of different thicknesses [77]. Malkin *et al.* studied where the mechanical waves are generated and where they travel to on the locust TM using COMSOL Multiphysics, and related the results to the existence of pretension in the locust TM. Their model provides explanation about generation and propagation of mechanical wave on the locust TM when stimulated by sound using specific mechanical properties found in the literature [77]. Hence, their finite analysis method does not provide a prediction of local stiffness variation, a mechanical property that seems to be key to understand the behaviour of the membrane. The mathematical models developed in this section do not only fit the obtained experimental data but they also allow determining some of the mechanical properties of the locust TM.

Generation of DPOAEs and presence of TWs on the TM have only been measured on the axis perpendicular to the plane described by the membrane, which will be referred to as z -axis (out-of-plane axis), either because of a technological limitations or the assumption that all the relevant physical

phenomena that take place on the locust TM uniquely happen in such direction.

Nevertheless, it seems obvious that a wave traveling within the plane that describes the membrane (xy -plane) with its amplitude of motion confined in the z -axis, a stretching (or pulling) of the membrane should also be observed, as a consequence, in-plane. This reasoning led some of the researchers in our group to study the mechanical behaviour of the locust TM in the xy -plane as a response to acoustic stimulation. To do so, they measured the motion of the locust TM along several transect lines using the 3D LDV. Each transect contained 13 points, measuring all the physiologically relevant attachment points of the locust TM (see Fig. 6.1). The direction of the transects was chosen in accordance to the measurements ran by Windmill *et al.* [11].

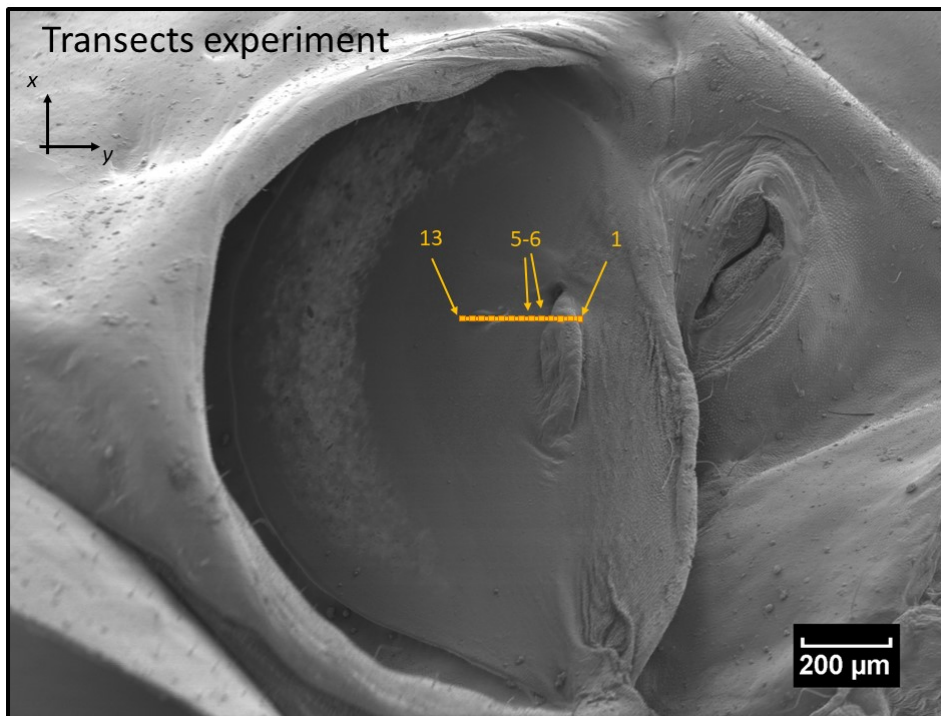


Fig. 6.1. SEM image of the locust TM (as presented in Fig. 1.8) in which the studied transect, composed by 13 points, is shown in yellow. The points were named correspondingly to their proximity to the FB, number 1 being the closest one and 13 the one located further away of it. SEM image obtained by Prof. James Windmill, published in his work *Tympanal travelling waves in migratory locusts* [11] and edited by Roger Domingo-Roca. Transect line representation in accordance to measurements performed by our colleagues.

The results showed that the motion of the measured points presents a coupled behaviour in the y -direction, leading to the reasoning that the mechanical motion of the significant attachment points of the locust TM (pyriform vesicle, PV and folded body, FB), as well as the in-between points, can be

described using the theory of coupled oscillators. The first step of this work is to fully understand the origin of the biological phenomena originated on the locust TM using the aforementioned measurements. To do so, several mathematical models based on the coupled oscillator theory were developed.

6.1.1 Mathematical models

The results obtained from the transect experiment performed by our colleagues (Fig. 6.1) showed that the individual scanned points of the membrane oscillate following the theory of coupled oscillators. Hence, to obtain a better understanding of their mechanical behaviour, three mathematical models were developed: (i) an unforced model (*i.e.* without considering a driving force) where three oscillators with the same mass are coupled using three springs with the same stiffness, (ii) three coupled oscillators with the same mass and connected by springs of the same stiffness where a driving force and damping are considered, and (iii) the addition of a fourth spring in model *ii*. These have been developed to demonstrate that the simpler the model is, the less accurate the results are. Furthermore, as the mathematical model includes more terms and takes more realistic consideration (such as a driving acoustic term and damping), relevant parameters such as the stiffness of the membrane can be obtained more accurately.

Unforced approximation

In the first mathematical approximation it was considered that the motion of the TM was not forced by any external force. In order to simplify, and as a starting point, three main points were considered (the PV, the FB, and an in-between oscillator corresponding to the membrane) with oscillators connected between them, as shown in Fig. 6.2.

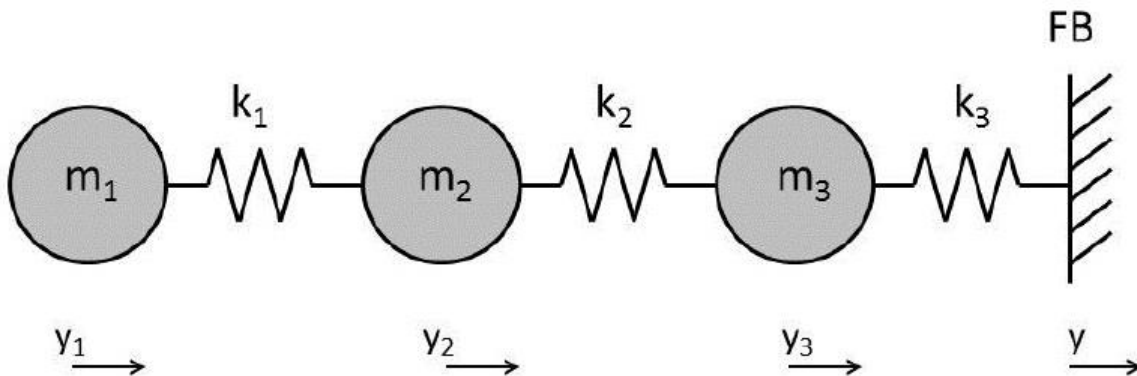


Fig. 6.2. Simplified mechanical representation of the locust's tympanum membrane. The three masses represent different experimental points and the fixed point (represented by a vertical line with diagonal smaller lines) represents the FB.

These three points, as well as the boundary conditions, were chosen in complete agreement with the experimental results obtained by our colleagues: the FB, a part of the thick membrane, was chosen as a fixed point as it was observed that at high frequencies its motion was several orders of magnitude lower than the rest of the points of the transect. Furthermore, the other three points (oscillators of the model) were chosen to be the nearest point to the PV (point 13 in Fig. 6.1), the PV itself, and a the middle point between the FB and the PV. The final consideration was that the oscillators were constrained in the x -direction and could only move in the y -direction, as the motion in the x -axis was experimentally observed to be much smaller than in the y -axis.

It was assumed, for simplicity, that all the oscillators have the same mass and that the stiffness across the membrane is uniform, leading to:

$$\begin{cases} m_1 = m_2 = m_3 \equiv m \\ k_1 = k_2 = k_3 \equiv k \end{cases} \quad (6.1)$$

As shown in Fig. 6.2, y_1 , y_2 , and y_3 correspond to the displacement of masses m_1 , m_2 , and m_3 , respectively. Thus, the equations of motion of the system are described by Eq.(6.2).

$$\begin{cases} m_1 \ddot{y}_1 = -k_1(y_1 - y_2) \\ m_2 \ddot{y}_2 = -k_2(y_2 - y_1) - k_2(y_2 - y_3) \\ m_3 \ddot{y}_3 = -k_3(y_3 - y_2) \end{cases} \quad (6.2)$$

which can be rewritten, for convenience, as:

$$\begin{cases} m\ddot{y}_1 + k(y_1 - y_2) = 0 \\ m\ddot{y}_2 + k(y_2 - y_1) + k(y_2 - y_3) = 0 \\ m\ddot{y}_3 + k(y_3 - y_2) = 0 \end{cases} \quad (6.3)$$

where \ddot{y}_i ($i = 1, 2, 3$) is the second derivative of displacement with respect to time of the i th oscillator.

The general solution of the system shown in Eq.(6.3) is given by:

$$\mathbf{T}\ddot{\vec{y}}_i + \mathbf{V}\vec{y}_i = 0 \quad (6.4)$$

This general solution is obtained when applying the Euler-Lagrange equations in the Lagrangian mechanics theory¹. The boldfaced quantities (\mathbf{T} , and \mathbf{V}) represent matrices, while the arrowed characters

¹Lagrangian mechanics is used to study the motion of discrete particles that have a finite number of degrees of freedom.

The reader can refer to several books to get familiarised with such a theory. *Hamiltonian and Lagrangian Mechanics* [220], for example.

refer to vectors. \mathbf{T} and \mathbf{V} stand for the matrices of the kinetic and potential energy, respectively, and in this case are given by:

$$\mathbf{T} = \begin{pmatrix} m & 0 & 0 \\ 0 & m & 0 \\ 0 & 0 & m \end{pmatrix}, \quad \mathbf{V} = \begin{pmatrix} k & -k & 0 \\ -k & 2k & -k \\ 0 & -k & k \end{pmatrix} \quad (6.5)$$

As \mathbf{T} is a diagonal matrix, $\mathbf{T}^{1/2}$ is a diagonal matrix which elements are the square roots of the characteristic values of \mathbf{T} .

$$\mathbf{T}^{1/2} = \begin{pmatrix} \sqrt{m} & 0 & 0 \\ 0 & \sqrt{m} & 0 \\ 0 & 0 & \sqrt{m} \end{pmatrix}, \quad \mathbf{T}^{-1/2} = \begin{pmatrix} 1/\sqrt{m} & 0 & 0 \\ 0 & 1/\sqrt{m} & 0 \\ 0 & 0 & 1/\sqrt{m} \end{pmatrix} \quad (6.6)$$

Hence, it is possible to write:

$$\mathbf{T}^{-1}\mathbf{V} = \mathbf{T}^{-1/2}(\mathbf{T}^{-1/2}\mathbf{V}\mathbf{T}^{-1/2})\mathbf{T}^{1/2} \quad (6.7)$$

Where $\mathbf{T}^{-1}\mathbf{V}$ is written as a product of symmetrical matrices ($\mathbf{T}^{-1/2}\mathbf{V}\mathbf{T}^{-1/2}$ and $\mathbf{T}^{\pm 1/2}$) that can be orthogonally diagonalised. The diagonalization of $\mathbf{T}^{-1/2}\mathbf{V}\mathbf{T}^{-1/2} \equiv \mathbf{W}$ must be now considered, where \mathbf{W} is a symmetric and positive matrix. Being U the orthogonal matrix that diagonalizes \mathbf{W} :

$$U\mathbf{W}U^{-1} = \mathbf{W}_D, \quad U^{-1} = U^T \quad (6.8)$$

It is then possible to rewrite:

$$\mathbf{T}^{-1}\mathbf{V} = \mathbf{T}^{-1/2}U^T\mathbf{W}_DU\mathbf{T}^{1/2} \quad (6.9)$$

Therefore \mathbf{W} is given by:

$$\mathbf{W} = \mathbf{T}^{-1/2}\mathbf{V}\mathbf{T}^{-1/2} = \begin{pmatrix} k/m & -k/m & 0 \\ -k/m & 2k/m & -k/m \\ 0 & -k/m & k/m \end{pmatrix} \quad (6.10)$$

Thus. Eq.(6.4) becomes:

$$\begin{pmatrix} \ddot{y}_1 \\ \ddot{y}_2 \\ \ddot{y}_3 \end{pmatrix} + \begin{pmatrix} k/m & -k/m & 0 \\ -k/m & 2k/m & -k/m \\ 0 & -k/m & k/m \end{pmatrix} \begin{pmatrix} y_1 \\ y_2 \\ y_3 \end{pmatrix} = \begin{pmatrix} 0 \\ 0 \\ 0 \end{pmatrix} \quad (6.11)$$

The solution to Eq.(6.11) will be given by diagonalising \mathbf{W} :

$$\det(\mathbf{W} - \omega^2\mathbf{I}) = 0 \quad (6.12)$$

where \mathbf{I} is the identity matrix in a three-dimensional space. Thus:

$$\det(\mathbf{W} - \omega^2 \mathbf{I}) = \begin{vmatrix} k/m - \omega^2 & -k/m & 0 \\ -k/m & 2k/m - \omega^2 & -k/m \\ 0 & -k/m & k/m - \omega^2 \end{vmatrix} = (k - m\omega^2)^2(2k - m\omega^2) - 2k^2 = 0 \quad (6.13)$$

From Eq.(6.13) it is possible to obtain the characteristic values (*eigenvalues*, ω_i) of the system described in Fig. 6.2, which are given by:

$$\begin{cases} \omega_1 = 0 \\ \omega_2 = \sqrt{k/m} \\ \omega_3 = \sqrt{3k/m} \end{cases} \quad (6.14)$$

Using the eigenvalues of the system it is possible to determine the characteristic vectors (*eigenvectors*, ξ_i) that describe the motion of the oscillators:

$$(\mathbf{W} - \omega^2 \mathbf{1}) \cdot \vec{\xi}_i = \vec{0} \quad (6.15)$$

Solving Eq.(6.15):

$$\vec{\xi}_1 = \frac{1}{\sqrt{3}} \begin{pmatrix} 1 \\ 1 \\ 1 \end{pmatrix} ; \quad \vec{\xi}_2 = \frac{1}{\sqrt{2}} \begin{pmatrix} 1 \\ 0 \\ -1 \end{pmatrix} ; \quad \vec{\xi}_3 = \frac{1}{\sqrt{6}} \begin{pmatrix} -1 \\ 2 \\ -1 \end{pmatrix} \quad (6.16)$$

As the eigenvectors are already orthogonal it is possible to use them to build the matrix \mathbf{U} that diagonalises \mathbf{W} :

$$\mathbf{U} = \begin{pmatrix} 1/\sqrt{3} & 1/\sqrt{3} & 1/\sqrt{3} \\ 1/\sqrt{2} & 0 & -1/\sqrt{2} \\ -1/\sqrt{6} & 2/\sqrt{6} & -1/\sqrt{6} \end{pmatrix} \quad (6.17)$$

Therefore:

$$\mathbf{U}\mathbf{W}\mathbf{U}^\top = \begin{pmatrix} 0 & 0 & 0 \\ 0 & k/m & 0 \\ 0 & 0 & 3k/m \end{pmatrix} \quad (6.18)$$

Which finally allows to finish the diagonalisation process:

$$\mathbf{T}^{-1}\mathbf{V} = \mathbf{T}^{-1/2}\mathbf{W}\mathbf{T}^{1/2}$$

$$\mathbf{A}\mathbf{T}^{-1}\mathbf{V}\mathbf{A}^{-1} = \mathbf{W}_D$$

$$\mathbf{A} = \mathbf{U}\mathbf{T}^{1/2}$$

$$\mathbf{A} = \begin{pmatrix} \sqrt{m/3} & \sqrt{m/3} & \sqrt{m/3} \\ \sqrt{m/2} & 0 & \sqrt{m/2} \\ -\sqrt{m/6} & \sqrt{2m/3} & -\sqrt{m/6} \end{pmatrix}, \quad \mathbf{A}^{-1} = \begin{pmatrix} \sqrt{1/3m} & \sqrt{1/2m} & -\sqrt{1/6m} \\ \sqrt{1/3m} & 0 & \sqrt{2/3m} \\ \sqrt{1/3m} & -\sqrt{1/2m} & -\sqrt{1/6m} \end{pmatrix} \quad (6.19)$$

Therefore, the equations of motion of each one of the oscillators are determined from the expression:

$$\ddot{\vec{y}}_i + \mathbf{A}^{-1} \mathbf{W}_D \mathbf{A} \vec{y} = \vec{0} \quad (6.20)$$

And introducing the generalized coordinates $\vec{\eta}_i = \mathbf{A} \vec{y}_i$, Eq.(6.20) becomes:

$$\ddot{\vec{\eta}} + \mathbf{W}_D \vec{\eta} = \vec{0} \quad (6.21)$$

$$\begin{cases} \ddot{\eta}_1(t) + \omega_1^2 = 0 \\ \ddot{\eta}_2(t) + \omega_2^2 = 0 \\ \ddot{\eta}_3(t) + \omega_3^2 = 0 \end{cases} \quad (6.22)$$

The generalised coordinates are a linear combination of the initial coordinates, which are normal modes of the system (*i.e.* they present an independent temporal evolution). The harmonic solutions to these equations are combinations of sinusoidal functions and are given by [221]:

$$\boxed{\eta_i(t) = \eta_i(0) \cos(\omega_j t) + \frac{\dot{\eta}_i(0)}{\omega_i} \sin(\omega_j t)} \quad (6.23)$$

From Eq.(6.23) it is possible to obtain the equations of motion in generalized coordinates:

$$\begin{cases} \eta_1(t) = \eta_1(0) + \dot{\eta}_1(0)t \\ \eta_2(t) = \eta_2(0) \cos(\omega_2 t) + \frac{\dot{\eta}_2(0)}{\omega_2} \sin(\omega_2 t) \\ \eta_3(t) = \eta_3(0) \cos(\omega_3 t) + \frac{\dot{\eta}_3(0)}{\omega_3} \sin(\omega_3 t) \end{cases} \quad (6.24)$$

Notice from Eq.(6.23) that the normal modes are expressed as a function of the initial conditions $\eta_i(0)$ and $\dot{\eta}_i(0)$, which correspond to the initial position and velocity, respectively, of each oscillator. To obtain the coupled equations of motion $y_i(t)$ as a function of the initial conditions $y_i(0)$ and $\dot{y}_i(0)$ it is necessary to undo the transformation $\eta_i = \mathbf{A} y_i$.

$$\vec{y}(t) = \mathbf{A}^{-1} \vec{\eta}(t) \leftrightarrow \eta(0) = \mathbf{A} \vec{y}(0), \quad \dot{\eta}(0) = \mathbf{A} \dot{\vec{y}}(0) \quad (6.25)$$

$$\begin{cases} y_1(t) = \sqrt{1/3m} \eta_1(t) + \sqrt{1/2m} \eta_2(t) - \sqrt{1/6m} \eta_3(t) \\ y_2(t) = \sqrt{1/3m} \eta_1(t) + \sqrt{2/3m} \eta_3(t) \\ y_3(t) = \sqrt{1/3m} \eta_1(t) - \sqrt{1/2m} \eta_2(t) - \sqrt{1/6m} \eta_3(t) \end{cases} \quad (6.26)$$

where:

$$\begin{cases} \eta_1(t) = \sqrt{\frac{m}{3}} [y_1(t) + y_2(t) + y_3(t)] \\ \eta_2(t) = \sqrt{\frac{m}{2}} [y_1(t) - y_3(t)] \\ \eta_3(t) = \sqrt{\frac{m}{6}} [-y_1(t) + 2y_2(t) - y_3(t)] \end{cases} \quad (6.27)$$

Thus, combining Eq.(6.24), Eq.(6.26), and Eq.(6.27), the final equations of motion of the system can be obtained.

$$\begin{aligned} y_1(t) &= \frac{1}{3} \{y_1(0) + y_2(0) + y_3(0) + [\dot{y}_1(0)\dot{y}_2(0) + \dot{y}_3(0)] t\} + \\ &+ \frac{1}{2} \left\{ [y_1(0) - y_3(0)] \cos(\omega_2 t) + \frac{1}{\omega_2} [\dot{y}_1(0) - \dot{y}_3(0)] \sin(\omega_2 t) \right\} + \\ &- \frac{1}{6} \left\{ [-y_1(0) + 2y_2(0) - y_3(0)] \cos(\omega_3 t) + \frac{1}{\omega_3} [-\dot{y}_1(0) + 2\dot{y}_2(0) - \dot{y}_3(0)] \sin(\omega_3 t) \right\} \end{aligned} \quad (6.28)$$

$$\begin{aligned} y_2(t) &= \frac{1}{3} \{y_1(0) + y_2(0) + y_3(0) + [\dot{y}_1(0)\dot{y}_2(0) + \dot{y}_3(0)] t\} + \\ &+ \frac{1}{3} \left\{ [-y_1(0) + 2y_2(0) - y_3(0)] \cos(\omega_3 t) + \frac{1}{\omega_3} [-\dot{y}_1(0) + 2\dot{y}_2(0) - \dot{y}_3(0)] \sin(\omega_3 t) \right\} \end{aligned} \quad (6.29)$$

$$\begin{aligned} y_3(t) &= \frac{1}{3} \{y_1(0) + y_2(0) + y_3(0) + [\dot{y}_1(0)\dot{y}_2(0) + \dot{y}_3(0)] t\} + \\ &- \frac{1}{2} \left\{ [y_1(0) - y_3(0)] \cos(\omega_2 t) + \frac{1}{\omega_2} [\dot{y}_1(0) - \dot{y}_3(0)] \sin(\omega_2 t) \right\} + \\ &- \frac{1}{6} \left\{ [-y_1(0) + 2y_2(0) - y_3(0)] \cos(\omega_3 t) + \frac{1}{\omega_3} [-\dot{y}_1(0) + 2\dot{y}_2(0) - \dot{y}_3(0)] \sin(\omega_3 t) \right\} \end{aligned} \quad (6.30)$$

Therefore, following this model, the mechanical motion on the locust TM described in the y -direction can be expressed as a linear combination of Eq.(6.28), Eq.(6.29), and Eq.(6.30). The reader must consider that Eq.(6.28), Eq.(6.29), and Eq.(6.30) are reasonably simplified when introducing the initial conditions for displacement and velocity given by the experimental results.

$$y_1(0) = \dot{y}_1(0) = \dot{y}_2(0) = \dot{y}_3(0) = 0 \quad (6.31)$$

Leading to:

$$y_1(t) = \frac{y_2(0)}{3} [1 - \cos(\omega_3 t)] + y_3(0) \left[\frac{1}{3} - \frac{1}{2} \cos(\omega_2 t) + \frac{1}{6} \cos(\omega_3 t) \right] \quad (6.32)$$

$$y_2(t) = \frac{y_2(0)}{3} [1 + 2 \cos(\omega_3 t)] + \frac{y_3(0)}{3} [1 - \cos(\omega_3 t)] \quad (6.33)$$

$$y_3(t) = \frac{y_2(0)}{3} [1 - \cos(\omega_3 t)] + y_3(0) \left[\frac{1}{3} + \frac{1}{2} \cos(\omega_2 t) + \frac{1}{6} \cos(\omega_3 t) \right] \quad (6.34)$$

Since $\omega_2 = \sqrt{k/m}$, and $\omega_3 = \sqrt{3k/m}$, it is possible to express Eq.(6.32), Eq.(6.34), and Eq.(6.32) as:

$$y_1(t) = \frac{y_2(0)}{3} [1 - \cos(\sqrt{3}\omega_2 t)] + y_3(0) \left[\frac{1}{3} - \frac{1}{2} \cos(\omega_2 t) + \frac{1}{6} \cos(\sqrt{3}\omega_2 t) \right] \quad (6.35)$$

$$y_2(t) = \frac{y_2(0)}{3} [1 + 2 \cos(\sqrt{3}\omega_2 t)] + \frac{y_3(0)}{3} [1 - \cos(\sqrt{3}\omega_2 t)] \quad (6.36)$$

$$y_3(t) = \frac{y_2(0)}{3} [1 - \cos(\sqrt{3}\omega_2 t)] + y_3(0) \left[\frac{1}{3} + \frac{1}{2} \cos(\omega_2 t) + \frac{1}{6} \cos(\sqrt{3}\omega_2 t) \right] \quad (6.37)$$

Forced approximation

The second approximation considers a more realistic case in which the oscillators representing the membrane are forced by an external force, \vec{F} , the acoustic field. Adding this extra parameter into the model implies some changes in the solving process, as a damping parameter γ must be also introduced.

Hence, Eq.(6.4) becomes:

$$\mathbf{T}\ddot{\vec{y}} + 2\Gamma\mathbf{T}\dot{\vec{y}} + \mathbf{V}\vec{y} = \vec{F} \quad (6.38)$$

where $\gamma = 2\Gamma\mathbf{T}$ (for simplicity) is the damping acting on the system, and \vec{F} is chosen to be:

$$\vec{F} = F_0 \cos(\omega_F t) \begin{pmatrix} 1 \\ 1 \\ 1 \end{pmatrix} \quad (6.39)$$

where ω_F is the frequency of the exciting acoustic field and \vec{F} indicates the amplitude (F_0) and direction of the exciting force. Factorising \mathbf{T} and introducing the change of base that diagonalises $\mathbf{T}^{-1}\mathbf{V}$, Eq.(6.38) becomes:

$$\mathbf{TA}^{-1} \left[\mathbf{A}\ddot{\vec{y}} + 2\Gamma\mathbf{A}\dot{\vec{y}} + \mathbf{W}_D\mathbf{A}\vec{y} \right] = \vec{F} \quad (6.40)$$

Multiplying by \mathbf{AT}^{-1} and taking $\vec{\eta} = \mathbf{A}\vec{y}$:

$$\ddot{\vec{\eta}} + 2\Gamma\dot{\vec{\eta}} + \mathbf{W}_D\vec{\eta} = \mathbf{AT}^{-1}\vec{F}_0 \cos(\omega_F t) \quad (6.41)$$

The solutions to Eq.(6.41) have both a transitory and a stationary component. The stationary solutions of the normal modes are given by [221].

$$\eta_{j[s]}(t) = a_j^{(e)} \cos(\omega_F t) + a_j^{(i)} \sin(\omega_F t) \quad (6.42)$$

The parameters $a_j^{(e)}$ and $a_j^{(i)}$ are given by [221]:

$$a_j^{(e)} = F_0 \frac{\omega_j^2 - \omega_F^2}{(\omega_j^2 - \omega_F^2)^2 + (2\Gamma\omega_F)^2}, \quad a_j^{(i)} = F_0 \frac{2\Gamma\omega_F}{(\omega_j^2 - \omega_F^2)^2 + (2\Gamma\omega_F)^2} \quad (6.43)$$

Thus, the stationary equations of motion of the oscillators in this model are given by:

$$y_{[s]}(t) = \sum_{j,k,l=1}^n (\mathbf{A}^{-1}) \frac{(\omega_j^2 - \omega_F^2) \cos(\omega_F t) + 2\Gamma\omega_F \sin(\omega_F t)}{(\omega_j^2 - \omega_F^2)^2 + (2\Gamma\omega_F)^2} \mathbf{AT}^{-1} \vec{F} \quad (6.44)$$

where $q_{[s]}$ is the stationary solution. From Eq.(6.44) it is possible to determine the stationary equations of motion described by the system:

$$y_1^{(F)}(t) = \frac{F_0 \cos(\omega_F t)}{m} \left[\frac{(\omega_1^2 - \omega_F^2) \cos(\omega_F t) + 2\Gamma\omega_F \sin(\omega_F t)}{(\omega_1^2 - \omega_F^2)^2 + (2\Gamma\omega_F)^2} \right] \quad (6.45)$$

$$y_2^{(F)}(t) = \frac{F_0 \cos(\omega_F t)}{m} \left[\frac{(\omega_2^2 - \omega_F^2) \cos(\omega_F t) + 2\Gamma\omega_F \sin(\omega_F t)}{(\omega_2^2 - \omega_F^2)^2 + (2\Gamma\omega_F)^2} \right] \quad (6.46)$$

$$y_3^{(F)}(t) = \frac{F_0 \cos(\omega_F t)}{m} \left[\frac{(\omega_3^2 - \omega_F^2) \cos(\omega_F t) + 2\Gamma\omega_F \sin(\omega_F t)}{(\omega_3^2 - \omega_F^2)^2 + (2\Gamma\omega_F)^2} \right] \quad (6.47)$$

The superscript (F) refers to *forced*. As in subsection 6.1.1 the mechanical deflection of the membrane can be expressed as a linear combination of the individual stationary equations of motion of the different oscillators Eq.(6.45), Eq.(6.46), and Eq.(6.47), using the proportionality constant a' , b' , and c' .

$$\boxed{y_f^F(t) = a'y_1^{(F)}(t) + b'y_2^{(F)}(t) + c'y_3^{(F)}(t)} \quad (6.48)$$

6.1.2 Variations of the model

As it must have been noted by the reader at this point, the two mathematical models presented to describe the locust TM motion are the most simple ones someone could think of. Such models can be effectively improved by simply changing some of the parameters that describe the system, such as the stiffness of the membrane and the mass of the oscillators the most important ones. Nevertheless, using three different values of k ($k_1 \neq k_2 \neq k_3$) and m ($m_1 \neq m_2 \neq m_3$) add further difficulties when solving the system that describes the motion of the TM.

Another obvious modification to the system would be adding more oscillators, therefore adding extra terms of both kinetic and potential energy into the system, as we are trying to solve in a discrete way a problem described by a continuous system. By adding more oscillators, therefore, the solution of the problem will be more accurate. Nevertheless, the more oscillators the more complex it will be to analytically solve the problem. As an example, adding an extra term of potential energy (spring) connected into the left-hand side end of oscillator 1 (and assuming uniform values of both mass and stiffness) the equations of motion that describe the new system are:

$$\begin{cases} m\ddot{y}_1 + k(2y_1 - y_2) = 0 \\ m\ddot{y}_2 + k(-y_1 + 2y_2 - y_3) = 0 \\ m\ddot{y}_3 + k(2y_3 - y_2) = 0 \end{cases} \quad (6.49)$$

Eq.(6.49) therefore implies a change of the characteristic modes of the system and, therefore, the behaviour of the oscillators determined by the characteristic vectors. Following the same process as in the previous

cases, it is possible to determine the *eigenmodes* of the new system, which are given by:

$$\begin{cases} \omega_1 = \sqrt{(2 + \sqrt{2})k/m} \\ \omega_2 = \sqrt{2k/m} \\ \omega_3 = \sqrt{(2 - \sqrt{2})k/m} \end{cases} \quad (6.50)$$

which lead to the equations of motion:

$$\begin{aligned} y_1(t) &= \frac{1}{4} \left[y_1(0) - \sqrt{2}y_2(0) + y_3(0) \right] \cos(\omega_1 t) - \frac{1}{2} \left[-y_1(0) + y_3(0) \right] \cos(\omega_2 t) + \\ &+ \frac{1}{4} \left[y_1(0) + \sqrt{2}y_2(0) + y_3(0) \right] \cos(\omega_3 t) \end{aligned} \quad (6.51)$$

$$y_2(t) = \left[\frac{\sqrt{2}y_2(0) - y_1(0) - y_3(0)}{2\sqrt{2}} \right] \cos(\omega_1 t) + \left[\frac{y_1(0) + \sqrt{2}y_2(0) + y_3(0)}{2\sqrt{2}} \right] \cos(\omega_3 t) \quad (6.52)$$

$$\begin{aligned} y_2(t) &= \frac{1}{4} \left[y_1(0) - \sqrt{2}y_2(0) + y_3(0) \right] \cos(\omega_1 t) + \frac{1}{2} \left[-y_1(0) + y_3(0) \right] \cos(\omega_2 t) + \\ &+ \frac{1}{4} \left[y_1(0) + \sqrt{2}y_2(0) + y_2(0) \right] \cos(\omega_3 t) \end{aligned} \quad (6.53)$$

If the same considerations are taken into account in the forced model, the resulting equations of motion are given by:

$$\begin{aligned} y_1^{(F)}(t) &= \frac{F_0 \cos(\omega_F t)}{4m} \frac{(\omega_1^2 - \omega_F^2) \cos(\omega_F t) + 2\Gamma\omega_F \sin(\omega_F t)}{(\omega_1^2 - \omega_F^2)^2 + (2\Gamma\omega_F)^2} + \\ &+ \frac{F_0 \cos(\omega_F t)}{2m} \frac{(\omega_2^2 - \omega_F^2) \cos(\omega_F t) + 2\Gamma\omega_F \sin(\omega_F t)}{(\omega_2^2 - \omega_F^2)^2 + (2\Gamma\omega_F)^2} + \\ &+ \frac{F_0 \cos(\omega_F t)}{4m} \frac{(\omega_3^2 - \omega_F^2) \cos(\omega_F t) + 2\Gamma\omega_F \sin(\omega_F t)}{(\omega_3^2 - \omega_F^2)^2 + (2\Gamma\omega_F)^2} \end{aligned} \quad (6.54)$$

$$\begin{aligned} y_2^{(F)}(t) &= -\frac{F_0 \cos(\omega_F t)}{2\sqrt{2}m} \frac{(\omega_1^2 - \omega_F^2) \cos(\omega_F t) + 2\Gamma\omega_F \sin(\omega_F t)}{(\omega_1^2 - \omega_F^2)^2 + (2\Gamma\omega_F)^2} + \\ &+ \frac{F_0 \cos(\omega_F t)}{2\sqrt{2}m} \frac{(\omega_3^2 - \omega_F^2) \cos(\omega_F t) + 2\Gamma\omega_F \sin(\omega_F t)}{(\omega_3^2 - \omega_F^2)^2 + (2\Gamma\omega_F)^2} \end{aligned} \quad (6.55)$$

$$\begin{aligned} y_3^{(F)}(t) &= -\frac{F_0 \cos(\omega_F t)}{4m} \frac{(\omega_1^2 - \omega_F^2) \cos(\omega_F t) + 2\Gamma\omega_F \sin(\omega_F t)}{(\omega_1^2 - \omega_F^2)^2 + (2\Gamma\omega_F)^2} + \\ &- \frac{F_0 \cos(\omega_F t)}{2m} \frac{(\omega_2^2 - \omega_F^2) \cos(\omega_F t) + 2\Gamma\omega_F \sin(\omega_F t)}{(\omega_2^2 - \omega_F^2)^2 + (2\Gamma\omega_F)^2} + \\ &+ \frac{F_0 \cos(\omega_F t)}{4m} \frac{(\omega_3^2 - \omega_F^2) \cos(\omega_F t) + 2\Gamma\omega_F \sin(\omega_F t)}{(\omega_3^2 - \omega_F^2)^2 + (2\Gamma\omega_F)^2} \end{aligned} \quad (6.56)$$

Further modifications of the model that would lead to a more accurate prediction of the motion of the locust TM should include a two-dimensional (2D) array of oscillators and springs defining an array of 2D coupled oscillators (see Fig. 6.3).

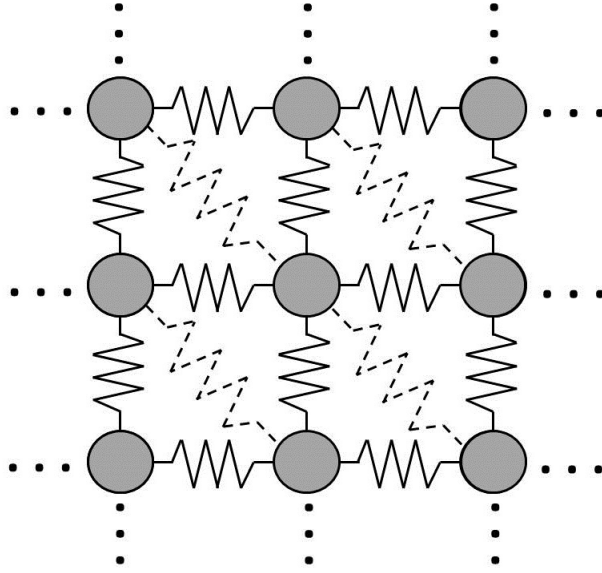


Fig. 6.3. Sketch of a 2D array of coupled oscillators that describe the membrane. The oscillators and the springs could present, respectively, different values of m and k . As a further consideration, one could also assume that the oscillators are not only connected to their first neighbours (as denoted by continuous springs), but also to their second-second order neighbours by springs of the same/different k (as denoted by dashed springs).

6.1.3 Understanding the generation of DPOAEs

DPOAEs are generated by non-linear systems and can be mathematically explained by solving the Duffing equation, as a single Duffing oscillator can produce intermodulation when simultaneously excited by two frequencies f_1 and f_2 . The detailed solution to a single Duffing oscillator can be found in several books [51, 55], but it is also presented in Appendix A.

A single Duffing oscillator driven by one unique frequency will not display intermodulation, as it is mathematically and physically impossible by definition. Therefore, as a starting point, the case in which a specific point of the membrane (*i.e.* a unique oscillator) was driven by two different frequencies ($f_1 \neq f_2$) of different amplitudes ($F_1 \neq F_2$) at the same time was studied. The simplest case is that in which the non-linear term is controlled by a dimensionless parameter ϵ (<1).

$$m\ddot{y} + c\dot{y} + ky + \beta\epsilon y^3 = \epsilon [\alpha F_1 \cos(f_1 t) + \beta F_2 \cos(f_2 t)] \quad (6.57)$$

where m , k , c , f_1 , and f_2 are the mass, stiffness, damping coefficient, and external driving frequencies, respectively, and α and β are mathematical parameters that control the degree of non-linearity of the system as well as the driving forces (*i.e.* α and β are either 0 or 1). Thus, it is easy to see that when the system is not excited by any external force (*i.e.* $\alpha = \beta = 0$) the equation of a damped unforced oscillator

is recovered. Considering now an external force acting on that same oscillator (*i.e.* $\alpha = 1$, $\beta = 0$, and in the specific case in which $\epsilon = 1$), the equation of motion of a driven oscillator is then recovered. In this case it must be noted that ϵ does not uniquely control the degree of non-linearity of the oscillator but it also has an impact on the amplitude of motion of the driving force, as it is also present in the right-hand side of Eq.(6.57). Now, if this single Duffing oscillator is driven by two different frequencies at the same time ($\alpha = \beta = 1$), its equation of motion becomes:

$$m\ddot{y} + c\dot{y} + ky + \epsilon y^3 = \epsilon [F_1 \cos(f_1 t) + F_2 \cos(f_2 t)] \quad (6.58)$$

It must be further noted that ϵ is weak enough not to cause chaotic motion [222]. The solution to Eq.(6.58) is given by a linear combination of the cosine of the two driving frequencies [222, 223].

$$y(t) = C_1 \cos(f_1 t + \delta_1) + C_2 \cos(f_2 t + \delta_2) \quad (6.59)$$

where the constants C_i , $i = 1, 2$ depend on ω_i and a transfer function similar to that present in the damped oscillator. Therefore, expanding the non-linear term present in Eq.(6.58) it is easy to see that intermodulation products appear:

$$\begin{aligned} y^3 &\propto [\cos(f_1 t + \delta_1) + \cos(f_2 t + \delta_2)]^3 \propto \quad (6.60) \\ &\propto \cos(f_1 t + \delta_1) + \cos(f_2 t + \delta_2) + \cos(3f_1 t + 3\delta_1) + \\ &+ \cos(3f_2 t + 3\delta_2) + \cos[(2f_1 + f_2)t + 2\delta_1 + \delta_2] + \\ &+ \cos[(2f_2 + f_1)t + 2\delta_2 + \delta_1] + \cos[(2f_1 - f_2)t + 2\delta_1 - \delta_2] + \\ &+ \cos[(2f_2 - f_1)t + 2\delta_2 - \delta_1] \end{aligned}$$

As previously stated in this Chapter, in highly non-linear systems the representation of the amplitude of motion of the oscillator as a function of the excitation frequency can reveal interesting features of the system, as well as corroborating a specific behaviour. To determine such a relationship, Eq.(6.57) must be solved using the method of Poincaré-Lindstedt, consisting in the removal of secular terms of the equation (see in detail in Appendix A).

It has been experimentally shown that the optimum frequency relationship that permits a maximal generation of DPOAEs in the locust is that in which $f_1/f_2 = 1.1$. Hence, using this feature, considering that $F_1 \approx F_2 \equiv F$, introducing the variable $\theta \equiv f_1 t$, and recalling $f_1 \equiv \omega$, it is easy to see that Eq.(6.58) becomes:

$$\omega^2 y'' + \gamma \omega y' + \frac{k}{m} y + \frac{\epsilon y^3}{m} = \frac{\epsilon F}{m} [\cos(\theta + \delta) + \cos(1.1\theta + \delta)] \quad (6.61)$$

where $\gamma = c/m$, $y'' \equiv d^2/d\theta^2$, and $y' = d/d\theta$. Using the perturbation method (considering the terms proportional up to the first order of ϵ) and assuming a transformation of the independent variable such as:

$$\begin{cases} y(\theta) = y_0(\theta) + \epsilon y_1(\theta) \\ \omega(\theta) = \omega_0 + \epsilon \omega_1 \end{cases} \quad (6.62)$$

with the initial conditions becoming $y_0(0) = A$, $y_1(0) = y_0'(0) = y_1'(0) = 0$. Solving the system (see Appendix B):

$$\omega^2 = \frac{1}{4} + \frac{\epsilon F}{m\gamma^2} \left[1 \pm \sqrt{1 + \frac{2\gamma^2}{A} - \frac{3mA^2\gamma^2}{2F}} \right] \quad (6.63)$$

The last mathematical model was developed to try to fully understand the generation of DPOAEs on the locust TM. In this last model, the mathematical parameter ϵ is considered not to only control the degree of non-linearity of the system but also the damping mechanism governing it. In this case, the equation of motion of the oscillator is given by:

$$\omega^2 y'' + \epsilon \gamma \omega y' + \frac{k}{m} y + \frac{\beta \epsilon y^3}{m} = \frac{\epsilon F}{m} [\alpha \cos(\theta + \delta) + \beta \cos(1.1\theta + \delta)] \quad (6.64)$$

In this case, the solutions when the system is not forced and when it is driven by a single frequency remain the same as in the previous case. Hence, it is interesting to study this system when driven by two different frequencies at the same time. The detailed solution is presented in Appendix B.

$$\omega^2 = \frac{k}{m} + \epsilon \left[\frac{3kA^2}{4m} \pm \sqrt{\frac{k}{m} \left(\frac{F^2}{kmA^2} - \gamma^2 \right)} \right] \quad (6.65)$$

Even though this model seems to be enough to explain the generation of DPOAEs on the locust TM (following from Eq.(6.61)), it must also describe the measured mechanical in-plane motion which, as it has been previously described, revealed a coupled behaviour. Thus, in order to obtain a mathematical model accurate enough that permits the detailed study of the locust TM, it is necessary to introduce coupling into the Duffing equation. Here two Duffing coupled oscillators are presented, as it is a system that can be analytically solved and provide accurate equations of motion. If more oscillators are added into the system, the solution becomes very difficult to determine analytically and numerical methods must be used. Let's consider two Duffing coupled oscillators as shown in Fig. 6.4.

The equations of motion of the system shown in Fig. 6.4 are given by:

$$\begin{cases} m \frac{d^2 y_1}{dt^2} + \epsilon \frac{dy_1}{dt} + \epsilon y_1^3 + k(y_2 - y_1) - \epsilon F_0 \cos(\omega t + \delta) = 0 \\ m \frac{d^2 y_2}{dt^2} + \epsilon \frac{dy_2}{dt} + \epsilon y_2^3 + k(y_2 - y_1) \end{cases} \quad (6.66)$$

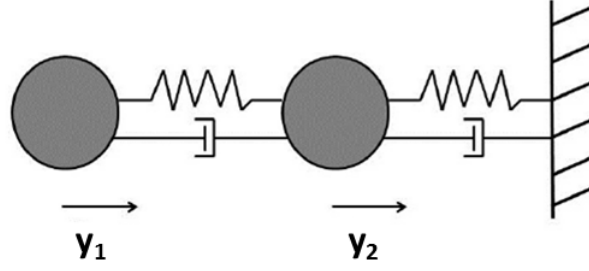


Fig. 6.4. Sketch of two Duffing coupled oscillators. This model needs to include both a dashpot and a spring between each oscillator to account for viscous effects.

The solution to this system is given by (see details in Appendix C):

$$y_1^{(0)}(\theta) = \frac{1}{2} \left\{ y_1^{(0)}(0) [1 + \cos(\lambda_1 \theta)] + y_2^{(0)} [-1 + \cos(\lambda_1 \theta)] \right\} \quad (6.67)$$

$$y_2^{(0)}(\theta) = \frac{1}{2} \left\{ y_1^{(0)} [1 - \cos(\lambda_1 \theta)] + y_2^{(0)} [1 + \cos(\lambda_1 \theta)] \right\} \quad (6.68)$$

where $y_i^{(0)}$ with $i = 1, 2$ are the initial conditions of the system and λ_1 is the first characteristic vector of the system. Taking $y_1^{(0)} = A$ and $y_2^{(0)} = B$ it is also possible to obtain the frequency response of the system. Considering $\delta = 0$:

$$\omega^2 = 1 + \frac{\epsilon}{32k(A+B)} (15A^3 - 3A^2B - 3AB^2 + 15B^3 - F_0) \quad (6.69)$$

and considering the phase of the driving force (*i.e.* $\delta \neq 0$):

$$\omega^2 = 1 + \frac{3\epsilon}{16m\lambda_1^2} (5A^2 - 6AB + 5B^2) \pm \frac{2\epsilon F_0}{m\lambda_1^2(A+B)} \sqrt{1 - \frac{\lambda_1^2 (A+B)^2}{4F_0^2}} \quad (6.70)$$

6.1.4 Application of the mathematical models

Once the mechanical behaviour of the locust TM was properly understood and mathematically described, mathematical models were used to fit the obtained experimental data from the transects (Fig. 6.1). It must be noted, firstly, that the experimental data must be treated before applying the mathematical models, as it was observed in the 3D LDV that the motion of the locust TM presents both a transitory and a stationary response (see Fig. 6.5) and the focus remains in the latter one as the former only lasts for a few milliseconds.

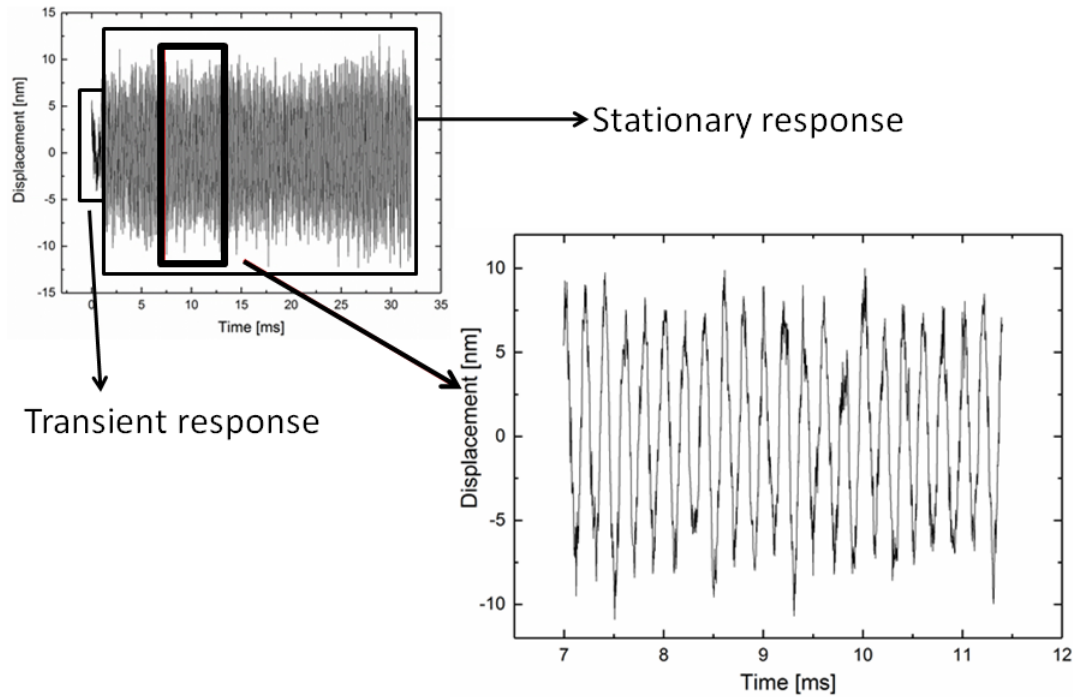


Fig. 6.5. The top-left graph shows the mechanical deflection of the locust TM in the time domain of point 1 (P1) of the studied transects (as shown in Fig. 6.1) when driven at 5 kHz.

As is shown in Fig. 6.1, four points on the locust TM were mainly studied; point 13 (P13) corresponds to the PV, points 5 and 6 (P5 and P6) are points on the membrane located between the FB and the PV, a region in which the membrane experiments a thinning of cuticle, and point 1 (P1) corresponds to the start of the FB. In all the models a fixed region of the membrane corresponding to the thickest part of the FB was considered, as experimental data revealed that such a region deflects several orders of magnitude less than the rest of the membrane. Nevertheless, the region of the FB in contact with the region in which the membrane experiments a thinning was measured to significantly move. Therefore, according to Fig. 6.2, P13, P5 and P6, and P1 can be described by $y_1(t)$, $y_2(t)$, and $y_3(t)$ respectively.

Hence, using the unforced coupled model described in Section 6.1.1 the mechanical deflection measured on the locust TM under single-tone stimulation (at a driving frequency of 5 kHz and at a sound pressure level of 70 dB SPL) was fitted and shown in Fig. 6.6. This was done explicitly to show how this first model cannot be used to describe in an accurate manner the motion of the locust TM as this is a forced system.

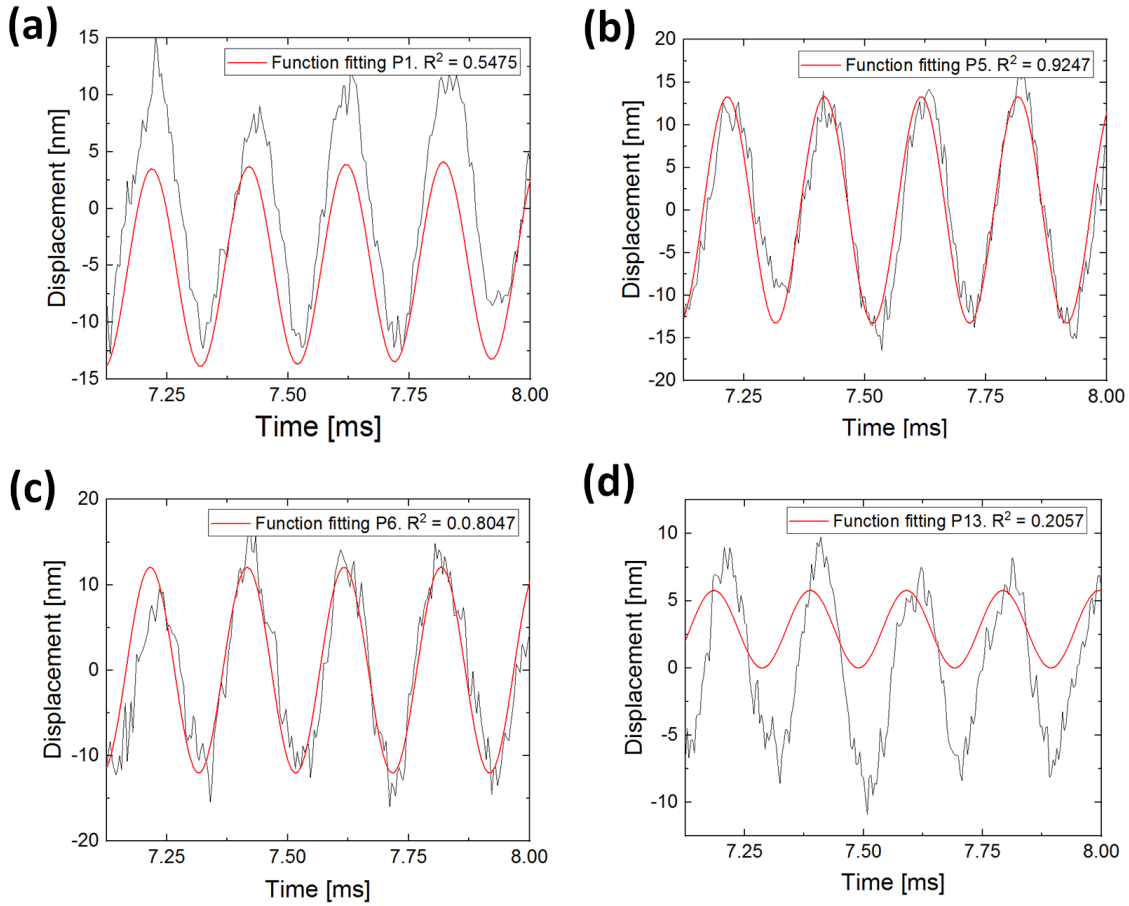


Fig. 6.6. (a)-(d) Show the fitting of the experimental data using the unforced coupled mathematical model described previously in this Chapter for P1, P5, P6, and P13 respectively. The fitting was done over 4.5 ms, but here only 4 cycles are shown over 0.875 ms.

The fitting details can be observed in Table 6.1.

Point	Mass [kg]	Fitting parameter c	R^2	k [N/m]
1	$3.9 \cdot 10^{-9}$	31334.53	0.5475	3.83
5	$3.2 \cdot 10^{-10}$	18098.82	0.9247	0.09828
6	$3.2 \cdot 10^{-10}$	18099.37	0.8047	0.1048
13	$3.0 \cdot 10^{-9}$	31042	0.2057	2.89

Table 6.1. Fitting details when using the unforced coupled mathematical model.

From the fitting parameters it is possible to obtain an approximation of the local stiffness of the locust TM, as $c = \omega_2 = \sqrt{k/m}$. Nevertheless, it must be noted that even though P5 and P6 are well fitted using the unforced coupled theory, P1 and P13 present a low R^2 value (the fitting parameter that determines the accuracy of the fitting function with the experimental data).

The fitting functions corresponding to the forced model (as described in 6.1.1) are shown in Fig. 6.7 and the fitting parameters are shown in Table 6.2.

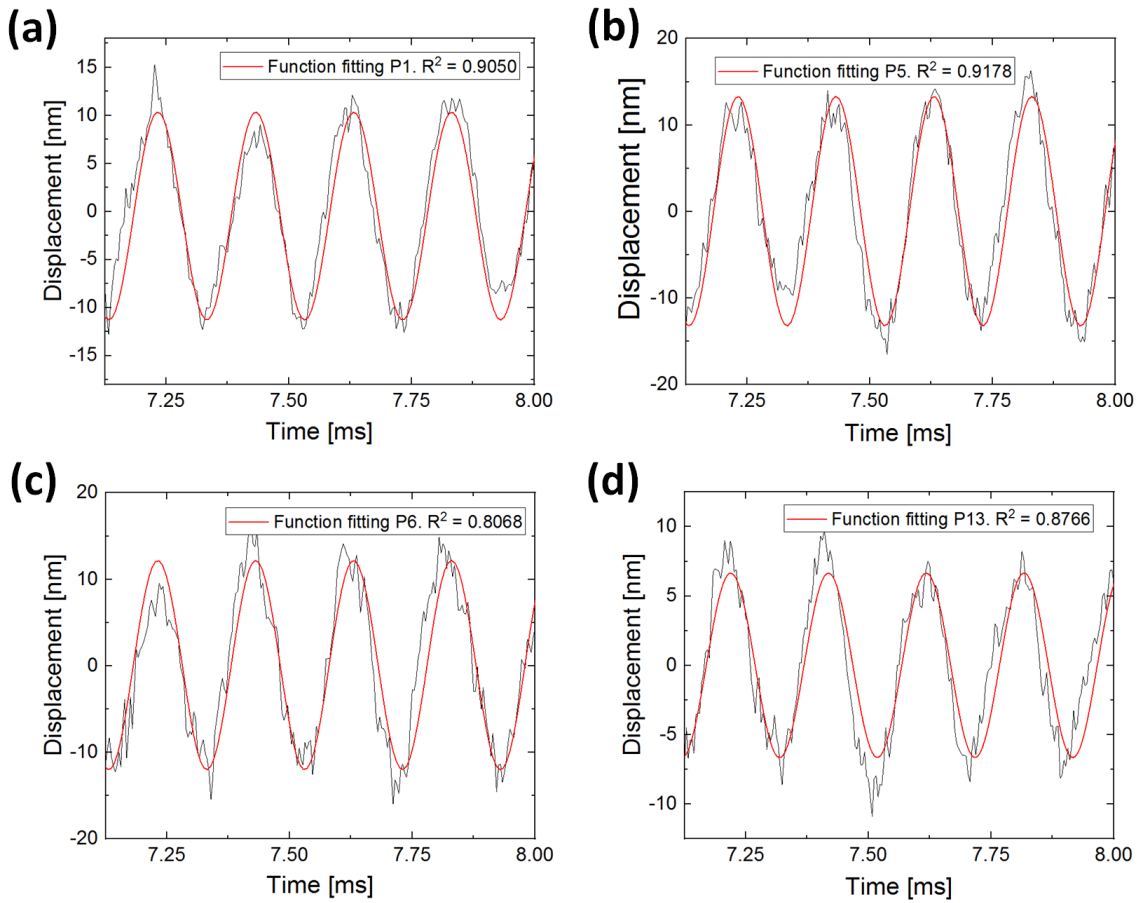


Fig. 6.7. (a)-(d) Show the fitting of the experimental data using the forced coupled mathematical model described previously in this Chapter for P1, P5, P6, and P13 respectively. The measurements were obtained at 5 kHz. The fitting was done over 4.5 ms, but here only 4 cycles are shown over 0.875 ms.

Even though this model gives better R^2 values it presents two main inconveniences: the most obvious one is that because $\omega_1 = 0$ it is not possible to obtain an estimation of the local stiffness of the PV. The second inconvenience is that the fitting parameter c is negative in all the studied cases, which gives a good fitting output but it does not have any physical sense as c has been chosen to be ω_2 and ω_3 for P5 and P6, and P1 respectively, which cannot be negative. Thus, a variation of the forced mathematical model must be applied in order to have not only a good fitting of the experimental data but also realistic parameters that allow to determine the mechanical properties of the system. Therefore, the equations obtained in the variation presented in Section 6.1.2 (addition of an extra term of potential energy) were applied to fit the experimental data (see Fig. 6.8 and Table 6.3).

Point	Mass [kg]	Fitting parameter c	R^2	k [N/m]
1	$3.9 \cdot 10^{-9}$	-14700.49	0.9050	0.2810
5	$3.2 \cdot 10^{-10}$	-15831.68	0.9178	0.0802
6	$3.2 \cdot 10^{-10}$	-15898.18	0.8068	0.08088
13	$3.0 \cdot 10^{-9}$	N/A	0.8766	N/A

Table 6.2. Fitting details when using the unforced coupled mathematical model.

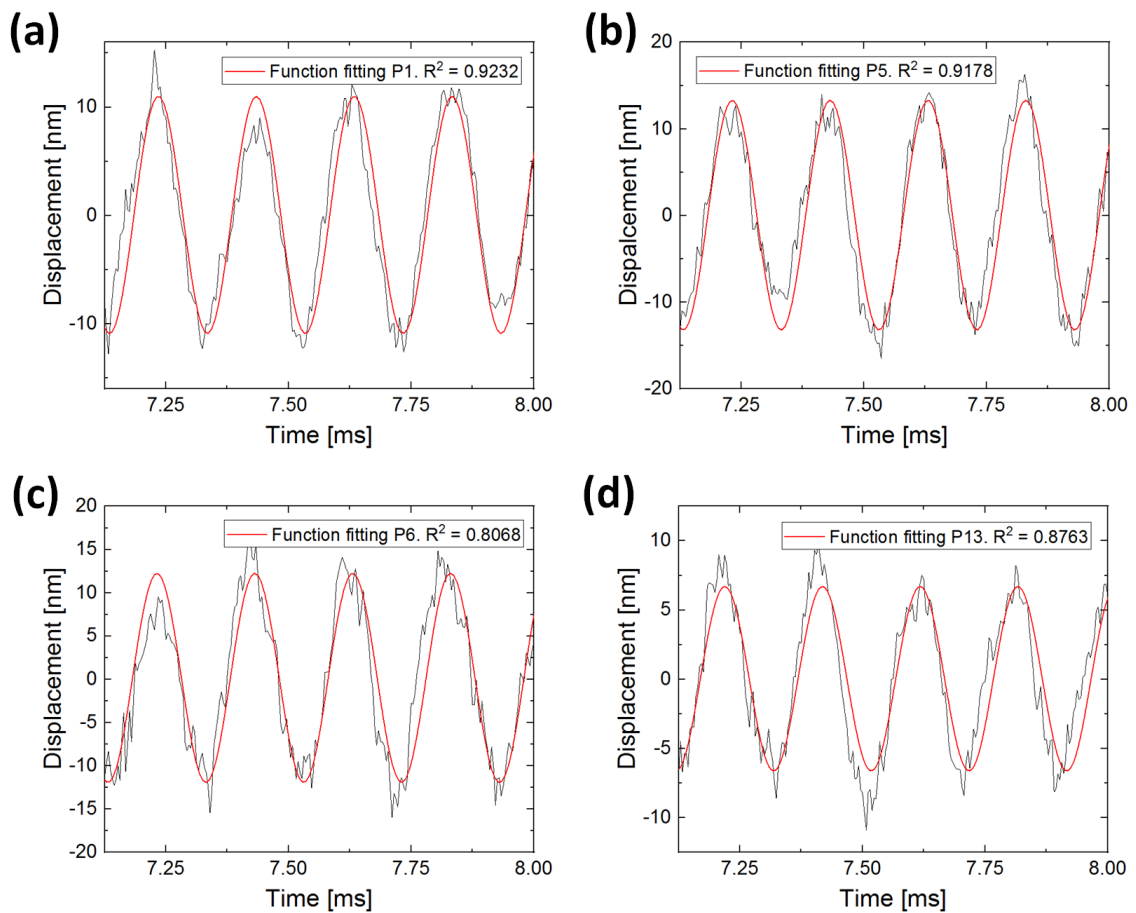


Fig. 6.8. (a)-(d) Show the fitting of the experimental data using the forced coupled complex mathematical model described previously in this Chapter for P1, P5, P6, and P13 respectively. The fitting was done over 4.5 ms, but here only 4 cycles are shown over 0.875 ms.

Point	Mass [kg]	Fitting par. c	Fitting par. e	Fitting par. f	R^2	k [N/m]
1	$3.9 \cdot 10^{-9}$	$8.1151 \cdot 10^8$	$2.7154 \cdot 10^8$	$-2.6573 \cdot 10^8$	0.9232	0.7283
5	$3.2 \cdot 10^{-10}$	$1.0051 \cdot 10^9$	$9.9532 \cdot 10^8$	N/A	0.9178	0.3189
6	$3.2 \cdot 10^{-10}$	$4.6116 \cdot 10^9$	$1.5997 \cdot 10^9$	N/A	0.8068	0.6530
13	$3.0 \cdot 10^{-9}$	$9.2773 \cdot 10^9$	$-5.5496 \cdot 10^9$	$9.2677 \cdot 10^9$	0.8763	27.8073

Table 6.3. Fitting details when using the forced complex coupled mathematical model.

It must be noted that adding an extra spring (*i.e.* an extra term of potential energy) in the mathematical model has a huge impact when determining the local stiffness of the system. In this case, as the equations of motion of each oscillator present a dependency in multiple ω_i ($i = 1, 2, 3$), the local stiffness has been worked out as an average of all the possible real values. In this case $c = \omega_1^2 = (2 + \sqrt{2})k/m$, $e = \omega_2^2 = 2k/m$, and $f = \omega_3^2 = (2 - \sqrt{2})k/m$.

The spring stiffness constants estimated from the mathematical models lead to values of stiffness of the locust TM from about 0.9104 kPa on the FB and 1.1123 GPa on the PV, whereas in the in-between points the stiffness of the membrane takes values of 12.76 kPa and 26.12 kPa in regions of the same dimensions as the PV. These results are in accordance with the experimental results obtained by Vincent and Wegst [224] in which they determined that stiffness can vary from 1 kPa in highly hydrated regions of the membrane (*i.e.* those containing a higher amount of endocuticle) up to 20 GPa in isotropic regions of the membrane when measuring parallel to the chitin orientation in the tibia flexor (*i.e.* regions with extremely low content of endocuticle). Their study suggested that stiffness hugely depends on the amount of hydrated cuticle present in the measured area (concentrated in the endocuticle), leading to softer structures as more endocuticle is present in them. Considering the analysis of the membrane performed by Stephen & Bennet-Clark [41] in which they observed a higher presence of endocuticle in the FB, it makes sense that this structure presents lower values of stiffness than the PV, and the in-between points (which are mainly composed by mesocuticle) are stiffer than the FB but less stiff than the PV. Furthermore, it has been shown that ageing has a huge impact on the mechanical properties of the tissues of the locust, as it has been reported that deposition of endocuticle takes place as the locust gets older, leading to a decrease of stiffness of the structure [224].

It has been presented in the previous section that a single Duffing oscillator could generate intermodulation on the locust TM, which uniquely depends on the non-linear term governing the system. Nevertheless, when applying the Duffing model on the locust TM, it must be coupling several Duffing oscillators as the experimental data revealed a coupled behaviour. Thus, the production of DPOAEs was studied by using a coupled Duffing system (see Fig. 6.9). It must be noted that a single Duffing oscillator does not reproduce the so-called skeleton curve (see Appendix B) when driven by two different frequencies at the same time, and this is why the parameter ϵ must be taken into consideration to control not only the degree of non-linearity of the system but also its damping mechanism (see Appendices B and C). Again, it must be noted that DPOAEs are generated in all the Duffing systems described in this thesis in which the oscillator(s) is(are) driven by two frequencies at the same time as their generation depends on the non-linear term, which is proportional to y^3 . As the solution to the system depends on both driving frequencies, it is easy to see that DPOAEs will always appear due to the expansion of the non-linear term. Thus, it is necessary that the proposed mathematical model also reproduces the characteristic skeleton curve of a Duffing oscillator, as it has been measured to happen on the locust TM.

Fig. 6.9 confirm the presence of intermodulation in the locust TM (Fig. 6.9a and b), and its theoretical prediction (Fig. 6.9c). The experimental data was obtained by one of our colleagues where frequencies of 10 kHz and 11 kHz were played, measuring single points of the physiologically relevant regions of the locust TM. The simulations results were obtained solving the relevant equations using Mathematica.

6.2 Development of 3D-printable materials

When developing photocurable 3D-printing materials there are three main parameters to take into consideration: (i) the oligomers that compose the polymeric structure, (ii) the species that will start the photopolymerization process (photoinitiator), and (iii) the UV blocker that will avoid light scattering and over-curing during the 3D-printing process. For all the photo-curable composite materials developed during this thesis, the photoinitiator Phenylbis(2,4,6-trimethylbenzoyl)phosphine oxide, commonly known as Irgacure 819, has been used (which molecular structure and absorption spectrum can be seen in Fig. 6.10(a) and Fig. 6.10(b), respectively). Irgacure 819 has been selected because it has been shown

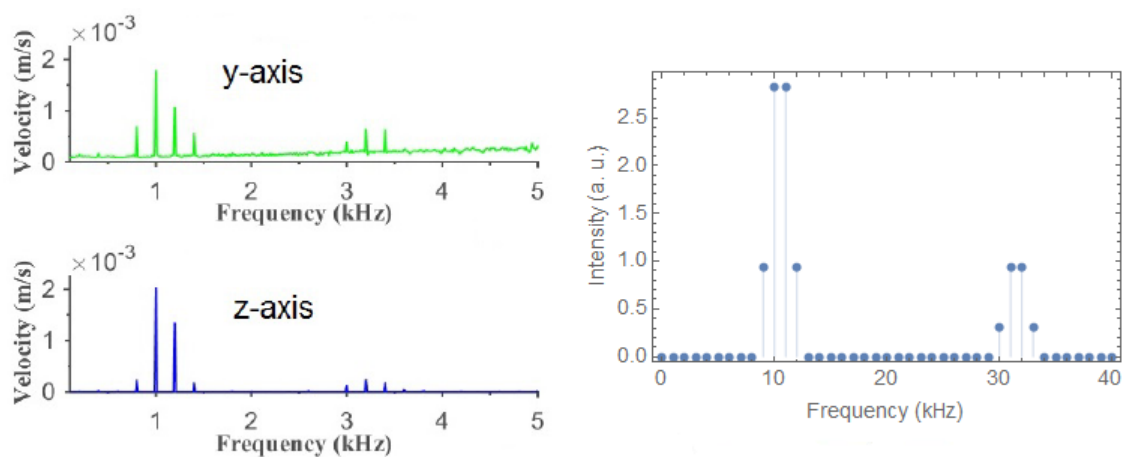


Fig. 6.9. The left-hand-side image shows the response of the locust membrane near the PV in both y - and z -axes when excited at 1 and 1.1 kHz at the same time. It can be observed that maximum velocity happens at the driving frequencies. Furthermore, generation of harmonics and distortion product otoacoustic emissions can also be observed. The right-hand-side graph shows the simulation obtained from the proposed mathematical model described in this section.

to present good photoinitiation activity when exposed to UV light (as the UV LED wavelength of the ASIGA PicoPlus 27 3D Printer is of 385 nm and the absorption spectrum maximum of Irgacure 819 is in the range of 397 nm) as well as it has been reported that it follows a photoinitiation process that does not require accelerators such as tertiary amines, simplifying the production process [225].

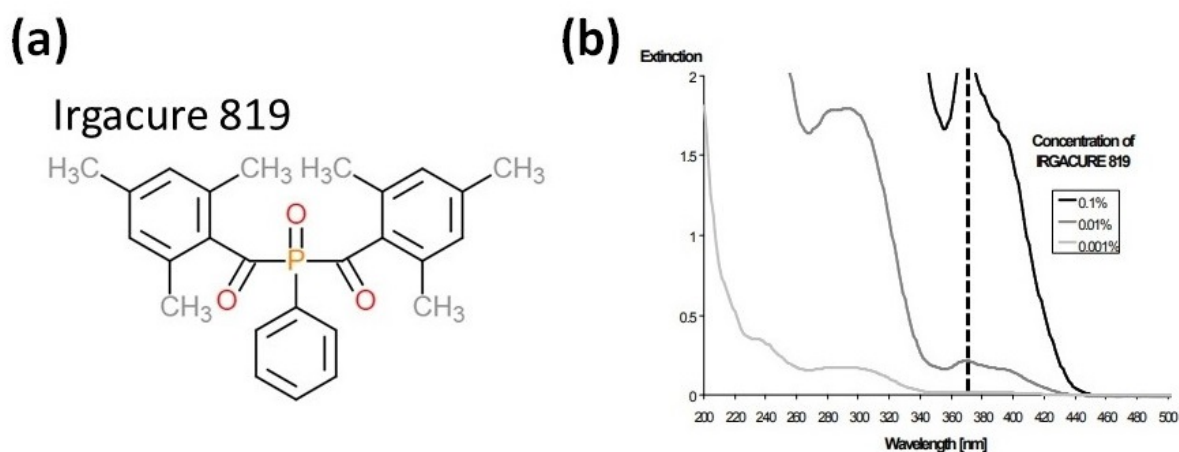


Fig. 6.10. (a) Shows the molecular structure of Irgacure 819 and (b) shows its light absorption spectrum with the peak highlighted with a black dashed line. Image obtained from [226].

Two main polymeric photoreactive materials were used during the course of this thesis to prove that materials with sensibly different mechanical properties can be 3D-printed using a same 3D printer

by simply modifying some of the 3D-printing settings. The 3D-printable developed materials are poly(ethylene glycol) diacrylate (PEGDA) and bisphenol-A ethoxylate dimethacrylate (BEMA), which synthesis process is described later in this Section. These materials were later modified by embedding functional NPs within the polymeric matrices in order to provide functionality (piezoelectricity and magnetism) after 3D-printing.

When introducing NPs within the polymeric matrix, apart from a photoinitiator, the presence of a UV blocker is also necessary when developing photocurable 3D-printable materials in order to avoid Mie scattering (which takes place when the size of NPs is of the same order of magnitude than the wavelength of the UV light, $d_{NP} \approx \lambda_{UV}$) and, therefore, ensure a good 3D-printing resolution [227]. Hence, using SUDAN I as a dye is a good choice as it can be easily dissolved within liquid polymer matrices. SUDAN I's azobenzene moieties are light-sensitive and are responsible of blocking UV light, preventing light scattering and therefore improving 3D-printing resolution. Moreover, by accurately controlling the amount and type of dye, it is possible to finely tune the mechanical properties of the resulting composite due to the azobenzene² moieties' light-responsive properties [111], arising from the π -electrons in the p -orbitals of the sp^2 hybridized nitrogen atoms. Azo moieties can be used in polymer matrices as both dispersed un-linked molecules and constituting unit polymer chains [228].

6.2.1 Synthesis of 3D-printable materials

Synthesis of 3D-printable BEMA and PEGDA

3D-printable BEMA was developed by mixing BEMA with Irgacure 819 at 1 wt%. The mixture was left under magnetic stirring for 24 hours to ensure cross-linking of the polymer chains. 0.2 wt% of SUDAN I was then added with respect to BEMA and the whole mixture was put into a THINKY AER-250 mechanical mixer, mixing for 3 minutes at 1500 rpm and de-foaming it for 2 minutes at 1200 rpm. Finally, the mixture was indirectly sonicated in a water bath for 5 minutes before 3D-printing. A control sample was made using a screen-printing technique with layer thickness of 50 μm , using an R&K control coater, curing every layer under UV light for 1 minute using an Intertronics IUUV250 Hand Lamp (Intertronics, Kidlington, England, UK). The exact same process was followed using PEGDA instead of BEMA.

²Azobenzene is a molecule with the ability to undergo reversible transformation between two isomers with specific absorption spectra. Both linear and cyclic isomerization can be obtained from azo moieties.

Non-3D-printable BEMA and PEGDA, Irgacure 819, and SUDAN I were all purchased from Sigma Aldrich (Gillingham, England, UK). Furthermore, PlasWhite was also used at the start of the project, a commercially available 3D-printing polymer provided by ASIGA.

Synthesis of piezoelectric and magnetic 3D-printable particulate composites

To develop the piezoelectric polymer-based particulate composite material, a similar process to that described in the previous subsection was followed. In this case, a 0.1 wt% of SUDAN I was used with respect to the polymeric matrix (for both BEMA and PEGDA) as a 0.2 wt% loading was observed to block the majority of UV photons, resulting in poor 3D-printing resolution or even the complete failure of 3D-printing process. BaTiO₃ NPs (100 nm, 200 nm, and 500 nm) were added into the 3D-printable polymeric matrix at different wt% reaching a maximum loading of 75 wt%. Even though high wt% loadings are possible to achieve, this is a parameter that needs to be optimised in order to obtain a good balance between 3D-printing accuracy and piezoelectric output signal, as discussed later in this Chapter (see subsection 6.2.4). Before 3D-printing, control samples were built using the same process as described in the previous section.

The same process was followed to produce the 3D-printable magnetic-particulate composite material. In this case, Fe₃O₄ NPs of 50-100 nm size were embedded within the polymeric matrices at different wt% loadings (25, 50, and 75 wt%) using a THINKY AER-250 mechanical mixer, mixing the composite for 3 minutes at 1500 rpm, and de-foaming it for 2 minutes at 1200 rpm. After mechanical mixing, samples of the different magnetic composites were made using the screen printing technique (RK control coater) at a slice thickness resolution of 50 μ m. Every layer was cured under UV light for two minutes using an Intertronics IUV250 Hand Lamp (Intertronics, Kidlington, England, UK). Furthermore, a hybrid composite material was also developed using Fe NPs through the screen printing technique. Notwithstanding, such material could not be 3D-printed due to the special measures that must be taken when working with Fe NPs, as an exothermic reaction takes place when used under normal conditions which, if not properly controlled, may lead to combustion. As it happened with the piezoelectric 3D-printable composites, high loadings of magnetic NPs can be achieved, but they tend to aggregate and form big NP clusters that lead to poor 3D-printing resolution. Hence, this is a parameter that must be optimised in order to ensure a good balance between magnetic response and 3D-printing resolution,

as discussed later in this Chapter (see subsection 6.2.5)

BaTiO₃ NPs were obtained from US Research Nanomaterials, Inc. (Houston, TX, USA) whereas Fe₃O₄ NPs were purchased from Sigma Aldrich (catalogue number 637106).

6.2.2 Morphological study

SEM images of the synthesized samples can be seen in Fig. 6.11 and Fig. 6.12, where several observations can be done. Firstly, it can be seen that when screen-printing the materials, the thickness of the layers is not uniform. This is because during the manufacturing process it is difficult to control the exact thickness of each layer due to the viscosity of the material. The second observation is that there is a clear difference between layers crosslinking when using the 3D printer or the screen-printer. Whereas the former provides good crosslinking between layers due to a low UV-light exposition time (Fig. 6.12a,b), the latter does not provide good adhesion between layers as each one of them is fully cured, leading to non-functional radicals that cannot start the polymerization process when a new layer of uncured polymer is put onto it (Fig. 6.11a,b and Fig. 6.12c). It can also be seen that when working with low wt% loadings, NPs present a more uniform distribution within the polymer (Fig. 6.12a) whereas when working with high weight fractions NPs tend to agglomerate and create clusters (Fig. 6.11a,b,c and Fig. 6.12c). Furthermore, it has been observed that NPs do not uniquely agglomerate within the polymer but they also accumulate onto the surface of the resulting cured material, creating smaller clusters (Fig. 6.11b and Fig. 6.12d). Nevertheless, the majority of NPs have been observed to remain in-between layers (Fig. 6.11d and Fig. 6.12d).

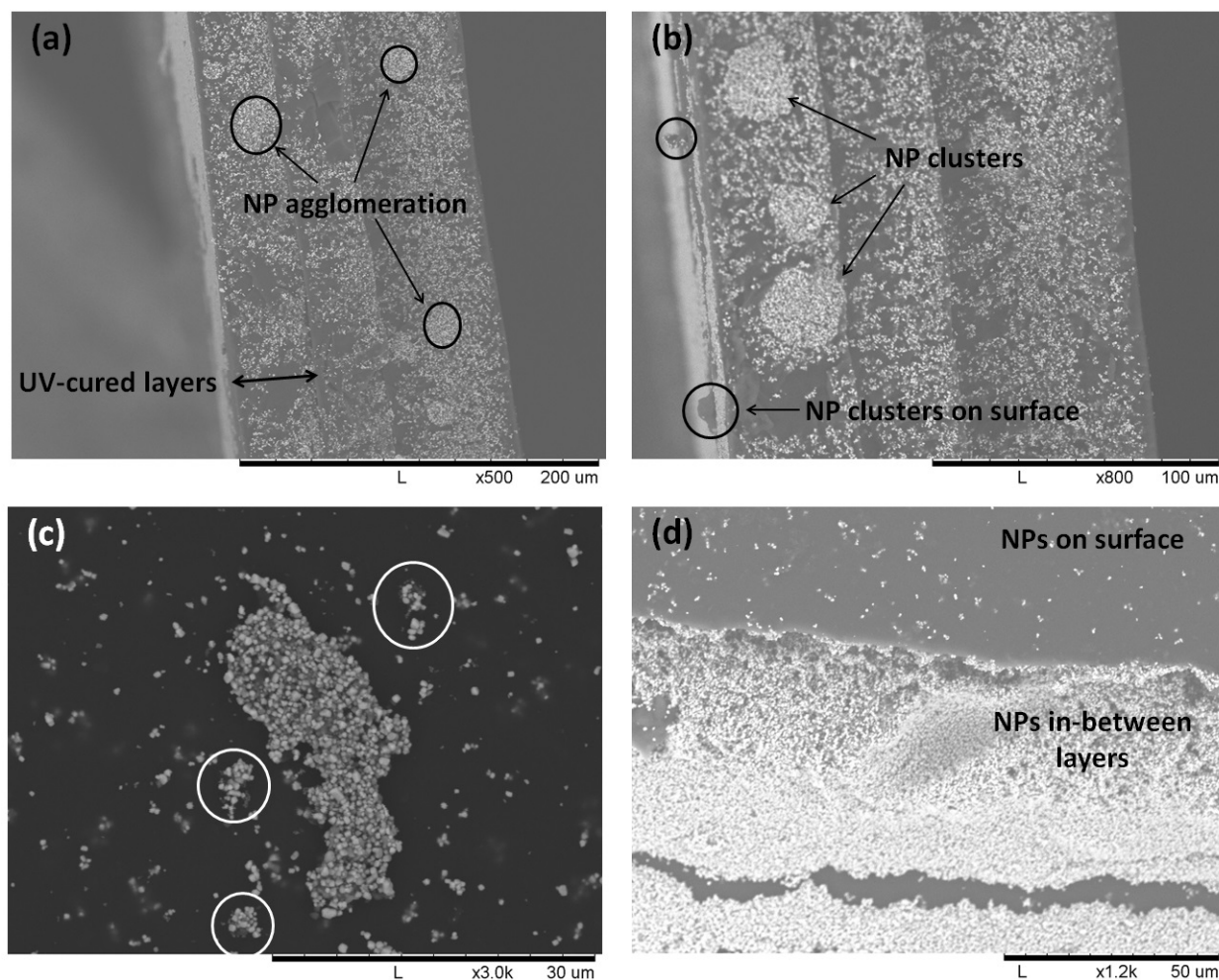


Fig. 6.11. SEM images of screen-printed BaTiO₃ NPs (33 wt%) embedded within BEMA. (a) Cross-section of one of the screen-printed magnetic samples in which the layers can be seen, (b) Cross-section of one of the screen-printed piezoelectric samples at higher magnification, (c) On-top image that shows NP agglomeration on the surface of the composite, and (d) One of the screen-printed samples when one of the layers has been removed.

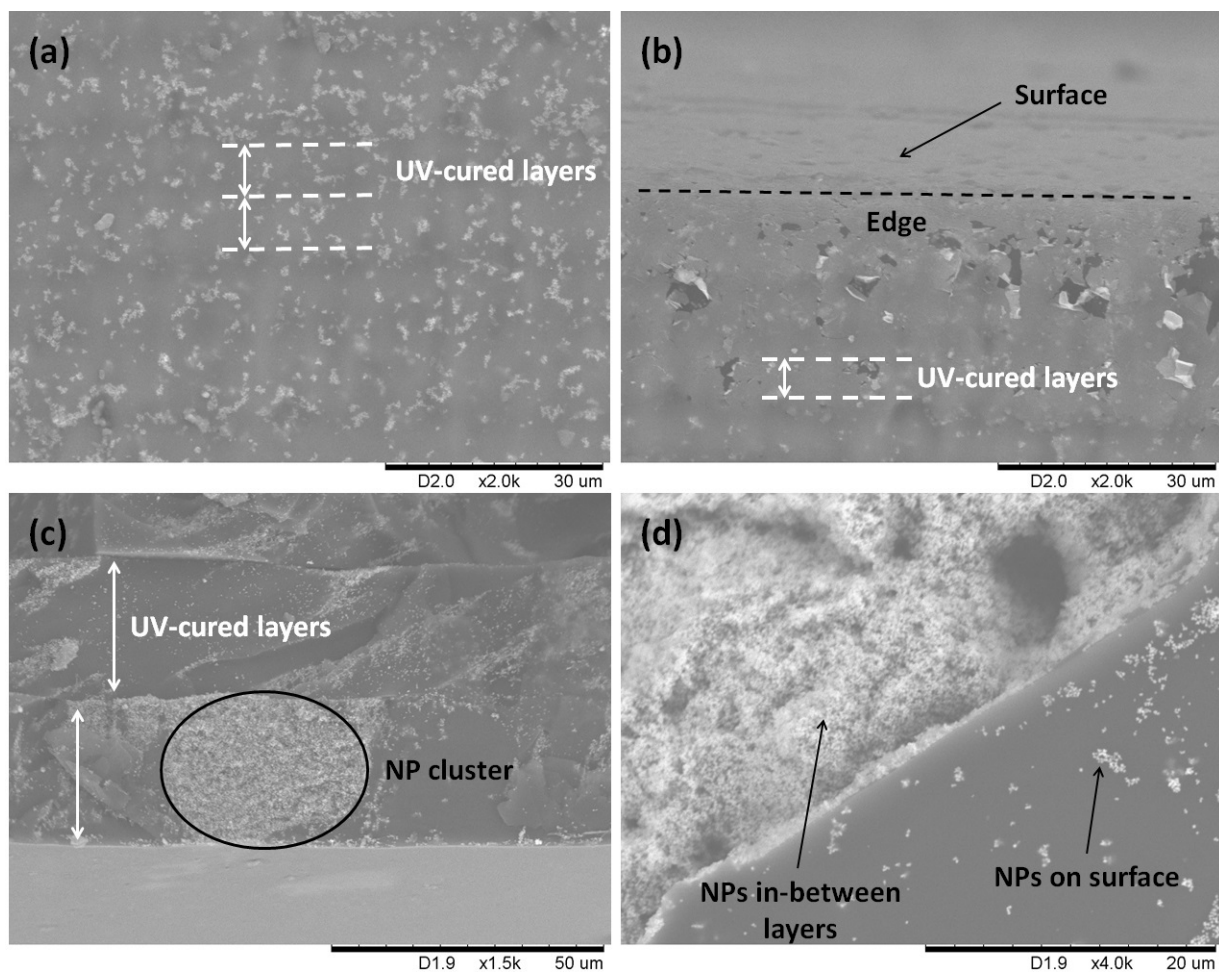


Fig. 6.12. SEM images of the 3D- and screen-printed magnetite NPs (50 wt%) embedded within PEGDA. (a) Cross-section of one of the 3D-printed magnetic samples in which the 3D-printed layers can be seen, (b) The edge of one of the 3D-printed samples, (c) Cross section of one of the screen printed samples, and (d) One of the screen-printed samples when one of the layers has been removed.

Agglomeration of NPs is a common phenomenon when embedding NPs within polymeric matrices [138, 229]. This is a major problem as agglomeration and aggregation of NPs prevents obtaining improved properties of the resulting composite material. These phenomena have been attributed to the direct mutual attraction between NPs via van der Waals forces or chemical bonds [138]. The strategies for avoiding aggregation and agglomeration are mainly attributed to particle coating by a capping agent, application of coupling agent or compatibilizer and charging the filler surface to separate them via electrostatic repulsions [138].

Agglomeration and aggregation effects can be prevented using surfactants [229], and some studies suggest that viscous media also help its prevention when using polymers with long ethylene oxide (EO) chains [138, 229], producing a decrease of the existing van der Waals forces between NPs. One of the advantages of BEMA with respect to other 3D-printable polymeric matrices and other commercial materials is the presence of long EO chains, which seems to decrease NPs aggregation due to an increase of viscosity of the fluid.

6.2.3 Mechanical properties

One of the main concerns when developing new composite materials is how the mechanical properties of each individual material influences the mechanical properties of the resulting composite. The mechanical properties of interest in this thesis are mainly three: the elastic modulus, the density, and the acoustic impedance, as all three of them play, in a way or another, an important role in the mechanic-acoustic response of the material. Whereas the elastic modulus and the density of the composite, altogether with the geometry of the 3D-printed part, will determine the characteristic frequencies of the sensor, its acoustic impedance will define how much resistance the material offers to sound propagation. Hence, it is possible to study the general tendency of these mechanical properties when working with particulate composite materials by using Eq.(6.71)- (6.74) [230]

$$E_c = E_m \frac{E_m + (E_f - E_m)V_f^{2/3}}{E_m + (E_f - E_m)V_f^{2/3} (1 - V_f^{1/3})} \quad (6.71)$$

$$\rho_c = V_f \rho_f + (1 - V_f) \rho_m \quad (6.72)$$

$$v^{(L)} = \sqrt{E_c / \rho_c} \quad (6.73)$$

$$Z = \rho_c v^{(L)} = \sqrt{E_c \rho_c} \quad (6.74)$$

where E , V_f , ρ , $v^{(L)}$, and Z are the elastic modulus, the filler's volume fraction, the density, the longitudinal velocity, and the acoustic impedance, respectively, and the sub-indices c , m , and f refer to the composite, matrix, and filler, respectively. It can be seen that Eq.(6.71) is similar to the Sato-Furukawa relationship, Eq.(3.36) presented in Chapter 3, Section 3.5, with the difference that Sato and Furukawa introduced a parameter accounting for the degree of adhesion between the filler and the matrix. Nevertheless, Eq.(6.71) becomes very useful to study the mechanical properties of the composite material as a function of both E_f and E_m . Furthermore, at this point it must be mentioned that filler fractions will be referred in weight percentages (FWF), but Eq.(3.36) and Eq.(6.71) are a function of the filler's volume fraction (FVF). The relationship between FWF and FVF can be obtained using the densities of the two components of the composite [231]:

$$FVF = \left[1 + \frac{\rho_f}{\rho_m} \left(\frac{1}{FWF} - 1 \right) \right]^{-1} \quad (6.75)$$

As previously mentioned, it is possible to study the tendency by which the mechanical properties of the resulting composite will be depending on the relationship between E_f and E_m , and express it as a function of V_f . Hence, four main situations must be considered when developing a particulate composite material: (i) when $E_f \ll E_m$, (ii) when $E_f \gg E_m$, (iii) when $E_f \lesssim E_m$, and (iv) when $E_f \gtrsim E_m$. The tendencies of the different mechanical properties of the resulting particulate composites according to these previous 4 situations can be easily simulated and plotted, as it can be observed in Fig. 6.13.

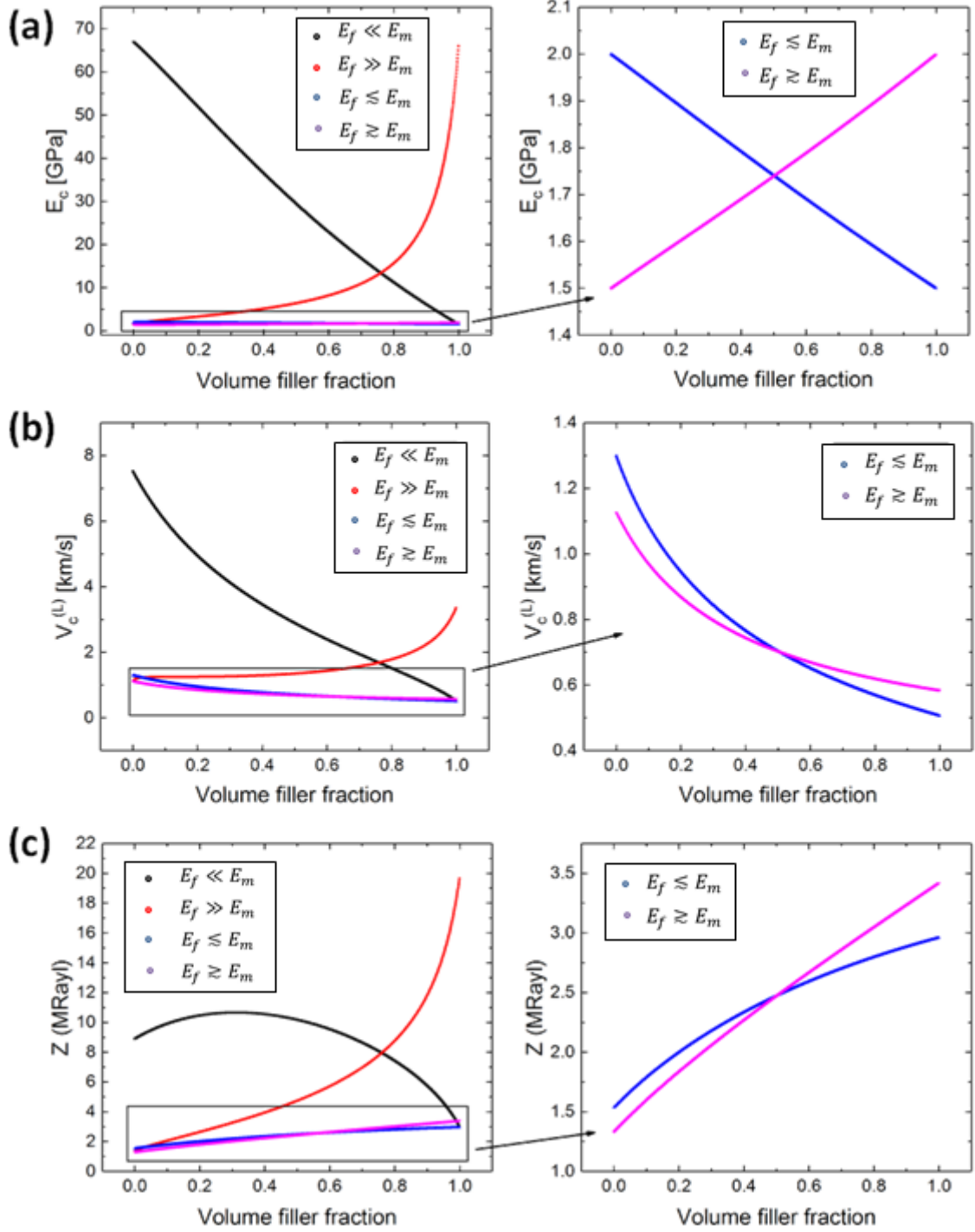


Fig. 6.13. (a), (b), and (c) show, respectively, the simulation results of the mechanical properties (elastic modulus, E_c , longitudinal velocity, $v_c^{(L)}$, and acoustic impedance, Z_c) as a function of the filler volume fraction when working with particulate composite materials. Plots obtained when using Eq.(6.71)-(6.74).

It can be observed from Fig. 6.13 that different tendencies can be found for E_c , $v_c^{(L)}$, and Z_c depending on the relationship between E_f and E_m . These tendencies were studied to understand which is the effect of the relative elastic modulus on the property of interest of the resulting composite. The resulting mechanical properties of particulate composite materials are detailed below:

- E_c : Studying the elastic modulus of the resulting particulate composite has become one of the trickiest parameters to analyse, as very different tendencies can be observed when working with the four different limiting cases. When the elastic modulus of the matrix is much higher than that of the filler (Fig. 6.13(a), black plot), adding low percentages of filler barely affects E_c (*i.e.* $E_c \approx E_m$). As the volume percentage of filler increases, E_c decays until $E_c = E_f$ when considering a 100% volume fraction of filler. The opposite tendency can be observed when the elastic modulus of the filler is higher than that of the matrix. In that case, nevertheless, the increase of E_c takes place at a much faster rate than in the previous case, presenting an asymptote at 100% volume fraction of filler.

It is very interesting to look at the cases in which E_f and E_m are of the same order of magnitude, as they present completely opposite linear trends that follow the same tendency as the one previously explained: E_c decreases when the filler volume % increases when $E_f \lesssim E_m$, whereas it increases when $E_f \gtrsim E_m$.

- $v_c^{(L)}$: Longitudinal velocity of particulate composite materials turns out to be much easier to study than E . In this case, the value of $v_c^{(L)}$ decreases with filler content except in the case in which $E_f \gg E_m$, where the increase is not as prominent as when $E_f \ll E_m$ (unlike in E_c , where even though the trends were opposite, its increase/decrease was of the same order of magnitude). From Fig. 6.13(b) it can be seen that when E_f and E_m are of the same order of magnitude (and irrespective of which one is higher), the longitudinal velocity of the particulate composite decreases.
- Z_c : The study of acoustic impedance of the resulting particulate composite is analogous to that of longitudinal velocity. In this case, though, it increases in every case except when $E_f \ll E_m$. It can be seen from Fig. 6.13(c) that only when E_f is of different order of magnitude than E_m , the impedance of the composite presents a parabolic decrease with filler fraction. The biggest increase of impedance takes place when $E_f \gg E_m$, presenting an asymptote at 100% volume fraction of filler. When both E_m and E_f are of the same order of magnitude, the impedance of the resulting composite tends to increase in both cases at a different rate.

Hence, having an idea of how the mechanico-acoustic properties of particulate composites change with respect to filler fraction, is of great help when developing new composite materials, as it opens the possibility of producing the material starting at the desired filler fraction. In our case, $E_m \ll E_f$ both when working with barium titanate and magnetite NPs, meaning that E_c and $v_c^{(L)}$ increase and decrease,

respectively, with increasing filler fraction. Furthermore, in this range of filler fraction, Z_c increases in the $E_m \ll E_f$ regime, but it must be taken into consideration that from a certain filler fraction this tendency is reversed.

The mechanical properties of the synthesized materials were measured using the nanoindentation technique, from which the $P - h$ curves were obtained and can be observed in Fig. 6.14.

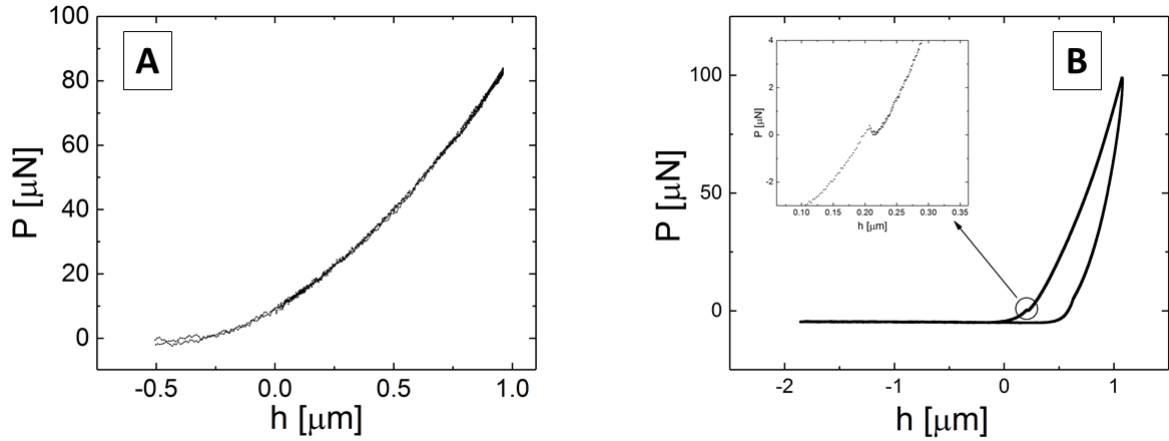


Fig. 6.14. (a) and (b) show the load-displacement curves of BEMA and PEGDA, respectively, with Irgacure 819 (1 wt%) and SUDAN I (0.2 wt%), without any NP loading. BEMA presents an elastic behaviour (as the initial penetration depth is fully recovered) whereas PEGDA shows a plastic mechanical behaviour (as permanent deformation is induced and the initial penetration depth is not recovered) in which crack formation is promoted (pop-in event), as shown in the top-left corner graph.

The main difference that can be observed between BEMA and PEGDA is their mechanical behaviour: whereas 3D-printable BEMA presents a purely elastic mechanical behaviour (*i.e.* h recovers its initial position when the force is removed), 3D-printable PEGDA shows a plastic mechanical behaviour (*i.e.* the deformation of the material remains constant after the force is removed). The $P - h$ curves do not only determine the type of behaviour of the material but they also provide some of their mechanical properties, as discussed in Chapter 3, Section 3.3. Hence, using Eq.(3.21)-(3.26) it is possible to determine E and H . Even though an increase of E and H was measured when increasing UV-light exposure time, these were not significant enough to change the elastic and plastic behaviours of BEMA and PEGDA, respectively. Table 6.4 shows the measured change of these mechanical properties. Furthermore, as PlasWhite was one of the first 3D-printable materials used in this project, its mechanical properties and its corresponding $P - h$ loop (Fig. 6.15) were also investigated.

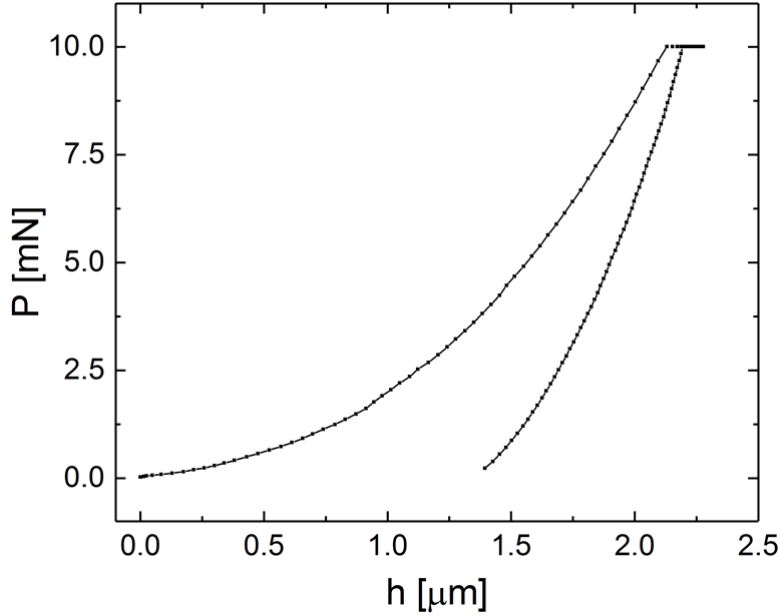


Fig. 6.15. P - h loop of PlasWhite in which a maximum applied load of 10 mN has been applied. PlasWhite presents plastic mechanical behaviour as the initial penetration depth is not recovered during nanoindentation.

PEGDA presented a parabolic increase of E with respect to UV light exposure time ($R^2 = 0.99931$). PEGDA's hardness dependency with UV exposure time was measured to follow a logarithmic increase ($R^2 = 0.9999$). On the other hand, both E and H for BEMA were observed to follow a parabolic increase ($R^2 = 0.9988$ and $R^2 = 0.9971$, respectively). As it can be seen from Fig. 6.15, PlasWhite presents a plastic mechanical behaviour in the same way as 3D-printable PEGDA does. Nevertheless, and as a main difference with both 3D-printable BEMA and PEGDA, PlasWhite presents values of both E and H three orders of magnitude higher. Hence, it is possible to see from Fig. 6.14, Fig. 6.15, and Table 6.4

Material	Exposure time (s)	$E \pm \text{s.e. (MPa)}$	$H \pm \text{s.e. (MPa)}$
BEMA	2	1.4205 ± 0.0087	0.4221 ± 0.0024
BEMA	4	3.070 ± 0.010	0.7471 ± 0.0054
BEMA	6	4.384 ± 0.027	0.926 ± 0.0075
BEMA (fully cured)	13	14.13 ± 0.15	3.94 ± 0.84
PEGDA	2	123.28 ± 1.07	20.74 ± 0.24
PEGDA	4	266.71 ± 2.74	36.75 ± 0.60
PEGDA	6	380.74 ± 4.71	45.55 ± 0.88
PEGDA (fully cured)	13	900.68 ± 32.65	62.79 ± 1.07
PlasWhite	N/A	1442.27 ± 48.91	115.76 ± 5.75

Table 6.4. Values of elastic modulus (E) and hardness (H) of both 3D-printable BEMA and 3D-printable PEGDA obtained from the $P - h$ curves using Eq.(3.21)-(3.26). The reported values of both H and E are an average of 36 tests performed on each sample.

that three materials with completely different mechanical properties can be 3D-printed using a same 3D printer. The main advantage of such feature is that depending on the application of the desired sensor, it is possible to choose the material presenting the most adequate mechanical properties for such purpose.

Mechanical properties of NP enhanced polymers

Once the possibility to 3D-print different polymer-based materials presenting a wide range of mechanical properties was shown, piezoelectric and magnetic NPs were added within the different matrices to provide the resulting 3D-printed materials specific functionalities. When trying to embed NPs within PlasWhite, even though the resulting composites were observed to be functional after screen-printing (both piezoelectric and magnetic), it was not possible to obtain any good 3D-printing resolution even when adding UV blockers into the mixture. This is hypothesized to happen because of the presence of specific oligomers, surfactants, photoinitiators, UV-blockers, and pigments that produce quaternary amino groups when adding extra components within the ASIGA-manufactured material. Nevertheless, this is only an assumption as the manufacturer does not provide the fabrication details nor the components used to develop such material. Hence, PlasWhite was discarded when developing functional 3D-printable particulate composite materials.

The next step was to determine the mechanical properties of the piezo- and magneto-polymer composites using the same approach as that followed with the polymeric materials. The mechanical properties of the piezo- and magneto-polymer composites were studied at different NP loadings, which are reported in Table 6.5.

It is possible to plot the $P - h$ curves of the composite materials using the nanoindenter, which provides information about their elasticity/plasticity. Some of the curves can be seen in Fig. 6.16.

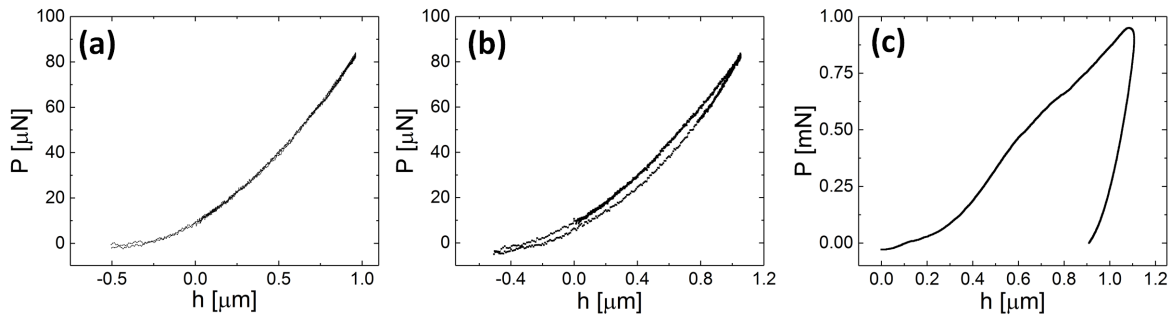


Fig. 6.16. (a) and (b) Show the $P - h$ curves of different regions of piezo-BEMA composites, revealing a local changes of the mechanical behaviour of the sample attributed to NPs agglomeration. This same mechanical behaviour was measured for most BEMA-based composites, being more apparent at higher weight loadings. (c) Shows the $P - h$ curve of BaTiO_3 NPs embedded within PEGDA. The same mechanical behaviour was observed in all the PEGDA-based composites.

BEMA					
Exposure time (s)	BaTiO₃	Fe₃O₄	Fe	$E \pm$ s.e. (MPa)	$H \pm$ s.e. (MPa)
4	30	-	-	3.018 ± 0.035	0.7158 ± 0.0028
4	50	-	-	2.964 ± 0.040	0.745 ± 0.011
4	75	-	-	5.635 ± 0.052	1.600 ± 0.028
Fully cured	20	-	-	21.71 ± 0.62	1.86 ± 0.10
Fully cured	30	-	-	36.34 ± 0.74	4.46 ± 0.14
Fully cured	40	-	-	30.46 ± 0.96	2.67 ± 0.15
Fully cured	50	-	-	18.30 ± 0.62	0.986 ± 0.040
Fully cured	60	-	-	38.56 ± 0.75	4.57 ± 0.13
Fully cured	70	-	-	22.22 ± 0.24	1.678 ± 0.027
Fully cured	-	5	-	25.91 ± 1.96	1.85 ± 0.29
Fully cured	-	25	-	35.51 ± 0.73	4.03 ± 0.11
Fully cured	-	50	-	46.91 ± 1.15	6.10 ± 0.23
Fully cured	-	-	25	23.38 ± 1.00	1.83 ± 0.11
Fully cured	-	-	50	34.43 ± 2.09	3.30 ± 0.29

PEGDA					
Exposure time (s)	BaTiO₃	Fe₃O₄	Fe	$E \pm$ s.e. (GPa)	$H \pm$ s.e. (MPa)
Fully cured	10	-	-	2.039 ± 0.011	205.18 ± 1.69
Fully cured	33	-	-	2.324 ± 0.054	225.81 ± 7.36
Fully cured	50	-	-	2.253 ± 0.043	229.81 ± 8.07
Fully cured	66	-	-	3.063 ± 0.077	286.76 ± 7.04
Fully cured	-	25	-	0.362 ± 0.026	10.61 ± 1.42
Fully cured	-	50	-	0.936 ± 0.033	124.10 ± 5.49

Table 6.5. Mechanical properties of the BEMA- and PEGDA-based functional composite materials. Exposure time refers to how long each layer was cured under UV light (in seconds). The sizes of the NPs were 500 nm, 50-100 nm, and 25 nm for BaTiO₃, Fe₃O₄, and Fe, respectively.

Most of the BEMA-based particulate composite materials presented an elastic behaviour (Fig. 6.16a) even though a low degree of plasticity was measured at specific regions of the material, associated to NP agglomerations (Fig. 6.16b), a behaviour more noticeable at higher NP loadings. On the other hand, and as shown in Fig. 6.14b, all the PEGDA-based particulate composites presented a plastic mechanical behaviour.

It is possible to predict what the elastic modulus of particulate composite materials will be using the models described earlier in this section (Eq.(3.36) and Eq.(6.71)). The obtained results are shown in Table 6.6.

BEMA					
Exposure time (s)	BaTiO₃	Fe₃O₄	Fe	E_{SF} (MPa)	E_{M2} (MPa)
4	30	-	-	3.020 ($j = 0.77$)	2.26
4	50	-	-	2.956 ($j = 0.75$)	3.24
4	75	-	-	5.640 ($j = 0.12$)	5.31
Fully cured	20	-	-	15.68	22.46
Fully cured	30	-	-	16.56	25.17
Fully cured	40	-	-	17.69	28.30
Fully cured	50	-	-	19.23	32.24
Fully cured	60	-	-	21.51	37.69
Fully cured	70	-	-	25.29	46.21
Fully cured	-	5	-	14.64	18.48
Fully cured	-	25	-	16.37	24.63
Fully cured	-	50	-	19.99	34.13
Fully cured	-	-	25	15.70	22.55
Fully cured	-	-	50	18.14	29.51
PEGDA					
Exposure time (s)	BaTiO₃	Fe₃O₄	Fe	E_{SF} (GPa)	E_{M2} (GPa)
Fully cured	10	-	-	0.95	1.17
Fully cured	33	-	-	1.05	1.52
Fully cured	50	-	-	1.19	1.86
Fully cured	66	-	-	1.68	2.38
Fully cured	-	25	-	N/A	N/A
Fully cured	-	50	-	0.94 ($j = 0.97$)	N/A

Table 6.6. Prediction of the mechanical properties of the BEMA- and PEGDA-based functional composite materials using the two models described earlier in this section: E_{SF} using Eq.(3.36) and E_{M2} using Eq.(6.71) $j = 0$ unless otherwise stated. The sizes of the NPs were 500 nm, 50-100 nm, and 25 nm for BaTiO₃, Fe₃O₄, and Fe, respectively.

Fig. 6.17 shows the plot of the values reported in Table 6.5 and Table 6.6.

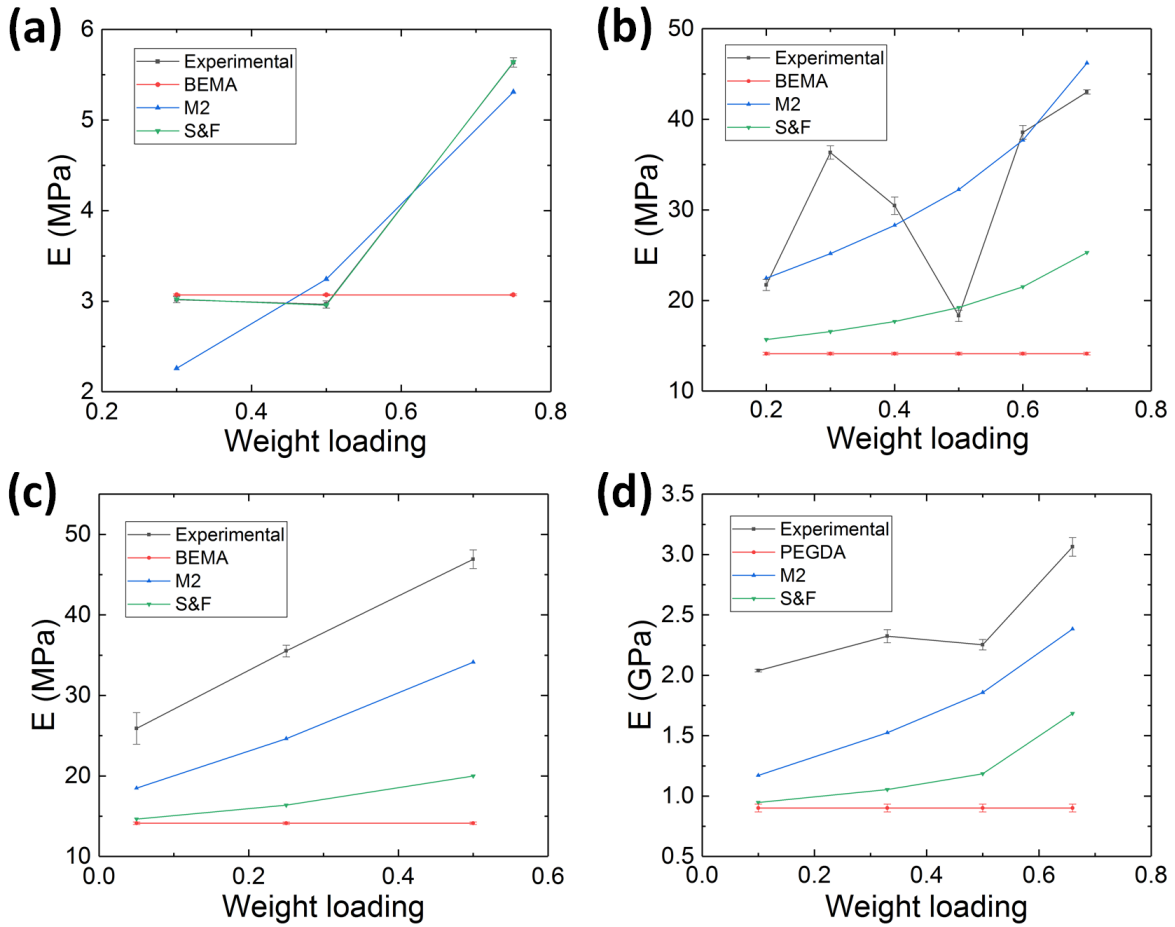


Fig. 6.17. (a)-(d) Show the plots of both the theoretical and experimental elastic moduli of the different particulate composites for (a) BTO:BEMA composites UV-cured for 4 seconds, (b) BTO:BEMA composites fully cured, (c) Fe_3O_4 :BEMA fully cured, and (d) BTO:PEGDA, respectively. Constant values of BEMA and PEGDA are shown in red lines in the four graphs. In (a), the experimental results perfectly match the Sato and Furukawa model, being the two plots superimposed.

Comparing Table 6.5, Table 6.6, and Fig. 6.17, several conclusions can be drawn. Firstly, it can be observed that the Sato and Furukawa model predicts perfectly the elastic moduli of particulate composites at low E values (roughly below 10 MPa) by adjusting the adhesion parameter j . On the other hand, when working with materials that present higher E values, it has been found that Eq.(6.71) provides a better approximation of E_c . Nevertheless, when dealing with materials presenting E values of the order of the GPa, the prediction is not as precise but it still seems to provide a better approach than the Sato and Furukawa equation. The reason behind this lies in the fact that Eq.(6.71) takes into consideration both E_f and E_m , whereas the Sato and Furukawa model determines E_c only using the elastic modulus of the matrix and the fraction volume filler. It can be seen from Table 6.6 that when measuring the

fully-cured composites, the Sato and Furukawa model provides its best approximation when $j = 0$ (*i.e.* when perfect adhesion between NPs and matrix occurs), whereas when studying partially cured samples, the accuracy of the model depends on the adhesion parameter, which seems to be dependent on NP loading. The second main observation that can be done from Table 6.5, Table 6.6, and Fig. 6.17 is that the experimental measurements report some variability (becoming more apparent from Fig. 6.17b and Fig. 6.17d) associated to non-homogeneous NP distribution. Finally, it must be noted at this point that the less precise predicted values are those corresponding to plastic materials. This is because the values of E have been determined using the Oliver-Pharr method, which is perfectly valid for elastic materials but presenting lower reliability when applied to plastic materials (as it uses the unloading segment of the $P - h$ curve, as described in Chapter 3, Section 3.3). It must be further noted that both theoretical models recover the BEMA E value when considering a 0 wt% of filler.

6.2.4 Piezoelectric composite materials

Several piezoelectric composite particulate materials were developed in the course of this thesis using different NP sizes (200 nm and 500 nm) and concentrations. Furthermore, other parameters like poling field, poling time, poling temperature, and poling medium must be considered, as well as the rate at which the poling field is applied.

Hence, it was noted that when a very high voltage was applied directly onto the sample, this led to electric breakdown. Therefore, controlled electric field ramps had to be applied at a rate of 0.2 kV per minute until the maximum desired electric field was reached. It was also noted when poling the piezo-composite materials that irrespectively of their thickness, they would not support voltages higher than 3 kV and, therefore, this value was used as a limit. Three poling times were firstly used in order to optimize the polling process: 30 minutes, 1 hour, and 2 hours. Whereas a significant difference of the piezoelectric coefficient could be observed between the samples poled for 30 minutes and 1 hour, the piezoelectric coefficient of the samples poled for 2 hours did not present important changes, as reported in Table 6.7.

Sample	d_{33}^{30}	d_{33}^1	d_{33}^2
BaTiO ₃ :PEGDA, 20wt%	0.813	2.007	2.107
BaTiO ₃ :PEGDA, 30wt%	1.249	4.163	4.205
BaTiO ₃ :PEGDA, 40wt%	0.660	2.143	2.23

Table 6.7. d_{33} values of BaTiO₃ samples embedded within PEGDA at different loading rates and poled for 30 minutes, 1 hour, and 2 hours, respectively. Used BaTiO₃ size was 500 nm.

As previously mentioned, another two parameters that were observed to influence the polling process were polling time and temperature: whereas these two parameters did not seem to have an impact on the resulting d_{33} value of the composite, they facilitated the whole process. Polling the samples within silicon oil at high temperature (above 100 degrees Celsius) helps avoiding electric break down of the samples. Ideally, the electric field must be applied to the sample during both the heating up and cooling down processes in order to ensure that the domains are not re-oriented in a different direction of that of the applied electric field due to thermal effects.

Obvious differences were observed when using 200 nm and 500 nm size NPs: whereas a clear abrupt increase of the d_{33} coefficient was observed when using 500 nm NPs for both PEGDA and BEMA (Fig. 6.18a and Fig.6.18b respectively), no clear trend was observed when using 200 nm NPs size. It must be noted, nevertheless, that the blue dashed line shown in Fig. 6.18 is not a fitting function but it shows the tendency.

It can be noted from Fig. 6.18 that even though slightly different d_{33} values are measured when comparing BEMA- and PEGDA-based composites (using a same NP size), the same trend is observed presenting a peak at a 75 wt%. These variations of the d_{33} coefficient are associated to non-uniform distributions of NPs, resulting in changes of the electric domains. The polling process was normalised after this optimisation process, consisting of the application of a voltage of 3 kV at a rate of 0.2 kV per minute across the samples for one hour in silicon oil at 120°C.

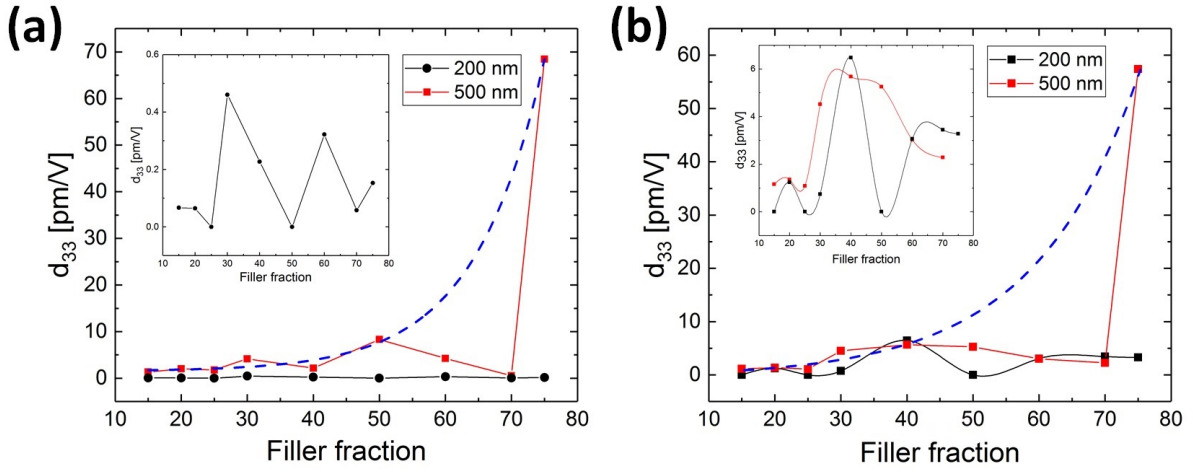


Fig. 6.18. (a) and (b) Show the d_{33} values the 200 nm and 500 nm PEGDA- and BEMA-based piezoelectric composite materials, respectively. The solid points connected by solid lines represent experimental points, and the blue dashed lines show the exponential growth trend, which is not the fitting function of the experimental data.

6.2.5 Magnetic composite materials

8 mm square samples of 0.120 ± 0.010 mm thickness were screen-printed to obtain the $M - H$ curves and study the magnetic properties of the samples as a function of the NP load. After these properties were studied, three different samples were 3D-printed: a small square-shaped membrane (5 mm^2) with a thickness of 2.5 mm, and two larger square-shaped membranes (10 mm^2) of 2.5 mm and 1 mm thickness (see Fig. 6.19). The small sample was 3D-printed at a 5 wt% of Fe_3O_4 :BEMA, whereas the two large samples were 3D-printed at a concentration of 25 wt%. Furthermore, samples containing Fe NPs at different wt% were also developed using the screen-printing technique, as well as a layered hybrid sample consisting of alternating layers of $\text{Fe}_3\text{O}_4(50)$:Irg.PEGDA and $\text{Fe}(50)$:Irg.PEGDA. These samples were developed using five $100 \mu\text{m}$ thickness layers.

The $M - H$ hysteresis loops of the magnetic composites containing Fe_3O_4 and Fe NPs are shown in Fig. 6.20, and their corresponding H_r and M_r values are reported in Table 6.8. It was observed that, irrespective of the NPs wt%, the composites containing magnetite presented a soft ferromagnetic behaviour whereas those containing Fe NPs were superparamagnetic. Furthermore, it was observed that neither the type of polymeric matrix, nor the photo-initiator used, have any impact on the magnetic properties of the composites. Therefore, the NPs type, size, and concentration are the only determining parameters directly influencing M_r . Constant coercive fields were measured when increasing the wt %.

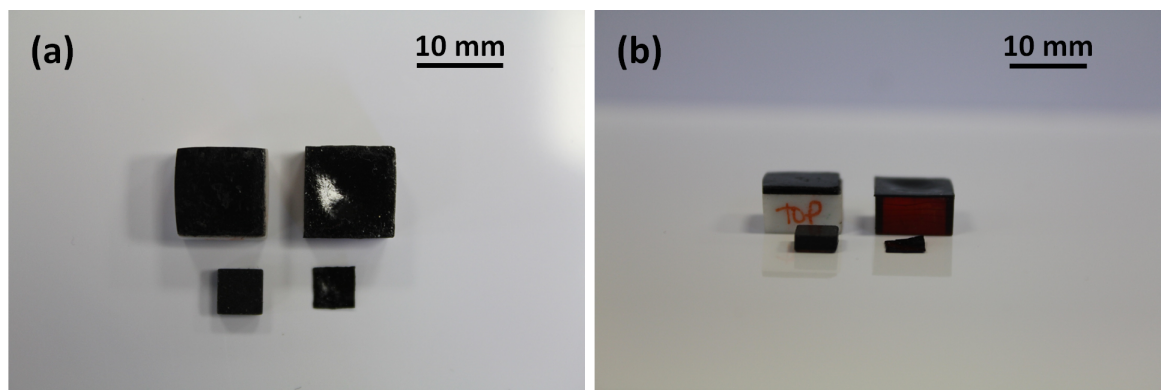


Fig. 6.19. 3D-printed and screen-printed samples. The big samples lie on a 3D-printed support made of commercially-available 3D-printable materials. (a) and (b) show the top and front view of the samples, respectively.

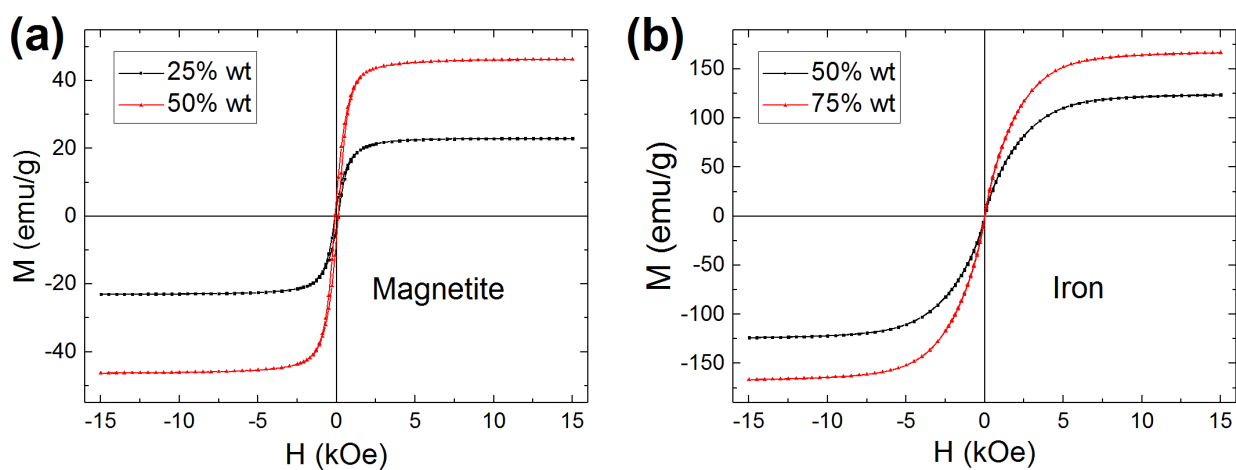


Fig. 6.20. $M - H$ hysteresis loop of (a) Fe_3O_4 composites at 25 wt% and 50 wt% concentrations, and (b) Fe composites at 50 wt% and 75 wt%. It can be seen from (a) and (b) that the magnetite-based composites present a ferromagnetic behaviour, whereas the iron-based composites present superparamagnetic behaviour, respectively.

Sample	m [mg]	M_r [emu/g]	H_c [Oe]	μ_r
Fe(50):Irg.BEMA	3.3	100	16	2.44
Fe(50):Irg.PEGDA	5.1	124	16	1.60
Fe(50):Tri.BEMA	4.5	87	17	2.00
Fe(75):Irg.PEGDA	3.8	167	15	3.08
Fe ₃ O ₄ (25):Irg.BEMA	4.1	22	107	1.60
Fe ₃ O ₄ (50):Irg.BEMA	3.9	46	105	2.23
Fe ₃ O ₄ (50):Irg.PEGDA	4.3	50	105	2.51
Fe ₃ O ₄ (25):Tri.BEMA	4.0	46	104	2.24
Layered hybrid	5.4	66	74	2.06

Table 6.8. Values of the magnetisation of saturation and the intensity of the coercive field of all the synthesized samples. The number in parenthesis corresponds to the wt % of magnetic NPs. Irg and Tri stand for Irgacure 819 and triarylsulfonium hexafluorophosphate salts mixed 50% in propylene carbonate, which are two different photoinitiators. The layered hybrid consisted of alternate 500 μm layers of Fe(50):Irg.BEMA and Fe₃O₄(50):Irg.BEMA.

The hybrid sample was observed to feature the best combination of magnetic properties of each of the individual composite materials, as it reported a high M_r value and the presence of a non-negligible coercive field, as shown in Fig. 6.21.

M_r and H_c are not the only magnetic properties possible to determine from the $M - H$ curves. It is also possible to determine the relative permeability, μ_r , of the composites doing the analysis of the plot. The magnetic field, \vec{B} , can be related to both M and H using the following expression:

$$\vec{B} = \mu_0(\vec{H} + \vec{M}) \quad (6.76)$$

where μ_0 is the permeability of free space and takes the value of $4\pi \cdot 10^{-7}$ H/m. Therefore, it is easy to determine the value of \vec{B} at each coordinate of the $M - H$ plot by using Eq.(6.76). Plotting the $B - H$ curve is equivalent to plotting the $M - H$ curve. It is then possible to build the $B - H$ curve and then determine dB/dH to plot the $dB/dH - H$ curve. An example is shown in Fig. 6.22.

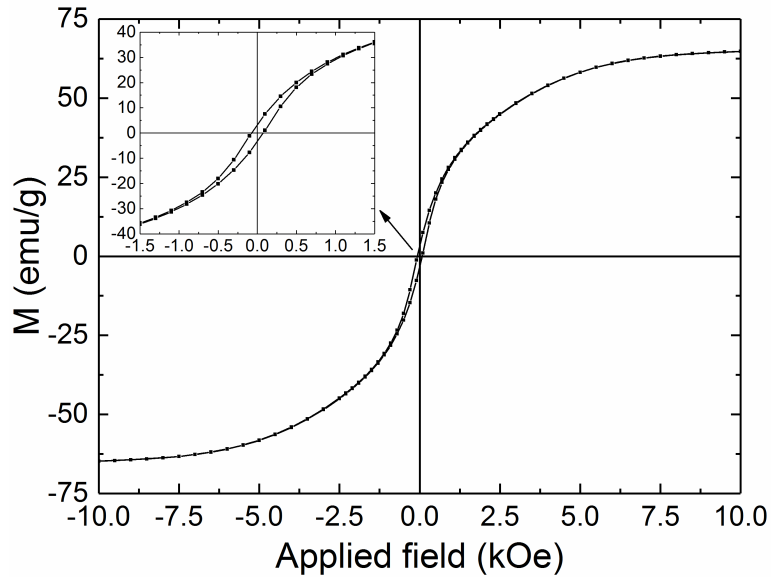


Fig. 6.21. Hysteresis loop of the hybrid magnetic composite material, composed by several layers of Fe(50):Irg.BEMA, and Fe₃O₄(50):Irg.BEMA. The top-left corner graph shows a close-up look at the low-field regime in which the ferromagnetic behaviour of the sample can be observed.

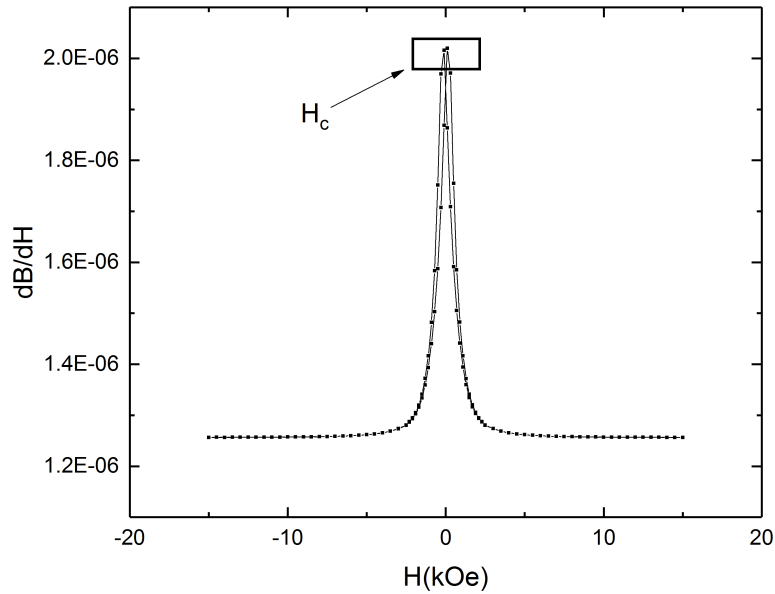


Fig. 6.22. $dB/dH - H$ plot derived from the $M - H$ curves measured using the VSM. The H_c values are highlighted. This is the example for Fe₃O₄(25):Irg.BEMA, but all the $dB/dH - H$ gave the same shape, providing maximum dB/dH values at H_c .

Hence, evaluating the dB/dH value at H_c provides a good approximation of the permeability of the material. Finally, all magnetic permeability values are given as a comparison with μ_0 , defining μ_r as:

$$\mu_r = \frac{\mu}{\mu_0} \quad (6.77)$$

being μ the permeability of the studied material. The obtained μ_r values are shown in Table 6.8.

As mentioned in Chapter 5, Section 5.3, the VSM can be used to determine the type of interaction taking place between ferromagnetic NPs embedded within a matrix by plotting the curve of change of magnetic moment, ΔM , as shown in Fig. 6.23 for the composites containing magnetite. The shape of the ΔM curves revealed the presence of a dipolar coupled system, in which the interactions attempt to demagnetize the material ($\Delta M < 0$).

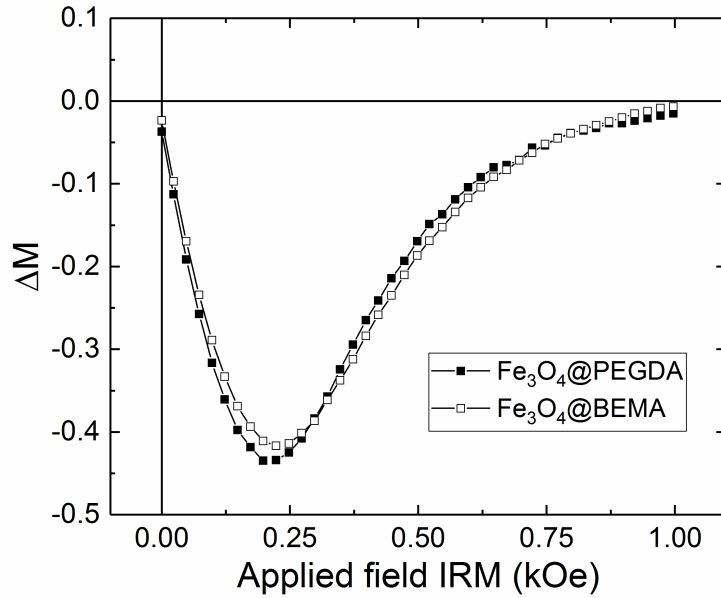


Fig. 6.23. Change of magnetic moment of the synthesized magnetic composites, ΔM curves for the Fe_3O_4 composite at 50 wt % within PEGDA (solid black squares), and for the Fe_3O_4 composite at 50 wt% within BEMA (empty squares).

The type of polymer in which magnetite NPs are embedded does not play any role in the type of interaction taking place between them, as it can be seen in Fig. 6.23. The size of the NPs was determined by fitting the $M - H$ loops using Eq.(4.20). An example of one of the fittings is shown in Fig. 6.24.

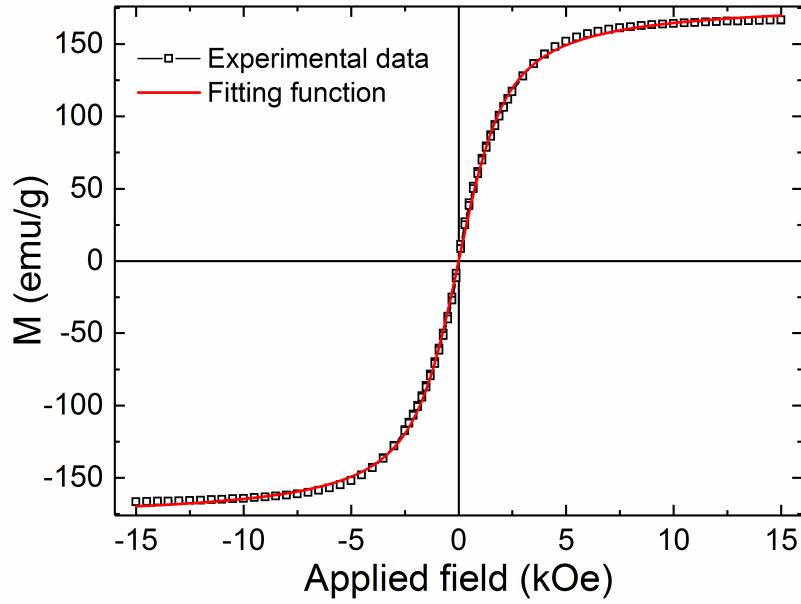


Fig. 6.24. Fitting of the $M - H$ curve of one of the Fe composites using the Langevin function. The empty squares show the experimental data and the continuous red line shows the fitting function.

The NP sizes determined using the Langevin function (Eq.(4.20)) are shown in Table 6.9. Two different values of d were determined in each case; one corresponding to the experimental M_r measured with the VSM, and another one corresponding to the M_r value obtained from the fitting function (top and bottom one, respectively, in Table 6.9 in OriginPro®).

Sample	M_r [emu/g]	NP size [nm]
Fe(50):Irg.BEMA	100	4.076
	110	3.95
Fe(50):Irg.PEGDA	124	2.23
	135	2.17
Fe(50):Tri.BEMA	87	2.14
	100	2.047
Fe(75):Irg.PEGDA	167	2.10
	180	2.042
Fe₃O₄(25):Irg.BEMA	23	10.84
	24	10.72
Fe₃O₄(50):Irg.BEMA	46	8.88
	48	8.79
Fe₃O₄(50):Irg.PEGDA	50	8.95
	51	8.87
Fe₃O₄(25):Tri.BEMA	46	8.87
	48	8.77

Table 6.9. NPs sizes determined from the $M - H$ plots using Eq.(4.20). Two sizes were determined for each sample in which the experimental and the fitting M_r values were used.

It was observed that using the experimental or the fitting M_r value did not present a big difference in determining the NPs size, yielding to maximum errors of 4.55% when determining d . Nevertheless, the average magnetite NP size was calculated to be 9.34 nm with a fitting average accuracy of a 99.88% but the size reported by the manufacturer is of 50-100 nm, showing that Eq.(4.20) does not provide a good approximation to determine d of ferromagnetic NPs, but it does provide an accurate estimation of those presenting superparamagnetic behaviour.

Fe_3O_4 :BEMA at 25 wt% was chosen to be 3D-printed as the composite containing a 50 wt % of magnetite NPs, even though it presented higher M_r values, did not show an accurate 3D-printing resolution. The 3D-printed samples presented a permanent magnetic field in which the magnetic domains were randomly distributed (see Fig. 6.25).

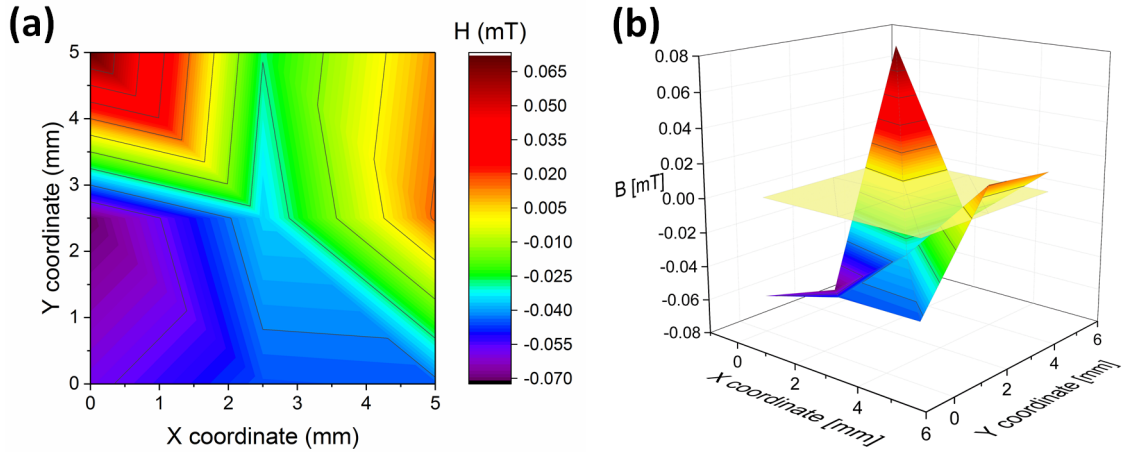


Fig. 6.25. (a) Shows a surface plot of the orientation and intensity of the measured magnetic field of the magnetic domains of the small non-poled 3D-printed sample and (b) shows its 3D representation. The light yellow surface represents the geometry of the surface.

The magnetic field generated by the samples was measured using a GM07/GM08 Gaussmeter (Hirst Magnetic Instruments Ltd., Cornwall, United Kingdom). Thus, poling of the samples was needed to provide them with a good North/South (N/S) distribution of the magnetic domains, which was achieved by placing the samples in between two NdFeB magnets during 2 hours at 150°C . The magnetic field generated by the polling magnets is shown in Fig. 6.26.

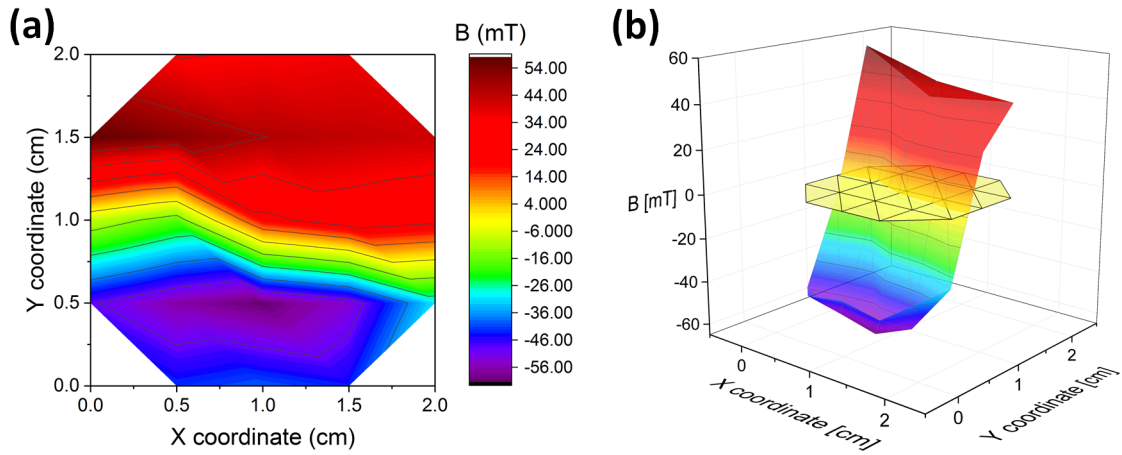


Fig. 6.26. (a) Shows a surface plot of the orientation and intensity of the measured magnetic field of the magnetic domains of the NdFeB and (b) shows its 3D representation. The light yellow surface represents the geometry of the surface.

It can be seen from Fig. 6.26 that the N/S poles of the polling magnet are well defined over its surface and the intensity of the magnetic field is symmetric, which contrasts with the intensity and distribution of the magnetic field generated by a 3D-printed sample before magnetic polling.

The magnetic field generated by the 3D-printed samples after magnetic poling is shown in Fig. 6.27, in which the generated magnetic field has been normalised with the background magnetic field, which includes components from equipment present in the laboratory (*i.e.* oscilloscopes, microphones, and computers) as well as a component arising from the Earth's magnetic field. The background magnetic field was measured to be 0.089 mT. It must be noted from the symmetry of the N/S poles of the 3D-printed samples (Fig. 6.26 and Fig. 6.27) that the direction of the magnetic domains after poling depends on the relative position with the poling magnets, as they present this characteristic N/S distribution (Fig. 6.26). Nevertheless, all the samples presented permanent magnetization reaching maximum values of magnetic field of 1.025 mT. It is possible to optimize the magnetic field of the 3D-printed samples by locating them at specific positions of the NdFeB magnets during the polling process.

Fig. 6.27 shows that even though the polarity of the 3D-printed magnets is well-defined, the field intensity is not completely uniform in two of the samples. This is associated with the non-uniform distribution of the NPs within the polymeric matrix, as well as to aggregation of NPs taking place.

Avoiding agglomeration of NPs has been shown to diminish using more viscous fluids as polymer matrices, as well as the use of surfactants, which play a key role in reducing the Van der Waals forces that cause agglomeration [138, 229]. It must also be taken into consideration that when working with magnetic NPs, Van der Waals forces are not the only forces involved in the formation of NP clusters, but also the magnetic forces between them are involved, which might make the process to reach a more uniform NP distribution more arduous [229].

Even though some of the magnetic properties of the samples still need to be optimized, the possibility to 3D-print permanent magnets presents a revolution in the production process, as the magnetic properties of these composites can be finely tuned by adjusting specific parameters of the composite materials such as the type, size, and concentration of the filler, thus enhancing their applicability range by working with soft permanent ferromagnetic materials or with superparamagnetic composites. Furthermore, developing them through additive manufacturing implies a huge decrease of the production cost, and also the 3D-printing process allows for a customization and personalization process to make desired parts adapted to the users' needs. Also, the ability to 3D-print a wide variety of magnetic composite materials (permanent and non-permanent, hard and soft, ferromagnetic and superparamagnetic) by simply changing the print material reservoir also allows for the combination of different materials in order to blend their properties (as shown with the hybrid sample) and make them present the most suitable magnetic characteristics, allowing to fulfil specific and diverse demands.

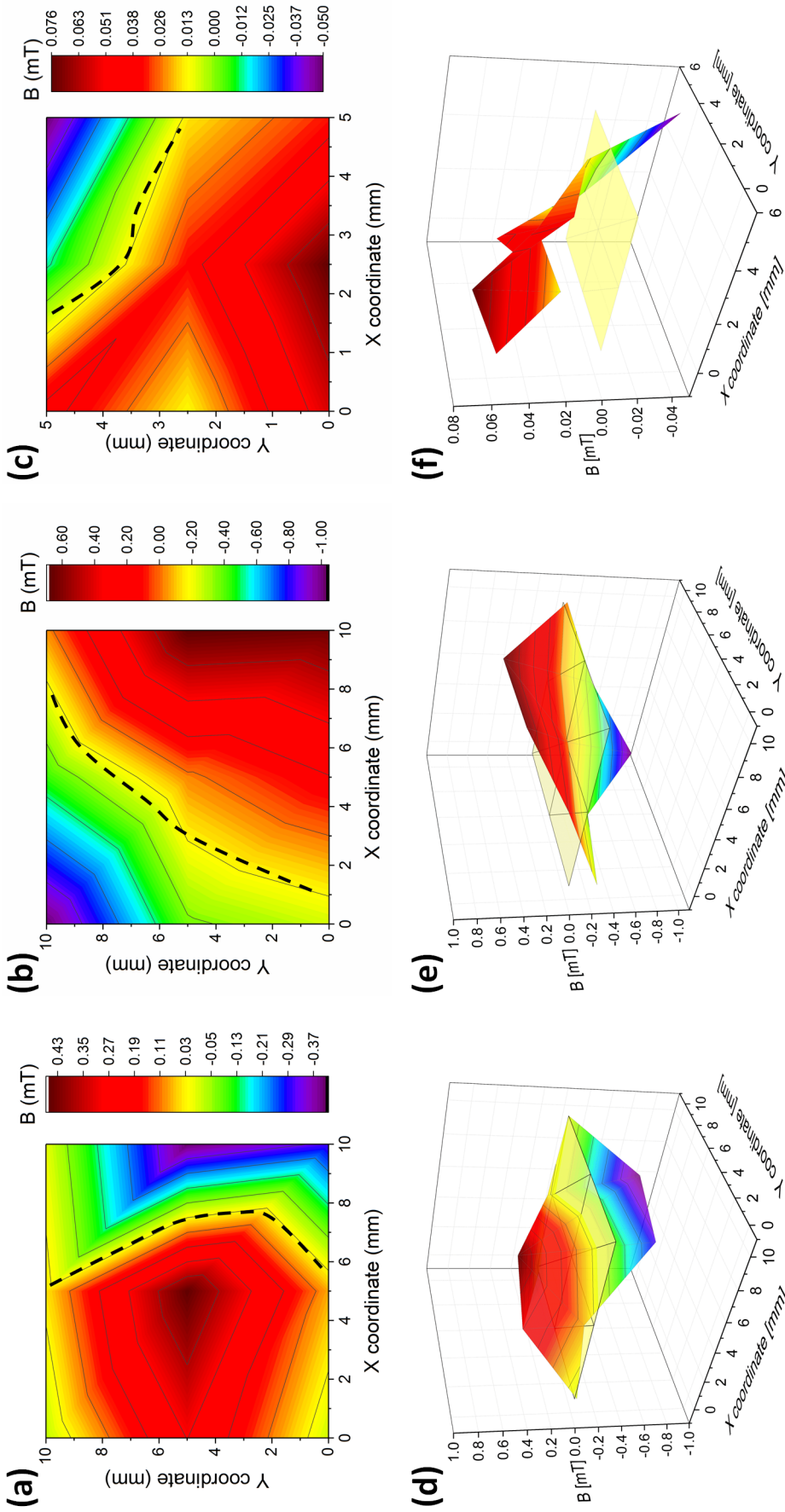


Fig. 6.27. (a)-(c) Show the experimental plot of the magnetic field orientation and intensity after magnetic polling of the 3D-printed big square thick, the 3D-printed square thin, and the 3D-printed small square samples, respectively. (d)-(f) Show the 3D representation of the intensity and orientation of the magnetic field created by the samples, where the light yellow surfaces indicate the geometry of the samples.

The main relevance of this part of the study is the possibility to 3D-print permanent magnets at the micro-scale at high resolution. Hence, apart of reporting the magnetic properties of the samples, it is also important to determine the 3D-printing resolution limits when using these magnetic materials. Fig. 6.28 shows a 3D-printed magnetic hollow half-sphere with 1 mm holes. The base of the half-sphere is of 10 mm and the lateral separation between holes is of 0.5 mm. This sample was 3D-printed using 5 wt% Fe_3O_4 (50-100 nm) in BEMA.

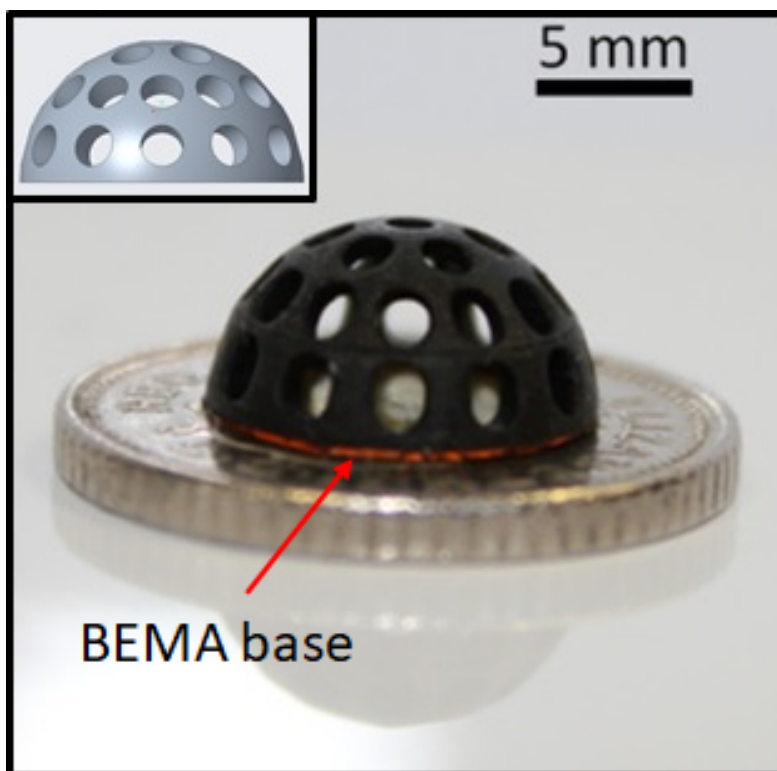


Fig. 6.28. 3D-printed magnetic hollow half-sphere. The 1mm holes are separated 0.5 mm from each other. The diameter of the base is 10 mm. The magnetic structure was 3D-printed on a 0.2 mm BEMA base. The corresponding computer-aided design (CAD) file is shown in the top-left corner.

Two main observations were made when 3D-printing particulate composite materials. The first one is the impossibility to 3D-print one of these materials (either piezoelectric or magnetic) directly on the metallic holder (building area) of the 3D printer. Even though the explanation of this feature is unclear to us, the repulsion forces acting between them could be one of the factors influencing such feature. Thus, before 3D-printing any particulate composite, a thin layer of polymer needs to be previously 3D-printed in order to ensure crosslinking. On the other hand, this becomes a positive feature when 3D-printing hybrid materials. The second observation is that when adding NPs within a polymeric matrix, the 3D-printed part does not present the expected dimensions, meaning that a compensation factor needs

to be added when developing the CAD file to obtain the desired dimensions. This compensation factor depended on the material used and had to be determined for each individual print.

The most important feature when developing functional 3D-printable composite materials is to keep the best possible balance between 3D-printing resolution and output signal. Even though it was observed that the piezo-composite materials presented highest d_{33} values at concentrations of 75 wt% for 500 nm NPs, 3D-printing resolution at those concentrations was dramatically low, as sizes smaller than 2 mm were impossible to print. This same phenomenon was observed for the magnetic 3D-printable composites, being this the justification of choosing specific filler concentrations over others.

6.3 3D-printed parts and sensors

6.3.1 Cochlea-based passive sound amplifiers: mechanical resonators

The first 3D-printed devices were passive mechanical sound amplifiers built using PlasWhite in order to get familiarised with the 3D printer settings. The dimensions and shapes of these mechanical amplifiers are shown in Fig. 6.29.

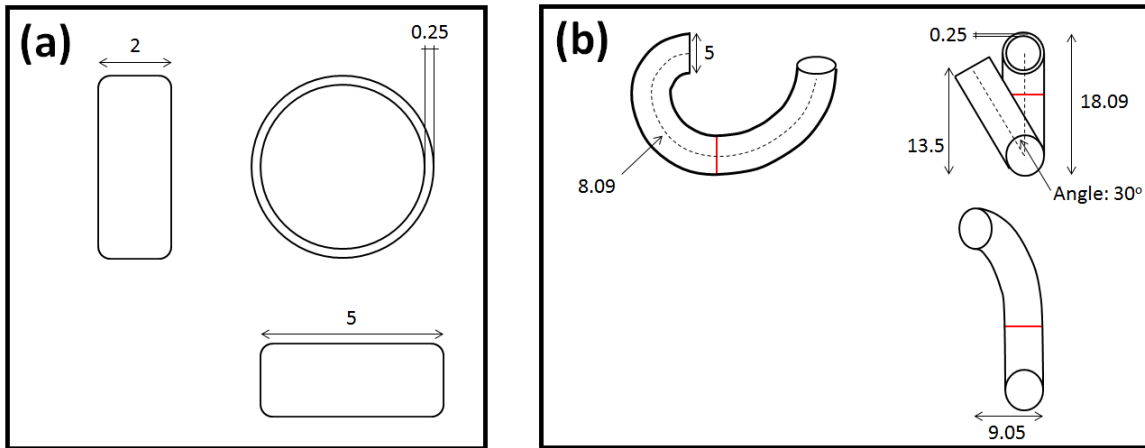


Fig. 6.29. Dimensions in mm of (a) a reference disk, and (b) golden-ratio tube with an interface, highlighted in red.

In all cases, the membrane was not 3D-printed but a 50 μm thickness Kapton film was glued on the large hole of the structures. Kapton was chosen for its thickness and mechanical properties, as they are similar to those 3D-printed with BEMA. As it can be seen from Fig. 6.29b, there is an interface splitting the complex structure in two different regions. A third resonator was 3D-printed

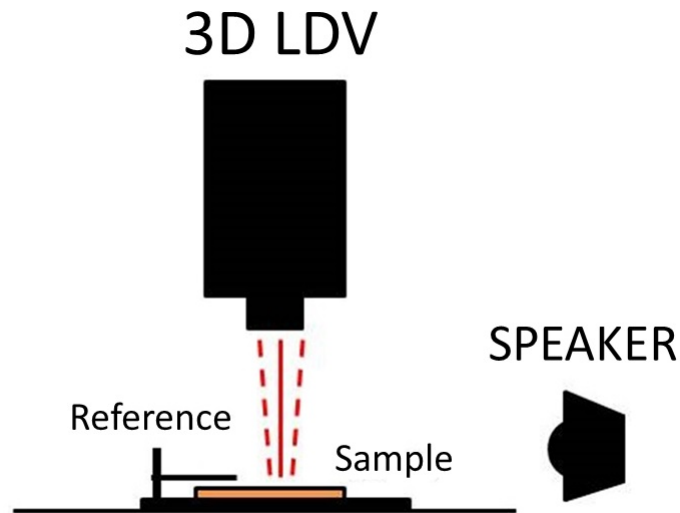


Fig. 6.30. Schematic set up to test the acoustic response of the 3D-printed sensor. The loudspeaker sits behind the sensor at a distance that ensures the far-field regime, and the 3D-LDV head stays on top of the sensor. The sensor was fixed on the table, and a Bruel & Kjaer 4138 microphone was used as a reference.

without such interface. The acoustic response of all the resonators was assessed using a 3D LDV system with an MSA-100-3D scanning head (Polytec, Waldbrom, Germany). The acoustic response of the 3D-printed resonators was measured under wideband stimulation from 1 to 26 kHz in the far field regime, changing the speaker at 17 kHz. The velocity of motion of the membrane and the SPL dB near it were simultaneously recorded. The SPL dB was recorded using a Bruel & Kjaer 4138 precision pressure microphone (Naerum, Denmark) and preamplifier (Bruel & Kjaer, 2633), with its diaphragm parallel to the sound direction to maximize the response and using a calibrated stimulus sound level of 65 dB re 20 μ Pa (35 mPa), as schematically shown in Fig. 6.30. The results can be seen in Fig. 6.31.

One of the main advantages of the 3D LDV is the ability to measure the amplitude of motion in all three dimensions of space, reporting that the relevant oscillations take place on the z -axis and only noise-level sound is detected in both x - and y -axes. The z -axis displacement of the reference membrane was determined by averaging three different samples, and it showed resonance peaks at 1.73, 4.043, 5.054, 7.47, 9.23, and 11.78 kHz with high noise levels. When measuring the resonators a much clearer resonance spectrum was observed. The noise level was observed to decrease in different ways: whereas the sample without an interface presented a low frequency noise decrease (below 10 kHz), the one with an interface showed a better noise filtering at higher frequencies (above 10 kHz).

Even though the resonators presented extra resonance peaks due to a change of geometry of the structure, the main peak at 9.23 kHz was observed to be clearly amplified for the resonator presenting an interface, whereas it was observed to be shifted to 10.23 kHz for the resonator without interface and slightly amplified. Both resonators presented a peak at 1.99 kHz, which amplitude of motion was

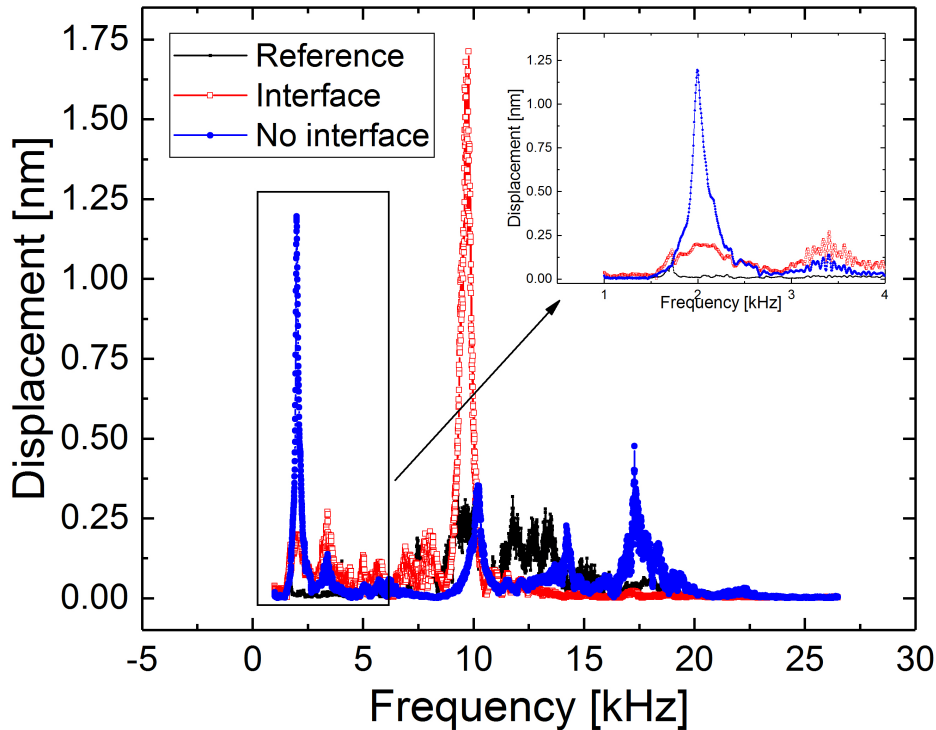


Fig. 6.31. The black, red, and blue lines show the displacement in the z -axis of the reference disk (plotted as an average of three different samples), the resonator with interface, and the resonator without interface, respectively. The top-right corner graph shows a closer look to lower frequencies (below 4 kHz).

much higher for the resonator without an interface. Furthermore, all the peaks measured after 10 kHz presented higher amplitudes of motion for the resonator without interface.

The amplification provided by the resonator with an interface is thought to be more efficient due to the pressure waves created in the second region of the resonator due to the oscillation of the middle membrane. Furthermore, in that case, the noise level at low frequencies is attributed to their higher degree of dispersion, whereas high frequencies are more directional, providing an explanation to why lower frequencies (below 4 kHz) are more amplified in both structures than in the reference sample.

Hence, the possibility to 3D-print polymer-based acoustic resonators able to both passively amplify sound waves and reduce noise level is possible following from the presented results.

6.3.2 Locust TM-based resonators

As it has been introduced in Chapter 1, Section 1.4.3, the locust TM presents a simple structure that allows for acoustic frequency selectivity due to smooth changes of the membrane's thickness. As previously discussed, discerning different frequencies is not the unique function of the non-uniform thickness of the membrane, but it also leads to nonlinear effects that can be exploited for purposes related to signal processing analysis. All the 3D-printed sensors studied in the course of this thesis were developed using BEMA unless otherwise specified.

First approach

The aim of this section is to develop 3D-printed sensors that exploit this feature in order to avoid the development of complex cochlea-based systems that require complicated signal processing tools to perform acoustic frequency selectivity.

The first developed resonator consisted of a rectangular beam presenting two different thickness regions, as schematically shown in Fig. 6.32. The membrane was 3D-printed using BEMA and fixed onto a solid PlasWhite (a commercial material developed by ASIGA) structure in a way that its four edges were fixed and the rest of it could freely vibrate (see Fig. 6.33), reproducing the set up of the

locust TM in the best possible way.

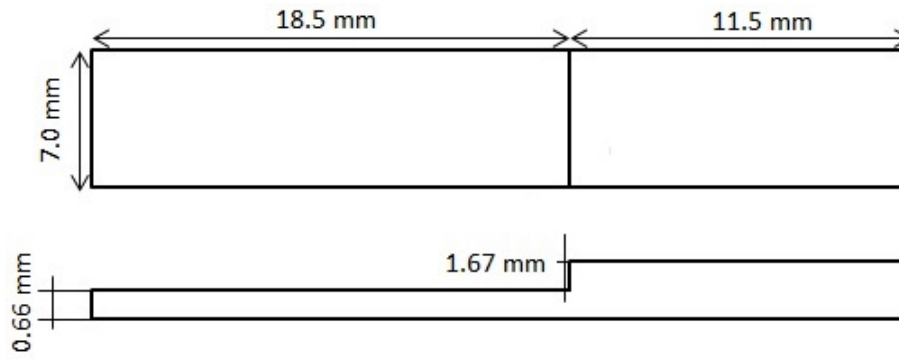


Fig. 6.32. Sketch of the first 3D-printed locust-inspired resonator. The top and bottom images show, respectively, the top and side view of the resonator with its corresponding dimensions.

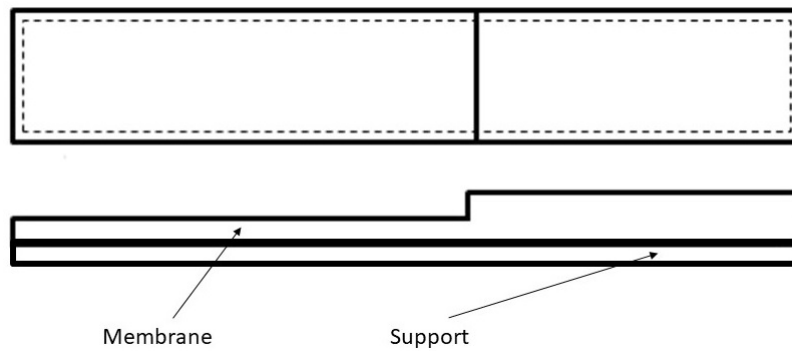


Fig. 6.33. Sketch of the resonator with the support structure. The top and bottom images show, respectively, the top and side view of the resonator when the supports are added.

The motion of the resonator was measured using the 3D LDV with an MSA-100-3D scanning head (Polytec, Waldbrom, Germany). The acoustic response of the 3D-printed sensor was measured under acoustic wideband stimulation (300 Hz to 17 kHz) using a 4" 40 W loudspeaker (Maplin Electronics Ltd., Barnsley, England) in the far-field regime by simultaneously recording the velocity of motion of the sensor and the sound pressure level near it using a Bruel & Kjaer microphone (Naerum, Denmark) and preamplifier (Bruel & Kjaer, 2633), with its diaphragm parallel to the sound direction to maximise the response and using a calibrated stimulus sound level of 65 dB re 20 μ Pa (35 mPa), as schematically shown in Fig. 6.30. Values of coherence between the vibrometer and microphone signals below 85% were withdrawn in order to ensure data reliability over the entire extent of the scanned area. Propagation of TWs was also studied in this resonator using the 3D LDV by drawing a transect line from edge to edge of the membrane at five different frequencies (single tone analysis). The motion across the membrane becomes apparent when the response is displayed for every 10° of phase. TWs can be characterised as a part of the analysis of the vibration of the 3D-printed sensor, as they move in time, making the vibration change with both position and time, and their velocity and wavelength can be determined using Eq.(6.79) and Eq.(6.80) [11].

$$\delta_t = \delta_\phi / 2\pi f \quad (6.78)$$

$$v_{TW} = \delta_x / \delta_t \quad (6.79)$$

$$\lambda_{TW} = 2\pi \delta_x / \delta_\phi \quad (6.80)$$

where f is the frequency, δ_ϕ is the phase difference between the two points, δ_t is the travel time, and δ_x is the distance travelled. v_{TW} and λ_{TW} are the velocity and the wavelength of the TW, respectively. To run these experiments, more than 3000 points were measured, providing an accurate representation of the membrane's motion *via* a contactless process, and allowing the measurement of the average displacement of the different regions of the sensor at specific frequencies using the fast Fourier transform (FFT) module of the 3D LDV system, which were normalised with the SPL dB (Table 6.10).

Frequency (kHz)	Thick region		Thin region	
	z/dB (pm/dB)	z/Pa (nm/Pa)	z/dB (pm/dB)	z/Pa (nm/Pa)
0.60	11.80	53.23	9.62	44.18
0.80	15.16	29.40	9.82	19.04
1.00	5.79	12.34	2.91	5.085
1.90	14.60	13.39	44.53	51.79
2.20	8.35	7.51	39.24	65.081
3.00	11.63	22.19	14.58	30.97
5.00	7.41	6.67	2.80	5.51
8.00	4.52	2.24	6.38	9.27
10.00	2.73	3.80	1.78	7.38

Table 6.10. Values of the average amplitude of motion of the thick and thin regions of the 3D-printed resonator in the vertical direction (z -axis) under single frequency acoustic stimulation.

When acoustically stimulated by single-frequency inputs, the 3D-printed resonator displayed larger amplitudes of motion at frequencies below the first resonant frequency on the thick region, whereas the opposite trend was observed at higher frequencies on the thin region (Table 6.10). Simulation techniques using COMSOL confirmed the experimental behaviour (Fig. 6.34).

Furthermore, the presence of TWs was observed by 3D LDV analysis and also confirmed by COMSOL simulation techniques (Fig. 6.35), revealing an increase of the TW's velocity of propagation (v_{TW}) with frequency on the thin membrane at low frequencies, and a decrease of v_{TW} with frequency on the thick membrane at high frequencies (Table 6.11), giving values close to the material's speed of sound, which is determined by Eq.(1.2).

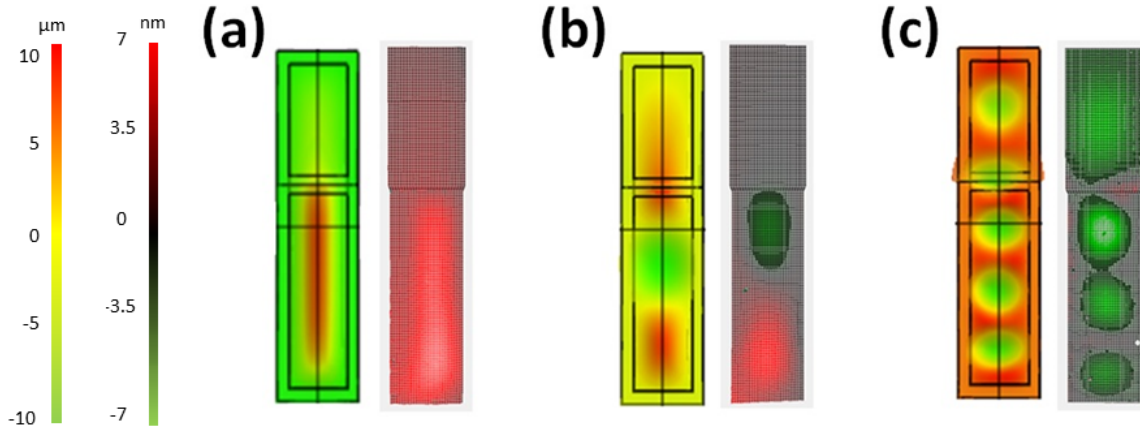


Fig. 6.34. (a-c) Simulation (left) and experimental (right) mechanical deflection of the 3D-printed resonator at 1 kHz, 2.2 kHz, and 5 kHz respectively.

Frequency (kHz)	Thick region		Thin region	
	v_{TW} (m/s)	λ_{TW} (mm)	v_{TW} (m/s)	λ_{TW} (mm)
2.2	-	-	27.79	11.21
3.0	-	-	51.52	17.17
5.0	71.63	14.33	30.48	5.77
8.0	53.92	6.74	-	-
9.0	48.29	5.37	-	-

Table 6.11. Values of the velocities and wavelengths of the TWs measured onto the 3D-printed sensor.

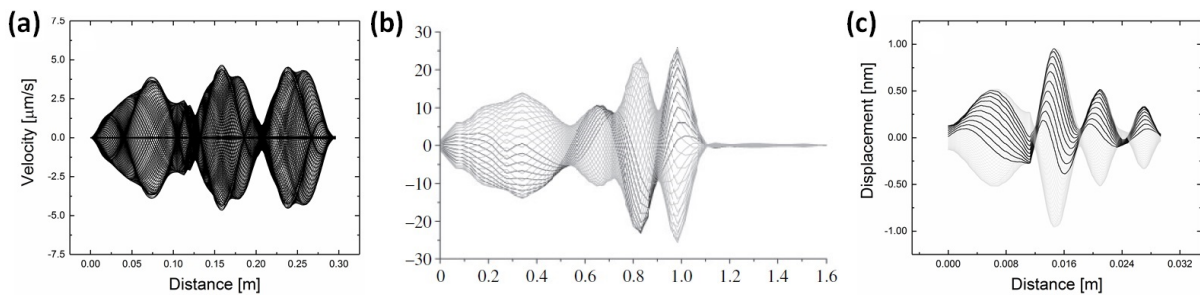


Fig. 6.35. (a-c) Show the representation of the TWs observed in COMSOL, the locust TM, and the 3D-printed resonator, respectively. The middle image was kindly provided by Prof. Windmill, from his work *Tympanal travelling waves in migratory locusts* [11]. In this image, Windmill *et al.* plotted the measured gain as a function of the distance across the locust TM.

For each frequency, the deflections of the membrane do not stay in the same position, but they travel across the membrane irrespective of the incidence angle of the sound field, modifying its envelope shape when varying the driving frequency. These behaviours match those observed on the locust's TM [11] (Fig. 6.35b), suggesting that the presence of TWs does not depend of any biological active process, but it is a phenomenon highly reliant on the geometry and structure of the membrane, a fact attributed to nonlinearities of the system attributed to a change of local mass and stiffness along the membrane. When a single-frequency sound stimulus impinges the ear, the local pressure changes periodically with time and the deformation of the membrane can be described by a nonlinear wave equation [11]. There is a characteristic place in the membrane where the frequency of the wave is matched by the frequency of the critical oscillators that describe the system. Far from this resonant point, the wave equation describes TWs that are linear for small vibration amplitudes. The fall in wave velocity implies an increase in the amplitude of the wave, leading to an increase of displacement of the wave as it approaches the resonant point [232]. Nevertheless, the direction of propagation of the TWs has been observed to be opposite to that measured on the locust TM for frequencies higher than 1 kHz, as confirmed by COMSOL simulation. The mechanoreceptor attachment points (FB and PV, as introduced in Chapter 1, Section 1.4.3) on the locust TM could explain this difference between the biological and the 3D-printed sensor, as they contribute a local increase of mass at specific regions of the locust TM. Furthermore, a non-perfect attachment of the 3D-printed membrane with the support structure might also play an important role on the direction of propagation of the TWs, as well as contributing to a non-perfect experimental mode shape (Fig. 6.35). Notwithstanding, a phenomenological match of the acoustic response can be observed between the 3D-printed sensor and the locust TM.

Second approach

As discussed in Chapter 1, Section 1.4.3, research regarding the relationship between the locust's TM morphology and structure with sound energy localization and frequency analysis revealed the presence of lipid-filled cavities within specific regions of the membrane (Fig. 1.9) [77]. In this second approach cavities of different shapes and arrangements were added into the resonators developed in the first approach. As in the previous case, mechanical analyses of these resonators, including measurements of surface velocity as a function of the incoming frequency, clarify the influence of those cavities on the response of the membrane. Three different resonators were used, which dimensions are shown in Fig. 6.36a-c and its top-view can be seen in Fig. 6.36d-f.

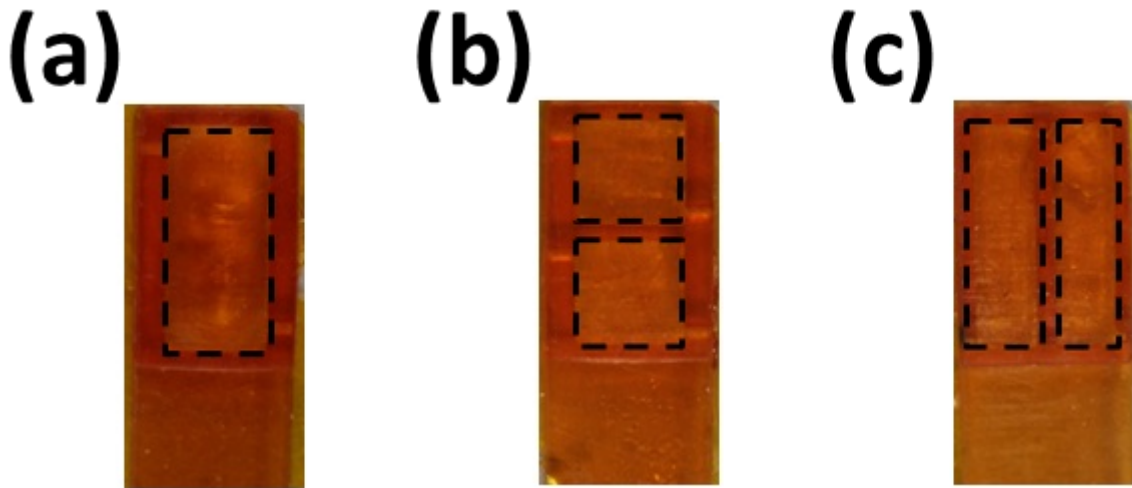


Fig. 6.36. Dimensions of the 3D-printed samples including several cavities in different distributions (a) resonator with one cavity in the thick region, (b) resonator with two square cavities in the thick region, and (c) resonator with two rectangular cavities in the thick region. The space between the cavities and the wall is 1 mm, and the space separating the cavities is 0.5 mm. (a) is 9.5 mm in length and 5 mm in wide, (b) are 5 mm side squares, and (c) are 10.5 mm length and 2.75 mm wide.

The resonators shown in Fig. 6.36 were tested both when they were empty (air-filled), and when they were filled with a mixture of isopropyl alcohol (IPA) and a blue dye. The dye was added into the mixture with IPA in order to be able to easily check if the cavities were properly liquid-filled. As in the previous approach, values of coherence below 85% were withdrawn in order to ensure data reliability over the entire extent of the scanned area, measuring more than 3000 points using the FFT module of the 3D LDV system. All the data were also normalised with the SPL dB measured in the vicinity of the membrane. Scans of the full membrane and of the thick membrane of all resonators were separately conducted to ensure the reliability of all results.

When analysing the mechanical behaviour of the full membrane, the same tendency as the one measured in the previous case was found, whereby the thin membrane presented larger amplitudes of motion at higher frequencies and vice versa. Thus, subsequent analyses focused on the thick region of the 3D-printed resonators, in which cavities of different shapes and filling (either air or IPA) were included in order to determine their role in the mechanical behavior of the membrane when acoustically stimulated. The characteristic frequencies of the thick region of the different resonators are shown in Table 6.12, as measured with the 3D LDV.

Solid	First characteristic frequency [kHz]					
	1 Cavity		2 Cavities		2 Cavities Rectangular	
	Air	IPA	Air	IPA	Air	IPA
1.38	1.83	1.56	2.42	2.40	2.00	2.32
1.59	2.02	1.94	2.77	2.74	2.71	2.80
1.74	4.87	4.80	5.51	5.06	3.92	3.54
1.99	5.51	5.15	6.95	5.94	4.91	3.86
2.28	8.19	8.30	8.28	8.00	5.24	4.88

Table 6.12. First characteristic frequencies (expressed in kHz) of the thick region of the 3D-printed resonators.

It must be noted from Table 6.12 is that the the characteristic frequencies of the samples with cavities enclosed within the thick region of the membrane show a shift down in their characteristic frequencies when they are IPA-filled. This frequency shift could be explained by the presence of small air bubbles within the cavities, involuntary introduced during the filling process, as it has been previously shown that even the smallest of bubbles lead to a dramatic decrease in the resonant frequency of a liquid-filled cavity because of the coupling between the vibration of the bubble with that of the cavity, further suggesting that the pressure within the cavity depends on the location of the bubble [233].

After performing the eigenfrequency analysis, the mechanical behavior of the 3D-printed resonators was tested under single-frequency stimuli in order to determine both the average surface velocity (v_s) and displacement (d) of the membrane, as shown in Fig. 6.37.

It was observed when playing single tone stimuli that the sample with no cavities displayed the lowest values of both v_s and d at all frequencies when compared to the other resonators. The solid sample displayed maximum peaks of both v_s and d at its corresponding characteristic frequencies. The sample presenting one unique cavity showed values of v_s and d of the same order of magnitude up to 2 kHz, but higher values for both magnitudes from 2 to 5 kHz when the cavity was IPA-filled. At higher

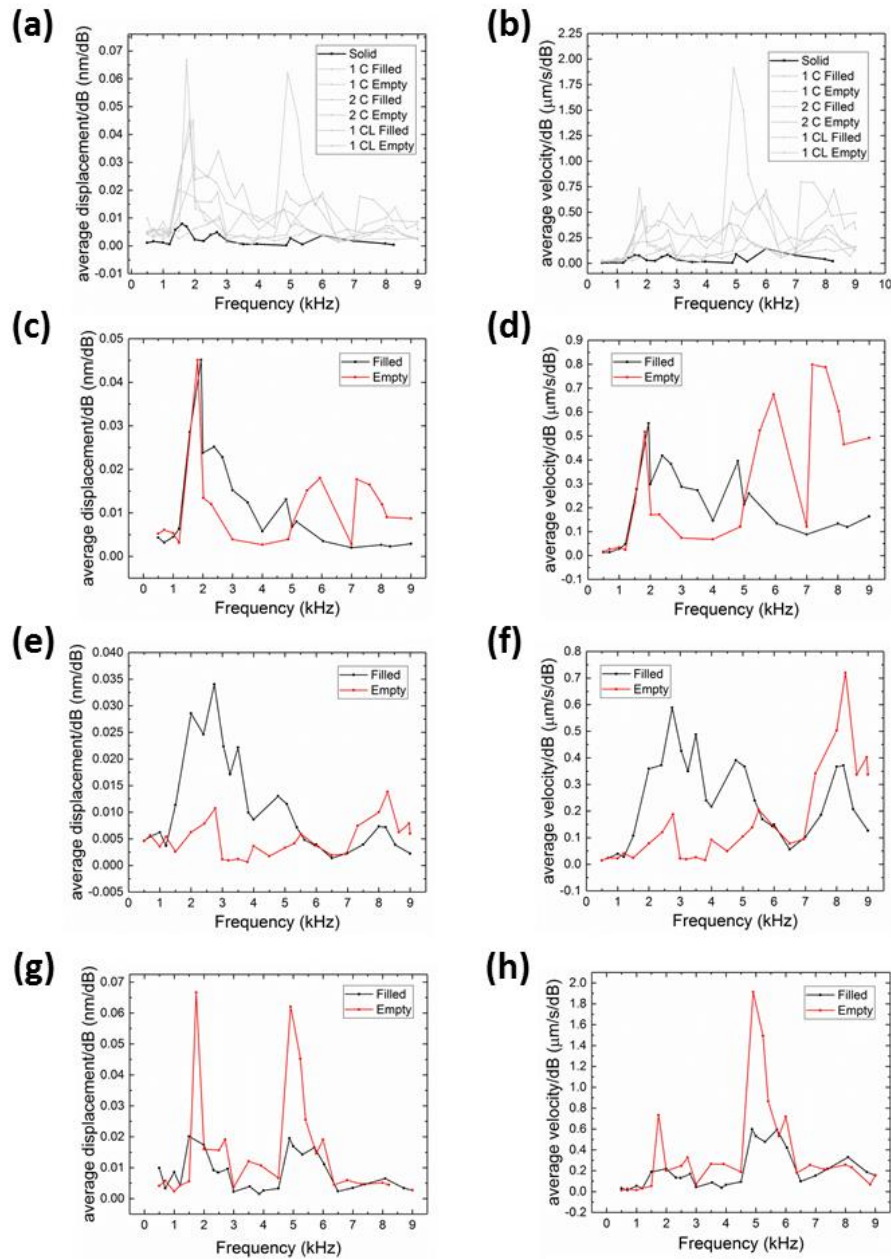


Fig. 6.37. Plots of the average surface displacement and average surface velocity of the 3D-printed resonators when stimulated under single tone stimuli. (a) and (b) show the plots for all the samples in which the ones without cavities are highlighted. (c) and (d) show the plots of the resonators presenting one cavity, (e) and (f) show the plots of the resonators presenting two square cavities, and (g) and (h) show the plots of the resonators presenting two rectangular cavities.

frequencies, such a tendency was observed to be inverted, and the air-filled cavity then presented higher values for both v_s and d . The resonator featuring two square cavities showed no noticeable difference between air- and IPA-filled cavities up to 1 kHz, but presented larger values of both v_s and d at higher frequencies when the cavities were IPA-filled. As in the previous sample, such a tendency was inverted at frequencies higher than 5 kHz. Finally, the resonator with rectangular cavities presented values of both v_s and d of the same order of magnitude over the entire studied frequency spectrum, with the exceptions of 1.74 kHz and 4.91 kHz being the strongest characteristic modes of the air-filled resonator.

Single-tone analysis of resonators additionally revealed the presence of TWs, which direction of propagation over the membrane was observed to present a strong dependency on the number and shape of the cavities, as well as a dependency over the filling (air or IPA), as shown in Fig. 6.38. This allowed a more in-depth analysis of the characteristics of the TWs, determining both their v_{TW} and λ_{TW} as in the previous case. The results are reported in Table 6.13.

Sample	v_{TW} (m/s)	λ_{TW} (m/s)	f (m/s)
Solid	53.89	7.70	7.00
1 Cavity Empty	5.76	4.80	1.20
1 Cavity Filled	10.34	4.34	2.38
2 Cavities Empty			
LHS Cavity	23.95	5.32	4.50
RHS Cavity	28.94	6.43	4.50
2 Cavities Filled			
LHS Cavity	32.38	5.76	5.63
RHS Cavity	24.44	4.34	5.63
2 Cavities Rec. Empty			
Top Cavity	18.68	6.23	3.86
Bottom Cavity	19.66	6.55	3.86
2 Cavities Rec. Filled			
Top Cavity	48.41	12.56	3.00
Bottom Cavity	45.20	11.73	3.00

Table 6.13. Values of v_{TW} and λ_{TW} of the measured TWs onto the 3D-printed samples.

The first comment that must be done on Table 6.13 is the impossibility to compare v_{TW} and λ_{TW} at a same frequency for different resonators, as TWs appear at different frequencies on each sample. Furthermore, a noticeable increase in v_{TW} with frequency (irrespective of the number, shape, and filling of the cavities) can be observed in the thick region of the membrane (see Fig. 6.39), as reported in several biological species [234–238]. Both the velocity and wavelength of the TW measured on the solid resonator matched the results presented in the previous case. The resonator with one cavity presented a constant λ_{TW} irrespective of its filling, whereas its v_{TW} was doubled up when IPA- filled. The resonator with two square cavities also presented a roughly constant λ_{TW} irrespective of the filling of the cavities, whereas the velocity of propagation was shown to slightly increase when the cavities were IPA-filled. Another important feature of this resonator is that the TWs present on the membrane (one on top of each cavity, as shown in Fig. 6.38) travelled in phase and propagated in the same direction. Finally, the resonator presenting two rectangular cavities was shown to present a significant increase

of both v_{TW} and λ_{TW} when the cavities were IPA-filled, and, additionally, it was the only of the resonators measured to present TWs in several directions at the same time: the first observed non-static oscillation pattern was observed to be two TWs travelling in opposite directions and adding up on top of each cavity, all of them travelling in phase and in the same direction (see Fig. 6.38f). When this same resonator was IPA-filled, TWs were observed over each of the cavities, travelling in phase and in the same direction at 3.86 kHz and travelling in phase and opposite direction at 5 kHz (see Fig. 6.38g-h).

Thus, it can be concluded from Table 6.13 and Fig. 6.38 that the mechanical properties of the TWs do not only depend on the local material properties of the membrane (or more generally the propagation media) but also on both their internal and external morphology and structure, leading to specific TW patterns that drive the mechanical deflection of the membrane generated by acoustic stimuli to distinct locations.

These observations suggest that the mechanical properties of TWs may vary with number, shape, distribution, and content of cavities contained within the membrane of resonators. Such findings unveil possible explanations for the presence of lipid-filled cavities within the locust TM; this peculiar feature of the insect's anatomy likely facilitates sound detection by passively increasing TW amplitude and velocity. This means that acoustic stimuli of lower intensity will still be able to generate TWs of a large enough amplitude to trigger transduction mechanisms within the relevant cohort of scolopidia, and will do so more efficiently thanks to their increased velocity.

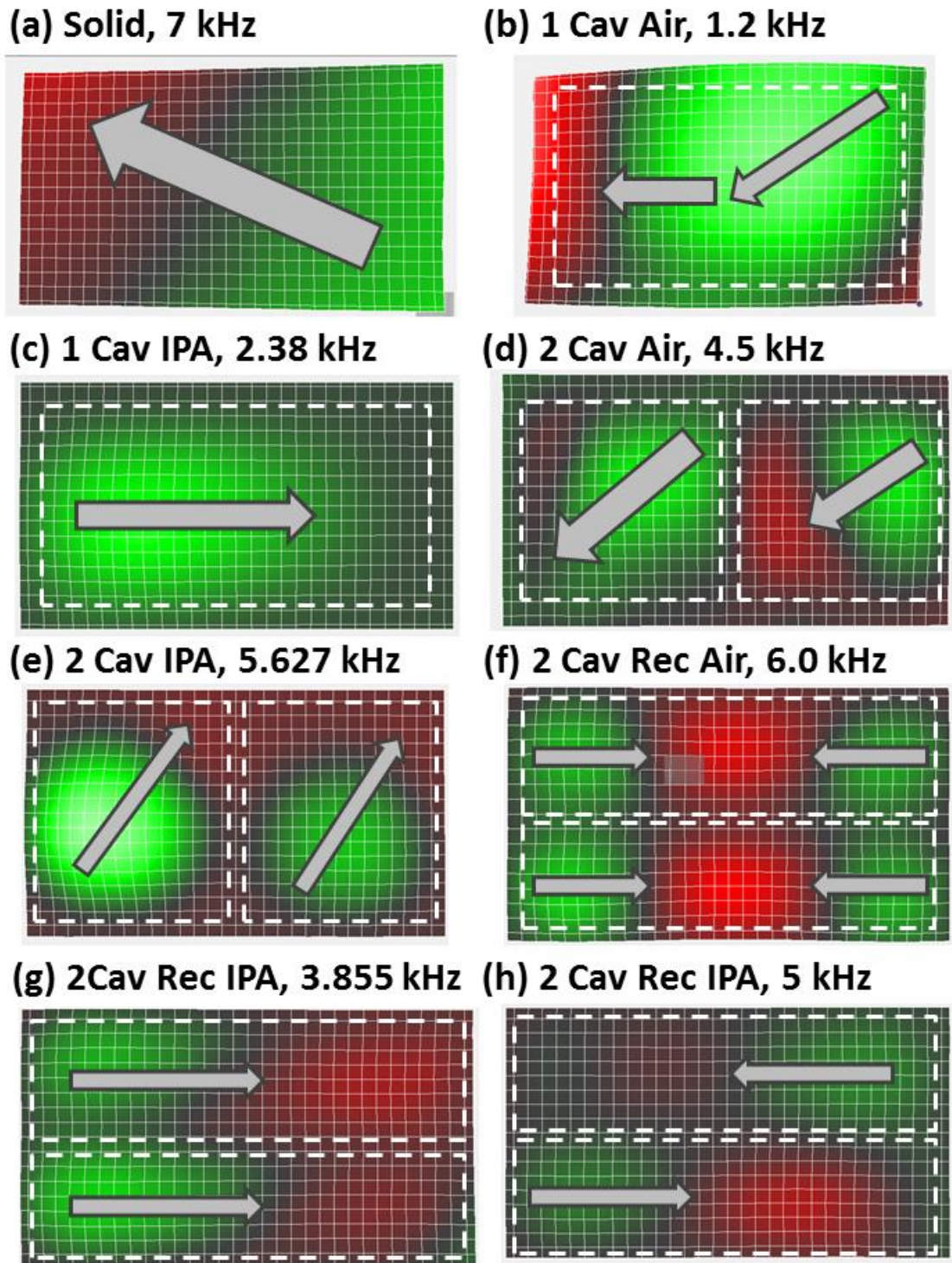


Fig. 6.38. 3D LDV top images of the thick membrane of the different 3D-printed resonators when stimulated by single tone stimuli. Traveling waves and their direction of propagation can be seen for (a) the solid resonator at 7 kHz, (b) 1 air-filled cavity resonator at 1.2 kHz, (c) 1 IPA-filled cavity resonator at 2.38 kHz, (d) 2 air-filled square cavities resonator at 4.5 kHz, (e) 2 IPA-filled square cavities resonator at 5.627 kHz, (f) 2 air-filled cavities resonator at 6 kHz, (g) 2 air-filled rectangular cavities resonator at 3.86 kHz, and (h) 2 IPA-filled rectangular cavities resonator at 5 kHz.

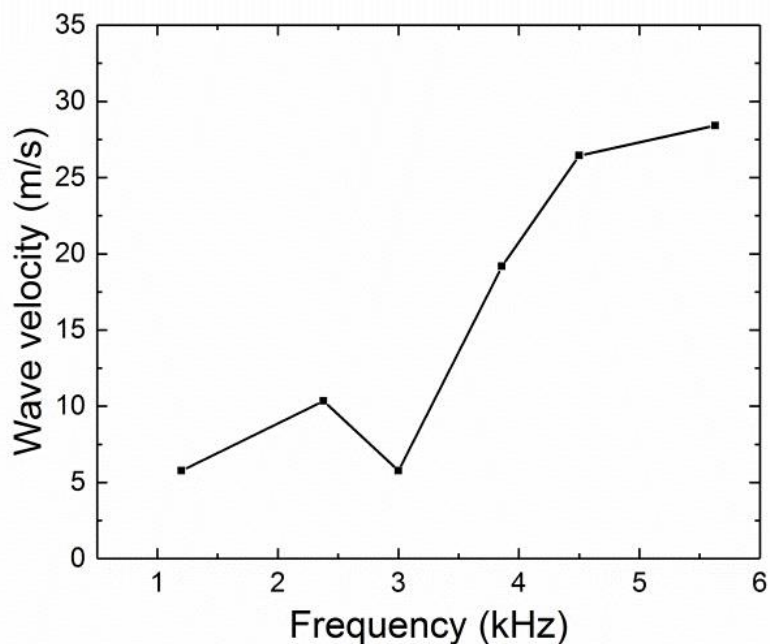


Fig. 6.39. Wave velocity of the traveling waves measured in the different BEMA (Irgacure 819 1 wt%, and SUDAN I 0.2 wt%) resonators at several frequencies

6.3.3 Functional bioinspired systems

Once the response of the 3D-printed locust TM-based resonators has been thoroughly studied, revealing their matching behaviour, it is possible to add a layer of 3D-printable BaTiO_3 @BEMA piezocomposite onto each of the membranes of the resonator described in the first approach. The sensor was 3D-printed in BEMA (1 wt% Irgacure 819, 0.2 wt% SUDAN I), and the piezoelectric layers were 3D-printed using $\text{BTO}(33)$ @BEMA(1 wt% Irgacure819, 0.2 wt% SUDAN I), as shown in Fig. 6.40. Hence, not only its mechanical characterization but also its piezoelectric (both direct and converse) response can be studied. The piezoelectric response of the sensor is shown in Fig. 6.41 and Fig. 6.42.

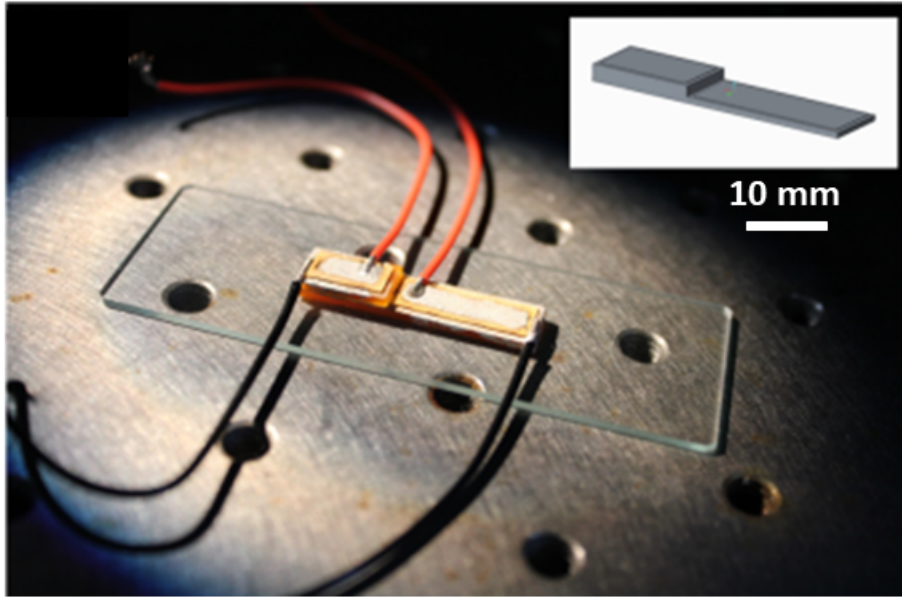


Fig. 6.40. Locust tympanal membrane (TM) bio-inspired 3D-printed sensor and its corresponding computer-aided design (CAD) file. The sensor is divided into two regions: a thick region and a thin region responding to lower and higher frequencies, respectively. The sensor was 3D-printed in BEMA (1 wt% Irgacure 819, 0.2 wt% SUDAN I), and the piezoelectric layers were 3D-printed using BTO(33)@BEMA(1 wt% Irgacure819, 0.2 wt% SUDAN I).

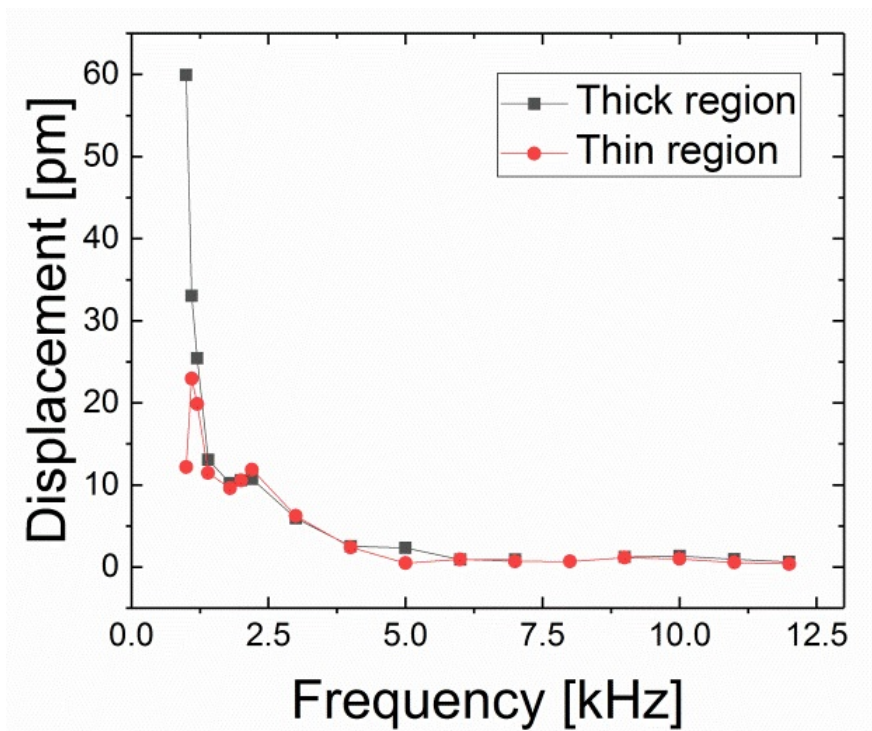


Fig. 6.41. Average displacement values of the different regions of the 3D-printed bio-inspired piezoelectric sensor when electrically stimulated within the frequency range of 1 kHz to 17 kHz.

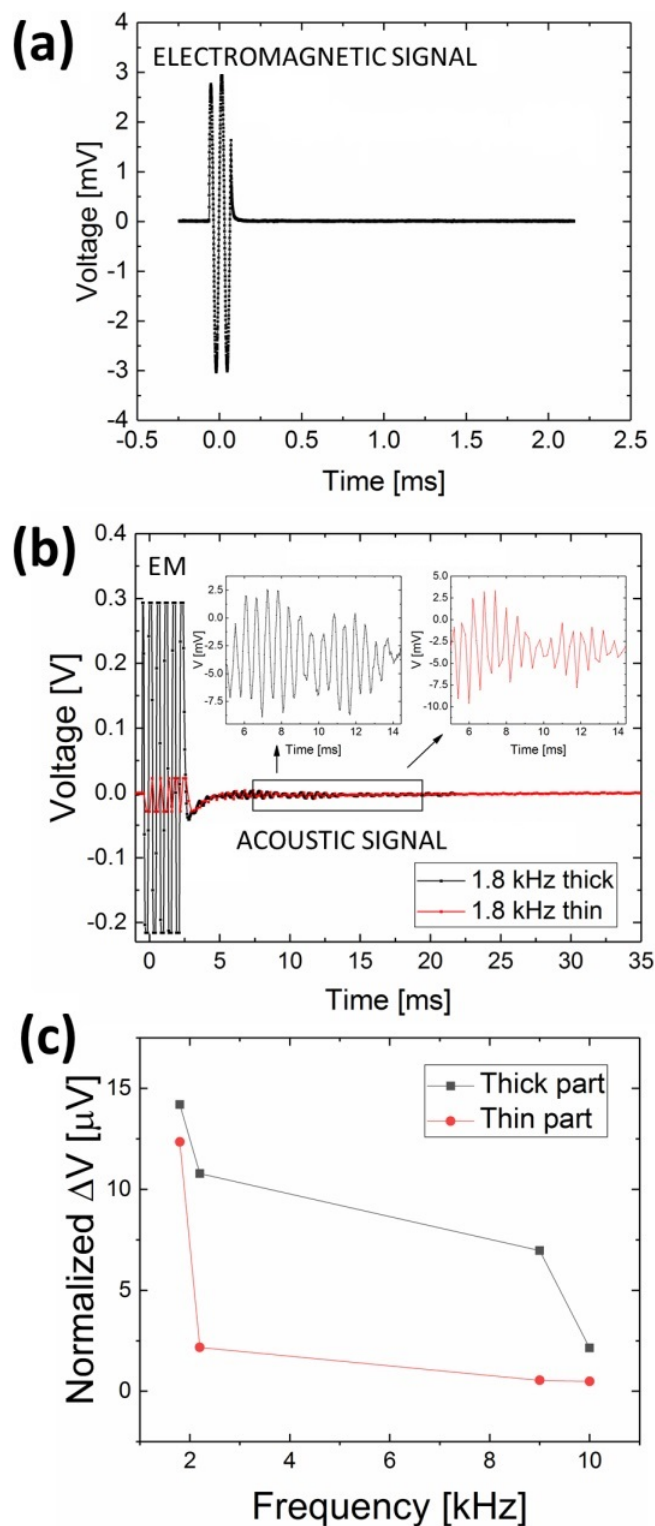


Fig. 6.42. (a) Shows the acoustic input signal at 15 kHz consisting of a burst of 2 cycles every 100 ms. (b) Shows the response of the 3D-printed device with its two well-differentiated regions at 1.8 kHz after averaging 128 times. The response is divided between the electromagnetic and the acoustic responses. The same experiment was performed within the range of 1 kHz to 17 kHz in steps of 1 kHz. (c) Shows the normalized values of the output voltage of the different regions under acoustic stimulation within the same frequency range, revealing larger output voltages in the thick region at all the studied frequencies.

Both the direct and converse piezoelectric responses were studied after poling the device at an electric field of 2.4 kV/mm. The output voltage was measured when the sensor was excited at single frequencies within the range of 1 kHz to 17 kHz, recording both the reference (Fig. 6.41a) and the piezoelectric response (Fig. 6.41b) at all frequencies. Bursts of 2 cycles every 100 ms, at an amplitude of $20 V_{pp}$ were used, varying the distance between the loudspeaker and the sensor from 35 cm to 10 cm in order to properly discern between electromagnetic and acoustic response. An acoustic amplifier was needed to reach high SPL dB values in order to get an electrical output from the sensor due to its low piezoelectric coefficient, as presented in Section 6.2.4. Moreover, a charge amplifier (factor 475) was also needed to properly record an electrical signal generated by direct piezoelectric effect of the 3D-printed device. The voltage difference, ΔV , was normalized against the B & K microphone output.

Even though the sensor seemed to respond to all frequencies within the range of 1 kHz to 17 kHz, it was only possible to clearly discern an electrical output arising from acoustic signals at 1.8 kHz, 2.2 kHz, 9 kHz, and 10 kHz, as shown in Fig. 6.42c. The two regions of the 3D-printed sensor were poled at an electric field of 2.4 kV/mm, for 1 hour at 120° in silicon oil. To confirm the piezoelectric behaviour of the 3D-printable piezoelectric material, the converse piezoelectric effect was tested for the two different regions of the sensor using sinusoidal inputs at different frequencies at amplitude of 10 V, and the mechanical deflection was measured using the 3D LDV (Fig. 6.41). Mechanical deflection of the sensor was successfully measured on both the thick and thin regions of the 3D-printed device. Reliable results were obtained up to 5 kHz, where higher amplitudes of motion were obtained below 3 kHz, and mechanical deflections of the same order of magnitude were obtained from 3 kHz to 5 kHz. At higher frequencies, all the values were measured to be at noise level.

Due to the low d_{33} coefficient of the 3D-printable piezoelectric material, it was not trivial to obtain a clear piezoelectric signal at all the studied frequencies. Therefore, the same experiments using the same set up were performed using PVDF films (50 μm thickness, $d_{33} = 30 \text{ pC/N}$) instead of the piezoelectric 3D-printable material, leading to the same acoustic frequency selection observed on the 3D LDV under acoustic stimulation, as it can be seen from Fig. 6.43.

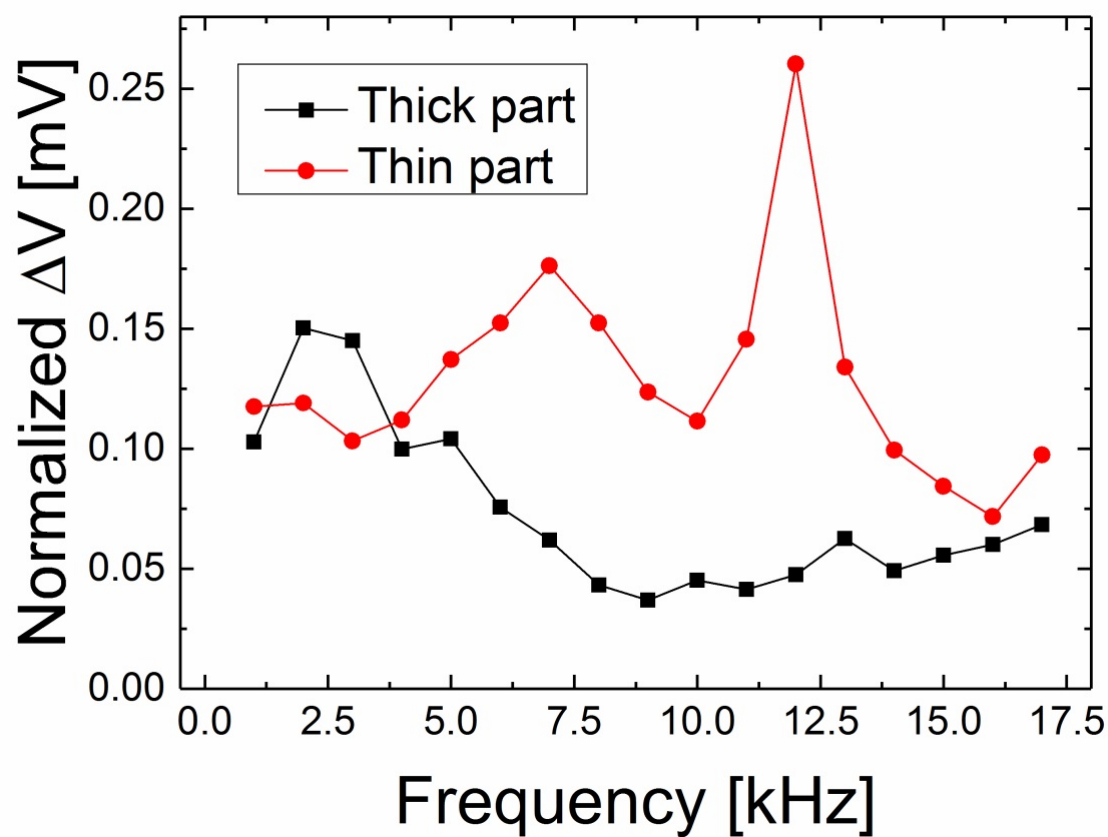


Fig. 6.43. Normalized values of the output voltage of the different regions of the sensor with PVDF films under acoustic stimulation within the frequency range of 1 kHz to 17 kHz in steps of 1 kHz revealing larger voltage outputs at lower frequencies in the thick region and *vice versa*.

Fig. 6.43 shows the normalized values of the output voltage when the sensor was stimulated under an acoustic field, leading to frequency selectivity, as the thick membrane shows larger amplitudes of motion at low frequencies, and the thin membrane shows larger amplitudes of motion at high frequencies, showing a sub-peak at 7 kHz. As in the previous case, the direct piezoelectric effect of the PVDF-based resonator can be obtained, as shown in Fig. 6.44.

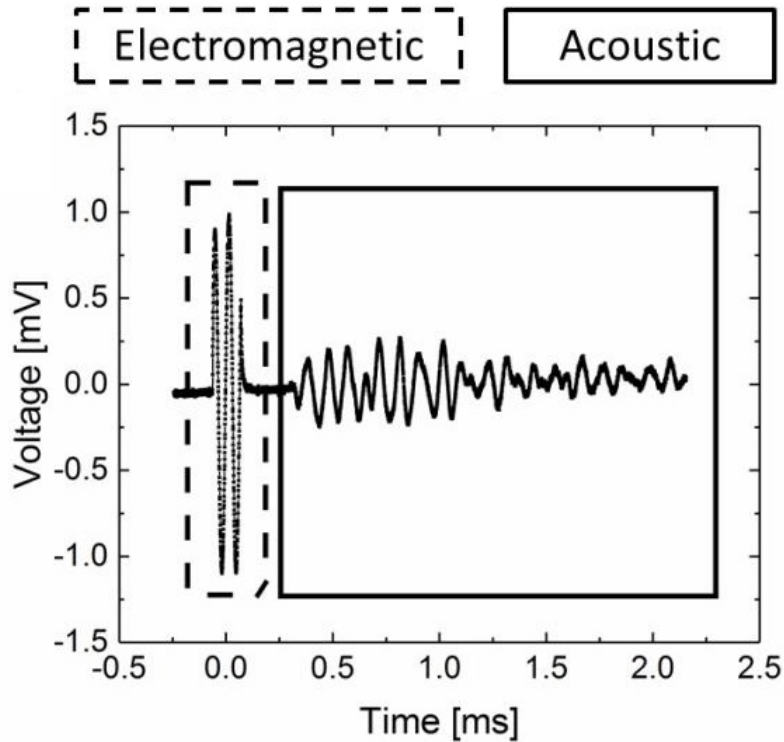


Fig. 6.44. Plot of the response of the device when two PVDF films are attached onto it, which is divided into the electromagnetic (dash-line box) and the acoustic response (solid-line box). The same experiment was repeated for all the sensors in the range of frequencies from 1 kHz to 17 kHz. All the measurements were averaged 128 times.

Comparing figures 6.41 to 6.44 it can be observed that a much clearer response in terms of acoustic frequency selectivity is obtained in the resonators using PVDF films. This is because the d_{33} value of PVDF is ten times larger than that measured for the piezoelectric 3D-printable BaTiO₃-based material. Hence, once the d_{33} coefficient of the 3D-printable material is improved, a response like the one observed in the PVDF-based resonator is expected to be measured. Nevertheless, this study shows the possibility to develop 3D-printable bioinspired functional resonators.

Chapter 7

Conclusions and Future Work

Several mathematical models have been developed to theoretically explain the motion of the locust TM. All the presented models are based on the theory of coupled oscillators, which allows not only to fit the mechanical motion of the membrane but also permits to theoretically predict the stiffness of the membrane. Several observations have been done in this regard: when the membrane is studied as an unforced system, the fitting of its motion is not accurate enough, leading to the introduction of a driving term that simulates the acoustic driving force. The addition of this term dramatically improves the fitting of the membrane motion. Nevertheless, it was noted that adding a damping term is indeed necessary in order to replicate in a more realistic manner the motion of the biological system. The introduction of such a term showed the best of fittings.

As discussed in early chapters of the thesis, the presence of DPOAEs was observed to take place on the locust TM, a feature that has been shown to be mathematically described using the Duffing oscillator theory. In order to develop a consistent model, coupling several Duffing oscillators has been shown in this thesis, providing a mathematical explanation to this nonlinear phenomenon. Furthermore, this model does not only provide a phenomenological description of the motion of the locust TM, but it also provides key information about the mechanisms that drive the generation of DPOAEs. Whereas it is strongly believed that such a phenomenon is driven by active biological processes, in this work it has been shown that a passive component reliant on the structure of the membrane helps producing them. It must be noted that, even though these models provide an accurate description of several phenomena taking place on the locust TM, as more oscillators and springs are introduced into the model a better fitting will be obtained. This is because of the discrete approximation of a continuum problem.

The development of several 3D-printable polymers with contrasting properties, not only mechanical but also further physical properties such as piezoelectricity and magnetism, has been achieved. Although the morphological study of the developed materials reveals the presence of NP agglomeration and clusters when adding functional fillers, the resulting composites are functionalised. Nevertheless, this is a factor to take into consideration to improve the properties of both the piezoelectric and the magnetic composites, as NP cluster formation is thought to be the main reason for low d_{33} coefficients, as well as presenting an issue during the poling process due to local variations of piezoelectric domains. Furthermore, it has been successfully shown that the mechanical properties of the developed 3D-printable composite materials follow the Sato & Furukawa model, presenting an increase of its elastic modulus as filler fraction increases.

The piezoelectric coefficient of the developed 3D-printable piezoelectric materials has been thoroughly studied as a function of several parameters. Firstly, it was observed that 500 nm NP size provided better output results than 200 nm NP-based composites. This is thought to be due to the generation of a larger dipole within the 500 nm NPs than the one generated in 200 nm NPs. The optimum output response is given at a NP concentration of 75 wt% for both PEGDA- and BEMA-based composites after poling them in silicon oil at 120°C for one hour. Big differences of d_{33} coefficients were measured when comparing samples poled for 30 minutes and 1 hour, respectively. When increasing the poling time to 2 hours under the same conditions, no significant differences were measured (up to differences of 4.88%). Furthermore, it was observed that irrespective of the sample's thickness and filler fraction, none of the piezoelectric composites would tolerate voltages higher than 3 kV, probably due to the structure of the polymer. Although the best d_{33} coefficient has been measured at 75 wt%, sub-peaks have been observed to take place at 33 wt% and 40 wt% for PEGDA- and BEMA-based composites, respectively. These sub-peaks are attributed to the balance between mass and generated output current.

The piezoelectric response of the 3D-printable material was successfully tested by both direct and converse piezoelectric processes, making it suitable for several applications in a more time-efficient process. Although further research is required to improve the d_{33} coefficient of the resulting polymer-based composite without losing 3D-printing resolution, the results showed the possibility to 3D-print piezoelectric composite materials that can be used for biomimetic applications such as acoustic frequency selectivity.

The possibility to 3D-print magnetic composites materials has also been demonstrated in this thesis, revealing the possibility to build permanent and non-permanent magnets presenting contrasting physical properties. Irrespective of the type and size of the filler, the highest and lowest M_r values were measured at the highest and lowest wt%, respectively, where the non-homogeneous distribution of NPs within the polymeric matrix play an important role. On the other hand, H_c values were observed to be independent of NP concentration and distribution, presenting larger values in magnetite-based composites, therefore suggesting that H_c values rely on NP size. The hybrid material presented a good combination of the aforementioned properties, even though further investigation needs to be done to optimise its response. The ΔM analyses revealed the presence of a dipolar coupled system in which the interactions between magnetic domains tend to demagnetize the material, a phenomenon arising from anisotropy effects. The relative permeability values were determined to be within the range of 1.60-3.08, depending on both the filler type and concentration.

The size of the NPs was theoretically determined by fitting the $M - H$ hysteresis loops using a Langevin function, which confirmed the superparamagnetic behaviour of the Fe-based composites. It was noted that the calculated size of the Fe_3O_4 -based composites did not match that reported by the manufacturer, suggesting that the Langevin function provides a good explanation of superparamagnetic systems, but does not work as well for those materials presenting a different magnetic behaviour. SEM images suggest agglomeration sizes of a few microns, but this technique did not permit an exact determination of the NPs size.

The 3D-printed materials were measured to be soft permanent magnets with randomly oriented magnetic domains, as expected after an STL process under normal conditions. In this study it has been proved that it is possible to re-arrange the orientation of the magnetic domains by using a simple poling process using a NdFeB permanent magnet with a well-defined polarity. Under this set up, the magnetic domains of the 3D-printed samples align with the field lines of the NdFeB magnet. Analogously to what happens in a piezoelectric poling process, the intensity and duration of the external applied field has been observed to have no influence in the magnetic properties of the 3D-printed samples, only re-arranging the direction of their magnetic domains.

Although the magnetic material was not used to develop any bio-inspired sensor, using the STL

3D-printing approach presents a great opportunity to produce polymer-based magnets with contrasting physical properties, as they may be of use in a variety of different fields that are in the zenith of their development, mainly in biotechnology, biomedicine and medical science, for example [80–83]. Furthermore, specific micro- and nano-systems that can be manipulated using external magnetic fields can also be developed in an easy and personalized way through additive manufacturing processes, allowing for applications in information storage, computer science, acoustic and non-acoustic pressure sensors, or the development of transformers amongst many other applications. The main follow-up objective of this thesis is to combine this material with the piezoelectric one to develop a 3D-printable acoustic pressure sensor.

A common feature between the piezoelectric and the magnetic 3D-printable composite materials is the importance of keeping a proper balance between 3D-printing resolution and output signal.

A set of sensors were developed using commercial 3D-printable material to prove the possibility of passive sound amplification. All of them presented the same membrane diameter and thickness, only changing the structure where the sound field was focused on. Whereas the reference membrane was observed to present the lowest amplitude values, the cochlear tubes presented a significant degree of the membrane motion when the same stimuli were played. The tube without interface presented a main amplification peak around 10 kHz, whereas that without an interface showed several amplification peaks, being the most relevant ones around 2 and 18 kHz. This difference in acoustic amplification between the two resonators is thought to be created by resonance phenomena that take place in the different regions of the structure. The tube without mechanical interface does not present this phenomenon, supporting this hypothesis. Furthermore, it was observed that these structures do not only amplify specific frequencies but they also perform a noise filtering process in a passive manner. Further study needs to be done in this regard, as it is hypothesised that using liquid fillers inside one of the regions of the interfaced tube would provide better amplification factors due to the change of the velocity of sound in liquids, as well as its acoustic impedance.

Once the possibility to perform acoustic processes in a passive manner using 3D-printed resonators by simply changing their structure and morphology was proved, several resonators bioinspired on the locust TM were developed, confirming their behaviour using simulation techniques. COMSOL confirmed the

experimental acoustic behaviour of the new 3D-printed sensor, which reproduces the behaviour observed on the locust TM, presenting higher amplitudes of motion at low frequencies on the thick region, and the opposite trend on the thin region, leading to acoustic frequency selection. The piezoelectric response of the 3D-printable material was successfully tested by both direct and converse piezoelectric processes. When adding cavities within the thick region of the 3D-printed membrane and studying its response under both acoustic wideband and single-tone stimulation, a decrease of characteristic frequencies in IPA-filled cavities was measured, a fact previously reported to happen when bubbles get enclosed within other liquid-filled cavities, leading to a dependence of the pressure produced by the fluid with bubble position. All the resonators with cavities (either if gas- or IPA-filled) presented larger values of both surface velocity and displacement than the control sample, which presented no cavities. The number, size, shape, and distribution of the cavities within the thick region of the membrane were observed to play an important role in the presence and direction of propagation of the TWs. Nevertheless, the velocity of TWs was shown to increase in the thick region of the membrane irrespective of such parameters. These observations clarify the selective pressures that might have driven the evolution of lipid-filled cavities in the locust auricular anatomy. Indeed, these features likely render the membrane comparatively more efficient in capturing low-intensity signals at ecologically-relevant frequencies, and passively augment the likelihood that those signals will activate scolopidia and trigger acoustic transduction. Furthermore, beside clarifying the role of known anatomical adaptations of the locust TM, all these observations could further inspire the development of new acoustic sensors, transducers, and actuators as part of the development of more efficient tonotopic microphones, bionic ears, and hearing aid devices.

Although this thesis presents an in-depth study of how to develop 3D-printed bioinspired functional sensors, there are still some areas open to further research to improve the quality of the resulting products. The main area needing further investigation is that involving the development of 3D-printable materials. Whereas resolution of the resulting parts does not present a problem, optimisation of the piezoelectric properties needs to be further studied, as d_{33} coefficients of around 3 pm/V still require amplification circuitry in order to obtain clear signals. Furthermore, these d_{33} values are still far away from d_{33} coefficients of other commercial (although they are not 3D-printable) materials such as PVDF, which presents d_{33} values up to 30 pm/V [239].

When working with cochlear tubes, the response of the membranes was only studied when the

acoustic field perpendicularly impinged it, but further research must be done in terms of directionality of the incoming sound to make sure that the amplification process takes place not only in one incoming sound direction but in all of them. Furthermore, horn-like structures are thought to provide better amplification factors, a feature that is also worth studying.

In terms of bioinspired sensors, it has been shown how to 3D-print a resonator able to perform acoustic frequency selectivity using two different regions. Nevertheless, this structure can be improved by adding more steps that oscillate at diverse frequencies in an efficient manner. This becomes one of the main priorities in terms of future work. Linked to this step, studying the effect of cavities within the membrane in different manners must also be further studied, as they have proved to provide several advantages in terms of surface displacement amplification and frequency selectivity. Lastly, combining these features (a structure of variable thickness with cavities embedded in it) becomes a real challenge in terms of future work.

In summary, this thesis presents, on one hand, the possibility to mathematically describe acoustic biophysical phenomena taking place on the locust TM and, on the other hand, the possibility to develop STL 3D-printable functional materials. These two fields can be combined to 3D-print polymer-based bio-inspired sensors, actuators, and resonators exploiting relevant biological features for technological applications that could be used, for instance, as hearing aid devices or microphones that could be potentially implemented in laptops, tablets, or phones. This process, nevertheless, is not a one-way process but it is actually twofold as development of bio-inspired sensors also provides some insight about biological phenomena that are not fully understood. Hence, this thesis shows how it is possible to establish a positive feedback relationship between these two fields, as shown in Fig. 7.1.

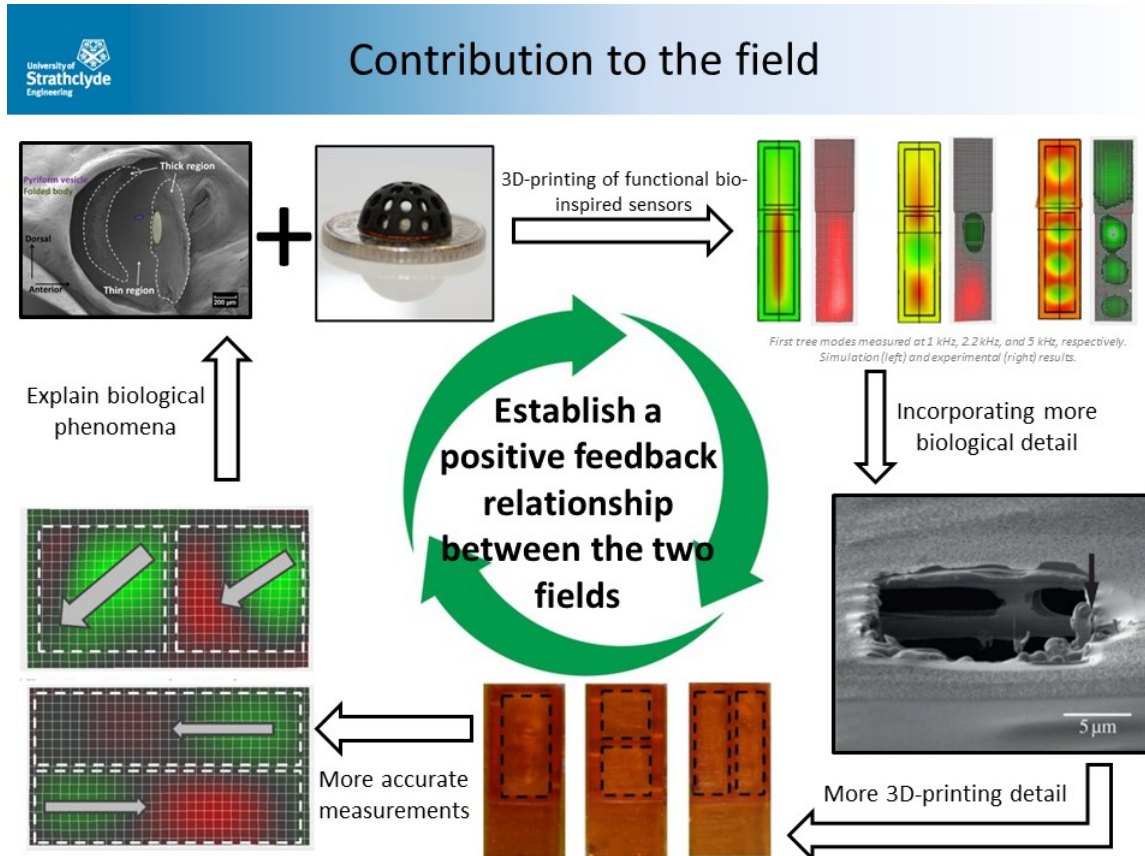


Fig. 7.1. Representation of the positive feedback full process. Starting with mathematical models of biological phenomena combined with functional 3D-printable materials it is possible to develop simple bio-inspired sensors and compare its response with the predicted by simulation techniques. Once such behaviour has been confirmed, it is possible to add an extra degree of complexity into the system and 3D-print more realistic samples and measure them again to compare its behaviour with that of the simplified sample. The observed differences can provide explanation of why specific biophysical phenomena take place in concrete organs of some animals.

Appendix A

Solution to the single Duffing oscillator

As presented in Eq.(1.21), the Duffing equation is given by:

$$\frac{d^2x}{dt^2} + 2\epsilon k \frac{dx}{dt} + x + \epsilon x^3 = \epsilon F_0 \cos(\omega t + \delta) \quad (\text{A.1})$$

considering the initial conditions to be given by:

$$x(0) = A \quad , \quad \frac{dx}{dt}(0) = 0 \quad (\text{A.2})$$

It is possible to solve the Duffing equation using the perturbation theory introducing the change of variable $\theta = \omega t$. Thus, Eq.(A.1) becomes:

$$\omega^2 \frac{d^2x}{d\theta^2} + 2\epsilon k \omega \frac{dx}{d\theta} + x + \epsilon x^3 = \epsilon F_0 \cos(\theta + \delta) \quad (\text{A.3})$$

$$\omega^2 \ddot{x} + 2\epsilon k \omega \dot{x} + x + \epsilon x^3 = \epsilon F_0 \cos(\theta) \cos(\delta) - \epsilon F_0 \sin(\theta) \sin(\delta) \quad (\text{A.4})$$

where the terms $\ddot{x} \equiv d^2x/d\theta^2$, and $\dot{x} \equiv dx/d\theta$ have been introduced for simplicity. Consider that both x and ω can be expanded in terms of ϵ such that:

$$\begin{cases} x = x_0(\theta) + \epsilon x_1(\theta) + \epsilon^2 x_2(\theta) + \dots \\ \omega = \omega_0 + \epsilon \omega_1 + \epsilon^2 \omega_2 + \dots \end{cases} \quad (\text{A.5})$$

Considering the terms proportional to ϵ , the initial conditions that define the system become:

$$\begin{cases} x_0(0) = A \quad , \quad x_i(0) = 0 \\ \dot{x}_0(0) = 0 \quad , \quad \dot{x}_i(0) = 0 \end{cases} \quad (\text{A.6})$$

for $i = 1, 2, 3, \dots$. Combining Eq.(A.4), Eq.(A.5), grouping in terms of ϵ , and considering an undamped system (*i.e.* $\delta = 0$):

$$\begin{cases} \omega_0^2 \ddot{x}_0 + x_0 = 0 \\ \omega_0^2 \ddot{x}_1 + x_1 = -2\omega_0\omega_1 \ddot{x}_0 - x_0^3 + F_0 \cos(\theta) \end{cases} \quad (\text{A.7})$$

The top equation in system A.7 corresponds to the terms proportional to ϵ^0 , whereas the bottom equation of the system correspond to those terms proportional to ϵ . It must be noted that for more accurate results, higher order terms can be further considered. Using the initial conditions it is easy to obtain the solution of the top equation presented in Eq.(A.7).

$$\begin{cases} x_0(\theta) = A \cos(\theta) \\ \omega_0 = 1 \end{cases} \quad (\text{A.8})$$

Introducing Eq.(A.8) into the bottom equation of the system of equations (A.7):

$$\ddot{x}_1 + x_1 = \left(F_0 + 2\omega_1 A - \frac{3A^3}{4} \right) \cos(\theta) - \frac{A^3}{4} \cos(3\theta) \quad (\text{A.9})$$

Getting rid of secular terms¹ it is possible to obtain ω_1 :

$$\begin{aligned} F_0 + 2\omega_1 A - \frac{3A^3}{4} &= 0 \\ 2\omega_1 &= \frac{3A^2}{4} - \frac{F_0}{A} \end{aligned} \quad (\text{A.10})$$

Combining Eq.(A.10) and Eq.(A.9) it is possible to obtain the analytic solution for $x_1(\theta)$.

$$x_1(\theta) = A_1 \cos(\theta) + B_1 \sin(\theta) + \frac{A^3}{32} \cos(3\theta) \quad (\text{A.11})$$

And the initial conditions presented in Eq.(A.6) require:

$$\begin{cases} A_1 = -A^3/32 \\ B_1 = 0 \end{cases} \quad (\text{A.12})$$

Thus, Eq.(A.11) finally becomes:

$$x_1(\theta) = -\frac{A^3}{32} \cos(\theta) + \frac{A^3}{32} \cos(3\theta) = \frac{A^3}{32} [\cos(3\theta) - \cos(\theta)] \quad (\text{A.13})$$

Thus, from the expansions in Eq.(A.5) it is possible to easily find the analytical solutions of both the motion and the frequency of the oscillator:

$$\boxed{x(\theta) = A \cos(\theta) + \frac{A^3 \epsilon}{32} [\cos(3\theta) - \cos(\theta)]} \quad (\text{A.14})$$

¹Secular terms are long non-periodic variation of the resonant frequency which when equal to 0 lead to non-periodic responses.

$$\boxed{\omega^2 = 1 + \epsilon \frac{3A^2}{4} - \frac{\epsilon F_0}{A}} \quad (\text{A.15})$$

This same system can be solved when considering a shifting phase (δ) generated by the exciting force that introduces a damping component into the system. Thus, Eq.(A.7) becomes:

$$\begin{cases} \omega_0^2 \ddot{x}_0 + x_0 = 0 \\ \omega_0^2 \ddot{x}_1 + x_1 = F_0 \cos(\theta) \cos(\delta) - F_0 \sin(\theta) \sin(\delta) - x_0^3 - 2\omega_0 k x_0 - 2\omega_0 \omega_1 \ddot{x}_0 \end{cases} \quad (\text{A.16})$$

And following the same process as before, it is possible to obtain the solution for $x_0(\theta)$ and ω_0 .

$$x_0(\theta) = A \cos(\theta) \omega_0 = 1 \quad (\text{A.17})$$

Therefore, the bottom equation in the system of equations (A.16) becomes:

$$\ddot{x}_1 + x_1 = \left[F_0 \cos(\delta) + 2\omega_1 A - \frac{3A^3}{4} \right] \cos(\theta) + [-F_0 \sin(\delta) + 2kA] \sin(\theta) - \frac{A^3}{4} \cos(3\theta) \quad (\text{A.18})$$

Making secular terms equal to 0 in order to remove long non-periodic solutions:

$$F_0 \sin(\delta) = 2kA \rightarrow \sin(\delta) = \frac{2kA}{F_0} \quad (\text{A.19})$$

$$F_0 \cos(\delta) + 2\omega_1 A - \frac{3A^3}{4} = 0 \quad (\text{A.20})$$

$$2\omega_1 A = \frac{3A^3}{4} - F_0 \cos(\delta) \rightarrow 2\omega_1 = \frac{3A^2}{4} \pm \sqrt{1 - \frac{4k^2 A^2}{F_0^2}} \quad (\text{A.21})$$

And following the same procedure as in the previous case it is possible to determine the analytical solution to $x_1(\theta)$, which is given by:

$$x_1(\theta) = \frac{A^3}{32} [\cos(3\theta) - \cos(\theta)] \quad (\text{A.22})$$

Thus:

$$\boxed{x(\theta) = A \cos(\theta) + \frac{\epsilon A}{32} [\cos(3\theta) - \cos(\theta)]} \quad (\text{A.23})$$

$$\boxed{\omega^2 = 1 + \frac{3\epsilon A^2}{4} \pm \frac{\epsilon F_0}{A} \sqrt{1 - \frac{4k^2 A^2}{F_0^2}}} \quad (\text{A.24})$$

When studying the equations of motion of a mechanical system it is possible to plot the *phase space* representation, which consists in plotting the set of velocities of the oscillator versus their corresponding position. When a system describes a periodic movement, the completion of a cycle will make the oscillator come back to its initial position. Another relevant representation in non-linear systems is the representation of the amplitude of motion of the oscillator over the frequency (or squared frequency, ω^2). This is because in forced/damped non-linear systems, the output of this latter representation will

present a bending defining the type of spring that defines it. Lastly, it is possible to study the power spectrum of the system by working out the discrete Fourier transform (f_k):

$$P(\omega_k) = f_k \bar{f}_k = |f_k|^2 \quad (\text{A.25})$$

Thus, as Eq.(A.23) presents a non-linear term and the exciting frequency is proportional to 3ω , a peak in the power spectrum at such frequency is expected to appear apart from ω (see Fig. A.1a). Now, if the oscillator is forced by two different frequencies ω_1 and ω_2 (with $\omega_2 > \omega_1$), the solution of the system will be proportional to both frequencies, and when expanding the non-linear term ($\propto x + \epsilon x^3$), intermodulation terms will appear (see Fig. A.1b).

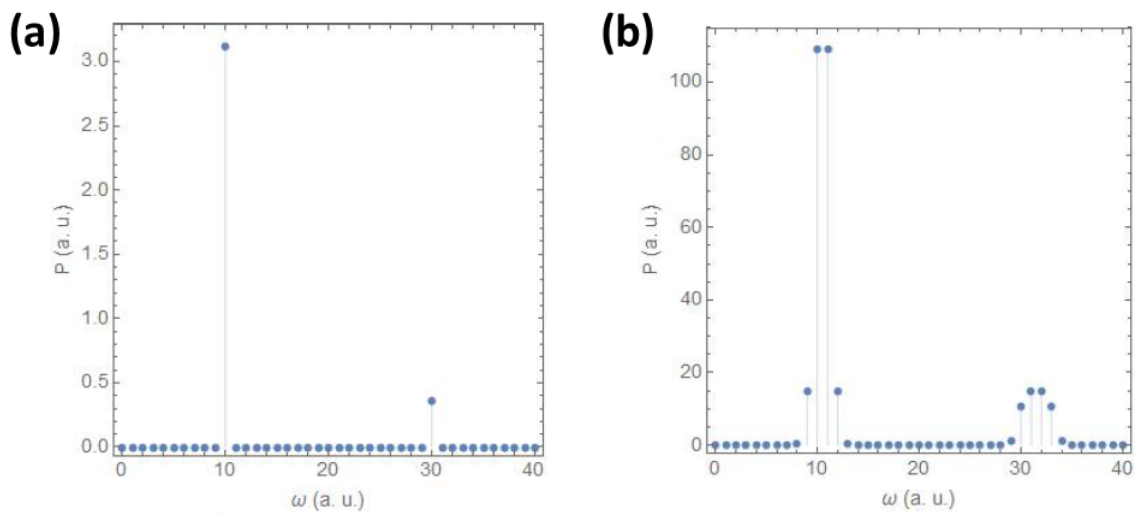


Fig. A.1. (a) Shows the power spectrum of a single Duffing oscillator excited by a single frequency ω_1 . The plot was obtained by using the parameters $\epsilon = 5$, $A = 1$, and $\omega_1 = 10$, all of them expressed in arbitrary units (a. u.). (b) Shows the power spectrum of a single Duffing oscillator excited by two external frequencies at the same time. The plot was obtained by using the parameters $\epsilon = 5$, $A = 1$, $\omega_1 = 10$, and $\omega_2 = 11$

Appendix B

Application of the perturbation method to solve the double-frequency driven single Duffing oscillator

This Appendix presents a detailed explanation of how Eq.(6.61) and Eq.(6.64) have been solved. To solve both equations the Poincaré-Lindstedt method was applied, consisting of getting rid of the secular terms present in the equations of motion (as briefly described in Appendix A). This method is one of the several approximations to the so-called perturbation method, which assumes that the final solution is an expansion in powers of a small control parameter (in our case ϵ). The first equation to solve using this approximation is Eq.(6.61):

$$\omega^2 y'' + \gamma \omega y' + \frac{k}{m} y + \epsilon y^3 = \frac{\epsilon F}{m} [\cos(\theta + \delta) + \cos(1.1\theta + \delta)] \quad (\text{B.1})$$

and assuming the expansion in powers of ϵ :

$$\begin{cases} y(\theta) = y_0(\theta) + \epsilon y_1(\theta) \\ \omega(\theta) = \omega_0 + \epsilon \omega_1 \end{cases} \quad (\text{B.2})$$

The equation of motion becomes:

$$\omega_0^2 y_0'' + \gamma \omega_0 y_0' + \frac{k}{m} y_0 + \epsilon \left(\omega_0^2 y_1'' + \omega_0 \gamma y_1' + \frac{k}{m} y_1 + 2\omega_0 \omega_1 y_0'' + \gamma \omega_1 y_0' + y_0^3 \right) = \frac{\epsilon F}{m} [\cos(\theta + \delta) + \cos(1.1\theta + \delta)] \quad (\text{B.3})$$

where those terms proportional to ϵ^2 or higher order are not considered. Grouping the terms by order of ϵ :

$$\begin{cases} \omega_0^2 y_0'' + \gamma \omega_0 y_0' + \frac{k}{m} y_0 = 0 \\ \omega_0^2 y_1'' + \gamma \omega_0 y_1' + \frac{k}{m} y_1 = \frac{F}{m} [\cos(\theta + \delta) + \cos(1.1\theta + \delta)] - 2\omega_0 \omega_1 y_0'' - \gamma \omega_1 y_0' - y_0^3 \end{cases} \quad (\text{B.4})$$

The solution to the top equation of the system (B.4) is given by:

$$y_0(\theta) = Ae^{-\gamma\theta} \cos(\theta) \quad (\text{B.5})$$

Introducing Eq.(B.5) into the bottom equation of the system (B.5):

$$\begin{aligned} & \omega_0^2 Ae^{-\gamma\theta} [\gamma^2 \cos(\theta) + 2\gamma \sin(\theta) - \cos(\theta)] + \gamma \omega_0 Ae^{-\gamma\theta} [-\gamma \cos(\theta) - \sin(\theta)] + \frac{k}{m} Ae^{-\gamma\theta} \cos(\theta) = \\ & = \omega_0^2 Ae^{-\gamma\theta} \gamma^2 \cos(\theta) + 2\gamma \omega_0^2 Ae^{-\gamma\theta} \sin(\theta) - \omega_0^2 Ae^{-\gamma\theta} \cos(\theta) - \gamma^2 \omega_0 Ae^{-\gamma\theta} \cos(\theta) - \gamma \omega_0 Ae^{-\gamma\theta} \sin(\theta) + \\ & + \frac{k}{m} Ae^{-\gamma\theta} \cos(\theta) \cos(\theta) = \cos(\theta) \left[\omega_0^2 \gamma^2 Ae^{-\gamma\theta} - \omega_0^2 Ae^{-\gamma\theta} - \gamma^2 \omega_0 Ae^{-\gamma\theta} + \frac{k}{m} Ae^{-\gamma\theta} \right] + \\ & + \sin(\theta) [2\gamma \omega_0^2 Ae^{-\gamma\theta} - \gamma \omega_0 Ae^{-\gamma\theta}] \end{aligned} \quad (\text{B.6})$$

As secular terms must be equal to 0, the system is simplified to:

$$\begin{cases} \omega_0^2 \gamma^2 Ae^{-\gamma\theta} - \omega_0^2 Ae^{-\gamma\theta} - \gamma^2 \omega_0 Ae^{-\gamma\theta} + \frac{k}{m} Ae^{-\gamma\theta} = 0 \\ 2\gamma \omega_0^2 Ae^{-\gamma\theta} - \gamma \omega_0 Ae^{-\gamma\theta} = 0 \end{cases} \quad (\text{B.7})$$

It must be noted that this system has 4 different possible solutions of ω_0 and all of them lead to the same behaviour of the oscillator:

$$\omega_0^{(1)} = 0 \quad (\text{B.8})$$

$$\omega_0^{(2)} = 1/2 \quad (\text{B.9})$$

$$\omega_0^{(3,4)} = \frac{m\gamma^2 \pm \sqrt{m}\sqrt{-4\gamma^2 k + 4k + \gamma^4 m}}{2m(\gamma^2 - 1)} \quad (\text{B.10})$$

For the solutions $\omega_0^{(3,4)}$ it must be noted that the system is undamped, $\omega_0^{(3,4)} = \sqrt{\frac{k}{m}}$, which is the expected solution for an harmonic oscillator. Considering $\omega_0^{(1)}$, $\omega_0^{(2)} = 0$ (as $\omega^2 = \omega_0^2 + 2\epsilon\omega_0\omega_1$), which does not make physical sense, meaning that terms proportional to ϵ^2 or higher order should be considered. Now, considering $\omega_0^{(2)}$ and taking into account that $\omega = \omega_0 + \epsilon\omega_1$ and, therefore, $\omega^2 \propto \omega_0^2 + 2\epsilon\omega_0\omega_1$ (as terms proportional to ϵ^2 or higher are not considered) it is easy to find $\omega_1^{(2)}$ from Eq.(B.4) that ω^2 is given by:

$$\omega^{(2)2} = \frac{1}{4} + \frac{\epsilon F}{m\gamma^2} \left[1 \pm \sqrt{1 + \frac{2\gamma^2}{A} - \frac{3mA^2\gamma^2}{2F}} \right] \quad (\text{B.11})$$

Finally, studying the cases $\omega_0^{(3,4)}$ following the same solving process:

$$\begin{aligned}
 \omega_0^2 y_1'' + \gamma \omega_0 y_1' + \frac{k}{m} y_1 &= \frac{F}{m} \cos(\theta) \cos(\delta) - \frac{k}{m} \sin(\theta) \sin(\delta) + \frac{k}{m} \cos(1.1\theta + \delta) + \\
 -2\omega_0 \omega_1 A e^{-\gamma\theta} [\gamma^2 \cos(\theta) + 2\gamma \sin(\theta) - \cos(\theta)] &- \gamma \omega_1 A e^{-\gamma\theta} [-\gamma \cos(\theta) - \sin(\theta)] + \\
 -A^3 e^{-3\gamma\theta} \left[\frac{3}{4} \cos(\theta) + \frac{1}{4} \cos(3\theta) \right] &= \\
 = \cos(\theta) \left[\frac{F}{m} \cos(\delta) - 2\omega_0 \omega_1 \gamma^2 A e^{-\gamma\theta} + 2\omega_0 \omega_1 A e^{-\gamma\theta} + \gamma^2 \omega_1 A e^{-\gamma\theta} - \frac{A^3}{4} e^{-3\gamma\theta} \right] &+ \\
 + \sin(\theta) \left[-\frac{F}{m} \sin(\delta) - 4\omega_0 \omega_1 \gamma A e^{-\gamma\theta} + \gamma \omega_1 A e^{-\gamma\theta} \right] &+ \frac{F}{m} \cos(1.1\theta + \delta) - \frac{A^3}{4} e^{-3\gamma\theta} \cos(3\theta)
 \end{aligned} \tag{B.12}$$

and making secular terms equal to zero:

$$\sin(\delta) = \frac{m\gamma\omega_1 A e^{-\gamma\theta}}{F} [1 - 4\omega_0] \tag{B.13}$$

where it must be noted that the system is undamped, $\delta = 0, \pi, \dots$, which is the expected solution for an harmonic oscillator. Recalling $Z \equiv 1 - 4\omega_0$ for simplicity:

$$\cos(\delta) \approx 1 - \frac{m^2 \gamma^2 \omega_1^2 A^2 Z^2}{2F^2} \tag{B.14}$$

assuming small time scales because the time of detection/processing sound of the locust is of the order of the microsecond (*i.e.* $e^{-\gamma/\theta} \rightarrow 0$):

$$\omega_1^{(3,4)} \left[2\omega_0 A + \gamma^2 A - 2\omega_0 A \gamma^2 - \omega_1 \frac{m\gamma^2 A^2 Z^2}{2F} \right] = \frac{3A^3}{4} - \frac{F}{m} \tag{B.15}$$

$$\omega_1^{(3,4)} = \frac{F \left[4\omega_0 (1 - \gamma^2) + 2\gamma^2 \pm \sqrt{4(2\omega_0 \gamma^2 - 2\omega_0 - \gamma^2)^2 - 2\gamma^2 Z^2 \left(\frac{3A^3 m}{F} - 4 \right)} \right]}{2Am\gamma^2 Z^2} \tag{B.16}$$

$$\omega_1^{(3,4)2} = \omega_0^{(3,4)2} + \frac{\epsilon F \omega_0^{(3,4)2}}{Am\gamma^2 Z^2} \left[4\omega_0 (1 - \gamma^2) + 2\gamma^2 \pm 4(2\omega_0 \gamma^2 - 2\omega_0 - \gamma^2)^2 - 2\gamma^2 Z^2 \left(\frac{3A^3}{4} - 4 \right) \right] \tag{B.17}$$

The representations of $\omega^{(3,4)2}$ and $\omega^{(2)2}$ are shown in Fig. B.1.

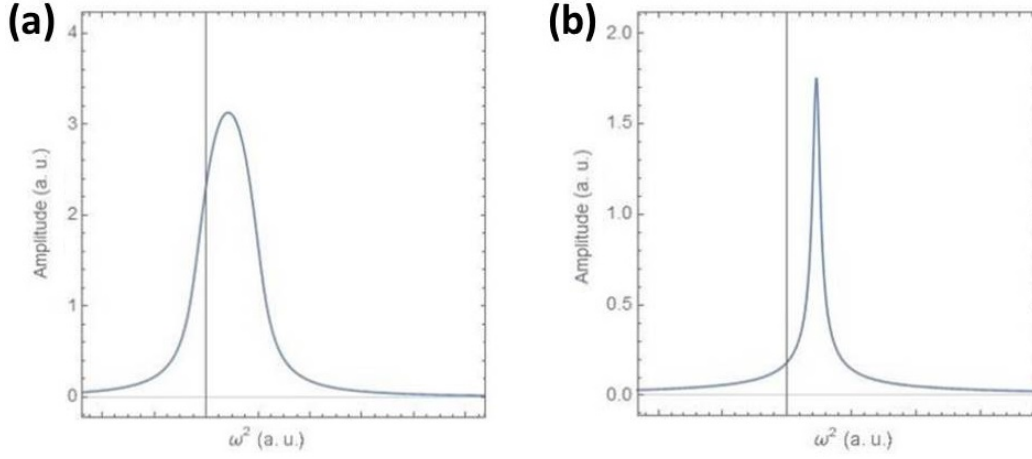


Fig. B.1. (a) and (b) Show the amplitude vs frequency representation of $\omega^{(2)2}$ and $\omega^{(3,4)2}$, respectively. The parameters used to plot these graphics are $\epsilon = 1$, $F = 10$, $m = 1$, $\gamma_1 = 1$, and $k = 1$, all in arbitrary units.

This same process was used to solve Eq.(6.64), in which ϵ controls both the degree of non-linearity of the system and the damping.

$$\omega^2 y'' + \epsilon \gamma \omega y' + \frac{k}{m} y + \epsilon y^3 = \frac{\epsilon F}{m} [\cos(\theta + \delta) + \cos(1.1\theta + \delta)] \quad (\text{B.18})$$

$$\begin{aligned} & (\omega_0 + \epsilon \omega_1)^2 (y_0'' + \epsilon y_1'') + \epsilon \gamma (\omega_0 + \epsilon \omega_1) (y_0' + \epsilon y_1') + \frac{k}{m} (y_0 + \epsilon y_1) + \epsilon (y_0 + \epsilon y_1)^3 = \quad (\text{B.19}) \\ & = (\omega_0^2 + 2\epsilon \omega_0 \omega_1 + \epsilon^2 \omega_1^2) (y_0'' + \epsilon y_1'') + \epsilon \gamma (\omega_0 y_0' + \epsilon \omega_0 y_1' + \epsilon \omega_1 y_0' + \epsilon^2 \omega_1 y_1') + \frac{k}{m} y_0 + \frac{k\epsilon}{m} y_1 + \\ & + \epsilon (y_0^3 + 3y_0^2 y_1 \epsilon + 3y_0 y_1^2 \epsilon^2 + y_1^3 \epsilon^3) = \frac{\epsilon F}{m} [\cos(\theta + \delta) + \cos(1.1\theta + \delta)] \end{aligned}$$

getting rid of the terms proportional to ϵ^2 and higher:

$$\omega_0^2 y_0'' + \omega_0^2 \epsilon y_1'' + 2\epsilon \omega_0 \omega_1 y_0'' + \epsilon \gamma \omega_0 y_0' + \frac{k}{m} y_0 + \frac{\epsilon k}{m} y_1 + \epsilon y_0^3 = \frac{\epsilon F}{m} [\cos(\theta + \delta) + \cos(1.1\theta + \delta)] \quad (\text{B.20})$$

grouping terms of ϵ :

$$\begin{cases} \omega_0^2 y_0'' + \frac{k}{m} y_0 = 0 \\ \omega_0^2 y_1'' + 2\omega_0 \omega_1 y_0'' + \gamma \omega_0 y_0' + \frac{k}{m} y_1 + y_0^3 = \frac{F}{m} [\cos(\theta + \delta) + \cos(1.1\theta + \delta)] \end{cases} \quad (\text{B.21})$$

The top equation can be easily solved, and its solution is given by:

$$y_0(\theta) = A \cos(\theta) \quad , \quad \omega_0 = \sqrt{k/m} \quad (\text{B.22})$$

Introducing y_0 and ω_0 into the bottom equation of the system of equations (B.21):

$$\omega_0^2 y_1'' + \frac{k}{m} y_1 = \frac{F}{m} \cos(\theta) \cos(\delta) - \frac{F}{m} \sin(\theta) \sin(\delta) + \frac{F}{m} \cos(1.1\theta + \delta) - 2\omega_1 \omega_0 y_0'' - \gamma \omega_0 y_0' - y_0^3 \quad (\text{B.23})$$

And the right-hand side of Eq.(B.23) becomes:

$$\begin{aligned} \frac{F}{m} \cos(1.1\theta + \delta) - \frac{A^3}{4} \cos(3\theta) + \cos(\theta) + \cos(\theta) \left[\frac{F}{m} \cos(\delta) + 2\omega_0\omega_1 A - \frac{3A^3}{4} \right] + \\ + \sin(\theta) \left[-\frac{F}{m} \sin(\delta) + \gamma\omega_0 A \right] = 0 \end{aligned} \quad (\text{B.24})$$

and making secular terms equal to 0 it is easy to find that:

$$\sin(\delta) = \frac{\sqrt{\gamma k}}{F} \gamma A \quad (\text{B.25})$$

and thus:

$$\cos(\delta) = \left[1 - \frac{mk\gamma^2 A^2}{F^2} \right]^{1/2} \quad (\text{B.26})$$

and, therefore:

$$\begin{aligned} \left[\frac{F^2}{m^2} - \frac{k}{m} \gamma^2 A^2 \right]^{1/2} + 2\omega_0\omega_1 A = \frac{3A^3}{4} \\ \omega_1 = \frac{3A^2}{8} \sqrt{\frac{k}{m}} \pm \frac{1}{2} \sqrt{\frac{F^2}{A^2 km} - \gamma^2} \end{aligned} \quad (\text{B.27})$$

and considering $\omega^2 = \omega_0^2 + 2\epsilon\omega_0\omega_1$:

$$\omega^2 = \frac{k}{m} + \epsilon \left[\frac{3A^2 k}{4m} \pm \sqrt{\frac{k}{m} \left(\frac{F^2}{A^2 km} - \gamma^2 \right)} \right] \quad (\text{B.28})$$

The representation of the amplitude of motion as a function of squared frequency can be observed in Fig. B.2. It must be noted that the two cases discussed in this Appendix generate intermodulation

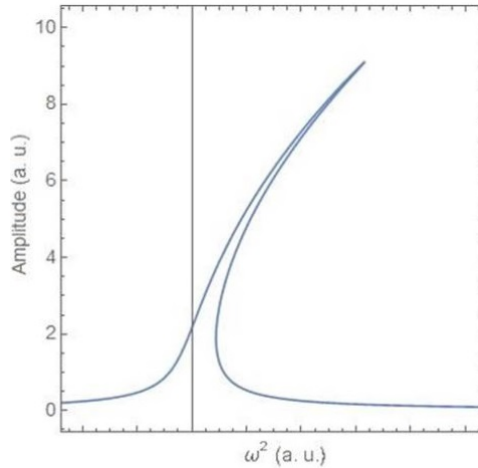


Fig. B.2. Amplitude vs ω^2

products, even not explicitly discussed, in a complete analogous way as described in Appendix A, as their generation depends on the non-linear governing the system as well as a multiple-frequency excitation.

Appendix C

Solution to a system of coupled Duffing oscillators

In this Appendix the solution to a system of two coupled Duffing oscillators is presented, as described in subsection 6.1.3. To do so the perturbation method has also been applied, as done in previous cases (Appendix B). The system to solve is:

$$\begin{cases} m \frac{d^2 y_1}{dt^2} + \epsilon \frac{dy_1}{dt} + \epsilon y_1^3 + k(y_2 - y_1) - \epsilon F_0 \cos(\omega t + \delta) = 0 \\ m \frac{d^2 y_2}{dt^2} + \epsilon \frac{dy_2}{dt} + \epsilon y_2^3 + k(y_2 - y_1) \end{cases} \quad (\text{C.1})$$

Introducing the change of variable $\theta = \omega t$, and the expansions around ϵ are given by $\omega = \omega_0 - \epsilon \omega_1$, $y_i = y_i^{(0)} + \epsilon y_i^{(1)}$ (with $i = 1, 2$). Introducing, for simplicity, $\ddot{y}_i^{(j)} = d^2 y_i^{(j)} / d\theta^2$, $\dot{y}_i^{(j)} = dy_i^{(j)} / d\theta$ (with $j = 0, 1$). Thus it is possible to rewrite the equations of the system of equations (C.1) and to group them in terms proportional to different orders of ϵ . Thus, two different systems of equations are obtained, one proportional to ϵ^0 and another one proportional to ϵ :

$$\begin{cases} m\omega_0^2 \ddot{y}_1^{(0)} + k(y_2^{(0)} - y_1^{(0)}) = 0 \\ m\omega_0^2 \ddot{y}_2^{(0)} + k(y_1^{(0)} - y_2^{(0)}) = 0 \end{cases} \quad (\text{C.2})$$

$$\begin{cases} m\omega_0^2 \ddot{y}_1^{(1)} - 2m\omega_0\omega_1 \dot{y}_1^{(0)} + \omega_0 \dot{y}_1^{(0)} + (y_1^{(0)})^3 + k(y_2^{(1)} - y_1^{(1)}) = F_0 \cos(\theta) \\ m\omega_0^2 \ddot{y}_2^{(1)} - 2m\omega_0\omega_1 \dot{y}_2^{(0)} + \omega_0 \dot{y}_2^{(0)} + (y_2^{(0)})^3 + k(y_1^{(1)} - y_2^{(1)}) = 0 \end{cases} \quad (\text{C.3})$$

The system of equations (C.2) can be easily solved using the linear coupled oscillator theory. Doing so, the equations of motion $y_i^{(0)}(\theta)$ can be found. Normalising $\omega_0 = 1$:

$$\begin{cases} \ddot{y}_1^{(0)} + \frac{k}{m} (y_2^{(0)} - y_1^{(0)}) = 0 \\ \ddot{y}_2^{(0)} + \frac{k}{m} (y_1^{(0)} - y_2^{(0)}) = 0 \end{cases} \quad (\text{C.4})$$

which in matrix form can be expressed as:

$$\begin{pmatrix} \ddot{y}_1^{(0)} \\ \ddot{y}_2^{(0)} \end{pmatrix} + \begin{pmatrix} -k/m & k/m \\ k/m & -k/m \end{pmatrix} \begin{pmatrix} y_1^{(0)} \\ y_2^{(0)} \end{pmatrix} = \begin{pmatrix} 0 \\ 0 \end{pmatrix} \quad (\text{C.5})$$

To obtain the eigenvalues of the system it is necessary to diagonalise the matrix:

$$\mathbf{W} = \begin{pmatrix} -k/m & k/m \\ k/m & -k/m \end{pmatrix} \quad (\text{C.6})$$

$$\det(\mathbf{W} - \lambda^2 \mathbf{1}) = \begin{vmatrix} -k/m - \lambda^2 & k/m \\ k/m & -k/m - \lambda^2 \end{vmatrix} = 0 \quad (\text{C.7})$$

which leads to the eigenvalues:

$$\boxed{\lambda_1^2 = -2k/m, \quad \lambda_2^2 = 0} \quad (\text{C.8})$$

and the corresponding eigenvectors:

$$\boxed{\vec{\xi}_1 = 1/\sqrt{2}(-1, 1), \quad \vec{\xi}_2 = 1/\sqrt{2}(1, 1)} \quad (\text{C.9})$$

It is possible to build the matrix of eigenvectors \mathbf{U} and its corresponding transpose, \mathbf{U}^\top :

$$\mathbf{U} = \begin{pmatrix} -1/\sqrt{2} & 1/\sqrt{2} \\ 1/\sqrt{2} & 1/\sqrt{2} \end{pmatrix} = \mathbf{U}^\top \quad (\text{C.10})$$

And thus it is possible to build the diagonal matrix $\mathbf{W}_D = \mathbf{U}\mathbf{W}\mathbf{U}^\top$, and the matrix $\mathbf{A} \equiv \mathbf{U}\mathbf{T}^{1/2}$.

$$\mathbf{W}_D = \begin{pmatrix} -2k/m & 0 \\ 0 & 0 \end{pmatrix}, \quad \mathbf{A} = \begin{pmatrix} -\sqrt{m/2} & \sqrt{m/2} \\ \sqrt{m/2} & \sqrt{m/2} \end{pmatrix} \Rightarrow \mathbf{A}^{-1} = \begin{pmatrix} -1/\sqrt{2} & 1/\sqrt{2} \\ 1/\sqrt{2} & 1/\sqrt{2} \end{pmatrix} \quad (\text{C.11})$$

Therefore, the system of equations (C.5) can be expressed as:

$$\begin{pmatrix} \ddot{y}_1^{(0)} \\ \ddot{y}_2^{(0)} \end{pmatrix} + \mathbf{A}^{(-1)} \mathbf{W}_D \mathbf{A} \begin{pmatrix} y_1^{(0)} \\ y_2^{(0)} \end{pmatrix} = \begin{pmatrix} 0 \\ 0 \end{pmatrix} \quad (\text{C.12})$$

and introducing the generalised coordinates $\vec{\eta}^{(0)} = \mathbf{A}\vec{y}^{(0)}$:

$$\vec{\eta}_i^{(0)} + \mathbf{W}_D \vec{\eta}_i^{(0)} = \mathbf{0} \quad (\text{C.13})$$

$$\begin{cases} \ddot{\eta}_1^{(0)} + \lambda_1^2 \eta_1^{(0)} = 0 \\ \ddot{\eta}_2^{(0)} + \lambda_2^2 \eta_2^{(0)} = 0 \end{cases} \quad (\text{C.14})$$

which solutions are given by:

$$\begin{cases} \eta_1^{(0)}(\theta) = \eta_1^{(0)}(0) \cos(\lambda_1 \theta) + \frac{\dot{\eta}_1^{(0)}(0)}{\lambda_1} \sin(\lambda_1 \theta) \\ \eta_2^{(0)}(\theta) = \eta_2^{(0)}(0) + \dot{\eta}_1^{(0)}(0) \theta \end{cases} \quad (\text{C.15})$$

Thus:

$$\mathbf{y}_i^{(0)}(\theta) = \mathbf{A}^{(-1)} \hat{\eta}_i^{(0)}(\theta) = \begin{pmatrix} \eta_1^{(0)}(\theta) \\ \eta_2^{(0)}(\theta) \end{pmatrix} \quad (\text{C.16})$$

$$\hat{\eta}_i^{(0)}(\theta) = \mathbf{A} \mathbf{y}_i^{(0)} = \begin{pmatrix} -\sqrt{m/2} & \sqrt{m/2} \\ \sqrt{m/2} & \sqrt{m/2} \end{pmatrix} \begin{pmatrix} y_1^{(0)}(\theta) \\ y_2^{(0)}(\theta) \end{pmatrix} \quad (\text{C.17})$$

$$\Rightarrow \begin{cases} y_1^{(0)}(\theta) = 1/\sqrt{2m} (-\eta_1^{(0)}(\theta) + \eta_2^{(0)}(\theta)) \\ y_2^{(0)}(\theta) = 1/\sqrt{2m} (\eta_1^{(0)}(\theta) + \eta_2^{(0)}(\theta)) \end{cases}, \quad \begin{cases} \eta_1^{(0)}(\theta) = \sqrt{m/2} (-y_1^{(0)}(\theta) + y_2^{(0)}(\theta)) \\ \eta_2^{(0)}(\theta) = \sqrt{m/2} (y_1^{(0)}(\theta) + y_2^{(0)}(\theta)) \end{cases} \quad (\text{C.18})$$

And finally:

$$\begin{cases} y_1^{(0)}(\theta) = \frac{1}{2} \{ y_1^{(0)}(0) [1 + \cos(\lambda_1 \theta)] + y_2^{(0)}(0) [-1 + \cos(\lambda_1 \theta)] \} \\ y_2^{(0)}(\theta) = \frac{1}{2} \{ y_1^{(0)}(0) [1 - \cos(\lambda_1 \theta)] + y_2^{(0)}(0) [1 + \cos(\lambda_1 \theta)] \} \end{cases} \quad (\text{C.19})$$

Using $y_i^{(0)}$ and their respective initial conditions (*i.e.* $y_1^{(0)}(0) = A$, $y_2^{(0)}(0) = B$, and $\dot{y}_1^{(0)}(0) = \dot{y}_2^{(0)}(0) = 0$) it is possible to find the terms of the solution proportional to ϵ . Thus, the top and bottom equations of the system of equations (C.3) become, respectively:

$$\begin{aligned} m\ddot{y}_1^{(1)} + m\omega_1 \lambda_1^2 (A+B) \cos(\lambda_1 \theta) - \frac{\lambda_1}{2} (A+B) \sin(\lambda_1 \theta) + \frac{1}{16} (5A^3 - 3A^2B + 3AB^2 - 5B^3) + \\ + \frac{\cos(\lambda_1 \theta)}{32} [15A^3 - 3A^2B - 3AB^2 + 15B^3] + \frac{\cos(2\lambda_1 \theta)}{16} (3A^3 + 3A^2B - 3AB^2 - 3B^3) + \\ + \frac{\cos(3\lambda_1 \theta)}{32} (A^3 + 3A^2B + 3AB^2 + B^3) + k(y_2^{(1)} - y_1^{(1)}) - F_0 \cos(\theta) = 0 \end{aligned} \quad (\text{C.20})$$

$$\begin{aligned} m\ddot{y}_2^{(1)} - m\omega_1 \lambda_1^2 (A+B) \cos(\lambda_1 \theta) + \frac{\lambda_1}{2} (A+B) \sin(\lambda_1 \theta) + \frac{1}{16} (5A^3 + 3A^2B + 3AB^2 + 5B^3) \\ + \frac{\cos(\lambda_1 \theta)}{32} (-15A^3 - 3A^2B + 3AB^2 + 15B^3) + \frac{\cos(2\lambda_1 \theta)}{16} (3A^3 - 3A^2B - 3AB^2 + 3B^3) + \\ + \frac{\cos(3\lambda_1 \theta)}{32} (-A^3 + 3A^2B - 3AB^2 + B^3) + k(y_1^{(1)} - y_2^{(1)}) = 0 \end{aligned} \quad (\text{C.21})$$

To set the secular terms equal to 0 it is needed to treat the argument $\lambda_1 \theta$ as a phase shift in θ , such that $\lambda_1 \theta = \theta + \theta(\lambda_1 - 1)$. Naming $\varphi \equiv \theta(\lambda_1 - 1)$ and using the trigonometric relationships $\cos(\theta + \varphi) =$

$\cos(\theta) \cos(\varphi) - \sin(\theta) \sin(\varphi)$ and $\sin(\theta + \varphi) = \sin(\theta) \cos(\varphi) + \cos(\theta) \sin(\varphi)$, Eq.(C.20) and Eq.(C.21)

become:

$$\begin{aligned}
 & m\ddot{y}_1^{(1)} + \frac{1}{16} (5A^3 - 3A^2B + 3AB^2 - 5B^3) + k(y_2^{(1)} - y_1^{(1)}) + \\
 & + \cos(\theta) \left\{ \left[m\omega_1 \lambda_1^2 (A+B) + \frac{15A^3 - 3A^2B - 3AB^2 + 15B^3}{32} \right] \cos(\varphi) - \frac{\lambda_1}{2} (A+B) \sin(\varphi) - F_0 \right\} + \\
 & + \sin(\theta) \left\{ \left[-m\omega_1 \lambda_1^2 (A+B) - \frac{15A^3 - 3A^2B - 3AB^2 + 15B^3}{32} \right] \sin(\varphi) - \frac{\lambda_1}{2} (A+B) \cos(\varphi) \right\} + \\
 & + \frac{\cos(2\lambda_1\theta)}{16} (3A^3 + 3A^2B - 3AB^2 - 3B^3) + \frac{\cos(3\lambda_1\theta)}{32} (A^3 + 3A^2B + 3AB^2 + B^3) = 0 \quad (C.22)
 \end{aligned}$$

$$\begin{aligned}
 & m\ddot{y}_2^{(1)} + \frac{1}{16} (5A^3 + 3A^2B + 3AB^2 + 5B^3) + k(y_1^{(1)} - y_2^{(1)}) + \\
 & + \cos(\theta) \left\{ \left[-m\omega_1 \lambda_1^2 (A+B) + \frac{-15A^3 - 3A^2B - 3AB^2 + 15B^3}{32} \right] \cos(\varphi) + \frac{\lambda_1}{2} (A+B) \sin(\varphi) \right\} + \\
 & + \sin(\theta) \left\{ \left[m\omega_1 \lambda_1^2 (A+B) - \frac{-15A^3 - 3A^2B - 3AB^2 + 15B^3}{32} \right] \sin(\varphi) + \frac{\lambda_1}{2} (A+B) \cos(\varphi) \right\} + \\
 & + \frac{\cos(2\lambda_1\theta)}{16} (3A^3 - 3A^2B - 3AB^2 + 3B^3) + \frac{\cos(3\lambda_1\theta)}{32} (-A^3 + 3A^2B - 3AB^2 + B^3) = 0 \quad (C.23)
 \end{aligned}$$

It must be noted that Eq.(C.22) and Eq.(C.23) are equivalent when studying their secular terms (with the exception of F_0). If $\varphi \approx 0$ and seeking for non-trivial solutions of the system (*i.e.* $A \neq B$), it is possible to find ω_1 :

$$\omega_1 = \frac{1}{64k(A+B)} (15A^3 - 3A^2B - 3AB^2 + 15B^3 - F_0) \quad (C.24)$$

as $\omega^2 = \omega_0 + \epsilon\omega_1$:

$$\boxed{\omega^2 = 1 + \frac{\epsilon}{32k(A+B)} (15A^3 - 3A^2B - 3AB^2 + 15B^3 - F_0)} \quad (C.25)$$

Considering the initial driving phase δ , Eq.(C.20) becomes:

$$\begin{aligned}
 & m\ddot{x}_1^{(1)} + k(x_2^{(1)} - x_1^{(1)}) + \frac{1}{16} (5A^3 - 3A^2B + 3AB^2 - 5B^3) + \quad (C.26) \\
 & + \cos(\theta) \left\{ \left[m\omega_1 \lambda_1^2 (A+B) + \frac{15A^3 - 3A^2B - 3AB^2 + 15B^3}{32} \right] \cos(\varphi) - \frac{\lambda_1}{2} (A+B) \sin(\varphi) - F_0 \cos(\delta) \right\} + \\
 & \sin(\theta) \left\{ \left[-m\omega_1 \lambda_1^2 (A+B) - \frac{15A^3 - 3A^2B - 3AB^2 + 15B^3}{32} \right] \sin(\varphi) - \frac{\lambda_1}{2} (A+B) \cos(\varphi) + F_0 \sin(\delta) \right\} + \\
 & \frac{\cos(2\lambda_1\theta)}{16} (3A^3 + 3A^2B - 3AB^2 - 3B^3) + \frac{\cos(3\lambda_1\theta)}{32} (A^3 + 3A^2B + 3AB^2 + B^3) = 0
 \end{aligned}$$

Again, assuming $\varphi \approx 0$ and setting the secular terms equal to 0:

$$F_0 \sin(\delta) = \frac{\lambda_1}{2F_0} (A+B) \rightarrow \sin(\delta) = \frac{\lambda_1}{2F_0} (A+B) \Rightarrow \cos(\delta) = \sqrt{1 - \frac{\lambda_1^2 (A+B)^2}{4F_0^2}} \quad (C.27)$$

$$\Rightarrow \omega_1 = \frac{3(5A^2 - 6AB + 5B^2)}{32m\lambda_1^2} + \frac{F_0}{m\lambda_1^2 (A+B)} \sqrt{1 - \frac{\lambda_1^2 (A+B)^2}{4F_0^2}} \quad (C.28)$$

And, therefore, ω^2 is given by:

$$\boxed{\omega^2 = 1 + \frac{3\epsilon}{16m\lambda_1^2} (5A^2 - 6AB + 5B^2) \pm \frac{2\epsilon F_0}{m\lambda_1^2 (A+B)} \sqrt{1 - \frac{\lambda_1^2 (A+B)^2}{4F_0^2}}} \quad (C.29)$$

References

- [1] J. K. Carrow and A. K. Gaharwar. Bioinspired polymeric nanocomposites for regenerative medicine. *Macromolecular Chemistry and Physics*, 216(3):248–264, 2015.
- [2] Q. Ye, F. Zhou, and W. Liu. Bioinspired catecholic chemistry for surface modification. *Chemical Society Reviews*, 40(7):4244–4258, 2011.
- [3] S. Kim, C. Laschi, and B. Trimmer. Soft robotics: a bioinspired evolution in robotics. *Trends in Biotechnology*, 31(5):287–294, 2013.
- [4] R. Pfeifer, M. Lungarella, and F. Iida. The challenges ahead for bio-inspired soft robotics. *Communications of the ACM*, 55(11):76–87, 2012.
- [5] G. C. H. E. de Croon, M. A. Groen, C. De Wagter, B. Remes, R. Ruijsink, and B. W. van Oudheusden. Design, aerodynamics and autonomy of the delfly. *Bioinspiration & Biomimetics*, 7(2):025003, 2012.
- [6] N. Zhao, Z. Wang, C. Cai, H. Shen, F. Liang, D. Wang, C. Wang, T. Zhu, J. Guo, Y. Wang, X. Liu, C. Duan, Wang H., Y. Mao, X Jia, H. Dong, X. Zhang, and J. Xu. Bioinspired materials: from low to high dimensional structure. *Advanced Materials*, 26(41):6994–7017, 2014.
- [7] J. Strauß and R. Lakes-Harlan. Evolutionary and phylogenetic origins of tympanal hearing organs in insects. In *Insect hearing and Acoustic Communication*, pages 5–26. Springer, 2014.
- [8] D. D. Yager. Structure, development, and evolution of insect auditory systems. *Microscopy Research and Technique*, 47(6):380–400, 1999.
- [9] R. R. Hoy and D. Robert. Tympanal hearing in insects. *Annual Review of Entomology*, 41(1):433–450, 1996.

-
- [10] P. T. Haskell. Stridulation and associated behaviour in certain orthoptera. 1. analysis of the stridulation of, and behaviour between, males. *The British Journal of Animal Behaviour*, 5(4):139–148, 1957.
- [11] J. F. C. Windmill, M. C Göpfert, and D. Robert. Tympanal travelling waves in migratory locusts. *Journal of Experimental Biology*, 208(1):157–168, 2005.
- [12] S. Bose, S. Vahabzadeh, and A. Bandyopadhyay. Bone tissue engineering using 3d printing. *Materials Today*, 16(12):496–504, 2013.
- [13] M. Guvendiren, J. Molde, R. M. D. Soares, and J. Kohn. Designing biomaterials for 3d printing. *ACS Biomaterials Science & Engineering*, 2(10):1679–1693, 2016.
- [14] J. A Lewis and B. Y. Ahn. Device fabrication: Three-dimensional printed electronics. *Nature*, 518(7537):42, 2015.
- [15] A. Uriondo, M. Esperon-Miguez, and S. Perinpanayagam. The present and future of additive manufacturing in the aerospace sector: A review of important aspects. *Proceedings of the Institution of Mechanical Engineers, Part G: Journal of Aerospace Engineering*, 229(11):2132–2147, 2015.
- [16] S. V Murphy and A. Atala. 3d bioprinting of tissues and organs. *Nature Biotechnology*, 32(8):773, 2014.
- [17] K. S Novoselov, A. K. Geim, S. V Morozov, D. Jiang, Y. Zhang, S. V. Dubonos, I. V. Grigorieva, and A. A. Firsov. Electric field effect in atomically thin carbon films. *Science*, 306(5696):666–669, 2004.
- [18] L. Feng, S. Li, Y. Li, H. Li, L. Zhang, J. Zhai, Y. Song, B. Liu, L. Jiang, and D. Zhu. Super-hydrophobic surfaces: from natural to artificial. *Advanced Materials*, 14(24):1857–1860, 2002.
- [19] D. Kim and J. Moon. Highly conductive ink jet printed films of nanosilver particles for printable electronics. *Electrochemical and Solid-State Letters*, 8(11):J30–J33, 2005.
- [20] 3D printing for Architects — Leapfrog 3D Printers. <https://www.lpfrg.com/en/professionals/architects/>. [Online; last accessed 08-January-2018].
- [21] 14 Ways 3D Printing Has Changed The Art World. http://www.huffingtonpost.co.uk/entry/3d-printing-art_n_5534459. [Online; last accessed 2089-January-2018].

-
- [22] J. Sun, W. Zhou, D. Huang, J. YH Fuh, and G. S. Hong. An overview of 3d printing technologies for food fabrication. *Food and Bioprocess Technology*, 8(8):1605–1615, 2015.
- [23] D. J. Mackie. *Biologically inspired acoustic systems: from insect ears to MEMS microphone structures*. PhD thesis, University of Strathclyde, 2015.
- [24] F. Hansen. Approximations for the thermodynamic and transport properties of high-temperature air. Technical report, National Aeronautics and Space Administration Washington DC, 1958.
- [25] G. S. K. Wong. Speed of sound in standard air. *The Journal of the Acoustical Society of America*, 79(5):1359–1366, 1986.
- [26] G. S. K. Wong and T. F. W. Embleton. Variation of the speed of sound in air with humidity and temperature. *The Journal of the Acoustical Society of America*, 77(5):1710–1712, 1985.
- [27] D. H. Peregrine. The acoustic bubble. by tg l eighton. academic press, 1994. 613 pp.£ 95. isbn 0-12-441920-8. *Journal of Fluid Mechanics*, 272:407–408, 1994.
- [28] L. Cremer and H. A. Müller. *Die wissenschaftlichen grundlagen der raumakustik*. Hirzel Stuttgart, 1978.
- [29] A. Moreno, J. G Zaragoza, and F. Alcantarilla. Generation and suppression of flutter echoes in spherical domes. *Journal of the Acoustical Society of Japan (E)*, 2(4):197–202, 1981.
- [30] N. Bilaniuk and G. S. K. Wong. Speed of sound in pure water as a function of temperature. *The Journal of the Acoustical Society of America*, 93(3):1609–1612, 1993.
- [31] M. F Bolotnikov, Y. A. Neruchev, Y. F. Melikhov, V. N. Vervevko, and M. V. Vervevko. Temperature dependence of the speed of sound, densities, and isentropic compressibilities of hexane+ hexadecane in the range of (293.15 to 373.15) k. *Journal of Chemical & Engineering Data*, 50(3):1095–1098, 2005.
- [32] M. Garstang, D. Larom, R. Raspet, and M. Lindeque. Atmospheric controls on elephant communication. *Journal of Experimental Biology*, 198(4):939–951, 1995.
- [33] D. Robert. The auditory behaviour of flying locusts. *Journal of Experimental Biology*, 147(1):279–301, 1989.
- [34] F. Lemoult, M. Fink, and G. Lerosey. Acoustic resonators for far-field control of sound on a subwavelength scale. *Physical Review Letters*, 107(6):064301, 2011.

-
- [35] S. A. Cummer, J. Christensen, and A. Alù. Controlling sound with acoustic metamaterials. *Nature Reviews Materials*, 1:16001, 2016.
- [36] H. F. Olson. *Elements of Acoustical Engineering*. D. Van Nostrand Company, 1947.
- [37] M. J. Crocker. *Handbook of acoustics*. John Wiley & Sons, 1998.
- [38] F. Coro and M. Kössl. Distortion-product otoacoustic emissions from the tympanic organ in two noctuid moths. *Journal of Comparative Physiology A*, 183(4):525–531, 1998.
- [39] F. Montealegre-Z. El refinado oído del saltamontes. *Investigacion y ciencia*, 2014.
- [40] F. Montealegre-Z, T. Jonsson, K. A. Robson-Brown, M. Postles, and D. Robert. Convergent evolution between insect and mammalian audition. *Science*, 338(6109):968–971, 2012.
- [41] R. O. Stephen and H. C. Bennet-Clark. The anatomical and mechanical basis of stimulation and frequency analysis in the locust ear. *Journal of Experimental Biology*, 99(1):279–314, 1982.
- [42] J. E. Yack. The structure and function of auditory chordotonal organs in insects. *Microscopy Research and Technique*, 63(6):315–337, 2004.
- [43] D. F. Eberl. Feeling the vibes: chordotonal mechanisms in insect hearing. *Current Opinion in Neurobiology*, 9(4):389–393, 1999.
- [44] L. A. Miller. Structure of the green lacewing tympanal organ (*chrysopa carnea*, neuroptera). *Journal of Morphology*, 131(4):359–382, 1970.
- [45] P. Kummer, T. Janssen, and W. Arnold. Suppression tuning characteristics of the $2f - 1f$ distortion-product otoacoustic emission in humans. *The Journal of the Acoustical Society of America*, 98(1):197–210, 1995.
- [46] M. Mauermann, S. Uppenkamp, P. W. J. van Hengel, and B. Kollmeier. Evidence for the distortion product frequency place as a source of distortion product otoacoustic emission (dpoae) fine structure in humans. ii. fine structure for different shapes of cochlear hearing loss. *The Journal of the Acoustical Society of America*, 106(6):3484–3491, 1999.
- [47] A. L. Thuras, R. T. Jenkins, and H. T. O’Neil. Extraneous frequencies generated in air carrying intense sound waves. *The Bell System Technical Journal*, 14(1):159–172, 1935.

-
- [48] D. T. Kemp. Otoacoustic emissions, their origin in cochlear function, and use. *British Medical Bulletin*, 63(1):223–241, 2002.
- [49] M. Faulstich and M. Kössl. Evidence for multiple dpoae components based upon group delay of the 2f1- f2 distortion in the gerbil. *Hearing Research*, 140(1-2):99–110, 2000.
- [50] J. Freets. Disentangle rf amplifier specs: intermodulation distortion and intercept points, 2016.
- [51] R. E. Mickens. *An introduction to nonlinear oscillations*. CUP Archive, 1981.
- [52] Identification of a Duffing Oscillator under Different Types of Excitation. <https://www.hindawi.com/journals/mpe/2010/695025/fig4/>. [Online; last accessed 07-March-2018].
- [53] K. Murali and M. Lakshmanan. Transmission of signals by synchronization in a chaotic van der pol–duffing oscillator. *Physical Review E*, 48(3):R1624, 1993.
- [54] G. Failla and A. Pirrotta. On the stochastic response of a fractionally-damped duffing oscillator. *Communications in Nonlinear Science and Numerical Simulation*, 17(12):5131–5142, 2012.
- [55] I. Kovacic and M. J. Brennan. *The Duffing equation: nonlinear oscillators and their behaviour*. John Wiley & Sons, 2011.
- [56] E. N. Lorenz. Deterministic nonperiodic flow. *Journal of the Atmospheric Sciences*, 20(2):130–141, 1963.
- [57] S. S. Motsa and P. Sibanda. A note on the solutions of the van der pol and duffing equations using a linearisation method. *Mathematical Problems in Engineering*, 2012, 2012.
- [58] A. Kandangath, S. Krishnamoorthy, Y.-C. Lai, and J. A. Gaudet. Inducing chaos in electronic circuits by resonant perturbations. *IEEE Transactions on Circuits and Systems I: Regular Papers*, 54(5):1109–1119, 2007.
- [59] G. C. Das and J. Sarma. A new mathematical approach for finding the solitary waves in dusty plasma. *Physics of Plasmas*, 5(11):3918–3923, 1998.
- [60] K. Wiesenfeld and B. McNamara. Period-doubling systems as small-signal amplifiers. *Physical Review Letters*, 55(1):13, 1985.
- [61] D. Möckel, E.-A. Seyfarth, and M. Kössl. Otoacoustic emissions in bushcricket ears: general characteristics and the influence of the neuroactive insecticide pymetrozine. *Journal of Comparative Physiology A*, 197(2):193–202, 2011.

-
- [62] Mechanoreceptors. <http://www.biology-pages.info/M/Mechanoreceptors.html>. [Online; last accessed 11-March-2017].
- [63] P. J. J. Lamoré and C. J. Keemink. Evidence for different types of mechanoreceptors from measurements of the psychophysical threshold for vibrations under different stimulation conditions. *The Journal of the Acoustical Society of America*, 83(6):2339–2351, 1988.
- [64] K. Jacobs, B. Otte, and R. Lakes-Harlan. Tympanal receptor cells of *schistocerca gregaria*: correlation of soma positions and dendrite attachment sites, central projections and physiologies. *Journal of Experimental Zoology Part A: Ecological Genetics and Physiology*, 283(3):270–285, 1999.
- [65] R. Lakes, K. Kalmring, and K.-H. Engelhard. Changes in the auditory system of locusts (*locusta migratoria* and *schistocerca gregaria*) after deafferentation. *Journal of Comparative Physiology A*, 166(4):553–563, 1990.
- [66] E. G. Gray. The fine structure of the insect ear. *Philosophical Transactions of the Royal Society B*, 243(700):75–94, 1960.
- [67] R. J. Pumphrey and A. F. Rawdon-Smith. Hearing in insects: The nature of the response of certain receptors to auditory stimuli. In *Proceedings of the Royal Society B: Biological Sciences*, volume 121, pages 18–27. The Royal Society, 1936.
- [68] A. Michelsen. Physiology of the locust ear. ii. frequency discrimination based upon resonances in the tympanum. *Zeitschrift für vergleichende Physiologie*, 1971.
- [69] G. A. Horridge. Pitch discrimination in orthoptera (insecta) demonstrated by responses of central auditory neurones. *Nature*, 185(4713):623, 1960.
- [70] A. Michelsen. Pitch discrimination in the locust ear: observations on single sense cells. *Journal of Insect Physiology*, 12(9):1119–1131, 1966.
- [71] A. V. Popov. Electrophysiological studies on peripheral auditory neurons in the locust. *Journal of Evolutionary Biochemistry and Physiology*, 1:239–250, 1965.
- [72] J. F. C. Windmill, S. Bockenhauer, and D. Robert. Time-resolved tympanal mechanics of the locust. *Journal of The Royal Society Interface*, 5(29):1435–1443, 2008.
- [73] L. A. Miller. Directional hearing in the locusts *schistocerca gregaria* forskål (acrididae, orthoptera). *Journal of Comparative Physiology*, 119(1):85–98, 1977.

-
- [74] D. Möckel, E.-A. Seyfarth, and M. Kössl. The generation of dpoaes in the locust ear is contingent upon the sensory neurons. *Journal of Comparative Physiology A*, 193(8):871–879, 2007.
- [75] M. Kössl and G. S. Boyan. Acoustic distortion products from the ear of a grasshopper. *The Journal of the Acoustical Society of America*, 104(1):326–335, 1998.
- [76] P. Dallos. The active cochlea. *Journal of Neuroscience*, 12(12):4575–4585, 1992.
- [77] R. Malkin, T. R. McDonagh, N. Mhatre, T. S. Scott, and D. Robert. Energy localization and frequency analysis in the locust ear. *Journal of The Royal Society Interface*, 11(90):20130857, 2014.
- [78] M. S. Weinberg, C. E. Dube, A. Petrovich, and A. M. Zapata. Fluid damping in resonant flexural plate wave device. *Journal of Microelectromechanical Systems*, 12(5):567–576, 2003.
- [79] A. A. Gubaidullin, O. Y. Kuchugurina, D. M. J. Smeulders, and C. J. Wisse. Frequency-dependent acoustic properties of a fluid/porous solid interface. *The Journal of the Acoustical Society of America*, 116(3):1474–1480, 2004.
- [80] L. A. Estroff and A. D. Hamilton. At the interface of organic and inorganic chemistry: Bioinspired synthesis of composite materials. *Chemistry of Materials*, 13(10):3227–3235, 2001.
- [81] T. Sun, L. Feng, X. Gao, and L. Jiang. Bioinspired surfaces with special wettability. *Accounts of Chemical Research*, 38(8):644–652, 2005.
- [82] C. Sanchez, H. Arribart, and M. M. G. Guille. Biomimetism and bioinspiration as tools for the design of innovative materials and systems. *Nature Materials*, 4(4):277–288, 2005.
- [83] M. Calisti, M. Giorelli, G. Levy, B. Mazzolai, B. Hochner, C. Laschi, and P. Dario. An octopus-bioinspired solution to movement and manipulation for soft robots. *Bioinspiration & Biomimetics*, 6(3):036002, 2011.
- [84] V. Kopman and M. Porfiri. Design, modeling, and characterization of a miniature robotic fish for research and education in biomimetics and bioinspiration. *IEEE/ASME Transactions on Mechatronics*, 18(2):471–483, 2013.
- [85] G. J. M. Krijnen, M. Dijkstra, J. J. van Baar, S. S. Shankar, W. J. Kuipers, R. J. H. de Boer, D. Altpeter, T. S. J. Lammerink, and R. Wiegerink. Mems based hair flow-sensors as model systems for acoustic perception studies. *Nanotechnology*, 17(4):S84, 2006.

-
- [86] M. Dijkstra, J. J. Van Baar, R. J. Wiegerink, T. S. J. Lammerink, J. H. De Boer, and G. J. M. Krijnen. Artificial sensory hairs based on the flow sensitive receptor hairs of crickets. *Journal of Micromechanics and Microengineering*, 15(7):S132, 2005.
- [87] J.-S. Lee, J. M. Hong, J. W. Jung, J.-H. Shim, J.-H. Oh, and D.-W. Cho. 3d printing of composite tissue with complex shape applied to ear regeneration. *Biofabrication*, 6(2):024103, 2014.
- [88] V. Mironov, T. Boland, T. Trusk, G. Forgacs, and R. R. Markwald. Organ printing: computer-aided jet-based 3d tissue engineering. *Trends in Biotechnology*, 21(4):157–161, 2003.
- [89] R. Gaetani, P. A. Doevendans, C. H. G. Metz, J. Alblas, E. Messina, A. Giacomello, and J. P. G. Sluijter. Cardiac tissue engineering using tissue printing technology and human cardiac progenitor cells. *Biomaterials*, 33(6):1782–1790, 2012.
- [90] K. Jakab, C. Norotte, F. Marga, K. Murphy, G. Vunjak-Novakovic, and G. Forgacs. Tissue engineering by self-assembly and bio-printing of living cells. *Biofabrication*, 2(2):022001, 2010.
- [91] J. G. Zhou, D. Herscovici, and C. C. Chen. Parametric process optimization to improve the accuracy of rapid prototyped stereolithography parts. *International Journal of Machine Tools and Manufacture*, 40(3):363–379, 2000.
- [92] B. Mueller. Additive manufacturing technologies—rapid prototyping to direct digital manufacturing. *Assembly Automation*, 32(2), 2012.
- [93] C. K. Chua, K. F. Leong, and C. S. Lim. *Rapid prototyping: principles and applications*. World Scientific, 2010.
- [94] E. Macdonald, R. Salas, D. Espalin, M. Perez, E. Aguilera, D. Muse, and R. B. Wicker. 3d printing for the rapid prototyping of structural electronics. *IEEE access*, 2:234–242, 2014.
- [95] B. C. Gross, J. L. Erkal, S Y Lockwood, C Chen, and DM Spence. Evaluation of 3d printing and its potential impact on biotechnology and the chemical sciences, 2014.
- [96] F. Xu, H. T. Loh, and Y. S. Wong. Considerations and selection of optimal orientation for different rapid prototyping systems. *Rapid Prototyping Journal*, 5(2):54–60, 1999.
- [97] G. Wypych. *Handbook of polymers*. Elsevier, 2016.

-
- [98] M. J. John and S. Thomas, editors. *Natural Polymers*. RSC Green Chemistry. The Royal Society of Chemistry, 2012. ISBN 978-1-84973-402-8. doi: 10.1039/9781849735193. URL <http://dx.doi.org/10.1039/9781849735193>.
- [99] D. A. Wahl and J. T. Czernuszka. Collagen-hydroxyapatite composites for hard tissue repair. *Eur Cell Mater*, 11:43–56, 2006.
- [100] K. Madhavan, D. Belchenko, and W. Tan. Roles of genipin crosslinking and biomolecule conditioning in collagen-based biopolymer: Potential for vascular media regeneration. *Journal of Biomedical Materials Research Part A*, 97(1):16–26, 2011.
- [101] D. W. Hutmacher. Scaffold design and fabrication technologies for engineering tissues—state of the art and future perspectives. *Journal of Biomaterials Science, Polymer Edition*, 12(1):107–124, 2001.
- [102] P. A. Gunatillake and R. Adhikari. Biodegradable synthetic polymers for tissue engineering. *European Cells and Materials*, 5(1):1–16, 2003.
- [103] A. K. Mohanty, M. Misra, and L. T. Drzal. Sustainable bio-composites from renewable resources: opportunities and challenges in the green materials world. *Journal of Polymers and the Environment*, 10(1-2):19–26, 2002.
- [104] P. D. Hustad. Frontiers in olefin polymerization: Reinventing the world’s most common synthetic polymers. *Science*, 325(5941):704–707, 2009.
- [105] P. Majumder. The 5 most important classification of polymers. *Journal of Biomaterials Science, Polymer Edition*, 8(1):63–75, 1997.
- [106] InnovateUs. What is the process of Polymerization? <http://www.innovateus.net/innopedia/what-process-polymerization>, 2013. [Online; last accessed 30-August-2017].
- [107] W. H. Carothers. Studies on polymerization and ring formation. i. an introduction to the general theory of condensation polymers. *Journal of the American Chemical Society*, 51(8):2548–2559, 1929.
- [108] R. F. Landel and L. E. Nielsen. *Mechanical properties of polymers and composites*. CRC press, 1993.

-
- [109] P. J. Bártolo. *Stereolithography: materials, processes and applications*. Springer Science & Business Media, 2011.
- [110] F. P. W. Melchels, J. Feijen, and D. W. Grijpma. A review on stereolithography and its applications in biomedical engineering. *Biomaterials*, 31(24):6121–6130, 2010.
- [111] I. Roppolo, A. Chiappone, A. Angelini, S. Stassi, F. Frascella, C. F. Pirri, C. Ricciardi, and E. Descrovi. 3d printable light-responsive polymers. *Materials Horizons*, 4(3):396–401, 2017.
- [112] B. M. Tymrak, M. Kreiger, and J. M. Pearce. Mechanical properties of components fabricated with open-source 3-d printers under realistic environmental conditions. *Materials & Design*, 58:242–246, 2014.
- [113] R. A. Giordano, B. M. Wu, S. W. Borland, L. G. Cima, E. M. Sachs, and M. J. Cima. Mechanical properties of dense polylactic acid structures fabricated by three dimensional printing. *Journal of Biomaterials Science, Polymer Edition*, 8(1):63–75, 1997.
- [114] Materials-Products Asiga. <https://www.asiga.com/products/materials/>. [Online; last accessed 29-August-2017].
- [115] Materiales de impresion 3D. <http://www.stratasys.com/es/materiales>. [Online; last accessed 29-August-2017].
- [116] ProtoLabs: Manufacturing Materials. <https://www.protolabs.co.uk/materials/select-a-material/>. [Online; last accessed 29-August-2017].
- [117] Fabricating Hand by Hand, For Those Without. <https://handsmith.org/>. [Online; last accessed 29-August-2017].
- [118] Saphium Biotechnologie. <http://www.saphium.eu/>. [Online; last accessed 29-August-2017].
- [119] High Strength 3D Printing - Markforged. <https://markforged.com/>. [Online; last accessed 29-August-2017].
- [120] Cartesian Co - Argentum. <https://cartesianco.com/>. [Online; last accessed 29-August-2017].
- [121] Biobots. <https://biobots.io/>. [Online; last accessed 29-August-2017].
- [122] Made in Space. <http://madeinspace.us/>. [Online; last accessed 29-August-2017].
- [123] Apis Cor. We print buildings. <http://apis-cor.com/en/>. [Online; last accessed 29-August-2017].

- [124] Natural Machines: The makers of foodini - a 3D food printer making all types of fresh, nutritious foods. <https://www.naturalmachines.com/>. [Online; last accessed 29-August-2017].
- [125] Polymer Database. Chain-growth versus step-growth polymerization. <http://polymerdatabase.com/polymer%20chemistry/Chain%20versus%20Step%20Growth.html>, 2015. [Online; last accessed 31-August-2017].
- [126] B. Depalle, Z. Qin, S. J. Shefelbine, and M. J. Buehler. Influence of cross-link structure, density and mechanical properties in the mesoscale deformation mechanisms of collagen fibrils. *Journal of the Mechanical Behavior of Biomedical Materials*, 52:1–13, 2015.
- [127] M. A. Tehfe, F. Louradour, J. Lalevée, and J.-P. Fouassier. Photopolymerization reactions: On the way to a green and sustainable chemistry. *Applied Sciences*, 3(2):490–514, 2013.
- [128] J.-P. Fouassier and J. LalevÁ. *Photoinitiators for Polymer Synthesis: Scope, Reactivity, and Efficiency*. John Wiley & Sons, 2012.
- [129] Polymer Science Learning Center. Free Radical Vinyl Polymerization. <http://www.pslc.ws/macrog/radical.htm>, 2003. [Online; last accessed 29-August-2017].
- [130] Free Radical Chemistry. https://s10.lite.msu.edu/res/msu/botonl/b_online/library/newton/Chy251_253/Lectures/Free_Radicals/FreeRadicals.html. [Online; last accessed 01-September-2017].
- [131] Polymer Science Learning Center. Cationic Vinyl Polymerization. <http://pslc.ws/macrog/cationic.htm>, 2003. [Online; last accessed 29-August-2017].
- [132] C. S. Lee, S. G. Kim, H. J. Kim, and S. H. Ahn. Measurement of anisotropic compressive strength of rapid prototyping parts. *Journal of Materials Processing Technology*, 187:627–630, 2007.
- [133] P. Alexander, S. Allen, and D. Dutta. Part orientation and build cost determination in layered manufacturing. *Computer-Aided Design*, 30(5):343–356, 1998.
- [134] D. Frank and G. Fadel. Expert system-based selection of the preferred direction of build for rapid prototyping processes. *Journal of Intelligent Manufacturing*, 6(5):339–345, 1995.
- [135] T. Mahrholz, J. Stängle, and M. Sinapius. Quantitation of the reinforcement effect of silica nanoparticles in epoxy resins used in liquid composite moulding processes. *Composites Part A: Applied Science and Manufacturing*, 40(3):235–243, 2009.

-
- [136] Y. Dong, D. Chaudhary, C. Ploumis, and K.-T. Lau. Correlation of mechanical performance and morphological structures of epoxy micro/nanoparticulate composites. *Composites Part A: Applied Science and Manufacturing*, 42(10):1483–1492, 2011.
- [137] N. Lachman and H. D. Wagner. Correlation between interfacial molecular structure and mechanics in cnt/epoxy nano-composites. *Composites Part A: Applied Science and Manufacturing*, 41(9):1093–1098, 2010.
- [138] Y. Zare. Study of nanoparticles aggregation/agglomeration in polymer particulate nanocomposites by mechanical properties. *Composites Part A: Applied Science and Manufacturing*, 84:158–164, 2016.
- [139] M. A. Meitl, Z.-T. Zhu, V. Kumar, K. J. Lee, X. Feng, Y. Y. Huang, I. Adesida, R. G. Nuzzo, and J. A. Rogers. Transfer printing by kinetic control of adhesion to an elastomeric stamp. *Nature Materials*, 5(1):33–38, 2006.
- [140] Y. Zare. Modeling the strength and thickness of the interphase in polymer nanocomposite reinforced with spherical nanoparticles by a coupling methodology. *Journal of Colloid and Interface Science*, 465:342–346, 2016.
- [141] R. Jin, L. Li, Y. Lian, X. Xu, and F. Zhao. Layered double hydroxide supported prussian blue nanocomposites for electrocatalytic reduction of H_2O_2 . *Analytical Methods*, 4(9):2704–2710, 2012.
- [142] Y. Zare, H. Garmabi, and F. Sharif. Optimization of mechanical properties of pp/nanoclay/caco₃ ternary nanocomposite using response surface methodology. *Journal of Applied Polymer Science*, 122(5):3188–3200, 2011.
- [143] A. Concustell, J. Sort, A. L. Greer, and M. D. Baró. Anelastic deformation of a pd 40 cu 30 ni 10 p 20 bulk metallic glass during nanoindentation. *Applied Physics Letters*, 88(17):171911, 2006.
- [144] E. Linul, L. Marsavina, T. Voiconi, and T. Sadowski. Study of factors influencing the mechanical properties of polyurethane foams under dynamic compression. In *Journal of Physics: Conference Series*, volume 451, page 012002. IOP Publishing, 2013.
- [145] W. C. Oliver and G. M. Pharr. An improved technique for determining hardness and elastic modulus using load and displacement sensing indentation experiments. *Journal of Materials Research*, 7(6):1564–1583, 1992.

- [146] J. B. Wachtman Jr, W. E. Tefft, D. G. Lam Jr, and C. S. Apstein. Exponential temperature dependence of young's modulus for several oxides. *Physical Review*, 122(6):1754, 1961.
- [147] Stiffness (Young's Modulus) — Fine Ceramics (Advanced Ceramics) — Kyocera. <http://global.kyocera.com/prdct/fc/list/tokusei/gousei/index.html>. [Online; last accessed 18-September-2017].
- [148] Polymers - Physical Properties. http://www.engineeringtoolbox.com/polymer-properties-d_1222.html. [Online; last accessed 18-September-2017].
- [149] F. D. Murnaghan. The compressibility of media under extreme pressures. *Proceedings of the National Academy of Sciences*, 30(9):244–247, 1944.
- [150] W. D. Callister Jr and D. G. Rethwisch. *Fundamentals of materials science and engineering: an integrated approach*. John Wiley & Sons, 2012.
- [151] A. C. Fischer-Cripps. A simple phenomenological approach to nanoindentation creep. *Materials Science and Engineering: A*, 385(1-2):74–82, 2004.
- [152] C. A. Schuh. Nanoindentation studies of materials. *Materials Today*, 9(5):32–40, 2006.
- [153] A. M. Minor, S. A. S. Asif, Z. Shan, E. A. Stach, E. Cyrankowski, T. J. Wyrobek, and O. L. Warren. A new view of the onset of plasticity during the nanoindentation of aluminium. *Nature Materials*, 5(9):697, 2006.
- [154] R. Saha and W. D. Nix. Effects of the substrate on the determination of thin film mechanical properties by nanoindentation. *Acta Materialia*, 50(1):23–38, 2002.
- [155] W. C. Oliver and G. M. Pharr. Measurement of hardness and elastic modulus by instrumented indentation: Advances in understanding and refinements to methodology. *Journal of Materials Research*, 19(1):3–20, 2004.
- [156] K. O. Kese, Z.-C. Li, and B. Bergman. Method to account for true contact area in soda-lime glass during nanoindentation with the berkovich tip. *Materials Science and Engineering: A*, 404(1-2):1–8, 2005.
- [157] M Stolka. *Encyclopaedia of polymer science and engineering*, 1988.
- [158] The Design of Composite Materials and Structures. <http://www.mse.mtu.edu/~drjohn/my4150/compositesdesign/cd1/cd1.html>, . [Online; last accessed 08-September-2017].

-
- [159] Property Averaging for Composites: Isostrain. https://fog.ccsf.edu/~wkaufmyn/ENGN45/Course%20Handouts/14_CompositeMaterials/09_Isostrain.html, . [Online; last accessed 08-September-2017].
- [160] J. C. Halpin. Stiffness and expansion estimates for oriented short fiber composites. *Journal of Composite Materials*, 3(4):732–734, 1969.
- [161] K. Prashantha, J. Soulestin, M. F. Lacrampe, M. Claes, G. Dupin, and P. Krawczak. Multi-walled carbon nanotube filled polypropylene nanocomposites based on masterbatch route: Improvement of dispersion and mechanical properties through pp-g-ma addition. *Express Polymer Letters*, 2(10):735–745, 2008.
- [162] R. Abraham, S. P. Thomas, S. Kuryan, J. Isac, K. T. Varughese, and S. Thomas. Mechanical properties of ceramic-polymer nanocomposites. *Express Polymer Letters*, 8(12), 2009.
- [163] T. P Selvin, J. Kuruvilla, and T. Sabu. Mechanical properties of titanium dioxide-filled polystyrene microcomposites. *Materials Letters*, 58(3-4):281–289, 2004.
- [164] E. D. Bliznakov, C. C. White, and M. T. Shaw. Mechanical properties of blends of hdpe and recycled urea-formaldehyde resin. *Journal of Applied Polymer Science*, 77(14):3220–3227, 2000.
- [165] D. W. Van Krevelen and K. Te Nijenhuis. *Properties of polymers: their correlation with chemical structure; their numerical estimation and prediction from additive group contributions*. Elsevier, 2009.
- [166] H. A. Sodano, D. J. Inman, and G. Park. A review of power harvesting from vibration using piezoelectric materials. *Shock and Vibration Digest*, 36(3):197–206, 2004.
- [167] R. E. Hummel. Electrical properties of polymers, ceramics, dielectrics, and amorphous materials. In *Electronic Properties of Materials*, pages 181–211. Springer, 2011.
- [168] S. Tadigadapa and K. Mateti. Piezoelectric mems sensors: state-of-the-art and perspectives. *Measurement Science and Technology*, 20(9):092001, 2009.
- [169] F. Levassort, M. Lethiecq, R. Desmare, and L. P. Tran-Huu-Hue. Effective electroelastic moduli of 3-3 (0-3) piezocomposites. *IEEE Transactions on Ultrasonics, Ferroelectrics, and Frequency Control*, 46(4):1028–1034, 1999.

-
- [170] R. Kar-Gupta and T. A. Venkatesh. Electromechanical response of 1–3 piezoelectric composites: an analytical model. *Acta Materialia*, 55(3):1093–1108, 2007.
- [171] R. Guinovart-Díaz, J. Bravo-Castillero, R. Rodríguez-Ramos, F. J. Sabina, and R. Martínez-Rosado. Overall properties of piezocomposite materials 1–3. *Materials Letters*, 48(2):93–98, 2001.
- [172] H. M. Matt and F. L. di Scalea. Macro-fiber composite piezoelectric rosettes for acoustic source location in complex structures. *Smart Materials and Structures*, 16(4):1489, 2007.
- [173] Y. Yang, L. Tang, and H. Li. Vibration energy harvesting using macro-fiber composites. *Smart Materials and Structures*, 18(11):115025, 2009.
- [174] D. Waller and A. Safari. Corona poling of pzt ceramics and flexible piezoelectric composites. *Ferroelectrics*, 87(1):189–195, 1988.
- [175] K. S Ramadan, D. Sameoto, and S. Evoy. A review of piezoelectric polymers as functional materials for electromechanical transducers. *Smart Materials and Structures*, 23(3):033001, 2014.
- [176] M. Kandpal, C. Sharan, P. Poddar, K. Prashanthi, P. R. Apte, and Ramgopal R. V. Photopatternable nano-composite (su-8/zno) thin films for piezo-electric applications. *Applied Physics Letters*, 101(10):104102, 2012.
- [177] B. Gross, R. Gerhard-Multhaupt, A. Berraissoul, and G. M. Sessler. Electron-beam poling of piezoelectric polymer electrets. *Journal of Applied Physics*, 62(4):1429–1432, 1987.
- [178] K.-I. Park, M. Lee, Y. Liu, S. Moon, G.-T. Hwang, G. Zhu, J. E. Kim, S. O. Kim, D. K. Kim, Z. L. Wang, and K. J. Lee. Flexible nanocomposite generator made of batio₃ nanoparticles and graphitic carbons. *Advanced Materials*, 24(22):2999–3004, 2012.
- [179] K.-B. Kim, D. K. Hsu, B. Ahn, Y.-G. Kim, and D. J. Barnard. Fabrication and comparison of pmn-pt single crystal, pzt and pzt-based 1-3 composite ultrasonic transducers for nde applications. *Ultrasonics*, 50(8):790–797, 2010.
- [180] J. J. Wang, F. Y. Meng, X. Q. Ma, M. X. Xu, and L. Q. Chen. Lattice, elastic, polarization, and electrostrictive properties of batio₃ from first-principles. *Journal of Applied Physics*, 108(3):034107, 2010.

-
- [181] Z.-Y. Shen and J.-F. Li. Enhancement of piezoelectric constant d_{33} in batio3 ceramics due to nano-domain structure. *Journal of the Ceramic Society of Japan*, 118(1382):940–943, 2010.
- [182] L. Dong, D. S. Stone, and R. S. Lakes. Enhanced dielectric and piezoelectric properties of x bazo3-(1- x) batio3 ceramics. *Journal of Applied Physics*, 111(8):084107, 2012.
- [183] P. Dineva, D. Gross, R. Müller, and T. Rangelov. Piezoelectric materials. In *Dynamic Fracture of Piezoelectric Materials*, pages 7–32. Springer, 2014.
- [184] J.-F. Capsal, E. Dantras, L. Laffont, J. Dandurand, and C. Lacabanne. Nanotexture influence of batio3 particles on piezoelectric behaviour of pa 11/batio3 nanocomposites. *Journal of Non-Crystalline Solids*, 356(11-17):629–634, 2010.
- [185] J. M. D. Coey. *Magnetism and magnetic materials*. Cambridge University Press, 2010.
- [186] H. A. M. Snelders. Oersted’s discovery of electromagnetism. *Romanticism and the Sciences*, pages 228–40, 1990.
- [187] R. Thompson. *Environmental magnetism*. Springer Science & Business Media, 2012.
- [188] M. Mikhaylova, D. K. Kim, N. Bobrysheva, M. Osmolowsky, V. Semenov, T. Tsakalagos, and M. Muhammed. Superparamagnetism of magnetite nanoparticles: dependence on surface modification. *Langmuir*, 20(6):2472–2477, 2004.
- [189] Y. Zhang, N. Kohler, and M. Zhang. Surface modification of superparamagnetic magnetite nanoparticles and their intracellular uptake. *Biomaterials*, 23(7):1553–1561, 2002.
- [190] J. Ge, Y. Hu, M. Biasini, W. P. Beyermann, and Y. Yin. Superparamagnetic magnetite colloidal nanocrystal clusters. *Angewandte Chemie International Edition*, 46(23):4342–4345, 2007.
- [191] F. Walz. The verwey transition—a topical review. *Journal of Physics: Condensed Matter*, 14(12):R285, 2002.
- [192] R. Aragón, D. J. Buttrey, J. P. Shepherd, and J. M. Honig. Influence of nonstoichiometry on the verwey transition. *Physical Review B*, 31(1):430, 1985.
- [193] C. E. Diebel, R. Proksch, C. R. Green, P. Neilson, and M. M. Walker. Magnetite defines a vertebrate magnetoreceptor. *Nature*, 406(6793):299, 2000.

- [194] R. B. Frankel, R. P. Blakemore, and R. S. Wolfe. Magnetite in freshwater magnetotactic bacteria. *Science*, 203(4387):1355–1356, 1979.
- [195] J. L. Kirschvink, A. Kobayashi-Kirschvink, and B. J. Woodford. Magnetite biomineralization in the human brain. *Proceedings of the National Academy of Sciences*, 89(16):7683–7687, 1992.
- [196] M. A. M. Banaclocha, I. Bókkon, and H. M. Banaclocha. Long-term memory in brain magnetite. *Medical Hypotheses*, 74(2):254–257, 2010.
- [197] R. Cano, M. Yus, and D. J. Ramón. Impregnated copper or palladium–copper on magnetite as catalysts for the domino and stepwise sonogashira-cyclization processes: a straightforward synthesis of benzo [b] furans and indoles. *Tetrahedron*, 68(5):1393–1400, 2012.
- [198] S. Mornet, S. Vasseur, F. Grasset, and E. Duguet. Magnetic nanoparticle design for medical diagnosis and therapy. *Journal of Materials Chemistry*, 14(14):2161–2175, 2004.
- [199] Q. Q. Xiong, J. P. Tu, Y. Lu, J. Chen, Y. X. Yu, Y. Q. Qiao, X. L. Wang, and C. D. Gu. Synthesis of hierarchical hollow-structured single-crystalline magnetite (Fe_3O_4) microspheres: the highly powerful storage versus lithium as an anode for lithium ion batteries. *The Journal of Physical Chemistry C*, 116(10):6495–6502, 2012.
- [200] G. Herzer. Grain size dependence of coercivity and permeability in nanocrystalline ferromagnets. *IEEE Transactions on Magnetics*, 26(5):1397–1402, 1990.
- [201] J. J. L. Morton. Magnetic properties of materials. part 2: Types of magnetism. *Trinity*, 2012.
- [202] C. Kittel. Physical theory of ferromagnetic domains. *Reviews of Modern Physics*, 21(4):541, 1949.
- [203] J.-F. Berret, O. Sandre, and A. Mauger. Size distribution of superparamagnetic particles determined by magnetic sedimentation. *Langmuir*, 23(6):2993–2999, 2007.
- [204] D. Robert and A. C. Lewin. Scanning laser vibrometry applied to the biomechanical study of a small auditory system. In *Third International Conference on Vibration Measurements by Laser Techniques: Advances and Applications*, volume 3411, pages 564–572. International Society for Optics and Photonics, 1998.
- [205] E. M. Lawrence, K. E. Speller, and D. Yu. Mems characterization using laser doppler vibrometry. In *Reliability, Testing, and Characterization of MEMS/MOEMS II*, volume 4980, pages 51–63. International Society for Optics and Photonics, 2003.

-
- [206] J. Sueur, J. F. C. Windmill, and D. Robert. Tuning the drum: the mechanical basis for frequency discrimination in a mediterranean cicada. *Journal of Experimental Biology*, 209(20):4115–4128, 2006.
- [207] J. F. C. Windmill, J. C. Jackson, E. J. Tuck, and D. Robert. Keeping up with bats: dynamic auditory tuning in a moth. *Current Biology*, 16(24):2418–2423, 2006.
- [208] M. C. Göpfert and D. Robert. Motion generation by drosophila mechanosensory neurons. *Proceedings of the National Academy of Sciences*, 100(9):5514–5519, 2003.
- [209] D. Robert and M. C. Göpfert. Novel schemes for hearing and orientation in insects. *Current Opinion in Neurobiology*, 12(6):715–720, 2002.
- [210] D. E. Oliver, V. Palan, G. Bissinger, and D. Rowe. 3-dimensional laser doppler vibration analysis of a stradivarius violin. In *Proceedings of the 25th International Modal Analysis Conference, Society for Experimental Mechanics, Bethel, CT, USA*, 2007.
- [211] M. Johansmann, Gm Siegmund, and Mm Pineda. Targeting the limits of laser doppler vibrometry. *Proceedings IDEMA*, pages 1–12, 2005.
- [212] S. J. Wildy, B. S. Cazzolato, and A. G. Kotousov. New damage detection technique based on governing differential equations of continuum mechanics. part ii: in-plane loading. In *Proceedings of the 6th Australasian Congress on Applied Mechanics*, page 731. Engineers Australia, 2010.
- [213] G. W. D. Spratt, P. R. Bissell, R. W. Chantrell, and E. P. Wohlfarth. Static and dynamic experimental studies of particulate recording media. *Journal of Magnetism and Magnetic Materials*, 75(3):309–318, 1988.
- [214] T. Thomson, K. O’Grady, and G. Bayreuther. Magnetization reversal mechanisms and time-dependent processes in thin tb/fe multilayer films. *Journal of Physics D: Applied Physics*, 30(11):1577, 1997.
- [215] P. R. Bissell, M. Cerchez, L. Stoleriu, R. W. Chantrell, and A. Stancu. The use of generalized δm plots in the magnetic characterization of particulate media. *Journal of Magnetism and Magnetic Materials*, 266(1-2):1–7, 2003.
- [216] H. W. F. Sung and C. Rudowicz. A closer look at the hysteresis loop for ferromagnets—a survey of misconceptions and misinterpretations in textbooks. *arXiv preprint cond-mat/0210657*, 2002.

- [217] E. P. Wohlfarth. Relations between different modes of acquisition of the remanent magnetization of ferromagnetic particles. *Journal of Applied Physics*, 29(3):595–596, 1958.
- [218] Pear interaction SEM. https://commons.wikimedia.org/wiki/File:Pear_interaction_SEM_english.svg. [Online; last accessed 20-August-2018].
- [219] A. Michelsen. Biophysics of sound localization in insects. In *Comparative Hearing: Insects*, pages 18–62. Springer, 1998.
- [220] J. Curry. Hamiltonian and lagrangian mechanics, vol. 1, 2013.
- [221] M Nebot. Oscilaciones acopladas. apuntes de clase., 2011.
- [222] C. Hutter, D. Platz, E. A. Tholén, T. H. Hansson, and D. B. Haviland. Reconstructing nonlinearities with intermodulation spectroscopy. *Physical Review Letters*, 104(5):050801, 2010.
- [223] E. Tholén. *Intermodulation in microresonators: for microwave amplification and nanoscale surface analysis*. PhD thesis, KTH, 2009.
- [224] J. F. V. Vincent and U. G. K. Wegst. Design and mechanical properties of insect cuticle. *Arthropod Structure & Development*, 33(3):187–199, 2004.
- [225] K. Ikemura, K. Ichizawa, M. Yoshida, S. Ito, and T. Endo. Uv-vis spectra and photoinitiation behaviors of acylphosphine oxide and bisacylphosphine oxide derivatives in unfilled, light-cured dental resins. *Dental Materials Journal*, 27(6):765–774, 2008.
- [226] Ciba Specialty Chemicals. Ciba IRGACURE 819. <http://www.xtgchem.cn/upload/20110629045602.PDF>. [Online; last accessed 08-March-2018].
- [227] S. Waheed, J. M. Cabot, N. P. Macdonald, T. Lewis, R. M. Guijt, B. Paull, and M. C. Breadmore. 3d printed microfluidic devices: enablers and barriers. *Lab on a Chip*, 16(11):1993–2013, 2016.
- [228] M. Rosales, A. K. M. Mabry, E. M. Nehls, and K. S. Anseth. Photoresponsive elastic properties of azobenzene-containing poly (ethylene-glycol)-based hydrogels. *Biomacromolecules*, 16(3):798–806, 2015.
- [229] C. Credi, A. Fiorese, M. Tironi, R. Bernasconi, L. Magagnin, M. Levi, and S. Turri. 3d printing of cantilever-type microstructures by stereolithography of ferromagnetic photopolymers. *ACS Applied Materials & Interfaces*, 8(39):26332–26342, 2016.

- [230] R. M. Jones. *Mechanics of composite materials*. CRC Press, 1998.
- [231] Formulae - Guide to composite materials -NetComposites. <https://netcomposites.com/guide-tools/guide/formulae/>. [Online; last accessed 07-March-2018].
- [232] G. A Manley and P. van Dijk. Otoacoustic emissions in amphibians, lepidosaurs, and archosaurs. In *Active Processes and Otoacoustic Emissions in Hearing*, pages 211–260. Springer, 2008.
- [233] H. Zhang, X. Wang, D. Chen, and C. Che. Resonant frequency shifts of a fluid filled cavity caused by a bubble. In *AIP Conference Proceedings*, volume 1096, pages 1604–1610. AIP, 2009.
- [234] M. B. Şerbetçioğlu and D. J. Parker. Measures of cochlear travelling wave delay in humans: I. comparison of three techniques in subjects with normal hearing. *Acta Oto-laryngologica*, 119(5): 537–543, 1999.
- [235] S. S. Narayan and M. A. Ruggero. Basilar-membrane mechanics at the hook region of the chinchilla cochlea. In *Recent Developments In Auditory Mechanics: (Including Free CD-ROM)*, pages 95–101. World Scientific, 2000.
- [236] W. S. Rhode and A. Recio. Study of mechanical motions in the basal region of the chinchilla cochlea. *The Journal of the Acoustical Society of America*, 107(6):3317–3332, 2000.
- [237] N. P. Cooper and W. S. Rhode. Basilar membrane mechanics in the hook region of cat and guinea-pig cochleae: sharp tuning and nonlinearity in the absence of baseline position shifts. *Hearing Research*, 63(1-2):163–190, 1992.
- [238] I. J. Russell and K. E. Nilsen. The location of the cochlear amplifier: spatial representation of a single tone on the guinea pig basilar membrane. *Proceedings of the National Academy of Sciences*, 94(6):2660–2664, 1997.
- [239] Precision Acoustics. Guid to using poled pvdf. pvdf properties and uses.